Title

Multi-scale investigations on the impacts of geologic fractures

Author

Higa, Justin T

Publication Date

2023

Peer reviewed|Thesis/dissertation

UNIVERSITY OF CALIFORNIA

Los Angeles

Multi-scale investigations on the impacts of geologic fractures

A dissertation submitted in partial satisfaction of the requirements for the degree Doctor of Philosophy in Geology

by

Justin Takeshi Higa

2023

ABSTRACT OF THE DISSERTATION

Multi-scale investigations on the impacts of

geologic fractures

by

Justin Takeshi Higa

Doctor of Philosophy in Geology

University of California, Los Angeles, 2023

Professor Seul Gi Moon, Chair

Fracturing is a fundamental mechanical weathering process that affects geology from global tectonics to local outcrops. Despite vast differences in size, fractures are formed through similar mechanisms and have interdependent relationships, where small fractures can contribute to the formation of larger ones and vice versa. Chapter 1 of this dissertation introduces the study of fractures and their wide-ranging effects on plate tectonics and landscape weathering. The subsequent chapters describe three research projects focused on the impacts of fractures on tectonic and geomorphological processes at two locations on the west coast of North America. These studies utilize a diverse array of methods from various fields, including geomorphology, structural geology, geochronology, hydrology, and geophysics. Together, this dissertation summarizes how fractures influence Earth's history in fault systems, weathered profiles, and landslides.

Chapter 2 describes how faults on microcontinents record the dynamic evolution of plate boundaries. However, most microcontinents are submarine and difficult to study. Here, I show that the southern part of the Isla Ángel de la Guarda (IAG) microcontinent, in the northern Gulf of California rift, is densely faulted by a late Quaternary-active normal fault zone. To characterize the onshore kinematics of this Almeja fault zone, I integrate remote fault mapping using high-resolution satellite- and drone-based topography with neotectonic field mapping. I then analyzed 13 luminescence ages from sediment deposits offset or impounded by faults to constrain the timing of fault offsets. I found that north-striking normal faults in the Almeja fault zone continue offshore to the south and likely into the nascent North Salsipuedes basin southwest of IAG. Late Pleistocene and Holocene luminescence ages indicate that the most recent onshore fault activity occurred in the last ~50 kyr. These observations suggest that the North Salsipuedes basin is kinematically linked with and continues onshore as the active Almeja fault zone. I suggest that fragmentation of the evolving IAG microcontinent may not yet be complete and that the Pacific-North America plate boundary is either not fully localized onto the Ballenas transform fault and Lower Delfin pull-apart basin or is in the initial stage of a plate boundary reorganization.

In Chapter 3, I explain how diverse mechanical and chemical processes contribute to the breakdown of fresh bedrock and generate the geologic critical zone (CZ) consisting of soil, saprolite, and weathered bedrock. The deep CZ can extend from 1 – 100's m below ground. However, the spatial and depth distribution of weathered bedrock is difficult to determine from Earth's surface. In this study, I investigate the deep CZ structures at a well-studied, steep, and forested site near Coos Bay, Oregon, USA, using a combination of geophysical methods and process-based modeling. P-wave seismic refraction surveys show a sharp velocity transition at a

surface-parallel, ~5 m-deep, and relatively slow velocity contour of 1220 m/s. I also show another transition near contours of 2200 m/s with spatially varying and undulating patterns. These boundaries may represent pervasively oxidized bedrock and fractured bedrock layers observed in a nearby, deep borehole. Then, comparison with Schmidt hammer and ground penetrating radar data reveal areas of highly weathered, porous, and heterogeneous soil and saprolite. I compare these datasets with two process-based models that predict weathered bedrock structures: one based on bedrock drainage of reactive water and the other on topographic stress-induced fracturing. Although these models can reproduce some first-order similarities in my surveys, the mismatch between simulated and inferred weathering may suggest other factors, such as pre-existing fractures, lithological heterogeneity, or landscape evolution, may contribute to variations in the deep CZ. Together, this study underscores the importance of site-specific field observations to evaluate bedrock weathering processes in natural landscapes.

Then, Chapter 4 investigates CZ controls on the occurrence of shallow soil landslides at the study site of Chapter 3, where mechanical and chemical processes may have generated weathered bedrock with increased porosities and hydraulic conductivities underneath soil. Field studies suggest that exfiltrating groundwater from weathered bedrock may be an important driver of initiating shallow landslides. However, variations of deep CZ structure are typically not considered in slope stability models due to a lack of information about the subsurface. Here, I conduct numerical experiments coupling process-based models of 1) deep critical zone development, 2) three-dimensional transient hydrology, and 3) multidimensional slope stability. I show that spatial variations of weathered bedrock thickness control the location of infiltrating and exfiltrating groundwater seepage, induce pore pressure variations at the soil-bedrock boundary, and impact shallow landslide occurrence, size, and location. This work suggests that characterizing

the deep CZ is critical for effectively simulating groundwater seepage and assessing the likelihood, magnitude, and timing of shallow landslides.

The dissertation of Justin Takeshi Higa is approved.

Giuseppe Formetta

Gilles F. Peltzer

An Yin

Seul Gi Moon, Committee Chair

University of California, Los Angeles

2023

Dedicated to Grandpa Suekichi Higa

Table of Contents

List of Figures

List of Tables

Acknowledgements

First, thank you to Seulgi Moon for advising me these past five years and teaching me how science is done. I greatly appreciate the long hours editing my manuscripts and presentations, planning fieldwork, and providing career guidance throughout the years. Thank you to my UCLA committee, An Yin and Gilles Peltzer, also for your guidance, discussions, and field trips that introduced me to Californian geology. Thank you to my committee member from the University of Trento, Giuseppe Formetta, for your thoughtful collaboration from across the globe and willingness to participate in my defense despite the time difference.

Thank you to the current and former members UCLA Geomorphology Lab for camaraderie and thousands of hours of friendship along the way. Marina Argueta, Nathan Brown, Xuesong Ding, Maya Gross, Amanda Hunt, Heather Kirkpatrick, Christina Kitamikado, Boontigan Kuhasubpasin, Josh Lee, Terry Lee, Gen Li, Al Neely, Zach Plante, Sourav Saha, and Kevin Shao, I cannot overstate how much I appreciate getting to know you all. Thank you to all the EPSS graduate and undergraduate students I have gotten to know over the years. And thank you to the EPSS admin, particularly Eric Wessenauer and Lauri Holbrook, for your guidance with fieldwork, gear, and logistics.

Thank you to my Hawai‘i friends who I followed to California, Michaela, Priscilla, Rise, and Varrick, for helping keep a piece of home with me here on the mainland. I also thank Cat, Diamond, Natalie, Orion, and Zach from UH Mānoa for hanging out with me whenever I was back home or visiting me in California. Also, thank you Emily for gaming with me.

I thank the Ryukyu Koten Afuso Ryu Ongaku Kenkyuu Choichi Kai Los Angeles and Hawai‘i for allowing me to continue sanshin during graduate school. Thank you, Ryan Sensei, Yuko, Don, and the entire Los Angeles class for having me, and thank you June Sensei, Kenton

Sensei, and Masanduu Sensei for your continued support from Hawai‘i. いっぺーにふぇーでーびる！

Lastly, thank you to my family. Mom, Dad, Lauren, Grandma Higa, Grandma and Grandpa Yamanoha, thank you for supporting me from near and far throughout my entire life. I would not be here without your constant encouragement. I look forward to using what I gained from UCLA to somehow repay you all for everything and I wish Grandpa Higa were still here to see this.

Chapter 2 is a version of Higa, J.T.*, Brown, N.D.*, Moon, S., Stock, J.M., Sabbeth, L., Bennett, S.E.K., Barajas, A.M., Argueta, M.O. (2022). Microcontinent Breakup and Links to Possible Plate Boundary Reorganization in the Northern Gulf of California, México. *Tectonics*, *41*, e2021TC006933. https://doi.org/10.1029 /2021TC006933. (* co-first author). Principal investigators for this project are Seulgi Moon, Joann M. Stock, and Arturo Martín-Barajas. We thank the Secretaría de Gobernación and SEMARNAT for permits, J. Lin and M. Say for fieldwork, R. Arce, M. Camacho, and I. Covarrubias Rodreguez for boat transportation, C. Athanassas, M. Darin, M. Diggles, M. Oskin, K. Scharer, one anonymous reviewer, and editors L. Giambiagi and M. Rusmore for thorough reviews, and X. Ding, H. Kirkpatrick, C. Kitamikado, B. Kuhasubpasin, S. Saha, and K. Shao for discussion. Support provided by NSF EAR-1728145 to Moon and EAR-1728690 to Stock, CONACYT 2014242561 to Martín-Barajas, National Aeronautics and Space Administration contract 80NM0018D0004 to Sabbeth at Jet Propulsion Laboratory, California Institute of Technology, and the U.S. Geological Survey's National Cooperative Geologic Mapping Program to Bennett. Topography and luminescence data produced here are available at the UCLA Dataverse repository (https://dataverse.ucla.edu/dataverse/iag1_project/).

Chapter 3 is a version of Higa, J.T., Formetta, G., Bellugi, D.G., Busti, R., Dietrich, W.E., Ebel, B.A., Milledge D.G., Moon, S., in prep. Spatially varying critical zone structures at a steep, forested site near Coos Bay, Oregon. Then, Chapter 4 is a version of Higa, J.T., Formetta, G., Bellugi, D.G., Busti, R., Dietrich, W.E., Milledge D.G., Ebel, B.A., Moon, S., in prep. Deep critical zone controls on shallow landslides: insights from numerical simulations in a steep, forested landscape. The principal investigator for these projects is Seulgi Moon. We thank S.P. Anderson, M. Gross, V. Jaramillo, B. Kuhasubpasin, J. Lee, T. Lee, S.J. Martel, D.M. Rempe, J.J. Roering, and M. Sanders for fieldwork and logistics, B. Kuhasubpasin for graphics, M.O. Argueta, X. Ding, Z. Langdalen, K.M. Schmidt, and K. Shao for discussion, R.W. Clayton and the Bedrock Critical Zone Network (W.S Holbrook, B.J. Carr, A.L. Li, and R.P. Callahan) for seismic discussion, D.A. Paige, T.M. Powell, and J. Venkatraman for ground penetrating radar discussion, J.L. Hayes for porosity code, and Weyerhaeuser Co. and S. Strain for permits. This work used computational and storage services associated with the Hoffman2 Shared Cluster provided by UCLA Institute for Digital Research and Education's Research Technology Group. Support provided by NSF EAR-1945431 and -2012073 to Moon and GSA Student Research Grant no. 13027-21 to Higa.

Vita

2024-2025	NSF Earth Sciences Postdoctoral Fellow, University of Hawai‘i at Mānoa
2022-2023	Virtual Student Federal Service Intern, Pacific Islands Water Science Center
2022	Candidate in Philosophy in Geology, University of California, Los Angeles
2020	M.S., Geology, University of California, Los Angeles
2018-2023	Graduate Student Researcher, University of California, Los Angeles
2018-2023	Teaching Assistant, University of California, Los Angeles
2018	B.S., Geology & Geophysics, University of Hawai‘i at Mānoa
2017-2018	Undergraduate Research Assistant/Geophysics Technician, Hawai‘i Groundwater and Geothermal Resources Center
2016-2017	‘Ike Wai Undergraduate Research Assistant, University of Hawai‘i at Mānoa

Publications

Higa, J.T., Formetta, G., Bellugi, D.G., Busti, R., Dietrich, W.E., Milledge D.G., Ebel, B.A., Moon, S., in prep. Deep critical zone controls on shallow landslides: insights from numerical simulations in a steep, forested landscape.

Higa, J.T., Formetta, G., Bellugi, D.G., Busti, R., Dietrich, W.E., Ebel, B.A., Milledge D.G., Moon, S., in prep. Spatially varying critical zone structures at a steep, forested site near Coos Bay, Oregon.

Higa, J.T.*, Brown, N.D.*, Moon, S., Stock, J.M., Sabbeth, L., Bennett, S.E.K., Barajas, A.M., Argueta, M.O. (2022). Microcontinent Breakup and Links to Possible Plate Boundary Reorganization in the Northern Gulf of California, México. *Tectonics*, *41*, e2021TC006933. https://doi.org/10.1029 /2021TC006933

Li, G.K., Moon, S., **Higa, J.T.** (2022). Residence Time of Over-Steepened Rock Masses in an Active Mountain Range. *Geophysical Research Letters*, *49*, e2021GL097319. https://doi.org/10.1029/2021GL097319

* Co-first author

Chapter 1: Introduction

1.1 Universal processes of mechanical weathering that fracture rocks across scales

Brittle deformation occurs when bonds in a continuous object break and cause a loss of cohesion between two parts of a material, also known as a fracture (Rowland et al., 2007; Twiss and Moores, 2007). This behavior is the basis for mechanical weathering, a ubiquitous geological process that affects surface geomorphology across temporal and spatial scales (Scott and Wohl, 2019). Recent work finds that the same mechanical processes affect fractures regardless of scale and are divided into two categories: sub-critical and critical cracking (Eppes, 2022). Sub-critical cracking refers to the steady propagation of a fracture tip that can slowly (10-9 – 103 m/Myr) weather and erode rock (Eppes and Keanini, 2017). Fracture propagation depends on the surrounding geologic stress field, where compressive and tensile stresses interact to create opening-mode or shear fractures (e.g., McTigue and Mei, 1981; Miller and Dunne, 1996). Geologists have also long understood that climate, through temperature and humidity (e.g., Anderson et al., 2013; Eppes and Keanini, 2017; Eppes et al., 2020; Gilbert, 1877), can accelerate sub-critical crack propagation and increase crack length. As fractures grow, longer cracks can increase crack tip stress intensities and sub-critical cracking rates in a positive feedback loop (Eppes, 2022; Erdogan, 1983). Then, fracturing may enter a stage of sporadic, unstable propagation over short timescales (i.e., seconds) during critical cracking, such as through spontaneous exfoliation fracturing (Collins et al., 2018) or rockfalls (Collins and Stock, 2016). Together, sub-critical and critical cracking are vital for processes that control landscape evolution worldwide.

Fractures across scales, from plate boundaries to outcrops, represent a continuum of cracks with interplays that shape geomorphology through time (Scott and Wohl, 2019). From small- to big-scale, crack tip propagation at the molecular level can grow a fault (Vermilye and

Scholz, 1998), first aseismically and then seismically as a fault lengthens (Preuss et al., 2019). Faults may also grow through linkage, forming complex and branching fault zones expressed at the surface (e.g., Scholz et al., 1993). Then, from big- to small-scale, fault activity and mountain uplift create outcrop-scale fractures in the form of damage due to inelastic deformation (e.g., Baden et al., 2022; Clarke and Burbank, 2010; Kirkpatrick et al., 2021; Slim et al., 2015). Thus, studying geological fractures requires an understanding of the scaled context behind their formation.

1.2 Plate boundary-scale fracturing

The study of plate tectonics examines fractures 1 – 1000 km in scale, which are some of the largest on Earth. Plate boundary-scale investigations provide geologists insight into how our planet evolved and is evolving from the crust to the mantle over billions of years (Huntington and Klepeis, 2018). Analog and numerical models detail how plate tectonics create mid-ocean ridges (e.g., Gerya, 2010; Oldenburg and Brune, 1972), strike-slip faults (e.g., Dooley and Schreurs, 2012; Zuza et al., 2017), pull-apart basins (e.g., McClay and Dooley, 1995; Naylor et al., 1986), and mountain ranges (e.g., Baden et al., 2022) in real-time. These faults are the surface expression of deeper mantle processes and can tell geologists information about mantle plumes (e.g., Abera et al., 2016; Umhoefer, 2011), subducted slab configuration (e.g., Merritts and Bull, 1989), and long-wavelength dynamic topography (e.g., Braun, 2010). Thus, understanding plate boundary-scale fracturing has implications for diverse crustal and mantle processes.

Then, studying plate boundary-scale fracturing improves our knowledge of active, Quaternary faulting, which often has complex and concealed histories that record large-scale Earth processes. Plate boundary reorganization, the migration of a tectonic boundary over geologic time (1 – 10's Myr), is one such process with crucial implications for rock fracturing. There is much effort in the neotectonics sphere to identify active from inactive faults during such reorganizations

(e.g., Behr et al., 2010; Blisniuk et al., 2021). Temporally variable fault activity, caused by interactions between conjugate faults, can also help determine the complex mechanics of linked fault systems (e.g., Hatem and Dolan, 2018; Rittase et al., 2014). These studies combine fault mapping, geochronology, and stress modeling to answer where active faults are located and how earthquakes nucleate along and grow a fault system. Could similar, detailed studies on smaller faults tell geologists about the activity and history of a broader plate boundary? Such a delve into neotectonics could illuminate the connections of minor fault systems to surrounding major tectonic structures and improve our understanding of seismic activity near plate boundaries.

1.3 Outcrop- to landscape-scale fracturing

Arguably the most seminal paper in geomorphology, Gilbert (1877), begins by discussing the first step of how cohesive rocks erode by "division," or fracturing, which is evident from outcrop-scale observations. The report describes mechanisms for temperature, rainfall, gravitational loading, and vegetation to fracture rock for later colluvial and fluvial transport. Today, geologists classify these interplays as processes affecting the critical zone, Earth's near-surface layer where wind, air, water, and biota work to alter pristine bedrock into weathered material (Anderson et al., 2007; Brantley et al., 2007; Riebe et al., 2017). Modern studies on the critical zone show how subsurface stresses (e.g., Moon et al., 2017; St. Clair et al., 2015) and reactive transport (e.g., Lebedeva and Brantley, 2013; Rempe and Dietrich, 2014) can control the form and weathering of landscapes. Because deep critical zone structures are difficult to predict from surface geology, recent studies use geophysical surveying to probe the top 10's of m of the critical zone (e.g., Flinchum et al., 2018; Ma et al., 2021; Pasquet et al., 2022; Wang et al., 2021). These works combine process-based weathering models with geophysical observations to determine the relative

effect of stresses and groundwater on critical zone formation. Such advancements allow scientists to study the critical zone and its important implications for life on Earth.

The critical zone is a reservoir for reactive groundwater and plays a vital role in Earth's water (Hahm et al., 2022; Hahm et al., 2019), solute (Anderson et al., 1997; Gu et al., 2020; Ma et al., 2021; Wang et al., 2021), and sediment (Neely et al., 2019; Sklar et al., 2017) cycles. Fractures and pores in the weathered critical zone can enhance groundwater storage capacity (e.g., Callahan et al., 2020; Hayes et al., 2019; Holbrook et al., 2014) and affect forest die-offs related to the reliance of trees on bedrock moisture and nutrients (Callahan et al., 2022; Hahm et al., 2022; Rempe and Dietrich, 2018). Then, fractures can facilitate the flow of this groundwater (Anderson et al., 1997; Montgomery et al., 1997) to increase subsurface pore pressures and bedrock landslide hazards (Iverson and Reid, 1992; Reid and Iverson, 1992). Exfiltration into overlying soil can also increase shallow soil landslide susceptibility, particularly after large rainstorms (e.g., Iverson and Major, 1986; Kim et al., 2018; Montgomery et al., 2009; Onda et al., 2004). These shallow landslides often scour to bedrock, revealing groundwater seeping from bedrock fractures (e.g., Montgomery et al., 1997). Understanding critical zone weathered bedrock structures and fractures is a timely endeavor, as climate change and human activity begin to negatively impact groundwater resources and landslide occurrences worldwide (Cendrero et al., 2020; IPCC, 2013). The question remains, how do fractures interact with weathering, groundwater flow, and landslides over natural landscapes? A holistic field and modeling study is necessary to understand the realistic influences of outcrop-scale bedrock fractures on finite natural resources and public safety.

1.4 Dissertation structure

This dissertation describes three projects studying fractures at different spatial scales to address gaps of knowledge in understanding how real-world fracture systems impact continental

rifting, critical zone weathering, and shallow landslide characteristics. The work herein will tackle (1) plate boundary evolution by examining faults of an onshore microcontinent and continental rift, (2) near-surface development of a deep, fractured, critical zone due to mechanical and chemical weathering, and (3) the effects of permeable, fractured bedrock and groundwater exfiltration in the critical zone on the occurrence, size, and location of shallow soil landslides. These studies are located at two benchmark sites in western North America and use a combination of field observations, process-based modeling, and remote sensing to examine how fractures affect near-surface geomorphic processes at large and small spatial scales.

Chapter 2 will provide the first high-resolution mapping and dating of a faulted terrace system on the Isla Ángel de la Guarda microcontinent in the Gulf of California, Baja California, México. Here, I examine a potential plate boundary reorganization, where the location of the nearby Pacific-North America plate boundary may be shifting eastwards across the island microcontinent. Because microcontinents are usually submarine (Nemčok et al., 2016), this study presents a rare opportunity to do fieldwork on an exposed, young, and rifting continental fragment along the oblique-divergent Pacific-North America plate boundary (Oskin et al., 2001; Stock, 2000; Umhoefer, 2011). Through fault mapping and luminescence dating, I describe an onshore fault system that is normal, active from at least 50 ka, and likely kinematically linked with offshore pull-apart basins. These results exemplify a dynamic plate boundary with more deformation off the major Pacific-North America plate boundary than previously thought. Thus, this work improves our understanding of plate boundary reorganization and the dynamics of a developing continental rift. Higa et al. (2022) presents the results from this chapter.

Chapter 3 will quantify complexities in the critical zone at a historically well-studied area near Coos Bay, Oregon, USA. This site has a wealth of hydrological (e.g., Anderson et al., 1997;

Ebel et al., 2007; Torres et al., 1998) and landslide (e.g., Bellugi et al., 2015a; Bellugi et al., 2015b; Montgomery et al., 2000) data and modeling. Here, I image the critical zone with new, near-surface geophysical surveys and compare these profiles with previous borehole cores and hand-augered pits (Anderson et al., 2002; Montgomery et al., 1997) to calibrate two process-based weathering models. I present near-surface seismic refraction surveys that show two main weathered structures at this site: (1) a shallow, surface-parallel, and pervasively weathered rock and saprolite layer and (2) a deeper, undulating, fractured and unweathered bedrock layer. These results show that the critical zone here is more structurally complex than initially thought. Such profiles cannot be explained by a single bedrock weathering model, suggesting the importance of multiple weathering processes, divide migration, and preferential weathering along fractures, faults, and bedding to develop the critical zone.

Chapter 4 builds off Chapter 3 to study how weathered bedrock structures from the process-based models above can influence shallow soil landslide occurrence, size, and location. Employing different modeled critical zones, a transient hydrologic model (Endrizzi et al., 2014), and a three-dimensional shallow soil landslide model (Bellugi et al., 2015a; Bellugi et al., 2015b; Milledge et al., 2014), the results herein show how complex, weathered, and fractured critical zone structures impact groundwater seepage and affect surface soil instability. I suggest that deep, fractured, and permeable critical zone structures can funnel water away from soils to increase stability and that the shallowing of relatively impermeable bedrock can focus groundwater exfiltration and slope instabilities at stream channels. Overall, this chapter suggests a controlling role of groundwater seepage on landslide hazards and a need for including realistic critical zones and fractures in future hydrology and slope stability models.

1.5 References

Abera, R., Van Wijk, J., Axen, G., 2016. Formation of continental fragments: The Tamayo Bank, Gulf of California, Mexico. Geology 44, 595-598. https://doi.org/10.1130/G38123.1

Anderson, R.S., Anderson, S.P., Tucker, G.E., 2013. Rock damage and regolith transport by frost: An example of climate modulation of the geomorphology of the critical zone. Earth Surface Processes and Landforms 38, 299-316. https://doi.org/10.1002/esp.3330

Anderson, S.P., Dietrich, W.E., Brimhall Jr, G.H., 2002. Weathering profiles, mass-balance analysis, and rates of solute loss: Linkages between weathering and erosion in a small, steep catchment. Geological Society of America Bulletin 114, 1143-1158. https://doi.org/10.1130/0016-7606(2002)114<1143:WPMBAA>2.0.CO;2

Anderson, S.P., Dietrich, W.E., Torres, R., Montgomery, D.R., Loague, K., 1997. Concentration-discharge relationships in runoff from a steep, unchanneled catchment. Water Resources Research 33, 211-225. https://doi.org/10.1029/96WR02715

Anderson, S.P., von Blanckenburg, F., White, A.F., 2007. Physical and chemical controls on the critical zone. Elements 3, 315-319. https://doi.org/10.2113/gselements.3.5.315

Baden, C.W., Shuster, D.L., Aron, F., Fosdick, J.C., Bürgmann, R., Hilley, G.E., 2022. Bridging earthquakes and mountain building in the Santa Cruz Mountains, CA. Science Advances 8, eabi6031. https://doi.org/10.1126/sciadv.abi6031

Behr, W., Rood, D., Fletcher, K., Guzman, N., Finkel, R., Hanks, T.C., Hudnut, K., Kendrick, K., Platt, J., Sharp, W., 2010. Uncertainties in slip-rate estimates for the Mission Creek strand of the southern San Andreas fault at Biskra Palms Oasis, southern California. Geological Society of America Bulletin 122, 1360-1377. https://doi.org/10.1130/B30020.1

Bellugi, D., Milledge, D.G., Dietrich, W.E., McKean, J.A., Perron, J.T., Sudderth, E.B., Kazian, B., 2015a. A spectral clustering search algorithm for predicting shallow landslide size and location. Journal of Geophysical Research: Earth Surface 120, 300-324. https://doi.org/10.1002/2014JF003137

Bellugi, D., Milledge, D.G., Dietrich, W.E., Perron, J.T., McKean, J., 2015b. Predicting shallow landslide size and location across a natural landscape: Application of a spectral clustering search algorithm. Journal of Geophysical Research: Earth Surface 120, 2552-2585. https://doi.org/10.1002/2015JF003520

Blisniuk, K., Scharer, K., Sharp, W.D., Burgmann, R., Amos, C., Rymer, M., 2021. A revised position for the primary strand of the Pleistocene-Holocene San Andreas fault in southern California. Science Advances 7, eaaz5691. https://doi.org/10.1126/sciadv.aaz5691

Brantley, S.L., Goldhaber, M.B., Ragnarsdottir, K.V., 2007. Crossing disciplines and scales to understand the critical zone. Elements 3, 307-314. https://doi.org/10.2113/gselements.3.5.307

Braun, J., 2010. The many surface expressions of mantle dynamics. Nature Geoscience 3, 825-833. https://doi.org/10.1038/ngeo1020

Callahan, R.P., Riebe, C.S., Pasquet, S., Ferrier, K.L., Grana, D., Sklar, L.S., Taylor, N.J., Flinchum, B.A., Hayes, J.L., Carr, B.J., 2020. Subsurface weathering revealed in hillslope-integrated porosity distributions. Geophysical Research Letters 47, e2020GL088322. https://doi.org/10.1029/2020GL088322

Callahan, R.P., Riebe, C.S., Sklar, L.S., Pasquet, S., Ferrier, K.L., Hahm, W.J., Taylor, N.J., Grana, D., Flinchum, B.A., Hayes, J.L., 2022. Forest vulnerability to drought controlled

by bedrock composition. Nature Geoscience 15, 714-719. https://doi.org/10.1038/s41561-022-01012-2

Cendrero, A., Forte, L.M., Remondo, J., Cuesta‐Albertos, J.A., 2020. Anthropocene geomorphic change. Climate or human activities? Earth's Future 8, e2019EF001305. https://doi.org/10.1029/2019EF001305

Clarke, B.A., Burbank, D.W., 2010. Bedrock fracturing, threshold hillslopes, and limits to the magnitude of bedrock landslides. Earth and Planetary Science Letters 297, 577-586. https://doi.org/10.1016/j.epsl.2010.07.011

Collins, B.D., Stock, G.M., 2016. Rockfall triggering by cyclic thermal stressing of exfoliation fractures. Nature Geoscience 9, 395-400. https://doi.org/10.1038/ngeo2686

Collins, B.D., Stock, G.M., Eppes, M.-C., Lewis, S.W., Corbett, S.C., Smith, J.B., 2018. Thermal influences on spontaneous rock dome exfoliation. Nature Communications 9, 762. https://doi.org/10.1038/s41467-017-02728-1

Dooley, T.P., Schreurs, G., 2012. Analogue modelling of intraplate strike-slip tectonics: A review and new experimental results. Tectonophysics 574, 1-71. https://doi.org/10.1016/j.tecto.2012.05.030

Ebel, B.A., Loague, K., Vanderkwaak, J.E., Dietrich, W.E., Montgomery, D.R., Torres, R., Anderson, S.P., 2007. Near-surface hydrologic response for a steep, unchanneled catchment near Coos Bay, Oregon: 2. Physics-based simulations. American Journal of Science 307, 709-748. https://doi.org/10.2475/04.2007.03

Endrizzi, S., Gruber, S., Dall'Amico, M., Rigon, R., 2014. GEOtop 2.0: simulating the combined energy and water balance at and below the land surface accounting for soil freezing, snow

cover and terrain effects. Geoscientific Model Development 7, 2831-2857. https://doi.org/10.5194/gmd-7-2831-2014

Eppes, M.C.M., 2022. Mechanical Weathering: A Conceptual Overview, Treatise on Geomorphology. Elsevier, Academic Press, pp. 30 - 45. https://doi.org/10.1016/B978-0-12-818234-5.00200-5

Eppes, M.C., Keanini, R., 2017. Mechanical weathering and rock erosion by climate‐dependent subcritical cracking. Reviews of Geophysics 55, 470-508. https://doi.org/10.1002/2017RG000557

Eppes, M.C., Magi, B., Scheff, J., Warren, K., Ching, S., Feng, T., 2020. Warmer, Wetter Climates Accelerate Mechanical Weathering in Field Data, Independent of Stress‐Loading. Geophysical Research Letters 47, 2020GL089062. https://doi.org/10.1029/2020GL089062

Erdogan, F., 1983. Stress intensity factors. Journal of Applied Mechanics 50, 992-1002.

Flinchum, B.A., Steven Holbrook, W., Rempe, D., Moon, S., Riebe, C.S., Carr, B.J., Hayes, J.L., St. Clair, J., Peters, M.P., 2018. Critical zone structure under a granite ridge inferred from drilling and three‐dimensional seismic refraction data. Journal of Geophysical Research: Earth Surface 123, 1317-1343. https://doi.org/10.1115/1.3167212

Gerya, T., 2010. Dynamical instability produces transform faults at mid-ocean ridges. Science 329, 1047-1050. https://doi.org/10.1126/science.1191349

Gilbert, G.K., 1877. Geology of the Henry Mountains. US Government Printing Office. https://doi.org/10.3133/70038096

Gu, X., Mavko, G., Ma, L., Oakley, D., Accardo, N., Carr, B.J., Nyblade, A.A., Brantley, S.L., 2020. Seismic refraction tracks porosity generation and possible CO2 production at depth

under a headwater catchment. Proceedings of the National Academy of Sciences 117, 18991-18997. https://doi.org/10.1073/pnas.2003451117

Hahm, W.J., Dralle, D.N., Sanders, M., Bryk, A.B., Fauria, K.E., Huang, M.-H., Hudson‐Rasmussen, B., Nelson, M.D., Pedrazas, M.A., Schmidt, L., 2022. Bedrock vadose zone storage dynamics under extreme drought: consequences for plant water availability, recharge, and runoff. Water Resources Research 58, e2021WR031781. https://doi.org/10.1029/2021WR031781

Hahm, W.J., Rempe, D.M., Dralle, D.N., Dawson, T.E., Lovill, S.M., Bryk, A.B., Bish, D.L., Schieber, J., Dietrich, W.E., 2019. Lithologically controlled subsurface critical zone thickness and water storage capacity determine regional plant community composition. Water Resources Research 55, 3028-3055. https://doi.org/10.1029/2018WR023760

Hatem, A.E., Dolan, J.F., 2018. A model for the initiation, evolution, and controls on seismic behavior of the Garlock fault, California. Geochemistry, Geophysics, Geosystems 19, 2166-2178. https://doi.org/10.1029/2017GC007349

Hayes, J.L., Riebe, C.S., Holbrook, W.S., Flinchum, B.A., Hartsough, P.C., 2019. Porosity production in weathered rock: Where volumetric strain dominates over chemical mass loss. Science Advances 5, eaao0834. https://doi.org/10.1126/sciadv.aao0834

Higa, J.T., Brown, N.D., Moon, S., Stock, J.M., Sabbeth, L., Bennett, S.E., Martín‐Barajas, A., Argueta, M.O., 2022. Microcontinent Breakup and Links to Possible Plate Boundary Reorganization in the Northern Gulf of California, México. Tectonics 41, e2021TC006933. https://doi.org/10.1029/2021TC006933

Holbrook, W.S., Riebe, C.S., Elwaseif, M., L. Hayes, J., Basler‐Reeder, K., L. Harry, D., Malazian, A., Dosseto, A., C. Hartsough, P., W. Hopmans, J., 2014. Geophysical

constraints on deep weathering and water storage potential in the Southern Sierra Critical Zone Observatory. Earth Surface Processes and Landforms 39, 366-380. https://doi.org/10.1002/esp.3502

Huntington, K., Klepeis, K., 2018. Challenges and opportunities for research in tectonics: Understanding deformation and the processes that link Earth systems, from geologic time to human time. A community vision document submitted to the US National Science Foundation, University of Washington, p. 84.

IPCC, 2013. The physical science basis: Contribution of working group I to the fifth assessment report of the intergovernmental panel on climate change. Cambridge University Press, Cambridge, United Kingdom and New York, NY, USA.

Iverson, R.M., Major, J.J., 1986. Groundwater seepage vectors and the potential for hillslope failure and debris flow mobilization. Water Resources Research 22, 1543-1548. https://doi.org/10.1029/WR022i011p01543

Iverson, R.M., Reid, M.E., 1992. Gravity-driven groundwater flow and slope failure potential: 1. Elastic Effective-Stress Model. Water Resources Research 28, 925-938. https://doi.org/10.1029/91WR02694

Kim, M.S., Onda, Y., Uchida, T., Kim, J.K., Song, Y.S., 2018. Effect of seepage on shallow landslides in consideration of changes in topography: case study including an experimental sandy slope with artificial rainfall. Catena 161, 50-62. https://doi.org/10.1016/j.catena.2017.10.004

Kirkpatrick, H.M., Moon, S., Yin, A., Harrison, T.M., 2021. Impact of fault damage on eastern Tibet topography. Geology 49, 30-34. https://doi.org/10.1130/G48179.1

Lebedeva, M.I., Brantley, S.L., 2013. Exploring geochemical controls on weathering and erosion of convex hillslopes: beyond the empirical regolith production function. Earth Surface Processes and Landforms 38, 1793-1807. https://doi.org/10.1002/esp.3424

Ma, L., Oakley, D., Nyblade, A., Moon, S., Accardo, N., Wang, W., Gu, X., Brubaker, K., Mount, G.J., Forsythe, B., 2021. Seismic Imaging of a Shale Landscape Under Compression Shows Limited Influence of Topography-Induced Fracturing. Geophysical Research Letters 48, e2021GL093372. https://doi.org/10.1029/2021GL093372

McClay, K., Dooley, T., 1995. Analogue models of pull-apart basins. Geology 23, 711-714. https://doi.org/10.1130/0091-7613(1995)023%3C0711:AMOPAB%3E2.3.CO;2

McTigue, D.F., Mei, C.C., 1981. Gravity-induced stresses near topography of small slope. Journal of Geophysical Research: Solid Earth 86, 9268-9278. https://doi.org/10.1029/JB086iB10p09268

Merritts, D., Bull, W.B., 1989. Interpreting Quaternary uplift rates at the Mendocino triple junction, northern California, from uplifted marine terraces. Geology 17, 1020-1024. https://doi.org/10.1130/0091-7613(1989)017%3C1020:IQURAT%3E2.3.CO;2

Milledge, D.G., Bellugi, D., McKean, J.A., Densmore, A.L., Dietrich, W.E., 2014. A multidimensional stability model for predicting shallow landslide size and shape across landscapes. Journal of Geophysical Research: Earth Surface 119, 2481-2504. https://doi.org/10.1002/2014JF003135

Miller, D.J., Dunne, T., 1996. Topographic perturbations of regional stresses and consequent bedrock fracturing. Journal of Geophysical Research: Solid Earth 101, 25523-25536. https://doi.org/10.1029/96JB02531

Montgomery, D.R., Dietrich, W.E., Torres, R., Anderson, S.P., Heffner, J.T., Loague, K., 1997. Hydrologic response of a steep, unchanneled valley to natural and applied rainfall. Water Resources Research 33, 91-109. https://doi.org/10.1029/96WR02985

Montgomery, D.R., Schmidt, K.M., Dietrich, W.E., McKean, J., 2009. Instrumental record of debris flow initiation during natural rainfall: Implications for modeling slope stability. Journal of Geophysical Research: Earth Surface 114. https://doi.org/10.1029/2008JF001078

Montgomery, D.R., Schmidt, K.M., Greenberg, H.M., Dietrich, W.E., 2000. Forest clearing and regional landsliding. Geology 28, 311-314. https://doi.org/10.1130/0091-7613(2000)28%3C311:FCARL%3E2.0.CO;2

Moon, S., Perron, J., Martel, S., Holbrook, W., St. Clair, J., 2017. A model of three-dimensional topographic stresses with implications for bedrock fractures, surface processes, and landscape evolution. Journal of Geophysical Research: Earth Surface 122, 823-846. https://doi.org/10.1002/2016JF004155

Naylor, M., Mandl, G.t., Supesteijn, C., 1986. Fault geometries in basement-induced wrench faulting under different initial stress states. Journal of Structural Geology 8, 737-752. https://doi.org/10.1016/0191-8141(86)90022-2

Neely, A.B., DiBiase, R.A., Corbett, L.B., Bierman, P.R., Caffee, M.W., 2019. Bedrock fracture density controls on hillslope erodibility in steep, rocky landscapes with patchy soil cover, southern California, USA. Earth and Planetary Science Letters 522, 186-197. https://doi.org/10.1016/j.epsl.2019.06.011

Nemčok, M., Sinha, S., Doré, A., Lundin, E., Mascle, J., Rybar, S., 2016. Mechanisms of microcontinent release associated with wrenching-involved continental break-up; a

review. Geological Society, London, Special Publications 431, 323-359. https://doi.org/10.1144/SP431.14

Oldenburg, D.W., Brune, J.N., 1972. Ridge transform fault spreading pattern in freezing wax. Science 178, 301-304. https://doi.org/10.1126/science.178.4058.301

Onda, Y., Tsujimura, M., Tabuchi, H., 2004. The role of subsurface water flow paths on hillslope hydrological processes, landslides and landform development in steep mountains of Japan. Hydrological Processes 18, 637-650. https://doi.org/10.1002/hyp.1362

Oskin, M., Stock, J., Martín-Barajas, A., 2001. Rapid localization of Pacific–North America plate motion in the Gulf of California. Geology 29, 459-462. https://doi.org/10.1130/0091-7613(2001)029%3C0459:RLOPNA%3E2.0.CO;2

Pasquet, S., Marçais, J., Hayes, J.L., Sak, P.B., Ma, L., Gaillardet, J., 2022. Catchment-Scale Architecture of the Deep Critical Zone Revealed by Seismic Imaging. Geophysical Research Letters 49, e2022GL098433. https://doi.org/10.1029/2022GL098433

Preuss, S., Herrendörfer, R., Gerya, T., Ampuero, J.P., van Dinther, Y., 2019. Seismic and aseismic fault growth lead to different fault orientations. Journal of Geophysical Research: Solid Earth 124, 8867-8889. https://doi.org/10.1029/2019JB017324

Reid, M.E., Iverson, R.M., 1992. Gravity-driven groundwater flow and slope failure potential: 2. Effects of slope morphology, material properties, and hydraulic heterogeneity. Water Resources Research 28, 939-950. https://doi.org/10.1029/91WR02695

Rempe, D.M., Dietrich, W.E., 2014. A bottom-up control on fresh-bedrock topography under landscapes. Proceedings of the National Academy of Sciences 111, 6576-6581. https://doi.org/10.1073/pnas.1404763111

Rempe, D.M., Dietrich, W.E., 2018. Direct observations of rock moisture, a hidden component of the hydrologic cycle. Proceedings of the National Academy of Sciences 115, 2664-2669. https://doi.org/10.1073/pnas.1800141115

Riebe, C.S., Hahm, W.J., Brantley, S.L., 2017. Controls on deep critical zone architecture: A historical review and four testable hypotheses. Earth Surface Processes and Landforms 42, 128-156. https://doi.org/10.1002/esp.4052

Rittase, W.M., Kirby, E., McDonald, E., Walker, J.D., Gosse, J., Spencer, J.Q., Herrs, A., 2014. Temporal variations in Holocene slip rate along the central Garlock fault, Pilot Knob Valley, California. Lithosphere 6, 48-58. https://doi.org/10.1130/L286.1

Rowland, S.M., Duebendorfer, E.M., Gates, A., 2007. Structural analysis and synthesis: a laboratory course in structural geology, 3rd ed. ed. Blackwell Publishing Ltd.

Scholz, C., Dawers, N., Yu, J.Z., Anders, M., Cowie, P., 1993. Fault growth and fault scaling laws: Preliminary results. Journal of Geophysical Research: Solid Earth 98, 21951-21961. https://doi.org/10.1029/93JB01008

Scott, D.N., Wohl, E.E., 2019. Bedrock fracture influences on geomorphic process and form across process domains and scales. Earth Surface Processes and Landforms 44, 27-45. https://doi.org/10.1002/esp.4473

Sklar, L.S., Riebe, C.S., Marshall, J.A., Genetti, J., Leclere, S., Lukens, C.L., Merces, V., 2017. The problem of predicting the size distribution of sediment supplied by hillslopes to rivers. Geomorphology 277, 31-49. https://doi.org/10.1016/j.geomorph.2016.05.005

Slim, M., Perron, J.T., Martel, S.J., Singha, K., 2015. Topographic stress and rock fracture: A two-dimensional numerical model for arbitrary topography and preliminary comparison

with borehole observations. Earth Surface Processes and Landforms 40, 512-529. https://doi.org/10.1002/esp.3646

St. Clair, J., Moon, S., Holbrook, W., Perron, J., Riebe, C., Martel, S., Carr, B., Harman, C., Singha, K., Richter, D.d., 2015. Geophysical imaging reveals topographic stress control of bedrock weathering. Science 350, 534-538. https://doi.org/10.1126/science.aab2210

Stock, J.M., 2000. Relation of the Puertecitos Volcanic Province, Baja California, Mexico, to development of the plate boundary in the Gulf of California. Special Papers-Geological Society of America, 143-156. https://doi.org/10.1130/0-8137-2334-5.143

Torres, R., Dietrich, W.E., Montgomery, D.R., Anderson, S.P., Loague, K., 1998. Unsaturated zone processes and the hydrologic response of a steep, unchanneled catchment. Water Resources Research 34, 1865-1879. https://doi.org/10.1029/98WR01140

Twiss, R.J., Moores, E.M., 2007. Structural geology, 2nd ed. ed. H.W. Freeman and Company, New York.

Umhoefer, P.J., 2011. Why did the Southern Gulf of California rupture so rapidly? Oblique divergence across hot, weak lithosphere along a tectonically active margin. GSA today 21, 4-10. https://doi.org/10.1130/G133A.1

Vermilye, J.M., Scholz, C.H., 1998. The process zone: A microstructural view of fault growth. Journal of Geophysical Research: Solid Earth 103, 12223-12237. https://doi.org/10.1029/98JB00957

Wang, W., Nyblade, A., Mount, G., Moon, S., Chen, P., Accardo, N., Gu, X., Forsythe, B., Brantley, S.L., 2021. 3D seismic anatomy of a watershed reveals climate‐topography coupling that drives water flowpaths and bedrock weathering. Journal of Geophysical Research: Earth Surface 126, e2021JF006281. https://doi.org/10.1029/2021JF006281

Zuza, A.V., Yin, A., Lin, J., Sun, M., 2017. Spacing and strength of active continental strike-slip faults. Earth and Planetary Science Letters 457, 49-62. https://doi.org/10.1016/j.epsl.2016.09.041

Chapter 2: Microcontinent Breakup and Links to Possible Plate Boundary Reorganization in the Northern Gulf of California, México

This chapter is modified from Higa, J.T., Brown, N.D., Moon, S., Stock, J.M., Sabbeth, L., Bennett, S.E.K., Barajas, A.M., and Argueta M.O., 2022. Microcontinent Breakup and Links to Possible Plate Boundary Reorganization in the Northern Gulf of California, México. *Tectonics*, *41*, e2021TC006933. https://doi.org/10.1029/2021TC006933.

2.1 Introduction

Microcontinents are fragments of continental lithosphere rifted away from a continent, now surrounded by oceanic lithosphere (Abera et al., 2016; Müller et al., 2001). Various mechanisms have been proposed for the isolation and tectonic evolution of microcontinents, each governed by a different tectonic setting (Nemčok et al., 2016). Continental fragments can become isolated by wrench faulting that forms strike-slip duplexes and stepovers between shear zones (e.g., Antobreh et al., 2009) or by horsetail splays via shearing of intervening blocks (e.g., Misra et al., 2014). Rifting across relatively parallel and overlapping spreading centers can also isolate microcontinents by two zones of extension and two sub-parallel transform boundaries (Nemčok et al., 2016) that can accommodate block rotation (Molnar et al., 2018). The role of a given microcontinent formation mechanism in the evolution of a plate boundary can be evaluated by constraining the orientation, sense of slip, and age of faulting on a microcontinent. However, most microcontinents are submarine (e.g., Nemčok et al., 2016), making them difficult to study.

The Gulf of California is a suitable location to study microcontinent formation, as several studies suggest other continental fragments have been completely or partially isolated here (Abera

et al., 2016; Lizarralde et al., 2007) since the late Miocene. Oblique rifting between the Pacific and North America plates initiated ~12.3 Ma across a broad region from west of Baja California (Spencer & Normark, 1979) to central Sonora (Gans, 1997). Transtensional strain localized into the 50 – 100 km-wide Gulf of California shear zone ~8 – 7 Ma (Bennett & Oskin, 2014; Bennett et al., 2016a). Continued focused rifting led to post-6.1 Ma (Oskin & Stock, 2003; Oskin et al., 2001) oblique opening of the Upper and Lower Tiburón pull-apart basins, which were kinematically linked by the dextral Tiburón fault (Figure 2.1a – b; e.g., Nagy & Stock, 2000). Then, the evolving plate boundary shifted westward (Aragón-Arreola & Martín-Barajas, 2007; Lonsdale, 1989) by ~2 Ma as the Ballenas transform fault linked with the nascent Lower Delfín pull-apart basin (Figure 2.1b – c; Nagy & Stock, 2000). As a result, the Upper and Lower Tiburón basins and Tiburón fault became inactive, transferring Isla Ángel de la Guarda (IAG) from the Pacific plate to the North America plate. At ≤ 2 Ma, a short right-step in the Ballenas transform fault system formed the North Salsipuedes basin, a narrow zone of extension southwest of IAG (Figure 2.1d – e; González-Fernández et al., 2005; Lonsdale, 1989).

Today, the Baja California microplate moves N56°W ± 1° at about 43 – 47 mm/yr (Plattner et al., 2007) with ~235 – 255 km of dextral displacement relative to Isla Tiburón (North America plate) since ~6 Ma (Bennett et al., 2016b; Bennett et al., 2015; Nagy & Stock, 2000; Oskin et al., 2001). The modern NW-striking Ballenas transform fault makes up the northwesternmost ~100 – 200 km of the >500 km-long Ballenas-Guaymas transform fault zone (Figure 2.2a), which continues southeast from IAG along the northeast margin of the Guaymas basin (Aragón-Arreola et al., 2005; Lonsdale, 1989). Many young extensional basins have formed at releasing steps in the en echelon Ballenas transform fault (González-Fernández et al., 2005; Lonsdale, 1989), along with structures resembling horsetail splays and submarine volcanoes

(Figure 2.2b; Aragón-Arreola & Martín-Barajas, 2007; Aragón-Arreola et al., 2005; Persaud et al., 2003; Plattner et al., 2015). Near IAG, the Ballenas transform fault becomes less discernable in bathymetry, from the North Salsipuedes basin to the Upper Delfín basin, as slip is partitioned from the transform fault into each basin towards the north (Persaud et al., 2003). Additionally, the structural connection between the Ballenas transform fault and the North Salsipuedes basin is diffuse (Lonsdale, 1989), as the basin is composed of multiple SE- and NW-dipping normal faults across a ~50 km-long zone of extension along the Ballenas transform fault (Plattner et al., 2015). Collectively, these characteristics indicate that the Ballenas transform fault is not simply a strike-slip or transform fault, but is instead a complex transtensional structure, which has led some to suggest that strain localization of the Pacific-North America plate boundary near IAG is incomplete (e.g., Persaud et al., 2003). Therefore, modern IAG is an evolving microcontinent, isolated as a distinct tectonic block but surrounded by transtensional faults, transitional crust, and pull-apart basins instead of true transform faults, oceanic crust, and spreading centers (Aragón-Arreola et al., 2005; González-Fernández et al., 2005).

Ongoing deformation surrounding IAG is recorded by the uplift of coastal terraces along the adjacent Baja California peninsula, with a mean uplift rate of 0.1 mm/yr since 1 Ma (Ortlieb, 1991). Such uplift is likely also deforming IAG. Deformation on E-W normal faults in northern IAG parallels that in the Lower Delfín basin (Delgado-Argote, 2000). In central IAG, geologic mapping and ages from deformed volcanic deposits suggest faults there are unrelated to modern deformation because post-Pliocene deposits are not deformed (Cavazos Alvarez, 2015). Interestingly, submarine volcanic hills (Figure 2.2b), thinned crust observed in seismic reflection surveys (Paz-López, 2000; Persaud et al., 2003), and historic earthquakes up to ~Mw 7 near southern IAG (Castro et al., 2021; Castro et al., 2017; López-Pineda et al., 2014) suggest that

extensional faults in the south could be active. However, the only published geologic map of southern IAG is 1:250,000-scale (Gastil et al., 1975) and does not show evidence for Quaternary fault activity or relate faults to active rifting or microcontinent formation processes.

In this paper, we examine the timing and kinematics of faults on southern IAG. Here, a modern, subaerial, and evolving microcontinent provides us with a rare opportunity to study microcontinent formation mechanisms. We focus on a fault zone that was first mapped, but not named, by Gastil et al. (1975), hereafter the Almeja fault zone. We characterize the orientation of this fault zone by remote analysis of high-resolution topography and neotectonic field mapping to document the extent and orientation of faults and determine their kinematic relation with offshore structures. We also determine depositional ages of faulted and unfaulted non-marine terraces and sediment from fault-related depressions using luminescence dating to constrain the local timing and slip rate on specific strands of the Almeja fault zone. Combining these results, we show that normal faults within the Almeja fault zone deform many generations of late Quaternary terraces on southern IAG and projects offshore into the active North Salsipuedes extensional basin. Lastly, we discuss potential mechanisms of ongoing deformation and implications for the future evolution of IAG and the larger Pacific-North America plate boundary.

2.2 Methods

2.2.1 Fault mapping

We used high-resolution data from satellite and drone images to map faults using two independent methods: 1) remote- and field-mapping (Sabbeth, 2020) and 2) a semi-automatic scarp detection method. High-resolution satellite images are from Google Earth (e.g., WorldView) and two 0.5-m resolution Pleiades satellite images. Then, we constructed a 3-m resolution digital elevation model (DEM) of the 150 km2 study area from the Pleiades satellite images (see extent

in Figure 2.2b) using the Ames Stereo Pipeline software (e.g., Beyer et al., 2018). For small portions of the study area with particularly dense fault arrays, or with high potential to use luminescence ages to bracket the timing of fault activity, we performed drone-based photographic surveys with a DJI Phantom 3 Advanced drone to create ~0.1-m resolution DEMs. We used the structure-from-motion photogrammetry method with Agisoft PhotoScan software to process ~2500 drone images with ~70% overlap into three DEMs with a total area of ~5 km2. We then rectified these products using ground control points recorded with a high-precision differential Trimble GPS receiver and processed using RTKLIB (Takasu et al., 2007).

2.2.1.1 Remote and field-based fault mapping

The Almeja fault zone cuts multiple generations of non-marine terraces, apparent in satellite images and DEMs of southern IAG (Figs. 2b, 3; Figure A1). Sabbeth (2020) presented a stratigraphic framework for multiple generations of Quaternary terraces here. We applied this framework to our terrace mapping surrounding our luminescence sample sites while considering terrace height above the active channel, local terrace generations, and our luminescence ages (Figure 2.4; Figure A2; Text A1).

We manually mapped the dense fault strands of the distributed Almeja fault zone from our DEMs and high-resolution satellite images (e.g., Worldview, Pleiades) using well-preserved landforms, such as terraces, as geomorphic markers whose original unfaulted geometry can be easily inferred (Figure 2.2b; Figure A1a; Burbank & Anderson, 2011). Faults are evident as measurable differences in topographic attributes such as elevation, slope, and aspect that abruptly cut through sedimentary terraces and volcanic hillslopes.

Based on inferred original terrace geometry, we can also determine whether dip-slip or strike-slip offsets are dominant. The dip-slip component of fault offset for any fault strand can be

measured from the vertical separation of terrace treads across its fault scarp. We estimated dip-slip displacements by extracting scarp-perpendicular topographic profiles from our ~0.1-m resolution drone-derived DEMs. Then, we fit lines to the correlative upthrown and downthrown terrace tread surfaces and estimated the displacement of these surfaces by varying fault dip using 100,000 Monte Carlo simulations per profile (Text A1; Duckworth et al., 2020; Thompson et al., 2002). We used a wide fault dip range (60° – 90°) similar to Duckworth et al., (2020) because we did not directly observe fault dip in the field and aimed to capture the fullest range of dip-slip displacement. Next, we estimated any strike-slip component of fault offset from the horizontal separation of abandoned terrace risers, which ideally are no longer affected by fluvial erosion. In some locations, field checking was required to determine if the apparent offsets were formed by faults or non-tectonic processes such as river incision. We combined our mapping, which uses remote-sensing data, with conventional neotectonic field-mapping from Sabbeth (2020) to fully characterize the Almeja fault zone.

2.2.1.2 Semi-automatic template matching

The extent of neotectonic field-mapping is often limited by field conditions, inaccessibility, subtle topography, or dense arrays of distributed faulting. To overcome these limitations and identify unmapped faults across a large region of interest, we extracted topographic scarps from our large 3-m resolution DEM using Scarplet, an open-source software package that semi-automatically identifies scarps by matching topographic curvature in a DEM with that of ideal template scarp profiles from the hillslope diffusion equation (described and discussed in Text A2; Hilley et al., 2010; Sare et al., 2019). This template matching algorithm searches for areas of scarp-like features (usually 10's of meters wide and 100's of meters long; Figure A2) within DEMs and produces raster grid maps of scarp properties such as best-fit orientation and amplitude (Figure

A1). We used a template length of 200 m, as in Sare et al. (2019), to capture scarp segments of similar length scales. Template matching also produces grid maps of morphologic age, also known as the degradation coefficient κt [m2]. This variable is the product of the hillslope diffusion constant κ [m2/ka] and absolute age of a scarp t [ka] and is also a proxy for scarp form. A high κt represents a diffuse scarp and results from either a high diffusion constant, old absolute scarp age, or both. Values of κ for scarps in extremely arid regions of the Dead Sea are < 1 m2/ka while those in arid to semi-arid regions of the Basin and Range province and western China vary between 1 – 5.5 m2/ka, showing a dependence on material properties and climate (e.g., Hanks, 2000). Because scarp diffusion processes assume the transport of unconsolidated material, morphologic ages reported for coherent volcanic lithologies cannot be used to infer scarp age but rather show the relative differences between the diffuseness of scarps. Lastly, template matching produces grid maps of signal-to-noise ratio (SNR; Figure 2.3), defined as the ratio of squared scarp amplitude and the squared misfit of real and template curvature. Template matching uses SNR to identify best-fit fault scarps by choosing a scarp orientation that maximizes SNR.

We analyzed three regions of our 3-m resolution DEM with template matching: two regions of layered, gently east-dipping Miocene-Pliocene volcanic bedrock (hereafter, the North and South Volcanic Hills; Sabbeth, 2020) and a region of dissected, primarily fluvial and alluvial, Quaternary terraces (hereafter, the Central Terraces; Figure 2.3). In all regions, our template matching analysis identified many scarp-like curvature profiles. SNR from template matching can be used as a binary classifier for these scarp-like features, where pixels above or below a certain threshold of $\log_{10}$(SNR) can be classified as fault scarp or non-fault scarp pixels, respectively. These pixels are compared against a master map of fault scarps from a 10 and 30 m buffer around the remote- and field-mapped faults for the Central Terraces and South Volcanic Hills, respectively.

We only performed this and subsequent analyses over the Central Terraces and South Volcanic Hills, as the North Volcanic Hills contained only one remote- and field-mapped fault that overlaps with the area analyzed with template matching. A wider buffer was used in volcanic bedrock to identify wider scarps related to higher scarp heights from greater fault offsets accumulated over more protracted fault histories or better preservation from a more coherent lithology.

To evaluate the diagnostic ability of $\log_{10}$(SNR) to detect faults, we create receiver operating characteristic curves (Figure A3) by plotting the true and false positive rates of fault identification at different $\log_{10}$(SNR) thresholds. True positive rate is the ratio of the total number of true fault scarp pixels classified by the $\log_{10}$(SNR) threshold as a fault and the total number of fault scarp pixels in the master map. False positive rate is calculated as the ratio of the total number of non-fault scarp pixels identified falsely as a fault scarp and the total number of non-fault scarp pixels in the master map. Then, we use the area under the receiver operating characteristic curve (AUROC) to evaluate the performance of such binary classifiers, following Sare et al. (2019), where AUROC = 1 is a perfect classifier and AUROC = 0.5 is a random classifier. Next, we determined a threshold value of $\log_{10}$(SNR), above which pixels will remain in our final fault scarp maps. We considered the median SNR from entire regions, median SNR within buffers around our remote- and field-mapped fault scarps, and the best classifier SNR to choose a threshold that best characterizes the Almeja fault zone in different lithologies (Text A3). We present classifier performance metrics, including the true positive rate, false positive rate, true negative rate, false negative rate, precision, and accuracy of the binary classifier at the final $\log_{10}$(SNR) threshold in Table A1.

Nonetheless, some topographic features identified after implementing the SNR threshold do not have tectonic origins, such as terrace risers, ridgelines, and erosional cliff bands related to

resistant, gently east-dipping, volcanic units. We post-process the SNR-filtered map by the location of terrace risers (by high topographic slope) and ridgelines (by the location of drainage divides from Scherler & Schwanghart, 2020), as discussed in Text A4. The classifier metrics for our post-processed fault map are also presented in Table A1.

Lastly, we use two-sample Kolmogorov-Smirnov and Wilcoxon rank sum statistical tests at the 5% significance level to compare the orientation of linearized fault scarps from template matching (Figure 2.3a – c; linearization of template matching results discussed in Text A5) to that from remote- and field-mapping (Figure 2.3d – f) in approximately the same locations (Figure A4). These tests examine whether two datasets have equal continuous distributions and medians, respectively. First, we compare results from the same region (e.g., South Volcanic Hills) varying the mapping method to determine if both methods produce consistent results. Then we compare results obtained from the same mapping method (e.g., template matching), varying the region to determine if there is a significant difference in orientation between locations across southern IAG.

2.2.2 Luminescence dating

To constrain the timing of fault offsets, we analyzed 13 sediment samples from five sites located on faulted terrace treads, in exposures of incised and faulted terraces, and from a fault-related local depression similar to a sag pond. Sites were chosen based on accessibility, the potential for material dateable using luminescence (e.g., sand-sized grains in laminated soft sediment), and proximity to well-characterized fault strands that offered opportunities to constrain their fault slip history.

Luminescence dating estimates the length of time sediment has been buried after sunlight exposure, which is often referred to as the depositional age, as the absorbed dose [Gy] divided by the geologic dose rate [Gy/ka]. The geologic dose rate refers to the natural radiation contribution

from cosmic rays and radionuclides within grains and clasts in the surrounding sediment matrix, which are dominated by the radioactive isotopes of U, Th, and K. We use in-situ and sediment matrix samples to estimate the concentrations of these elements and implement standard attenuation factors (Brennan et al., 1991; Guérin et al., 2012; Liritzis et al., 2013), internal K content (Huntley & Baril, 1997), and calculations and error propagations (Durcan et al., 2015) to convert these factors to dose rates.

To estimate the natural, absorbed, burial dose, we measured the laboratory equivalent dose (De) for each grain using a post-infrared infrared stimulated luminescence (p-IR $IRSL_{225}$) protocol, which measures the time-stable signal from feldspars (Buylaert et al., 2009). We do not analyze that of quartz grains because previous studies in nearby southern California show poor quality luminescence signals from quartz, possibly because of rapid exhumation of source rock and limited reworking of sediment (Lawson et al., 2012). In such cases, quartz signals are commonly overprinted by zircon and feldspar inclusions (Guralnik et al., 2015). Conversely, post-IR IRSL signals from K-feldspar samples have yielded excellent results in alluvial deposits from southern California (Rhodes, 2015) and southern Baja California (Brown et al., 2015). We use a TL-DA-20 Risø automated luminescence reader to make luminescence measurements (e.g., Figure A5; Bøtter-Jensen et al., 2003; Rhodes, 2015). We examine the p-IR $IRSL_{225}$ signal over the p-IR $IRSL_{290}$ signal because although p-IR $IRSL_{290}$ is a more stable signal, it is also less bleachable (Colarossi et al., 2015; Li & Li, 2011). We also tested for anomalous fading at room temperature on timescales of hours to two weeks and found no signal loss.

Single-grain De values were summarized using standard age models. For typical samples, we used the minimum age model, which assumes that only some grains were fully bleached before deposition (Galbraith et al., 1999). This condition would be expected for high energy fluvial

deposition, characteristic of desert storms, as sunlight may not fully bleach all sediment (Gray et al., 2017). For these calculations, we assume overdispersion (OD) values of 15%, a value typical of well-bleached single-grain feldspar samples in the region (Brown et al., 2015). Samples J1365 and J1370 exhibited low variability in De from individual grains with OD values of zero, suggesting that all grains comprise a single dose population that was well bleached before deposition. Based on the low OD, we use the central age model (Galbraith et al., 1999) assuming grains were fully bleached either during fluvial transport or on the surface before burial (Gray & Mahan, 2015; McGuire & Rhodes, 2015). Luminescent grains from sample J1324 were in field saturation and did not yield finite equivalent dose values. The resulting equivalent doses and ages for all samples are shown in Figure A6 and Table A2. Full sample preparation, geologic dose rate calculation, and methods for measuring equivalent dose are presented in Text A6.

2.3 Results

2.3.1 Fault orientations, offsets, and senses of slip

Our mapping defines the ~6 km-wide, ~N-S-oriented Almeja fault zone (Figure 2.3). Remote- and field-mapping identified NNW-striking faults in the North Volcanic Hills (Figure 2.3d), somewhat similar in orientation to the results from template matching (Figure 2.3a). In the Central Terraces, we mapped ~NNW-striking faults in the west and NNE- striking faults in the east (Figure 2.3e), which agree with those identified from template matching (Figure 2.3b). In the South Volcanic Hills, remote- and field-mapping identified NNE-striking faults (Figure 2.3f) that also agree with our template matching (Figure 2.3c). The Almeja fault zone is mapped continuously to the southwest coast of IAG and projects offshore from sea cliff exposures of steep, NNE-striking, WNW-dipping normal faults (Sabbeth, 2020). We obtained AUROC values of 0.57 and 0.56 for the Central Terraces and South Volcanic Hills, respectively (Table A1). AUROC values between

0.43 – 0.68 were obtained from similar applications in Sare et al. (2019), discussed in Section 2.4.1.1. Lastly, Kolmogorov-Smirnov and Wilcoxon tests reject that the orientation from remote- and field-mapping and template matching have equal distributions and medians for both the Central Terraces and the South Volcanic Hills. When both tests are administered to compare orientations from the Central Terraces and South Volcanic Hills holding the mapping method constant, it was also determined that the regions have statistically different continuous distributions and median orientations. Therefore, remote- and field-mapping and template matching record an along-strike change of fault orientation across southern IAG, from roughly N-S in the Central Terraces to roughly NNE-SSW in the South Volcanic Hills. Results from the North Volcanic Hills are omitted because some scarps may be related to lithology and not faults. Such false positives are also likely in the other regions, particularly the South Volcanic Hills where we do not analyze reconstructable geomorphic surfaces, such as terrace treads. Detection of false positives in volcanic rock is discussed in Section 2.4.1.1.

All faults mapped in the field by Sabbeth (2020) are normal faults, some with components of dextral slip. Here, we also identify several faulted late Quaternary terraces that suggest a dominance of normal dip-slip motion (Figure 2.4). Additionally, we map a ~1 km-long and 0.5 km-wide graben (Figure 2.5a), which displaces geomorphically young terrace treads. Its east-facing synthetic fault is suspected to continue north as a ~10 km-long, normal fault located at the toe of the major east-facing mountain front, hereafter the Mountain Front fault (Figure 2.2b). Thirdly, we document several structural depressions throughout southern IAG (Figure 2.6).

Many of the faults that cut the highest and presumably older Quaternary terraces surrounding the North Volcanic Hills and in the Central Terraces record little to no horizontal offset (e.g., Figure 2.7a – c; Figure A2). Younger terrace risers related to inactive inset terraces also

record little to no horizontal offset. However, we observe many measurable vertical offsets of terrace treads. For example, we estimate vertical offsets along one NNW-striking fault, labeled X on Figures 4a, 5b, and 7a, that cuts the highest terrace, T1, and lower inset terraces T1b, T1c, and T2. Here at our 'flight of terraces' site, we estimate that the tread of terrace T2 is vertically offset by fault X ~3.6 m (95% confidence interval 3.1 – 4.4 m) from three scarp profiles (Figure 2.7d). The T2 tread surface is affected by subtle fluvial incision on both sides of the fault (Figure 2.7a – c; Figure A7) but did not prevent us from creating a reliable planar fit to these terrace treads (Figure A8). The lowest terrace, T3, records no vertical offset and likely post-dates the most recent fault activity here.

We found only two fault strands with possible strike-slip offset, both from fluvially active Quaternary terrace risers near the South Volcanic Hills. One possible offset is observed on a NNE-striking fault with ~2 – 4 m of west-side-down offset located in the eastern part of the South Volcanic Hills, hereafter the Sag Pond fault as it forms a local depression similar to a sag pond (Figure A9a – c). Here, we estimate ~100 m of right separation of the northern margin of the modern arroyo. We found that the downthrown block west of the fault only exposes terrace deposits while volcanic bedrock has been uplifted and exposed beneath the erosional strath on the upthrown block, east of the fault (Figure A9c). Thus, we attribute this apparent horizontal offset to widening of the channel and ponding of sediments west of the more resistant, uphill-facing scarp. We find further corroborating evidence to the north, where we do not observe strike-slip offsets of volcanic bedrock or other arroyos (Sabbeth, 2020). The second fault strand with possible strike-slip offset is a NNE-striking, east-side-down fault located ~0.7 km east of the Sag Pond fault. A channel incised into abandoned late Quaternary terraces (T1 and T2) shows ~10 – 15 m of apparent dextral offset where it crosses this fault strand (Figure A9d – e). Along strike ~0.5 and ~0.7 km

farther south, two terrace risers (the T2/T1 riser) are right-laterally offset by ~12 – 20 m (Sabbeth, 2020). These observations suggest that these horizontal offsets could be from oblique-normal fault slip.

2.3.2 Late Quaternary ages of offset deposits

We determine the depositional ages of faulted and unfaulted sedimentary deposits to constrain the age of fault activity on southern IAG. We interpret that these extensive terraces have primarily non-marine, fluvial, and alluvial origins because we observe sediment deposits on strath surfaces with similar gradients to modern channels and risers that parallel those channels. At the 'flight of terraces' site (Section 2.3.1; Figure 2.4a; Figure 2.5b), we date sediment from terrace surfaces that provide ages of terrace abandonment. The surface age of the highest terrace (T1) is > ~200 ka (J1324, saturated signal), that of a faulted terrace (T2) is 11.7 ± 4.4 ka (J1365), and that of an unfaulted terrace (T3) is 6.5 ± 1.4 ka (J1366). A surface age from the lowest terrace (T3a) ~5 m above the active arroyo, located ~0.5 km downstream from the other samples, of 1.0 ± 0.2 ka (J1326) suggests ongoing fluvial incision.

At the 'incised terrace' site, ~1 km south of the 'flight of terraces' site, we report two depositional ages from an incised and inset terrace (T3) near several normal faults (Figure 2.4b). A west-facing cutbank exposes this inset terrace near a N-trending gully. We interpret this inset terrace as cut by a N-striking fault strand located at its back edge (Figure A10). The luminescence samples taken here, vertically spaced ~3 m in the cutbank and from terrace fill material, gave stratigraphically consistent ages of 73.9 ± 7.9 ka (J1317) and 37.6 ± 4.3 ka (J1318; Figure 2.6a). These ages are likely older than the abandonment age of T3 because these samples were taken from fill material beneath the T3 surface. Therefore, ages here provide a maximum age constraint for the most recent local fault offset to < ~38 ka.

At the ‘sag pond’ site (Figure 2.4c), ~3 km south of the ‘incised terrace’ site, we report a depositional age of 9.4 ± 0.8 ka (J1370) from sediment in a local depression similar to a sag pond impounded against an uphill-facing scarp in volcanic bedrock along the Sag Pond fault (Figure 2.6b). However, the deposits are not cut by this fault. Therefore, we suggest that the most recent offset of the Sag Pond fault occurred before 9.4 ± 0.8 ka.

At the ‘southern terraces’ site, ~1.5 km east of the ‘sag pond’ site, we report maximum age constraints for fault activity at two locations where T3 terrace deposits are cut by NW-striking normal faults exposed in arroyo cutbanks (Figure 2.4d). At the northern part of this site, faults form a ~30 m-wide graben, which is not discernable in the high-resolution DEMs because a 1 – 2 m-thick veneer of unfaulted T3 strath gravel overlies the faults that cut the underlying finer-grained sediments (blue line in Figure 2.6c). Depositional ages from the finer-grained terrace fill in the horst blocks of the NW-striking graben are 129.7 ± 17.0 ka (J1320) and 100.2 ± 9.2 ka (J1375). We constrained normal fault offset here to post-date 52.0 ± 4.7 ka (J1322) and 53.1 ± 5.5 ka (J1321) from closely spaced samples in faulted terrace fill from the graben block (Figure 2.6c). About 250 m south of this graben, we obtained depositional ages of 33.9 ± 3.0 ka (J1323) and 51.0 ± 4.5 ka (J1374) from faulted terrace fill under a T3 strath (Figure 2.6d). These ages are inverted, possibly from bioturbation of sample J1323 or a structural disturbance between the two samples. Nonetheless, the natural luminescence signals from both samples are well below saturation and did not fade on laboratory timescales. Similar to the ‘incised terrace’ site, all samples at the ‘southern terraces’ are of terrace fill material. These ages are likely older than the abandonment age of the unfaulted T3 strath. Thus, we cannot use these ages to correlate T3 surface abandonment ages across drainages. However, these ages provide constraints on the timing of local fault offsets, which we interpret to have occurred ≤ ~50 ka here.

2.4 Discussion

2.4.1 Fault distributions, orientations, and activity in southern IAG

2.4.1.1 Spatial patterns of fault orientations

Fault orientation analyses from both remote- and field-mapping and template matching record similar gradual changes of fault strike from north to south along the Almeja fault zone. In the North Volcanic Hills and Central Terraces, NNW- and N-striking normal faults do not align with either the NW-striking Ballenas transform fault or the NE-trending North Salsipuedes basin. Interestingly, in the South Volcanic Hills, NNE-striking normal faults from field-based mapping (Figure 2.3f) and template matching (Figure 2.3c) are sub-parallel to the nearby North Salsipuedes basin. Although we find agreeable changes of fault orientation from both mapping methods, there are minor discrepancies between their results.

In the North Volcanic Hills, both methods identify faults of somewhat similar orientations. However, the median fault orientation from template matching is ~10° counterclockwise of remote- and field-mapping. We find this mismatch because template matching is applied to volcanic bedrock where the method is capturing NW- to NNW-trending resistant cliff bands in gently E-dipping volcanic bedrock (Sabbeth, 2020) in addition to true fault scarps. But our remote- and field-mapping observes N-striking faults both within this volcanic bedrock and across terraces to the east and west of this exposure (Figure 2.3; Figure A4). Therefore, field context suggests our filtering of non-tectonic scarps performs poorly in this region and explains the mismatch.

In the Central Terraces and South Volcanic Hills, remote-and field-mapping and template matching cover a similar areal extent, allowing us to better compare the similarity between both methods. Template matching in the Central Terraces has an AUROC value of 0.57 when compared to the 10 m buffer around remote- and field-mapped faults, which is lower than a value of 0.7 that

is typically considered satisfactory. However, 0.57 is on par with AUROC from Sare et al. (2019; AUROC = 0.43 – 0.68) when scarp orientations allowed by the algorithm were not constrained to a certain range, as in this study. Also, median orientation from template matching is only ~5° clockwise of remote- and field-mapping. After post-processing, precision and accuracy increase from 0.11 to 0.22 and 0.61 to 0.83, respectively (Table A1). Therefore, we suggest template matching characterizes tectonic fault orientation and density well in the Central Terraces.

At the South Volcanic Hills, median orientation from template matching is ~20° clockwise of remote- and field-mapping. Nonetheless, we obtain an AUROC of 0.56 for this region, suggesting template matching performed similarly here compared to the Central Terraces. After post-processing, precision remains unchanged at 0.12 and accuracy increases from 0.68 to 0.85 (Table A1). Here, we observe template matching scarps that do not correspond to, but seem to be continuous with, remote- and field-mapped faults (Figure A11a). We also find ridges over volcanic rock that are closely aligned with mapped faults (Figure A11b). This pattern suggests that our template matching is detecting previously unmapped fault segments that may be controlling ridges here. Therefore, template matching may identify lineaments that are possible faults in the South Volcanic Hills, which can be confirmed with future field mapping.

Statistical tests show that results from both remote- and field-mapping and template matching in the same region are not statistically similar. Nonetheless, both methods suggest the same subtle changes in fault orientation from the Central Terraces to South Volcanic Hills, where we are confident that both methods capture tectonic fault scarps (~13° clockwise change for remote- and field-mapping and ~30° clockwise change for template matching, both from the median orientation of segments). Our comparison of remote- and field-mapping and template matching results, acceptable AUROC values, and consistent change of fault strike support that the

Almeja fault zone is sub-parallel and likely linked to the NE-trending North Salsipuedes basin at the southwest coast of IAG. We also show that template matching with field context can assess fault characteristics in inaccessible regions.

2.4.1.2 Late Quaternary fault activity

Our luminescence ages from five sites constrain late Quaternary fault activity within the Almeja fault zone by demonstrating that at least four fault strands have produced surface-rupturing earthquakes after ~50 ka (Figure 2.4). Although we constrained late Quaternary offset on only a few faults in this highly distributed fault zone, strands that lack direct age control cut terrace deposits that are correlative to our dated terrace units (Figure A2; Sabbeth, 2020). Thus, we interpret that most fault strands in the Almeja fault zone are late Quaternary active. Additionally, our mapping suggests potential continuity of the Almeja fault zone some distance offshore to the southwest. Remote- and field-mapping here, field-mapping from Sabbeth (2020), and the strike of steep fault scarps in bathymetry (~N42°E, perpendicular to strike of Ballenas transform fault ~N48°W; Plattner et al., 2015) align well with each other and presumably connect across the gap in high-resolution bathymetric data between the southwest IAG coast and ~2 – 3 km offshore (Figure 2.2b). Thus, we infer that faults in the North Salsipuedes basin are also late Quaternary active and linked with the Almeja fault zone.

We do not present a slip rate for the entire Almeja fault zone because dated terraces are spatially limited and we do not have a finite age for the highest terrace T1, where significant dip-slip occurred. This limitation prevents us from calculating an accurate cumulative dip-slip rate. However, we can determine the Holocene dip-slip rate of fault X based on finite ages from faulted and unfaulted terraces. Using the Monte Carlo dip-slip displacement of fault X on terrace T2 and luminescence ages from terraces T2 and T3, the median slip rate of fault X between ~5 – 15 ka is

0.64 mm/yr (95% confidence interval 0.35 – 1.6 mm/yr; Figure 2.7e; Figure A12) following methods from Gold & Cowgill (2011; Text A1). Although this rate does not consider cumulative slip across the width of the Almeja fault zone, it is greater than the mean uplift rate across Baja California since 1 Ma (~0.1 mm/yr; Ortlieb, 1991). Because both rates are calculated across different timescales, we cannot assess if the Almeja fault zone has consistently facilitated high uplift or if it has had a time-variable slip rate (e.g., Garlock fault, California; Rittase et al., 2014) since the late Miocene or Pliocene when offshore rift-related faulting commenced. Nonetheless, our data support that fault X has been active during the Holocene.

Historic seismicity also supports ongoing deformation on IAG, as the Ballenas transform fault, North Salsipuedes basin, and Almeja fault zone have hosted many large historic earthquakes, recently relocated onshore or directly offshore (Figure 2.2a; Figure A13; Castro et al., 2021; Castro et al., 2017). On 12 November 2003, a Mw 5.6 earthquake with a N-striking normal fault focal mechanism that has a minor dextral-oblique component occurred (López-Pineda et al., 2014) and was relocated < 1 km offshore of southern IAG's east coast, along strike of the Almeja fault zone (Figure A13; Castro et al., 2021; Castro et al., 2017). On 3 August 2009, a Mw 6.9 strike-slip earthquake on the Ballenas transform fault struck directly west of IAG (Plattner et al., 2015). On 21 December 2009, a Mw 4.8 earthquake with a dextral oblique-normal focal mechanism occurred and was relocated in the southern mountain range of IAG (Figure A13; Castro et al., 2021; Castro et al., 2017). These 2009 earthquakes may be related, similar to how north-south migrating earthquake swarms on the Ballenas transform fault between 1973 – 1977, 1980 – 1982, and 1997 – 2003 are thought to increase seismicity in the North Salsipuedes basin when residual elastic energy after the swarms were distributed to surrounding rocks (López-Pineda et al., 2014). Indeed, changes of Coulomb failure stress after large strike-slip earthquakes on the Ballenas transform

fault bring normal faults in the North Salsipuedes basin closer to failure (Plattner et al., 2015). Therefore, the earthquake cycle on the Ballenas transform fault may increase activity in the North Salsipuedes basin.

2.4.2 Microcontinent isolation mechanisms and future plate boundary reorganization

We first consider two strike-slip microcontinent isolation models, the wrench and horsetail models (Nemčok et al., 2016), to be responsible for the deformation of the Almeja fault zone. Dextral oblique-normal earthquakes have been recorded in the fault zone. However, while the Tiburón fault and Ballenas transform fault bound IAG (Figure 2.2a), the absence of a transtensional duplex across the island, which would have formed as both faults overlapped and developed stepovers, precludes that IAG is compatible with the wrench faulting isolation model (Figure 2.8a; Antobreh et al., 2009). Also, we would expect the duplex to be inactive today, contrary to our luminescence ages, as the overlapping was completed by ~2 Ma.

We do observe normal faults at high angles to the Ballenas transform fault throughout our study area (Figure 2.3) that may be associated with the tips of strike-slip horsetail structures terminating on the island (Figure 2.8b; e.g., Misra et al., 2014). A related hypothesis posits that the Almeja fault zone could be an expression of distributed transtension, off-fault strike-slip faulting splaying off the Ballenas transform fault, or dextral shear and secondary extension on faults with orientations that vary 10° – 30°. However, there is little evidence from geomorphic markers (only that in Figure A9d – e), field-mapping (Sabbeth, 2020), and earthquakes to suggest a significant, dextral component of fault motion onshore IAG. Therefore, it is unlikely that the entire Almeja fault zone represents horsetail strike-slip structures or is dominated by off-fault strike-slip faulting related to the Ballenas transform fault.

Another hypothesis for the role of the Almeja fault zone involves the Mountain Front fault and graben just north of our study area (Figure 2.2b). Marine seismic lines obtained from PEMEX Exploración y Producción (map extent in Mar-Hernández et al., 2012) suggest that the Mountain Front fault may continue offshore and intersect the NW-striking Tiburón fault east of IAG (Figure 2.8c). This suggested intersection is similar to how extensional faults and spreading centers in the inactive Lower Tiburón basin intersect the Tiburón fault (e.g., Figure 2.8a; Lonsdale, 1989). A related hypothesis is that the Almeja fault zone is an early splay of the North Salsipuedes basin and is becoming inactive while a hard link between the basin and the Ballenas transform fault is established. Both hypotheses require the Almeja fault zone to be a dying segment of the presumably inactive Lower Tiburón basin or active North Salsipuedes basin. However, the mountain front graben vertically displaces geomorphically young terraces by ~1 – 7 m (Figure 2.5a), which suggests recent activity that agrees with our late Quaternary offsets from luminescence ages farther south. These young offsets suggest that onshore activity is not waning, which does not support the wrench (Figure 2.8a) nor dying splay (Figure 2.8c) models as the driving mechanism that formed the Almeja fault zone.

Our data suggest that (1) the Almeja fault zone is kinematically linked to the North Salsipuedes basin and (2) is presently complementing extension in the overlapping Lower Delfín basin. We propose that the NW-SE-directed extension between the Ballenas transform fault and the Tiburón fault is partitioned between the Lower Delfin basin and the Almeja fault zone (Figure 2.8d). Fault orientation, sense of slip, and the age of fault offsets collected here and in Sabbeth (2020) agree with this two-part hypothesis. First, the onshore, N-striking, normal faults within the Almeja fault zone mapped in this study (Figure 2.3) and by Sabbeth (2020) suggest that the Almeja fault zone projects offshore into the North Salsipuedes basin (Figure 2.8e). This orientation and

slip behavior agree with the stress field related to the transtensional Pacific-North America plate boundary. Therefore, we propose that the North Salsipuedes basin is kinematically linked to the Almeja fault zone. Second, our luminescence ages constrain that the most recent normal fault offset on multiple fault strands occurred after ~50 ka. These ages and our slip rate estimate are similar to the activity of the North Salsipuedes basin, inferred from its submarine volcanic hills (Figure 2.2b), seismicity, and thinned crust (Paz-López, 2000). Together, the orientation, sense of slip, and activity of the Almeja fault zone suggest that it is presently active and kinematically linked to the North Salsipuedes basin rather than to the inactive Tiburón fault. This suggestion does not require that the Almeja fault zone is not structurally connected to the Tiburón fault via the Mountain Front fault. Offset sediment layers near the Upper Tiburón basin in the PEMEX seismic lines (e.g., Mar-Hernández et al., 2012) suggest such a linkage. Therefore, extension in the North Salsipuedes basin may be affecting normal slip across southern IAG up to the Tiburón fault.

Regardless of the mechanism, if the Almeja fault zone continues to extend, the southern tip of IAG may eventually break away from the larger, northern part of the island and could lead to further microcontinent fragmentation and produce a second, smaller block (Figure 2.8d) stranded within the transtensional plate boundary. Such breakup may exploit dynamic instabilities of the plate boundary (Gerya, 2010), such as the Almeja fault zone, which serves as a lithospheric preexisting weakness (Molnar et al., 2018). Thus, fragmentation of IAG may not be complete, and the Pacific-North America plate boundary is either not fully localized onto the Ballenas transform fault or is in the initial stage of a plate boundary reorganization.

2.5 Conclusions

IAG is an ideal location to study microcontinent evolution. The onshore, normal, Almeja fault zone is sub-parallel to and on-strike with the offshore North Salsipuedes extensional basin,

which is compatible with the hypothesis that these fault systems are kinematically linked across the shoreline. This linkage is further supported by late Quaternary onshore fault activity constrained by luminescence ages, historical seismicity, and extensional volcanic activity in the offshore basin. Combined, our results indicate that fragmentation and breakup of IAG are not yet complete and have likely been controlled by offshore extension in the North Salsipuedes basin since its inception ≤ 2 Ma. Therefore, a small portion of Pacific-North America plate motion may have been accommodated east of IAG for the past few million years or we may be capturing the early signs of a reorganization of the Pacific-North America plate boundary through the breakup of an evolving microcontinent.

2.6 Figures

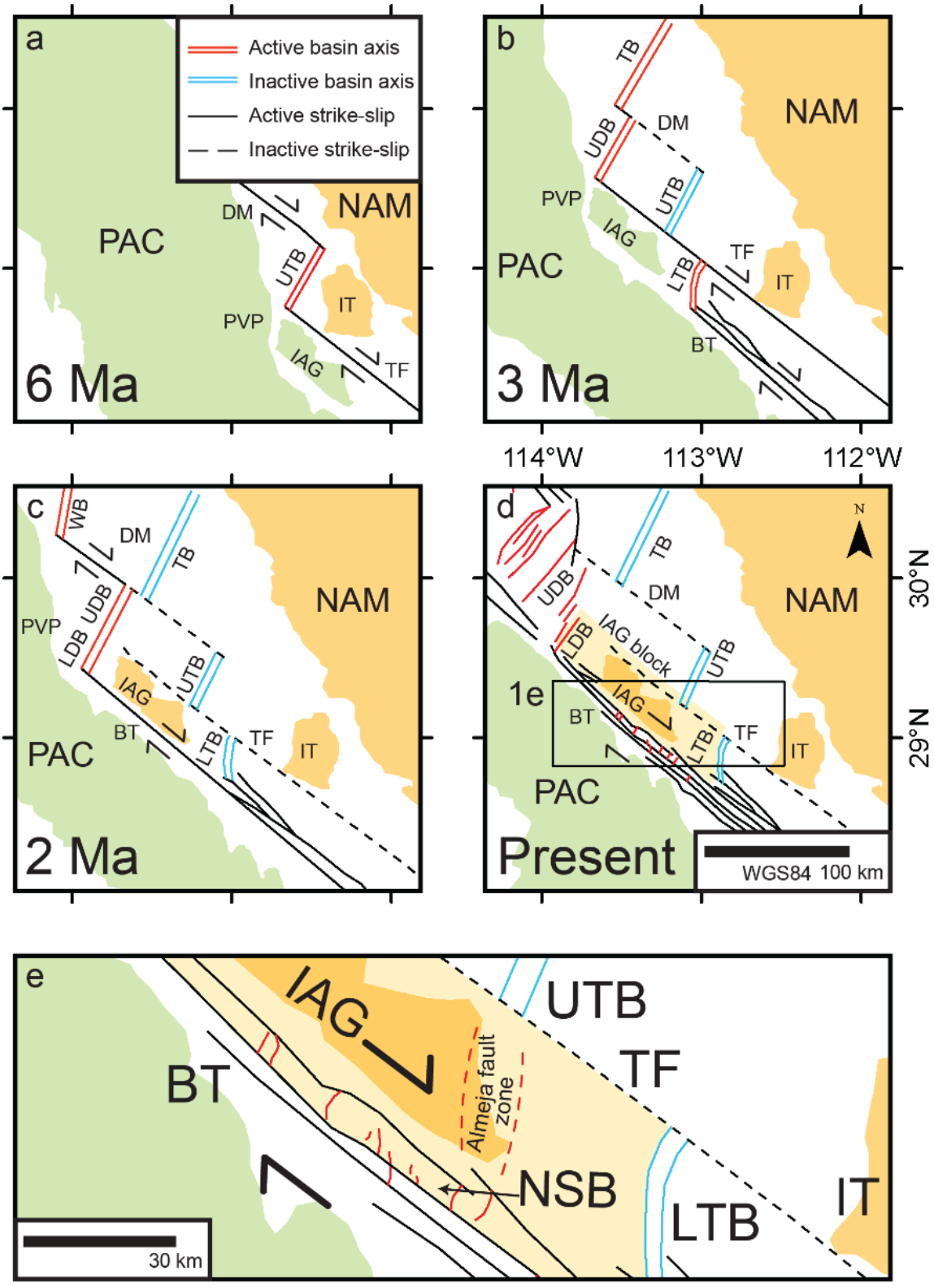
a
Active basin axis
Inactive basin axis
Active strike-slip
Inactive strike-slip
PAC
NAM
DM
UTB
IT
PVP
IAG
TF
6 Ma
b
TB
UDB
DM
NAM
PVP
IAG
UTB
PAC
LTB
TF
IT
BT
3 Ma
114°W
113°W
112°W
c
WB
DM
TB
NAM
PVP
LDB
UDB
UTB
IAG
BT
PAC
LTB
TF
IT
2 Ma
d
N
TB
UDB
DM
NAM
30°N
LDB
IAG block
UTB
1e
IAG
BT
LTB
TF
IT
PAC
29°N
Present
WGS84 100 km
e
IAG
UTB
TF
BT
Almeja fault zone
NSB
LTB
IT
30 km

Figure 2.1. Tectonic reconstruction of the northern Gulf of California and associated structures holding the North America plate fixed (Aragón-Arreola & Martín-Barajas, 2007; Bennett et al., 2016b; Stock, 2000) at (a) 6 Ma, (b) 3 Ma, (c) 2 Ma, and (d) present. Landmasses on the Pacific and North America plates are shown in green and orange, respectively. (e) Detailed map of southern Isla Ángel de la Guarda showing how the Almeja fault zone may connect with the North Salsipuedes basin (see location in Figure 2.1d). BT – Ballenas transform fault, DM – De Mar fault, IAG – Isla Ángel de la Guarda, IT – Isla Tiburón, LDB – Lower Delfín basin, LTB – Lower Tiburón basin, NAM – North America plate, NSB – North Salsipuedes basin, PAC – Pacific plate, PVP – Puertecitos Volcanic Province, TB – Tepoca Basin, TF – Tiburón fault, UDB – Upper Delfín basin, UTB – Upper Tiburón basin, WB – Wagner Basin.

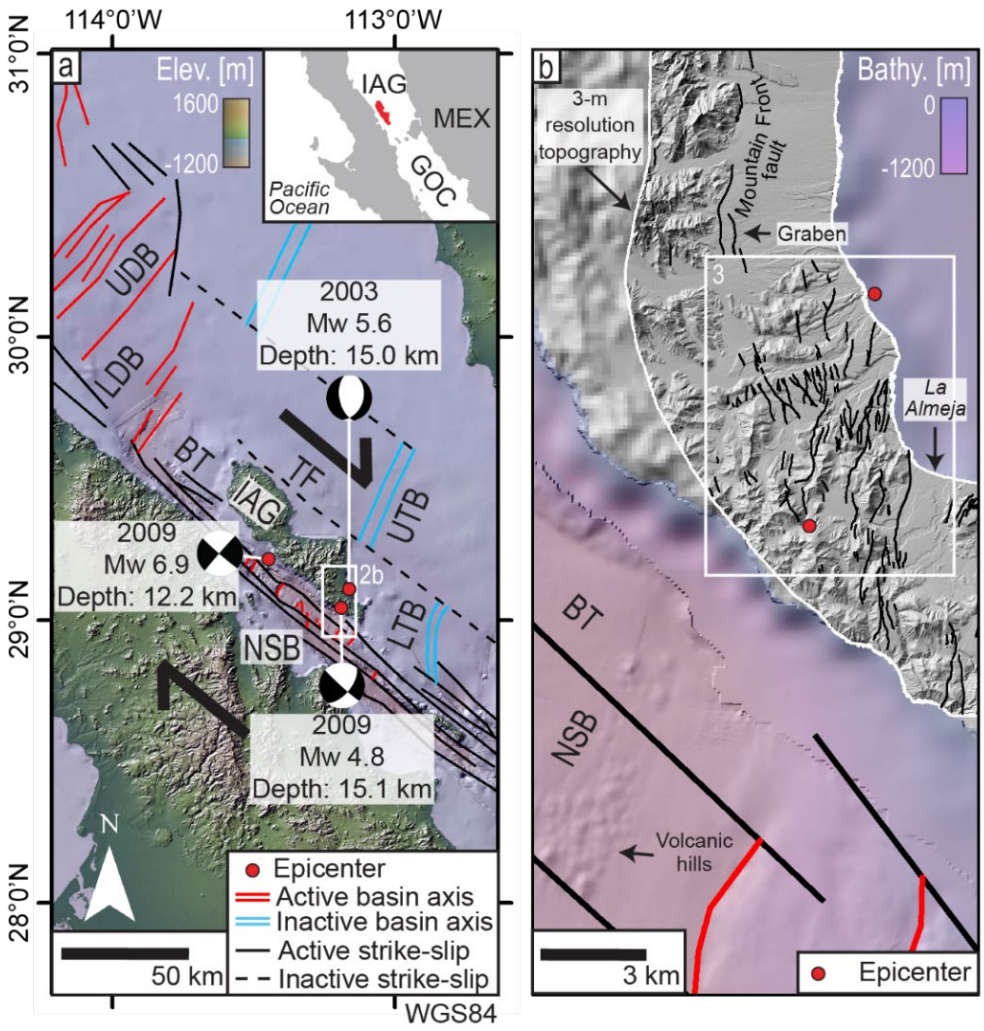

Figure 2.2. (a) Structural map of the Pacific-North America plate boundary in the northern Gulf of California (e.g., Stock, 2000), showing the Ballenas transform fault (BT), Lower and Upper Delfín basins (LDB and UDB), Lower and Upper Tiburón basins (LTB and UTB), North Salsipuedes basin (NSB), Tiburón fault (TF), and historic earthquake epicenters (Castro et al., 2021; Castro et al., 2017) and focal mechanisms (Dziewonski et al., 1981; Ekström et al., 2012). Basemap is shaded relief, digital elevation, and bathymetry from GeoMapApp (Ryan et al., 2009). (Inset) Location of Isla Ángel de la Guarda (IAG) in the Gulf of California (GOC), México (MEX). (b) 3-m resolution shaded relief map from 0.5-m resolution Pleiades images of southern IAG showing the Almeja fault zone (thin black lines; Sabbeth, 2020) and earthquake epicenters.

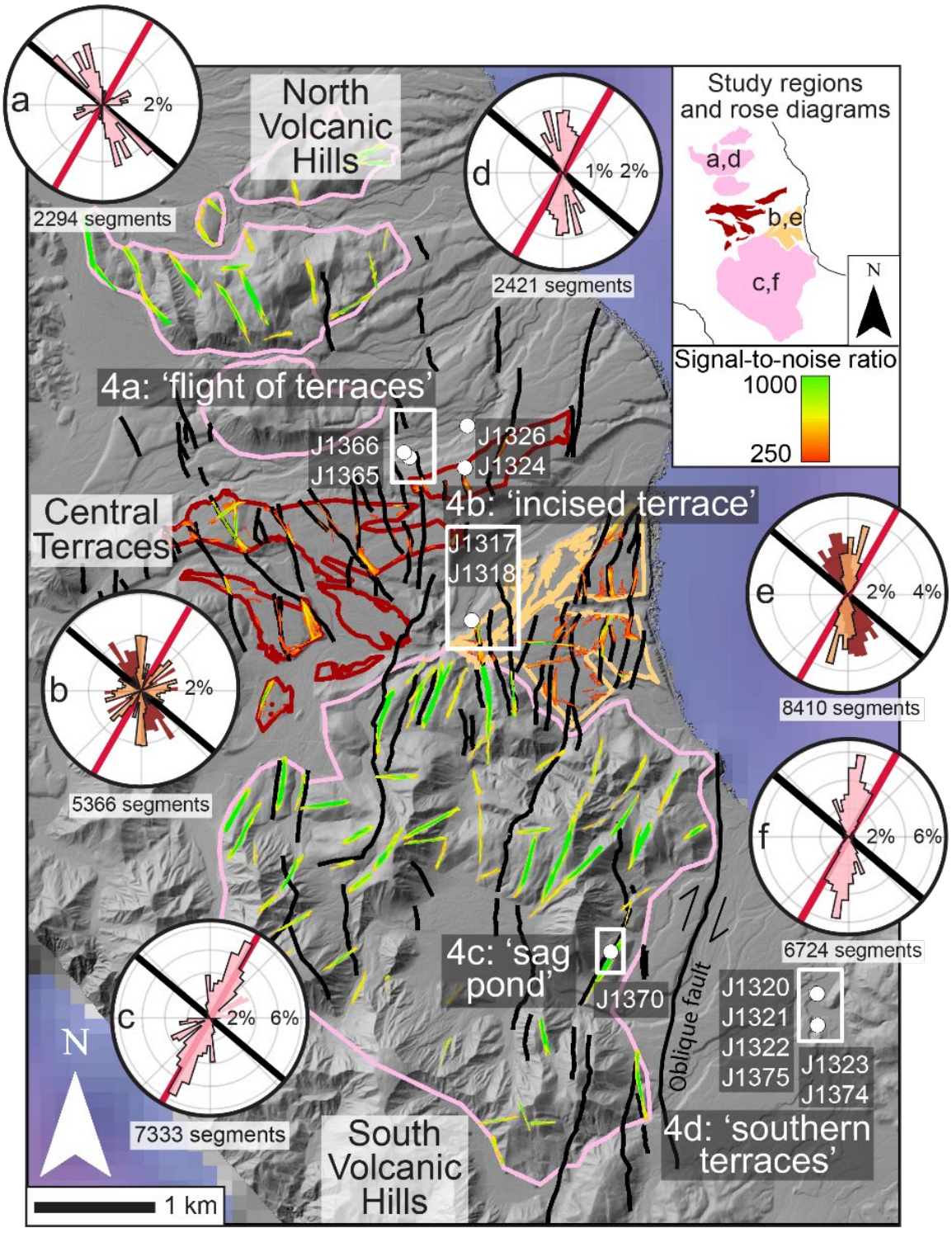
a
2%
2294 segments
North Volcanic Hills
d
1% 2%
2421 segments
Study regions and rose diagrams
a,d
b,e
c,f
N
Signal-to-noise ratio
1000
250
4a: 'flight of terraces'
J1366
J1365
J1326
J1324
4b: 'incised terrace'
J1317
J1318
Central Terraces
b
2%
5366 segments
e
2%
4%
8410 segments
f
2%
6%
6724 segments
4c: 'sag pond'
J1370
Oblique fault
J1320
J1321
J1322
J1375
J1323
J1374
4d: 'southern terraces'
c
2%
6%
7333 segments
N
South Volcanic Hills
1 km

Figure 2.3. Luminescence sites (white dots), faults from remote- and field-mapping (black lines = normal and oblique faults; Sabbeth, 2020), and scarps from template matching (colored by signal-to-noise ratio) on southern Isla Ángel de la Guarda. Basemap is a 3-m resolution shaded relief from 0.5-m resolution Pleiades images (extent shown in Figure 2.2b). Rose diagrams show orientations of 3-m fault scarp segments from (a-c) template matching and (d-f) remote- and field-mapping for three study regions colored by lithology: the North and South Volcanic Hills (pink) and Central Terraces (west: maroon, east: tan). Radial unit is calculated as percent of segments in a bin relative to the total number of segments. Each rose petal is an orientation bin of 6°. Average orientation of the Ballenas transform fault and North Salsipuedes basin near Isla Ángel de la Guarda are the thick black and red bars in each rose diagram, respectively. (Inset) Map of three study regions colored by lithology (same colors as above). Refer to Sabbeth (2020) for geologic maps showing volcanic bedrock and terraces and Figure A2 for local-scale terrace generations.

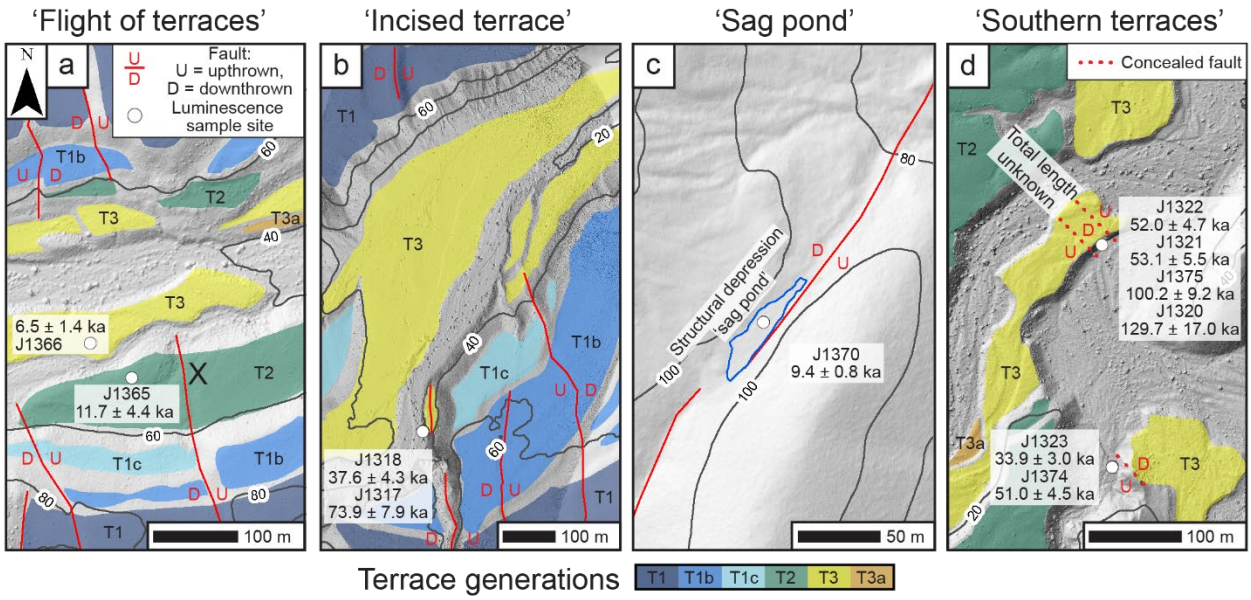

Figure 2.4. Luminescence sites and corresponding sample ages from the (a) 'flight of terraces' site with fault X, (b) 'incised terrace' site, (c) 'sag pond' site with local depression similar to a sag pond, and (d) 'southern terraces' site. Site locations in Figure 2.3. Basemaps are shaded relief from ~0.1-m resolution drone-derived elevation with 20-m elevation contours from 3-m resolution elevation from 0.5-m resolution Pleiades images. We follow the stratigraphic framework of terrace mapping by Sabbeth (2020) at nearby sites and present subdivided terrace levels here based on height above the active channel, local terrace generations, and luminescence ages.

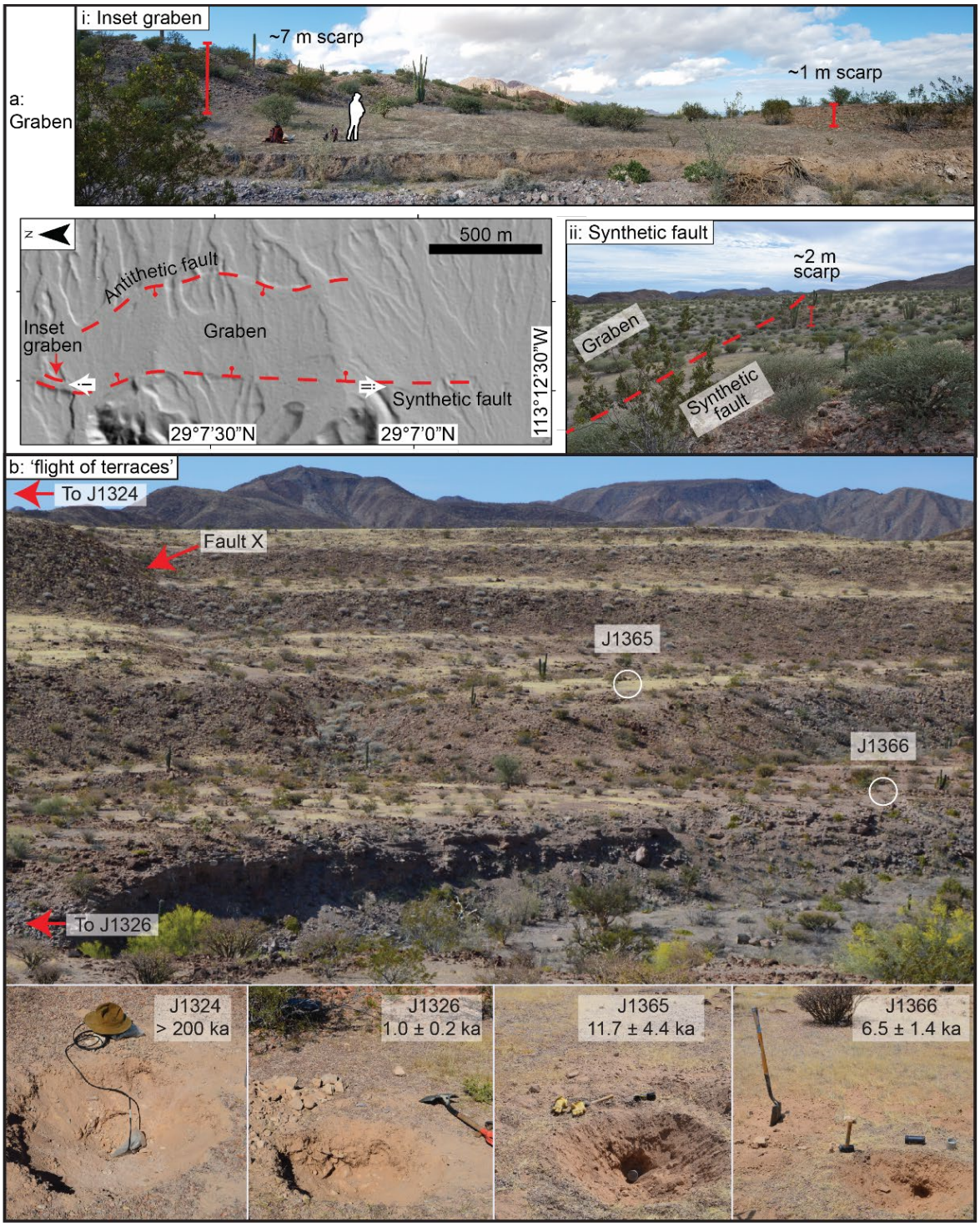

Figure 2.5. Map and field photos of the (a) graben showing (i) an inset graben and (ii) the synthetic fault. See Figure 2.2b for location of this graben along the Mountain Front fault. (b) View to southwest of 'flight of terraces' site and luminescence sample pits.

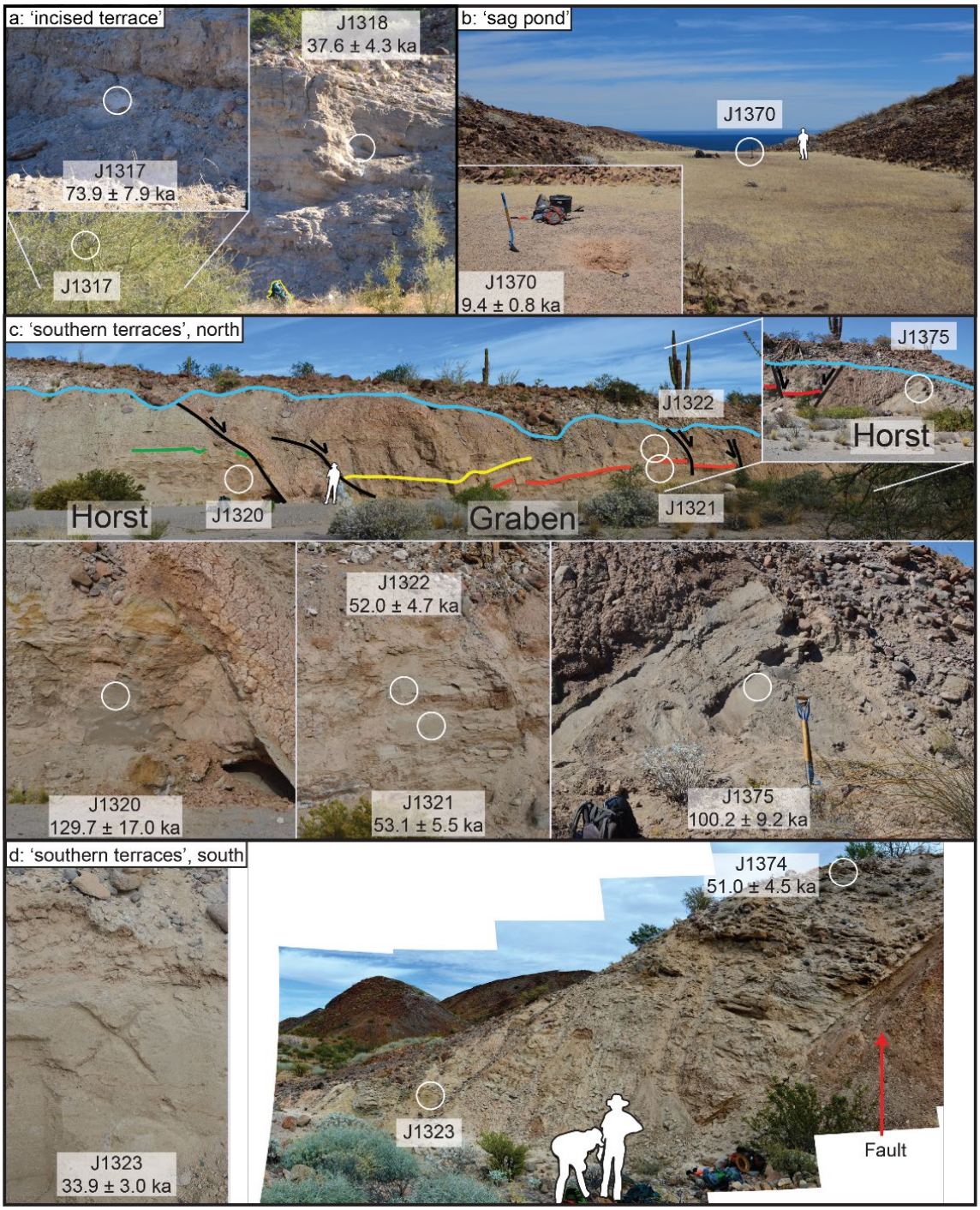

Figure 2.6. Luminescence site field photos. (a) Arroyo cutbank at the 'incised terrace' site, looking east. (b) 'Sag pond' site, looking north, and sample pit. (c) 'Southern terraces' site annotated with faults (black lines) and select stratigraphic layers (colored lines), looking north. (d) Samples located ~250 m south of the 'southern terraces' site, looking southeast.

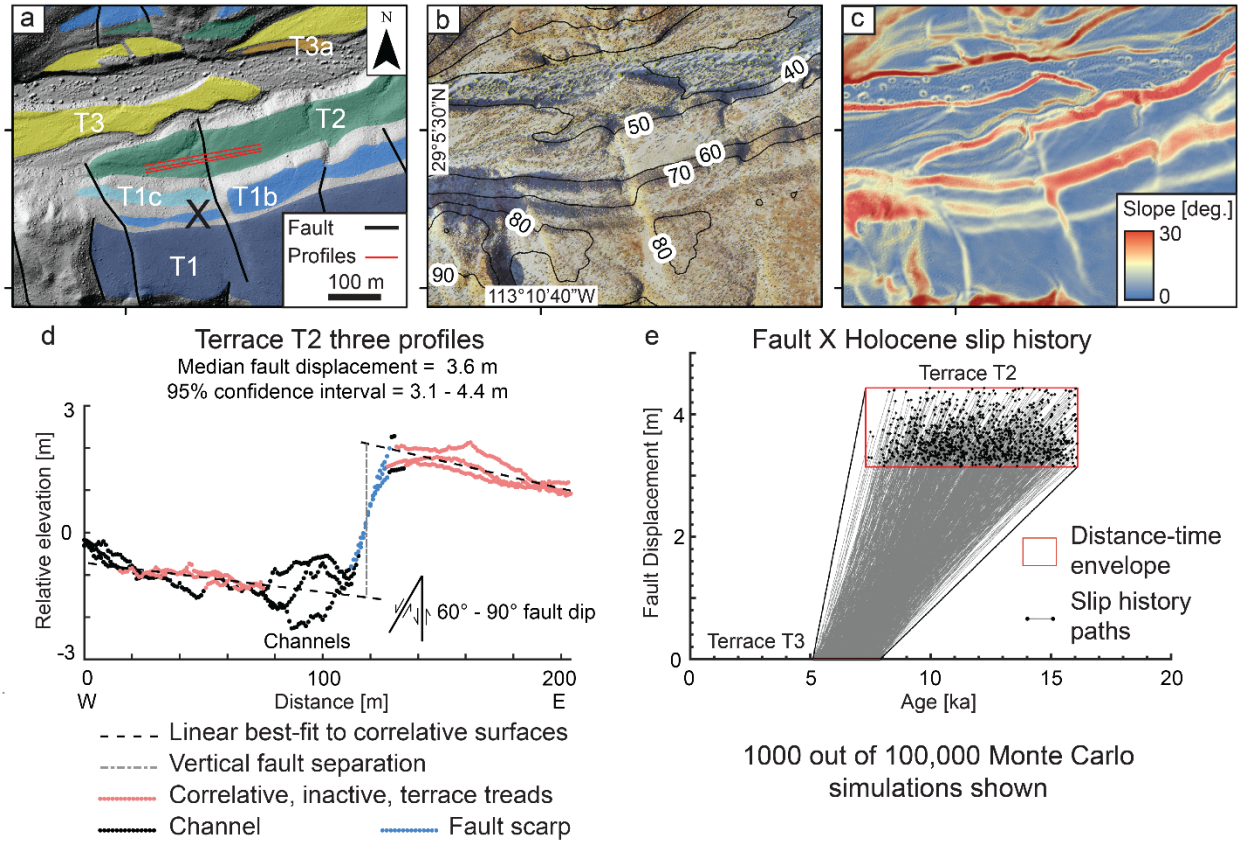

Figure 2.7. (a). Map of terrace tread surfaces, faults, and locations of three scarp profiles at the 'flight of terraces' site. Basemap is ~0.1-m resolution drone-derived shaded relief. (b) Stitched orthomosaic of drone images showing terrace surfaces with 10-m elevation contours from 3-m resolution digital elevation. (c) Slope map shows steep terrace risers (yellows to reds) with little to no horizontal offset. (d) Stacked scarp profiles of fault X on terrace T2 (3 profiles). We show sections of each profile colored by surface type. Reported fault displacement is the median from Monte Carlo simulations per terrace with fault dip between 60° – 90°, after Duckworth et al. (2020) and Thompson et al. (2002). (e) Slip history of fault X from depositional ages and Monte Carlo fault displacement estimates (after Gold & Cowgill, 2011). Distance-time envelopes are constrained by the standard deviation of depositional ages and 95% confidence interval of fault displacement.

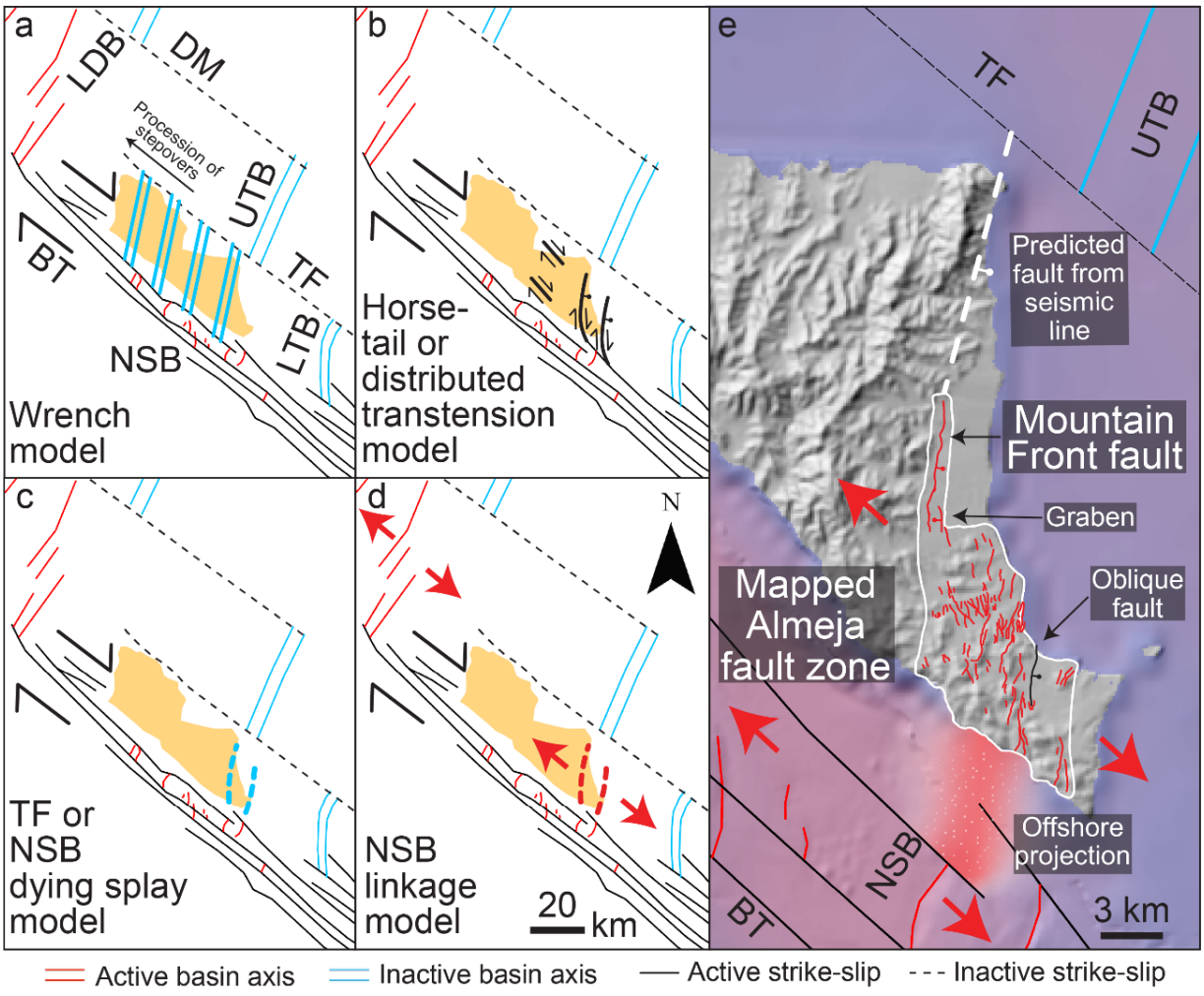

Figure 2.8. Proposed formation mechanisms of the Almeja fault zone as a (a) wrench fault or duplex structure with stepovers processing to the northwest, (b) horsetail or distributed transtensional structure from the Ballenas transform fault, (c) dying splay of the Tiburón fault or North Salsipuedes basin, and (d) kinematic link to the active North Salsipuedes basin. Tectonic structures from Aragón-Arreola & Martín-Barajas (2007), Bennett et al., (2016b), and Stock (2000) augmented by bathymetry. (e) Detailed interpretation of mapped faults in the Almeja fault zone. Abbreviations are the same as Figure 2.1.

2.7 References

Abera, R., Van Wijk, J., & Axen, G. (2016). Formation of continental fragments: The Tamayo Bank, Gulf of California, Mexico. *Geology, 44*(8), 595-598. https://doi.org/10.1130/G38123.1

Antobreh, A. A., Faleide, J. I., Tsikalas, F., & Planke, S. (2009). Rift–shear architecture and tectonic development of the Ghana margin deduced from multichannel seismic reflection and potential field data. *Marine and Petroleum Geology, 26*(3), 345-368. https://doi.org/10.1016/j.marpetgeo.2008.04.005

Aragón-Arreola, M., & Martín-Barajas, A. (2007). Westward migration of extension in the northern Gulf of California, Mexico. *Geology, 35*(6), 571-574. https://doi.org/10.1130/G23360A.1

Aragón-Arreola, M., Morandi, M., Martín-Barajas, A., Delgado-Argote, L., & González-Fernández, A. (2005). Structure of the rift basins in the central Gulf of California: Kinematic implications for oblique rifting. *Tectonophysics, 409*(1-4), 19-38. https://doi.org/10.1016/j.tecto.2005.08.002

Bennett, S. E., Oskin, M. E., Iriondo, A., & Kunk, M. J. (2016a). Slip history of the La Cruz fault: Development of a late Miocene transform in response to increased rift obliquity in the northern Gulf of California. *Tectonophysics, 693*, 409-435. https://doi.org/10.1016/j.tecto.2016.06.013

Bennett, S. E., Darin, M. H., Dorsey, R. J., Skinner, L. A., Umhoefer, P. J., & Oskin, M. E. (2016b). Animated tectonic reconstruction of the Lower Colorado River region: Implications for Late Miocene to Present deformation. *In Going LOCO, Investigations*

along the Lower Colorado River: Desert Studies Center Desert Symposium Field Guide and Proceedings, 73-86.

Bennett, S. E., & Oskin, M. E. (2014). Oblique rifting ruptures continents: Example from the Gulf of California shear zone. *Geology, 42*(3), 215-218. https://doi.org/10.1130/G34904.1

Bennett, S. E., Oskin, M. E., Dorsey, R. J., Iriondo, A., & Kunk, M. J. (2015). Stratigraphy and structural development of the southwest Isla Tiburón marine basin: Implications for latest Miocene tectonic opening and flooding of the northern Gulf of California. *Geosphere, 11*(4), 977-1007. https://doi.org/10.1130/GES01153.1

Beyer, R. A., Alexandrov, O., & McMichael, S. (2018). The Ames Stereo Pipeline: NASA's open source software for deriving and processing terrain data. *Earth and Space Science, 5*(9), 537-548. https://doi.org/10.1029/2018EA000409

Brennan, B., Lyons, R., & Phillips, S. (1991). Attenuation of alpha particle track dose for spherical grains. *International Journal of Radiation Applications and Instrumentation. Part D. Nuclear Tracks and Radiation Measurements, 18*(1-2), 249-253. https://doi.org/10.1016/1359-0189(91)90119-3

Brown, N., Rhodes, E., Antinao, J., & McDonald, E. (2015). Single-grain post-IR IRSL signals of K-feldspars from alluvial fan deposits in Baja California Sur, Mexico. *Quaternary International, 362*, 132-138. https://doi.org/10.1016/j.quaint.2014.10.024

Burbank, D. W., and R. S. Anderson (2011), Tectonic Geomorphology, Wiley, Oxford, U. K.

Buylaert, J.-P., Murray, A. S., Thomsen, K. J., & Jain, M. (2009). Testing the potential of an elevated temperature IRSL signal from K-feldspar. *Radiation Measurements, 44*(5-6), 560-565. https://doi.org/10.1016/j.radmeas.2009.02.007

Bøtter-Jensen, L., Andersen, C., Duller, G. A., & Murray, A. S. (2003). Developments in radiation, stimulation and observation facilities in luminescence measurements. *Radiation Measurements, 37*(4-5), 535-541. https://doi.org/10.1016/S1350-4487(03)00020-9

Castro, R., Carciumaru, D., Collin, M., Vetel, W., Gonzalez-Huizar, H., Mendoza, A., & Pérez-Vertti, A. (2021). Seismicity in the Gulf of California, Mexico, in the period 1901–2018. *Journal of South American Earth Sciences, 106*, 103087. https://doi.org/10.1016/j.jsames.2020.103087

Castro, R., Stock, J., Hauksson, E., & Clayton, R. (2017). Active tectonics in the Gulf of California and seismicity (M> 3.0) for the period 2002–2014. *Tectonophysics, 719*, 4-16. https://doi.org/10.1016/j.tecto.2017.02.015

Cavazos Alvarez, J. A. (2015). Estratigrafía de la cuenca central de la Isla Ángel de la Guarda: evidencia del inicio de extensión en el Golfo de California, (Master's thesis). Retrieved from Institutional Repository CICESE. (http://cicese.repositorioinstitucional.mx/jspui/handle/1007/961). Centro de Investigación Científica y de Educación Superior de Ensenada.

Colarossi, D., Duller, G., Roberts, H., Tooth, S., & Lyons, R. (2015). Comparison of paired quartz OSL and feldspar post-IR IRSL dose distributions in poorly bleached fluvial sediments from South Africa. Quaternary Geochronology, 30, 233-238. https://doi.org/10.1016/j.quageo.2015.02.015

Delgado-Argote, L. (2000). *Evolución tectónica y magmatismo Neógeno de la margen oriental de Baja California central,* (Doctoral dissertation). Retrieved from Repositorio Institucional de la UNAM.

(http://132.248.9.41:8880/jspui/handle/DGB_UNAM/TES01000285550). Universidad Nacional Autonoma de México.

Duckworth, W. C., Amos, C. B., Schermer, E. R., Loveless, J. P., & Rittenour, T. M. (2020). Slip and strain accumulation along the Sadie Creek fault, Olympic Peninsula, Washington. *Journal of Geophysical Research: Solid Earth*, 2020JB020276. https://doi.org/10.1029/2020JB020276

Durcan, J. A., King, G. E., & Duller, G. A. (2015). DRAC: Dose Rate and Age Calculator for trapped charge dating. *Quaternary Geochronology, 28*, 54-61. https://doi.org/10.1016/j.quageo.2015.03.012

Dziewonski, A., Chou, T. A., & Woodhouse, J. (1981). Determination of earthquake source parameters from waveform data for studies of global and regional seismicity. *Journal of Geophysical Research: Solid Earth, 86*(B4), 2825-2852. https://doi.org/10.1029/JB086iB04p02825

Ekström, G., Nettles, M., & Dziewoński, A. (2012). The global CMT project 2004–2010: Centroid-moment tensors for 13,017 earthquakes. *Physics of the Earth and Planetary Interiors, 200–201*, 1–9. https://doi.org/10.1016/j.pepi.2012.04.002

Galbraith, R. F., Roberts, R. G., Laslett, G. M., Yoshida, H., & Olley, J. M. (1999). Optical dating of single and multiple grains of quartz from Jinmium rock shelter, northern Australia: Part I, experimental design and statistical models. *Archaeometry, 41*(2), 339-364. https://doi.org/10.1111/j.1475-4754.1999.tb00987.x

Gans, P. B. (1997). Large-magnitude Oligo-Miocene extension in southern Sonora: Implications for the tectonic evolution of northwest Mexico. Tectonics, 16(3), 388-408. https://doi.org/10.1029/97TC00496

Gastil, R. G., Phillips, R. P., & Allison, E. C. (1975). *Reconnaissance geology of the state of Baja California* (Vol. 140): Geological Society of America.

Gerya, T. (2010). Dynamical instability produces transform faults at mid-ocean ridges. *Science, 329*(5995), 1047-1050. https://doi.org/10.1126/science.1191349

Gold, R. D., & Cowgill, E. (2011). Deriving fault-slip histories to test for secular variation in slip, with examples from the Kunlun and Awatere faults. *Earth and Planetary Science Letters, 301*(1-2), 52-64. https://doi.org/10.1016/j.epsl.2010.10.011

González-Fernández, A., Dañobeitia, J. J., Delgado-Argote, L. A., Michaud, F., Córdoba, D., & Bartolomé, R. (2005). Mode of extension and rifting history of upper Tiburón and upper Delfín basins, northern Gulf of California. *Journal of Geophysical Research: Solid Earth, 110*(B1). https://doi.org/10.1029/2003JB002941

Gray, H. J., & Mahan, S. A. (2015). Variables and potential models for the bleaching of luminescence signals in fluvial environments. *Quaternary International, 362*, 42-49. https://doi.org/10.1016/j.quaint.2014.11.007

Gray, H. J., Tucker, G. E., Mahan, S. A., McGuire, C., & Rhodes, E. J. (2017). On extracting sediment transport information from measurements of luminescence in river sediment. *Journal of Geophysical Research: Earth Surface, 122*(3), 654-677. https://doi.org/10.1002/2016JF003858

Guralnik, B., Ankjærgaard, C., Jain, M., Murray, A. S., Müller, A., Wälle, M., et al. (2015). OSL-thermochronometry using bedrock quartz: A note of caution. *Quaternary Geochronology, 25*, 37-48. https://doi.org/10.1016/j.quageo.2014.09.001

Guérin, G., Discamps, E., Lahaye, C., Mercier, N., Guibert, P., Turq, A., et al. (2012). Multi-method (TL and OSL), multi-material (quartz and flint) dating of the Mousterian site of

Roc de Marsal (Dordogne, France): correlating Neanderthal occupations with the climatic variability of MIS 5–3. *Journal of Archaeological Science, 39*(10), 3071-3084. https://doi.org/10.1016/j.jas.2012.04.047

Hanks, T. C. (2000). The age of scarplike landforms from diffusion-equation analysis. *Quaternary Geochronology: Methods and Applications, 4*, 313-338. https://doi.org/10.1029/RF004p0313

Hilley, G., DeLong, S., Prentice, C., Blisniuk, K., & Arrowsmith, J. (2010). Morphologic dating of fault scarps using airborne laser swath mapping (ALSM) data. *Geophysical Research Letters, 37*(4). https://doi.org/10.1029/2009GL042044

Huntley, D. J., & Baril, M. (1997). The K content of the K-feldspars being measured in optical dating or in thermoluminescence dating. *Ancient TL, 15*(1), 11-13.

Lawson, M. J., Roder, B. J., Stang, D. M., & Rhodes, E. J. (2012). OSL and IRSL characteristics of quartz and feldspar from southern California, USA. Radiation Measurements, 47(9), 830-836. https://doi.org/10.1016/j.radmeas.2012.03.025

Li, B., & Li, S.-H. (2011). Luminescence dating of K-feldspar from sediments: a protocol without anomalous fading correction. Quaternary Geochronology, 6(5), 468-479. https://doi.org/10.1016/j.quageo.2011.05.001

Liritzis, I., Stamoulis, K., Papachristodoulou, C., & Ioannides, K. (2013). A re-evaluation of radiation dose-rate conversion factors. *Mediterranean Archaeology and Archaeometry, 13*(3), 1-15.

Lizarralde, D., Axen, G. J., Brown, H. E., Fletcher, J. M., González-Fernández, A., Harding, A. J., et al. (2007). Variation in styles of rifting in the Gulf of California. *Nature, 448*(7152), 466-469. https://doi:10.1038/nature06035

Lonsdale, P. (1989). Geology and tectonic history of the Gulf of California. In E. L. Winterer, et al. (Ed.), *The Eastern Pacific Ocean and Hawaii* (Vol. N, pp. 499–521). Boulder, Colorado: Geological Society of America.

López-Pineda, L., Robles, L. Q., López, C. I. H., & Lozoya, H. E. R. (2014). Active segment of the 12 November 2003 Mw 5.6 earthquake at Salsipuedes oceanic basin, Gulf of California. Mexico. *Geofísica Internacional, 53*(1), 17-26. https://doi.org/10.1016/S0016-7169(14)71487-4

Mar-Hernández, E., González-Escobar, M., & Martin-Barajas, A. (2012). Tectonic framework of Tiburon Basin, Gulf of California, from seismic reflection evidence. International Geology Review, 54(11), 1271-1283. https://doi.org/10.1080/00206814.2011.636988

McGuire, C., & Rhodes, E. J. (2015). Downstream MET-IRSL single-grain distributions in the Mojave River, southern California: Testing assumptions of a virtual velocity model. *Quaternary Geochronology, 30*, 239-244. https://doi.org/10.1016/j.quageo.2015.02.004

Misra, A. A., Bhattacharya, G., Mukherjee, S., & Bose, N. (2014). Near N–S paleo-extension in the western Deccan region, India: does it link strike-slip tectonics with India–Seychelles rifting? *International Journal of Earth Sciences, 103*(6), 1645-1680. https://doi.org/10.1007/s00531-014-1021-x

Molnar, N. E., Cruden, A. R., & Betts, P. G. (2018). Unzipping continents and the birth of microcontinents. *Geology, 46*(5), 451-454. https://doi.org/10.1130/G40021.1

Müller, R. D., Gaina, C., Roest, W. R., & Hansen, D. L. (2001). A recipe for microcontinent formation. *Geology, 29*(3), 203-206. https://doi.org/10.1130/0091-7613(2001)029%3C0203:ARFMF%3E2.0.CO;2

Nagy, E. A., & Stock, J. M. (2000). Structural controls on the continent-ocean transition in the northern Gulf of California. *Journal of Geophysical Research: Solid Earth, 105*(B7), 16251-16269. https://doi.org/10.1029/1999JB900402

Nemčok, M., Sinha, S., Doré, A., Lundin, E., Mascle, J., & Rybar, S. (2016). Mechanisms of microcontinent release associated with wrenching-involved continental break-up; a review. *Geological Society, London, Special Publications, 431*(1), 323-359. https://doi.org/10.1144/SP431.14

Ortlieb, L. (1991). Quaternary shorelines along the northeastern Gulf of California, geochronological data and neotectonic implications. *Special Papers-Geological Society of America*, v. 254, 95–120.

Oskin, M., & Stock, J. (2003). Pacific–North America plate motion and opening of the Upper Delfín basin, northern Gulf of California, Mexico. *Geological Society of America Bulletin, 115*(10), 1173-1190. https://doi.org/10.1130/B25154.1

Oskin, M., Stock, J., & Martín-Barajas, A. (2001). Rapid localization of Pacific–North America plate motion in the Gulf of California. *Geology, 29*(5), 459-462. https://doi.org/10.1130/0091-7613(2001)029%3C0459:RLOPNA%3E2.0.CO;2

Paz-López, S. (2000). *Procesamiento e interpretación de datos sísmicos y gravimétricos en el norte del Golfo de California,* (Master's thesis). Retrieved from Institutional Repository CICESE. (http://cicese.repositorioinstitucional.mx/jspui/handle/1007/2085). Centro de Investigación Científica y de Educación Superior de Ensenada.

Persaud, P., Stock, J. M., Steckler, M. S., Martín-Barajas, A., Diebold, J. B., González-Fernández, A., & Mountain, G. S. (2003). Active deformation and shallow structure of

the Wagner, Consag, and Delfin basins, northern Gulf of California, Mexico. *Journal of Geophysical Research: Solid Earth, 108*(B7). https://doi.org/10.1029/2002JB001937

Plattner, C., Malservisi, R., Amelung, F., Dixon, T. H., Hackl, M., Verdecchia, A., et al. (2015). Space geodetic observation of the deformation cycle across the Ballenas Transform, Gulf of California. *Journal of Geophysical Research: Solid Earth, 120*(8), 5843-5862. https://doi.org/10.1002/2015JB011959

Plattner, C., Malservisi, R., Dixon, T. H., LaFemina, P., Sella, G., Fletcher, J., & Suarez-Vidal, F. (2007). New constraints on relative motion between the Pacific plate and Baja California microplate (Mexico) from GPS measurements. *Geophysical Journal International, 170*(3), 1373-1380. https://doi.org/10.1111/j.1365-246X.2007.03494.x

Rhodes, E. J. (2015). Dating sediments using potassium feldspar single-grain IRSL: initial methodological considerations. *Quaternary International, 362*, 14-22. https://doi.org/10.1016/j.quaint.2014.12.012

Rittase, W. M., Kirby, E., McDonald, E., Walker, J. D., Gosse, J., Spencer, J. Q., & Herrs, A. (2014). Temporal variations in Holocene slip rate along the central Garlock fault, Pilot Knob Valley, California. *Lithosphere, 6*(1), 48-58. https://doi.org/10.1130/L286.1

Ryan, W., Carbotte, S., Coplan, J., O'Hara, S., Melkonian, A., Arko, R., & Bonczkowski, J. (2009). Global multi-resolution topography synthesis. *Geochemistry, Geophysics, Geosystems, 10*(3), Q03014. https://doi.org/10.1029/2008GC002332

Sabbeth, L. (2020). *Provenance, structural geology, and sedimentation of the Miocene and Pliocene Californias,* (Doctoral dissertation). Retrieved from CaltechTHESIS. (https://resolver.caltech.edu/CaltechTHESIS:09212020-084147468). California Institute of Technology.

Sare, R., Hilley, G. E., & DeLong, S. B. (2019). Regional-Scale Detection of Fault Scarps and Other Tectonic Landforms: Examples From Northern California. *Journal of Geophysical Research: Solid Earth, 124*(1), 1016-1035. https://doi.org/10.1029/2018JB016886

Scherler, D., & Schwanghart, W. (2020). Drainage divide networks–Part 1: Identification and ordering in digital elevation models. *Earth Surface Dynamics, 8*, 245-259. https://doi.org/10.5194/esurf-8-245-2020

Spencer, J. E., & Normark, W. R. (1979). Tosco-Abreojos fault zone: A Neogene transform plate boundary within the Pacific margin of southern Baja California, Mexico. Geology, 7(11), 554-557. https://doi.org/10.1130/0091-7613(1979)7%3C554:TFZANT%3E2.0.CO;2

Stock, J. M. (2000). Relation of the Puertecitos Volcanic Province, Baja California, Mexico, to development of the plate boundary in the Gulf of California. *Special Papers-Geological Society of America*, 143-156.

Takasu, T., Kubo, N., & Yasuda, A. (2007). *Development, evaluation and application of RTKLIB: a program library for RTK-GPS.* Paper presented at the GPS/GNSS symposium, Tokyo, Japan.

Thompson, S. C., Weldon, R. J., Rubin, C. M., Abdrakhmatov, K., Molnar, P., & Berger, G. W. (2002). Late Quaternary slip rates across the central Tien Shan, Kyrgyzstan, central Asia. *Journal of Geophysical Research: Solid Earth, 107*(B9), ETG 7-1-ETG 7-32. https://doi.org/10.1029/2001JB000596

Chapter 3: Spatially varying critical zone structures at a steep, forested site near Coos Bay, Oregon

This chapter is modified from Higa, J.T., Formetta, G., Bellugi, D.G., Busti, R., Dietrich, W.E., Ebel, B.A., Milledge D.G., Moon, S., in prep. Spatially varying critical zone structures at a steep, forested site near Coos Bay, Oregon.

3.1 Introduction

Critical zone (CZ) scientists study processes that convert bedrock into regolith, controlled by the geo-, hydro-, bio-, and atmosphere (e.g., Anderson et al., 2007; Brantley et al., 2007; Riebe et al., 2017). Recent work suggests that the geologic CZ, consisting of unweathered bedrock, weathered bedrock, saprolite, and soil, can be formed by various weathering mechanisms, including reactive groundwater flow (Anderson et al., 2019; Lebedeva and Brantley, 2013, 2020; Rempe and Dietrich, 2014), frost cracking (Anderson et al., 2013), bioturbation (Brantley et al., 2017; Roering et al., 2010), and topographic stress fields (Slim et al., 2015; St. Clair et al., 2015). Researchers show the importance of such CZ weathering on forest-drought responses (Callahan et al., 2022; Hahm et al., 2022), groundwater storage (Callahan et al., 2020; Hayes et al., 2019; Holbrook et al., 2014), bedrock fracturing (Eppes and Keanini, 2017; Gu et al., 2020a), and landscape evolution (Dietrich and Perron, 2006; Litwin et al., 2022; Moon et al., 2017) across sites around the world (Banwart et al., 2012; Guo and Lin, 2016; White et al., 2015). Weathering may also increase bedrock and soil mass wasting hazards by weakening bedrock (Alberti et al., 2022; Li and Moon, 2021) and inducing groundwater exfiltration and seepage (e.g., Iverson and Major, 1986; Iverson and Reid, 1992; Reid and Iverson, 1992). Therefore, understanding the formation

of weathered bedrock structures in the CZ is critical for examining diverse near-surface and surface processes with scientific and societal impacts.

Recent studies use near-surface seismic refraction surveys to image the deep CZ, concealed by 1's to 100's of meters of weathered material (e.g., Flinchum et al., 2018; Ma et al., 2021; Pasquet et al., 2022; Wang et al., 2021). These works suggest a dichotomy between weathered bedrock structures, which can be surface-parallel, related to reactive transport (Lebedeva and Brantley, 2013; Rempe and Dietrich, 2014), or more complex and undulating, related to topographic stress (Moon et al., 2017; St. Clair et al., 2015). Weathered structures can be tied to specific P-wave velocity (Vp [m/s]) thresholds that trace different weathered boundaries in the CZ. For example, in crystalline rock, 1200 m/s or 4000 m/s are suggested to correlate to the boundaries between saprolite and weathered bedrock or weathered and unweathered bedrock, respectively (e.g., Callahan et al., 2020; Flinchum et al., 2018; St. Clair et al., 2015). These surveys reveal surface-parallel and undulating Vp structures, suggesting a controlling role of both reactive transport and topographic stress on bedrock weathering. However, similar studies at sedimentary sites often lack undulating Vp structures, leading researchers to suggest that reactive transport of groundwater is a more dominant weathering mechanism for this lithology (Gu et al., 2020b; Ma et al., 2021; Wang et al., 2021). Further geophysical studies to quantify CZs across diverse areas can help develop our understanding of deep CZ structures and processes hidden at the surface.

Researchers can also use geological and geophysical methods to quantify exposed and shallow weathering. Schmidt hammer measurements of rock hardness can be used to infer weathering, where softer rocks of the same lithology may have undergone more chemical or mechanical weathering than harder ones (Murphy et al., 2016; Viles et al., 2011; Von Voigtlander et al., 2018). Then, to examine the uppermost CZ, ground penetrating radar (GPR) may highlight

the controls of fractures and corestone formation (Orlando et al., 2016) and rooted vegetation (Guo et al., 2020) on soil and saprolite development. Recent advances also allow researchers to predict porosity structures from Vp in shallow soil and saprolite material based on rock physics models, important for understanding groundwater storage capacity (Callahan et al., 2020; Grana, 2016; Hayes et al., 2019; Holbrook et al., 2014). A combination of these methods may help delineate weathered structures and layering to further our knowledge of how fractures, pores, and other heterogeneities help to develop the CZ.

A well-studied, steep, and forested catchment underlain by sandstone near Coos Bay, Oregon, USA, is a site with extensive previous work to investigate CZ processes, including soil production (Heimsath et al., 2001), soil transport (Reneau and Dietrich, 1991; Roering et al., 1999), slope stability (e.g., Montgomery et al., 2009), and near-surface hydrology (e.g., Anderson et al., 1997; Torres et al., 1998). Extensive coring surveys provide one deep (Anderson et al., 2002) and nearly 200 shallow (Montgomery et al., 1997) constraints on weathered CZ structures. However, this site lacks two-dimensional field observations of deep CZ weathering from near-surface geophysical methods. Recent landslide modeling here assumes a simple subsurface, with soil directly overlying shallow and impermeable unweathered bedrock (e.g., Bellugi et al., 2015a; Bellugi et al., 2015b; Milledge et al., 2014). However, experimental and field results suggest that spatial variations in fractured and hydraulically conductive weathered layers (Anderson et al., 1997; Montgomery et al., 2002; Montgomery et al., 2009; Torres et al., 1998) may control the occurrence, size, and location of natural shallow landslides (Higa et al., in prep). Improved knowledge of CZ weathered structures from geophysics can enhance our understanding of landslide behavior, as well as groundwater storage, near-surface bedrock fracturing, and plant-groundwater dynamics at this site and more broadly across steep forested basins.

Here, we hypothesize that deep CZ structures at this Coos Bay site are not simple but complex and variable. We test this hypothesis by performing seismic refraction and GPR surveys to image the CZ. Using rock physics models, we can then invert porosity structures from our Vp profiles. We compare our geophysical measurements and inversions with direct observations of bedrock on outcrops or in cores and with predicted CZs using process-based weathering models. Our work reveals shallow, surface-parallel boundaries of saprolite or pervasively weathered rock and deep, undulating boundaries of weathered or fractured bedrock. A comparison between observed and modeled CZs suggests that a combination of chemical and mechanical weathering processes, in conjunction with weathering along inherited fractures and divide migration, created the complex CZ underlying this well-studied site.

3.2 Study site

We use the Coos Bay site as our study area for understanding CZ weathering because we can compare new geophysical data with historical documentation of weathering, hydrology, and landslides (e.g., Anderson et al., 1997; Montgomery et al., 2002; Montgomery et al., 2009; Torres et al., 1998). This site is located ~30 km northeast of Coos Bay in the Oregon Coast Range (Figure 3.1) and is almost entirely underlain by graywacke sandstone in the Eocene Tyee Formation (Baldwin and Beaulieu, 1973). The entire region is relatively steep, with a mean slope of 32° (95% confidence interval of 6° – 47°). Here and in the broader Pacific Northwest region, in-situ borehole measurements (McGarr and Gay, 1978; Zoback and Zoback, 1980), Holocene-active E-W trending fold axes (Kelsey, 1990; McInelly and Kelsey, 1990), and focal mechanisms (Spence, 1989) suggest N-S oriented maximum horizontal compressive stress from ambient tectonics related to the Cascadia subduction zone. Such tectonic activity contributes to the uplift and exhumation of our study area.

At Cape Arago, Cape Blanco, and Florence, Oregon, < 80 km from our study area, the mean and median uplift rate is ~0.2 mm/yr (Kelsey et al., 1994). Millennial-scale erosion rates from radiocarbon age dating suggest an average bedrock lowering rate of 0.07 mm/yr and an exfoliation rate of 0.09 mm/yr (Reneau and Dietrich, 1991). Relatively consistent rates using these methods, sediment yield rates from streams draining 1 – 1500 km^2 basins (0.05 – 0.08 mm/yr), and erosion rates from cosmogenic radionuclides in river sediment (0.117 mm/yr) suggest that the landscape is in dynamic equilibrium (Heimsath et al., 2001; Reneau and Dietrich, 1991). Workers extend this assumption at least through the Holocene due to the average residence time of this colluvium as 4000 – 6000 years from radiocarbon dating (Reneau and Dietrich, 1991) or 3500 years and 2300 years calculated from solute fluxes and uplift rates, respectively (Anderson et al., 2002). Previous studies found soil thickness between < 0.5 – 2 m from 195 hand-augered cores during piezometer installation at a benchmark site called CB1 (Figure 3.1c; Montgomery et al., 1997). Observations in shallow landslide scars (Cronkite-Ratcliff et al., 2022; Schmidt et al., 2001) and outcrops of weathered bedrock (Heimsath et al., 2001) find vegetation and tree roots hold this soil together, wedge saprolite apart, and mechanically weather the exfoliated sandstone into colluvium (Reneau and Dietrich, 1991).

Previous studies also examine the spatial variability of saprolite and weathered bedrock at the CB1 benchmark from those hand-augered cores (Montgomery et al., 1997). Saprolite is sparsely distributed here, with an average thickness of 0.23 ± 0.26 m from 36 cores (Anderson et al., 2002). These borings suggest the depth to weathered bedrock shallows downslope (Montgomery et al., 1997). Then, workers drilled a 35 m-deep borehole and obtained a core to study rock weathering at the CB1 ridgeline, hereafter the CB1 borehole (Figure 3.1c; Anderson et al., 2002; Anderson et al., 1997). The core had no recovery until three meters, after which

pervasively oxidized rock extends to 4.5 m, fractured bedrock extends to 9 m, and unweathered bedrock with silica- or calcite-filled veins and three faults extends to the bottom of the core (Anderson et al., 2002). From a regional estimate of 0.1 mm/yr for uplift rate, Anderson et al. (2002) estimates weathered bedrock and saprolite residence times of 50,000 ± 36,000 years, attributing the large standard deviation to uncertainties in uplift rate. Regardless, this estimate is an order of magnitude larger than that of soil and colluvium (Reneau and Dietrich, 1991). Then, measured porosity and volumetric strain increase, and bulk density decreases towards the surface in the deep and shallow cores (Anderson et al., 2002).

Groundwater flow through this porous and fractured weathered bedrock was found to be a major driver of chemical weathering at CB1 and could cause variations of hydraulic conductivity in the subsurface. Groundwater sampled from lower in the CB1 hollow, assumed to have been in contact with deep bedrock for relatively long periods (on month-timescales), consistently had higher solute fluxes than that exfiltrating higher up (Montgomery et al., 1997). This result agrees with chemical tracer experiments that show how exfiltrating flow through bedrock fractures mix old, solute-rich water with new water during wetting periods, particularly at channel heads (Anderson et al., 1997). Bedrock solutes were then found to be roughly equal to that from the much thinner soil layer (Anderson et al., 2002), emphasizing how physical contact between regolith and reactive water, such as in porous soil, enhances chemical weathering. Field and modeling work also suggests fracture flow controls soil saturation patterns (e.g., Ebel et al., 2007a; Ebel et al., 2007b) and subsequent shallow soil landslide occurrences (e.g., Montgomery et al., 1997; Montgomery et al., 2009). These findings highlight the need to quantify deep CZ structures to examine groundwater flow and landslide hazards.

3.3 Methods

3.3.1 Near-surface P-wave refraction and inversion

We surveyed five seismic refraction lines using up to four 24-channel RAS-24 Exploration Seismographs from Seistronix and a ~5 kg sledgehammer swung on a metal plate as our shot source (Table B1). We perform surveys with geophones linked together in lines of 12 – 96 channels. Geophone spacing varies between 1 – 3 m. Shot spacing varies between 3 – 9 m. For each shot location, we stack between 4 – 8 shots depending on the coherency of each shot. Using a trigger geophone, we record information for one second at a sample rate of one millisecond. For some surveys, we also perform off-end shots.

We manually picked P-wave arrival times and stacked the shots using Front End software from Geogiga Technology Corp, then used these times to invert for Vp profiles using a Bayesian approach (Huang et al., 2021). We use a LiDAR digital elevation model (DEM) of the study area coupled with locations taken with a differential Trimble GPS receiver and processed using the Real-Time Kinematic Library (Takasu et al., 2007) to obtain elevations for the Bayesian inversion. We use 15 Markov chains and iterate the model 10^5 or 10^6 times, saving every 100th iteration after the model accomplished 60% of its iterations (defined as a "burn-in" in Huang et al., 2021; Table B2). We impose a range of velocities between 300 – 6000 m/s as the bounds of expected Vp and begin the inversion with an initial velocity structure that increases with depth (300 m/s at the surface, 2000 m/s at 4.5 m-deep, and 4000 m/s until the bottom of the model). We then check that all inversions have a mean misfit < 3 ms (Table B2). Although we mask areas with low ray density, we do not mask areas with coefficients of variation > 50%, as in Huang et al. (2021). Instead, we present the mean model plus and minus the standard deviation of Vp from each Markov chain to show variations at all ranges of error for the inversion (Figure B1). We also compare weathering

inferred from Vp with rebound values as a measure of rock hardness taken with an Original Schmidt Concrete Test Hammer, Type N (Text B1; Figure B2 – B3).

3.3.2 Ground penetrating radar

Here, we use a GroundExplorer High Dynamic Range MALÅ GPR with a 450 MHz antenna to image the shallow structure of soil and saprolite with a 17 cm-diameter wheel, point interval of 2 cm, and measurement depth of 10 m. We also use the LiDAR DEM for these surveys and display them using GPRPy (Plattner, 2020). In GPRPy, we use an automatic gain control of 1, contrast of 5, and set zero time as two ns. This process highlights all reflectors in a survey at all two-way travel times, showing where we lose signal at depth. We also do not convert the y-axis from two-way travel time into distance because some surveys have hyperbola of different forms, which suggests variable radar velocity through different weathered material. However, we can estimate the depth of each GPR survey by assuming a constant velocity from observed hyperbolas or a mean soil velocity of 0.1 m/ns. We performed all GPR surveys along a seismic survey and name them according to corresponding line numbers. We also map GPR facies based on the relative roughness of GPR reflectors to differentiate between discontinuous or hummocky versus continuous or "smoother" regions of a profile (Text B2).

3.3.3 Porosity inversion

We utilize our Vp profiles to invert for soil and saprolite porosity using rock physics models (Grana, 2016; Holbrook et al., 2014). We calculate bulk and shear moduli and Poisson's ratio for a bulk mineral assemblage at this study area with a Voigt-Reuss-Hill average. This approximation is dependent on the bulk and shear moduli of individual minerals and estimated bulk percentage of each mineral in a landscape (Grana, 2016; Mavko et al., 2009). We use the mineralogy from rounded average values of pervasively oxidized bedrock at the CB1 borehole

(Table B3; Anderson et al., 2002), assuming minerals that are not quartz or feldspar are clay. Then, we use Hertz-Mindlin contact theory to recalculate the dry bulk and shear moduli (Holbrook et al., 2014; Mindlin, 1949). These recalculated moduli depend on critical porosity, a threshold porosity above which the material must be suspended, and contact number, the number of grain contacts on a single grain. Next, we invert Vp into porosity using a Bayesian inverse method to find the best-fit porosity for a given Vp and overburden pressure. Following Holbrook et al. (2014) and Grana (2016),

$$V_p = \sqrt{\frac{K+\frac{3}{4}G}{\rho}}, \tag{3.1}$$

$$P_{eff} = (\rho - \rho_a)gD, \tag{3.2}$$

$$\rho = \phi\rho_a + (1-\phi)\rho_s, \tag{3.3}$$

where K and G [Pa] are dry bulk and shear moduli, respectively, ρ [kg/m^3] is bulk density, P_{eff} [Pa] is effective overburden pressure, D [m] is depth, ρ_a = 0 kg/m^3 is air density, and ρ_s = 2650 kg/m^3 is the density of the solid mineral phase. We perform a sensitivity test iterating through all combinations of realistic critical porosities (0.36 – 0.40 m³/m³, 0.01 m³/m³-increments; Dvorkin and Nur, 2005) and contact numbers (4 – 14 grains, 1-grain increments; Mavko et al., 2009; Murphy, 1982) for sandstone, then average these porosity inversions for our final result (Table B4). This inversion outputs a minimum porosity, as we assume pores are dry. Recent studies use measured saturation and Gassman's equation to implement a saturated bulk modulus into the Bayesian inverse method (Callahan et al., 2020; Hayes et al., 2019; Holbrook et al., 2014). As we

do not have a measure for saturation during our seismic surveys, we use our dry assumption to infer relative porosity differences. We also do not vary the shape of pores, assuming spherical inclusions (Grana, 2016). Thus, we only invert velocities < 1200 m/s (Vp of saprolite and soil), as this method is less suited for fractured, weathered bedrock with pores shaped like cracks (e.g., Callahan et al., 2020). Refer to Holbrook et al. (2014) and Grana (2016) for more information on this method.

3.3.4 Critical zone bedrock weathering models

We apply two weathering models to explain three-dimensional bedrock weathering that we imaged with P-wave refraction. We use a bedrock drainage weathering model calibrated at CB1 (Rempe and Dietrich, 2014) and a topographic stress model that workers suggest can predict CZ structures in crystalline bedrock (St. Clair et al., 2015). If a given model is a good predictor of bedrock weathering, we expect the distribution of Vp interpolated along the predicted weathered boundary to have a small standard deviation because Vp is correlated with weathering (e.g., Flinchum et al., 2018).

3.3.4.1 Bedrock drainage

Rempe and Dietrich (2014) provide a framework for modeling bedrock weathering based on the drainage of reactive water from under hillslopes to stream channels. This model assumes that the saturated zone below the water table is unreactive and preserves unweathered bedrock. Thus, the water table is a proxy for the top of unweathered bedrock. Rempe and Dietrich (2014) defines a constant ratio of $Z_{b0}/Z_{s0} = 0.83$ at the CB1 site, where Z_{b0} [m] and Z_{s0} [m] are unweathered bedrock and topographic fluvial relief at the CB1 ridgeline, respectively. This ratio approximates the 9 m-deep boundary between fractured and unweathered bedrock in the CB1 borehole. Recent work also found that a Z_{b0}/Z_{s0} ratio of 0.9 predicts a depth of 4.5 m in the CB1 borehole, similar to

the boundary between pervasively oxidized and weathered bedrock (Higa et al., in prep), which other studies also attribute to bedrock drainage weathering (Flinchum et al., 2018). Here, we expand upon Rempe and Dietrich (2014) to estimate three-dimensional CZ weathered structures across the benchmark site using bedrock drainage.

We can calculate sitewide topographic fluvial relief Z_s [m] and multiply this by a constant Z_{b0}/Z_{s0} ratio to solve for sitewide unweathered bedrock fluvial relief Z_b [m], assuming $Z_b = Z_{b0}$. Then, subtracting Z_b from Z_s will provide an estimation for weathered bedrock thickness, which we refer to as the constant model (Text B3). Rempe and Dietrich (2014) also describes a process-based approach to model the topographic surface and water table and obtain Z_b and Z_s (Text B3). This approach improves upon the constant model, which relies on the assumption that hillslope length L [m] does not vary across the entire study area. The equation for Z_b is based on nonlinear soil transport (Roering et al., 1999) and that for Z_s is from the one-dimensional, steady state Boussinesq equation for groundwater flow and the water table (Bear, 1988). These formulations utilize spatially varying L to calculate Z_b and Z_s across the study area (Text B3). Similar to the constant model, subtracting Z_b from Z_s will provide a measure of weathered bedrock thickness in what we refer to as the variable model. In addition, Z_s can be obtained directly from digital elevation instead of modeled using nonlinear transport. Subtracting theoretical Z_b from DEM-derived Z_s is what we refer to as the topography model.

Together, we create three critical zones for comparison with seismic refraction surveys (Text B3). All models use the LiDAR DEM of the study area to calculate different considerations for Z_b and Z_s. The constant model produces the CZ model we call CZ(RD4m) and is based on applying a Z_{b0}/Z_{s0} ratio of 0.9 across the benchmark site. We also test our assumption of a constant L by comparing a measured L = 76 m with the distribution of L measured across the study area in

the DEM (Section 3.4.5.1). Then, the variable and topography models produce CZ(RDvar) and CZ(RDtopo), respectively. All three models aim to reproduce the 4.5 m-deep boundary between pervasively weathered and fractured bedrock at the CB1 borehole. CZ(RDvar) and CZ(RDtopo) are also calibrated with site-specific material density and erosion parameters (Table B5). However, CZ(RDvar) and CZ(RDtopo) depend on hydraulic conductivity K [m/s], which was found to vary by orders of magnitude at CB1 (e.g., Montgomery et al., 2002). Thus, we perform a sensitivity analysis on the coupled parameters K/θ [m/s], where θ is unitless porosity, to determine the best ratio that reproduces the 4.5 m-deep boundary (Text B3).

3.3.4.2 Topographic stress

Several studies suggest that a subsurface stress field, combining effects from ambient tectonic compression, gravitational loading, and topographic variation, can control fracture openness, hereafter topographic stress (e.g., McTigue and Mei, 1981; Miller and Dunne, 1996; Molnar, 2004; Moon et al., 2017; Moon et al., 2020; Savage et al., 1985; Savage and Swolfs, 1986; St. Clair et al., 2015). Recent works assume a linear-elastic, homogenous, and isotropic material and model stress fields using a boundary element model, Poly3D (Thomas, 1993). Despite such simplified rock properties, topographic stress fields could predict CZ weathering in crystalline lithologies and corroborated structures observed in Vp profiles (Flinchum et al., 2018; Moon et al., 2017; St. Clair et al., 2015). These works find that a threshold least compressive principal stress (LCS) in the topographic stress field corresponds well to the boundary between fractured and unweathered rock observed in P-wave refraction surveys. Similarly, we test various topographic stress scenarios to estimate weathered profiles observed in refraction surveys across our study area.

Following Moon et al. (2017), we prepare our LiDAR DEM for topographic stress modeling (Text B4). Under this topographic surface, we can apply ambient tectonic compression

(Table B6) to simulate topographic stresses with Poly3D and constant rock properties (Table B7). We query for the total stress field within a three-dimensional grid with 5 m horizontal and 3 m vertical resolution of various dimensions for different sites (Table B7). After obtaining the total topographic stress field, we extract the three-dimensional LCS field. We find the LCS magnitude located 9 m-deep at the CB1 borehole and assume this value corresponds to a threshold LCS, where more tensional or compressional stresses will open or close bedrock fractures, respectively. We use an isosurface of this threshold LCS as our sitewide depth to unweathered bedrock, assuming this threshold is constant across the entire site. To remove surface artifacts, we mask this map where depths are < 5 m-deep and fill these cells with a shallow depth of 0.02 m. We output a 5 m-resolution depth to unweathered bedrock map and resample this map to 2 m-resolution.

Here, we test three variations of ambient tectonic conditions (compression positive). CZ(stress1) employs isotropic compression with a magnitude of 5 MPa, which is assumed to be relatively strong (St. Clair et al., 2015). CZ(stress2) employs isotropic compression with a magnitude of 1 MPa, which is assumed to be relatively weak (St. Clair et al., 2015). We use previously established maximum horizontal, minimum horizontal, and vertical depth gradients of 0.020 MPa/m, 0.020 MPa/m, and 0.026 MPa/m, respectively, for CZ(stress1) and CZ(stress2). Lastly, CZ(stress3) uses the average stress magnitude and orientation from 14 data points in a compilation of in-situ stress measurements from the west coast of the United States and Canada (Brown and Hoek, 1978; Heidbach et al., 2018; Lindner and Halpern, 1978). We use data from such a large area because such in-situ measurements are sparse near our study area (Table B6; Text B4). We then calculate a linear least squares regression of depth against stress magnitude to extrapolate an estimate of maximum horizontal, minimum horizontal, and vertical stress magnitude and orientation at the surface as well as a depth gradient for each component to use in

CZ(stress3; Figure B4). Thus, we can output a map of depth to unweathered bedrock based on a threshold LCS for three topographic stress CZ models to reproduce the 9 m-deep boundary between fractured and unweathered bedrock at the CB1 borehole.

3.4 Results

3.4.1 P-wave refraction surveys

We perform five near-surface P-wave refraction surveys across our study area: three at an eastern site and two at the CB1 benchmark site (Figure 3.1; Text B5). We find Vp varies between 400 – 3500 m/s from all surveys (Table B8). Lines 1 and 2 are less than 40 m-long and reveal Vp < 10 m-deep beneath a ~3 m-tall outcrop and an unpaved road on competent but fractured sandstone, respectively (Figure 3.2a – b; Figure B5). Lines 3, 4, and 5 are > 40 m-long and reveal Vp structures between 30 – 60 m-deep (Figure 3.2c – e; Figure B6 – B8). Vp contours < 1000 m/s are relatively surface-parallel in all three surveys. In particular, the top five meters of Line 4 shows a relatively sharp, surface parallel transition of Vp at a similar depth to the 4.5 m-deep boundary in the CB1 borehole between pervasively oxidized and fractured rock. However, Lines 3 and 4 show deep, concave up, undulations of Vp contours between 1000 – 3500 m/s. The undulation for Line 3 has an amplitude of ~10 m, focused at ~60 m along the survey where an E-W oriented spur ridge extends out-of-plane of the profile (Figure 3.1b; Figure B6b). The undulation for Line 4 has an amplitude of ~15 m and is located between 30 – 60 m along the survey. Similar to Line 3, the Line 4 undulation is also where a N-S oriented spur ridge is located (Figure 3.1c). Additionally, Lines 4 and 5 have regions of fast Vp, > 2500 m/s, isolated from deeper areas of similar Vp in the survey. Line 4 has two subsurface bodies of fast Vp between 0 – 15 m along the survey, while that of Line 5 is centered at ~20 m along the survey. Both bodies are ~5 m-wide.

3.4.2 Comparing Vp with exposed outcrops and borehole profiles

Exposures along Lines 1 and 2 allow us to compare inverted Vp with observed geology. Vp at the surface of Line 1 is ~500 m/s or less, corresponding to a layer of dark brown soil exposed in the adjacent outcrop, particularly between 15 – 36 m along the line (Figure 3.2a; Figure B5a – B5d). Below to about three m-deep, Vp increases to ~1000 m/s where we find lighter saprolite and weathered bedrock. Along Line 2, we calculate the mean Vp of exposed fractured, competent rock by averaging the surface Vp along the survey and from the inverse of slope using a least square fitting of P-wave travel distance against source-to-geophone Vp first arrival times. We obtain Vp estimations of 1236 ± 204 m/s and 1220 ± 43 m/s for this exposure from the average and least squares methods, respectively (Figure 3.2b; Figure B5e – h).

We can also compare the weathered profile of the CB1 borehole (Anderson et al., 2002) and Vp at the same location on Line 4, which crosses the borehole at 27 m along the survey. Vp where the borehole begins to recover pervasively oxidized rock, at the boundary of pervasively oxidized and fractured bedrock, and at the boundary of fractured and unweathered bedrock are 850 ± 251 m/s, 1744 ± 948 m/s, and 2214 ± 726 m/s, respectively (Figure 3.3a). Then, unweathered bedrock Vp is > 2200 m/s along the borehole profile. A Vp contour of ~1220 m/s obtained from the top of fractured bedrock in Line 2 produces a surface parallel boundary. That of ~2200 m/s obtained from the top of unweathered bedrock in the CB1 borehole produces an undulating boundary, with undulations in similar locations to out of plane spur ridges (Figure 3.1b – c; Figure 3.2). We use 1220 m/s from Line 2 instead of 1740 m/s from the CB1 borehole due to the latter's larger standard deviation (Section 3.5.2.1).

We then compare the Vp profile where Lines 4 and 5 intersect (Figure 3.3b – c) to examine Vp anisotropy. Mean anisotropy increases from the surface and reaches a maximum at about six

m-deep, indicating that the Vp of Line 4 is 1324 m/s faster than that of Line 5. Then, mean anisotropy decreases to 0 m/s at ~12 m-deep and switches sign below. However, standard deviation bounds overlap at depths deeper than 12 m.

3.4.3 Ground penetrating radar surveys

We used GPR along all five seismic refraction surveys (Figure B5 – B9). GPR velocities inferred from hyperbolas are between 0.03 – 0.3 m/ns. Line 1 has several hyperbolas. However, these features are less apparent than those in Lines 2 – 5 (Figure B9). Mapping GPR reflectors by roughness, we identify several profiles with spatial variations of thick hummocky facies. For Line 1, hummocky facies are thinner between 0 – 15 m than between 15 – 36 m, which thickens to a two-way travel time of ~50 ns (Figure 3.4a). Assuming a GPR velocity for soil of 0.1 m/ns, this hummocky layer is about 2 m-thick here. Similarly for Line 4, hummocky facies thicken in two locations: 15 m and 90 m along the survey to two-way travel times of ~25 ns. Using a measurable GPR velocity from one hyperbola of ~0.05 m/ns, we estimate these hummocky facies to be at most one m-thick (Figure 3.4b).

3.4.4 Comparing soil and saprolite porosity with ground penetrating radar

We invert Vp profiles for the minimum bound of porosity assuming dry pores at Lines 1 and 4 because these surveys are roughly subparallel to the strike of sandstone bedding and have a layer of pervasively oxidized bedrock and soil observed at the surface or in the CB1 borehole (Figure 3.4c – d). Mean porosity for all surveys is similar to that measured in weathered bedrock here (0.2 – 0.3 m^3/m^3), while their 95% confidence intervals span measured weathered bedrock to saprolite values (0.1 – 0.5 m^3/m^3; Table B8; Anderson et al., 2002). The highest porosity for Line 1 (> 0.4 m^3/m^3) is located roughly within 5 m of the surface, particularly at the north end where the GPR survey finds the thickest hummocky facies (Figure 3.4a). Then, the highest porosity for

Line 4 (~0.5 m^3/m^3) is located at roughly 15 m along the survey in a forested part of the western end of the line. The eastern end also reenters the forest from a roadbed, but porosities do not increase to the extent they do to the west. Both the east and west ends are where we find thick, hummocky GPR facies (Figure 3.4b) and several large trees (Figure B7c – d). Lastly, we also invert Line 3 for porosity and produce values similar to those of Lines 1 and 4 (Figure B10; Table B8).

3.4.5 Comparing critical zone weathering models and Vp profiles

3.4.5.1 Bedrock drainage models

We present structures produced by our bedrock weathering models within the benchmark site (white outline in Figure 3.5a – b; Figure B11; Table B9). For CZ(RD4m), we find that an L of 76 m measured at CB1 (Rempe and Dietrich, 2014) approximates the mode of measured L across the benchmark (Figure B12). The best fit K/θ for CZ(RDvar), and CZ(RDtopo) are $10^{-11.025}$ m/s and $10^{-11.125}$ m/s, respectively. CZ(RD4m), CZ(RDvar), and CZ(RDtopo) have similar ranges of predicted depth to unweathered bedrock, calibrated to the same 4.5 m-deep boundary between pervasively oxidized and fractured bedrock in the CB1 borehole (Table B9). However, CZ(RDvar) and CZ(RDtopo) have over 30 more percentage points of depth < 0.5 m in the benchmark site than CZ(RD4m). This difference leads to unweathered bedrock exposed at the surface for CZ(RDvar) and CZ(RDtopo) farther away from mapped channels and overall thinner weathered bedrock than CZ(RD4m). In particular, CZ(RDvar) and CZ(RDtopo) have bedrock exposed in the CB1 hollow where hand-augered cores from Montgomery et al. (1997) measure depths to competent bedrock up to 2 m-deep. Then, we interpolate the Vp from Line 4 along each boundary predicted by these CZ(RD) models and calculate the variation of this Vp population. Here, CZ(RD4m) has the lowest standard deviation out of the three models (Table B10). This boundary is similar to the 1220 m/s Vp contour, the approximate Vp estimated at Line 2 (Figure 3.5c; Section 3.4.2).

3.4.5.2 Topographic stress models

From our linear least squares fit of depth against the most and least compressive horizontal and vertical stress magnitude, we determine such magnitudes at the surface as 1 MPa, 1 MPa, and 0 MPa. We also determine their respective stress depth gradients as 0.049 ± 0.005 MPa/m, 0.027 ± 0.003 MPa/m, and 0.026 ± 0.003 MPa/m. We orient the most compressive horizontal stress N-S based on geological and tectonic evidence (Section 3.2).

Altogether, CZ(stress1), CZ(stress2), and CZ(stress3) have similar ranges of depths at the benchmark site with LCS thresholds of -0.02, 0.12, and 0.11 MPa, respectively. These thresholds approximate the 9 m-deep boundary in the CB1 borehole (Table B9). Differences arise when considering the spatial distribution of shallow bedrock in these models. CZ(stress3) has the least coverage of unweathered bedrock < 0.5 m deep, with shallow bedrock concentrated at mapped channels. CZ(stress2) has similar shallow unweathered bedrock but with deeper unweathered bedrock, up to 30 m deeper, under a ridge to the southeast (Figure B11). CZ(stress1) has the most unweathered bedrock < 0.5 m-deep, with more of these shallow areas extending upslope into hollows compared to CZ(stress2) and CZ(stress3). Short wavelength artifacts ~5 m-across include areas of shallow bedrock surrounded by deep bedrock, particularly under ridges for CZ(stress1). These artifacts may be due to shallow, tensile LCS above the deeper boundary between weathered and unweathered bedrock related to the topographic surface.

Again, we can compare Vp along boundaries predicted by our CZ(stress) models (Figure B11). At Line 3, CZ(stress1) has an undulation between 40 – 60 m along the survey (Figure 3.6a – b). This undulation is laterally offset from that observed in Vp by ~20 m. No other CZ(stress) model here shows a similar undulation (Figure 3.6c – d). At Line 4, CZ(stress1) and CZ(stress3) show undulations, with that of CZ(stress1) more apparent than CZ(stress3; Figure 3.6e – h). Again,

there is a lateral mismatch of 5 – 10 m between modeled and observed undulations. For Line 4, CZ(stress2) has the lowest standard deviation for Vp interpolated along the predicted boundary followed by CZ(stress3; Figure B11; Table B10). These boundaries are mostly shallower than the 2200 m/s Vp contour, which is the approximate Vp estimated 9 m-deep in the CB1 borehole, except in the far western part of the line (Figure 3.3a; Figure 3.5c; Figure B11). Here, we focus on CZ(stress3) because this model uses measured estimations of tectonic stress and has undulations similar to the Line 4 Vp profile despite CZ(stress2) having the lowest standard deviation.

3.5 Discussion

3.5.1 Porosity generation in soil and saprolite

The similar spatial distribution of high inverted porosities and hummocky GPR facies suggest internal consistencies between predicted areas of porous material and disturbed soil and saprolite layers. Overlapping ranges of inverted porosities and from that observed by Anderson et al. (2002) in soil to weathered bedrock suggest that our estimation of mineralogy from CB1 borehole data, assumption of dry pores, and application of the inversion on Vp < 1200 m/s may sufficiently approximate relative porosity variations at the benchmark site (Table B8). Tree roots can generate a fraction of porosity here by bioturbating soil and wedging apart saprolite (Guo et al., 2020; Heimsath et al., 2001). The highest porosities of Line 4 (> 0.45 m^3/m^3; Figure 3.4d) occur where the forested west end of the GPR survey shows a layer of hummocky reflectors punctuated by several hyperbolas that could be large roots (Figure B7; Figure B9a – b). A facies thickness of about one meter here (Section 3.4.3) agrees with soil depths measured near the top of the CB1 hollow of < 1 m-deep (Montgomery et al., 1997; Montgomery et al., 2009). We also find similar hyperbolas between 2 – 6 m along Line 5, where we pass several large trees (Figure B9c). However, we find hyperbolas at Line 2 ~9 m along an unpaved road where there likely have not

been many large trees growing in recent times (Figure B9d). These hyperbolas seemingly trace a boundary between the hummocky and horizontal reflectors and may show corestones or a rough boundary between saprolite and fractured rock. Nonetheless, our porosity inversion and GPR survey provide consistent evidence suggesting that tree roots disturb pervasively weathered material within hummocky facies.

Bioturbation from rooting is likely not the only source of porosity at the study site. Line 1 is currently clear-cut and does not have hyperbolas as apparent as Lines 4 and 5 (Figure B9e). Yet, porosity for the top 3 – 4 m of Line 1 is > 0.4 m^3/m^3, similar to that on the forested west end of Line 4. Part of this porosity may be a legacy of roots and tree throw before deforestation (Korup et al., 2019), estimated between 2013 – 2016 from satellite images. Other possible sources of porosity are burrowing animals (Heimsath et al., 2001), landslides or soil creep (e.g., Roering et al., 1999), and exfoliation fracturing (Anderson et al., 2002). Chemical dissolution accounted for only ~5% of porosity at CB1 (Anderson et al., 2002). Therefore, our comparison of Vp, GPR, and porosity suggests that many mechanical weathering processes affect the internal structures of soil and saprolite at the benchmark site.

3.5.2 Vp profiles suggest complex weathered rock structures at the benchmark site

3.5.2.1 Surface-parallel pervasively-weathered and fractured bedrock boundary

The Line 4 Vp survey likely suggests a surface parallel boundary between pervasively oxidized and fractured bedrock at the benchmark site. The large standard deviation of 1744 ± 948 m/s, the Vp at the 4.5 m-deep boundary between pervasively oxidized and fractured bedrock in the CB1 borehole (Figure 3a), may originate from the borehole's proximity to the adjacent, deep undulation of faster Vp. Here, inversions in parallel for the Bayesian method may produce Vp profiles with different undulation geometries that increase the deviation. Regardless, this range

encompasses the Vp of exposed bedrock at Line 2 of ~1220 m/s from our averaging and least squares methods (Section 3.4.2; Figure B5). The substrate of Line 2 is likely similar to the top of fractured bedrock, as this survey is over an unpaved road. Softer, more oxidized material (i.e., material in the nearby Line 1 outcrop) may have been removed during road construction, preserving the more competent, fractured rock below. Also, a Vp of 1220 m/s is similar to that for the boundary between saprolite and fractured bedrock observed in crystalline bedrock (e.g., Callahan et al., 2020; Flinchum et al., 2018) and within the range for sedimentary rock (e.g., Ma et al., 2021) at other locations. Because 1744 ± 948 m/s has a large error and is faster than that established in previous works, we use 1220 m/s from Line 2 as our universal Vp boundary between pervasively weathered and fractured bedrock in our study area of relatively constant lithology (Baldwin and Beaulieu, 1973). The 1220 m/s contour is relatively surface-parallel in Line 4 (Figure 3.5c). Thus, we suggest a surface-parallel layer of pervasively oxidized rock at the benchmark site.

3.5.2.2 Undulating fractured and unweathered bedrock boundary

We suggest the boundary between fractured and unweathered bedrock undulates across Line 4, particularly at the locations of spur ridges (Figure 3.1b – c; Figure 3.2). The Vp of 2200 m/s we find at this boundary in the CB1 borehole (Figure 3.3a) is roughly half that observed in crystalline bedrock (e.g., St. Clair et al., 2015) and less than that of fractured to unweathered sandstone at other locations (~3500 m/s; Geldart and Sheriff, 2004; Koesoemadinata and McMechan, 2004). However, unweathered bedrock at the benchmark site has abundant silica- and calcite-filled fractures that can reduce Vp (Anderson et al., 2002). We observe much faster Vp deeper in Line 4, which likely represents Tyee Sandstone with lower fracture abundance (Anderson et al., 2002). Thus, we interpret 2200 m/s as an endmember Vp representing the uppermost unweathered bedrock. Using this threshold, we suggest that the boundary between fractured and

unweathered bedrock undulates across Line 4 and reveals a complex subsurface bedrock structure (Figure 3.5c).

Then, Vp profiles of Lines 4 and 5 highlight seismic anisotropy at the benchmark site. Our observed anisotropy that starts near zero and increases with depth agrees with recent studies that find shallow soil mixing and weathering along fractures can decrease and increase seismic anisotropy, respectively (Eppinger et al., 2021). At the benchmark site, soil mixing may keep anisotropy low within the first two meters of the profile. Anisotropy increases as inherited saprolite and weathered bedrock fabrics are preserved. Of note is that Line 4 is roughly parallel to sandstone bedding, whereas Line 5 is perpendicular (Text B5; Montgomery et al., 1997). Weathering exacerbated by reactive transport along sandstone bedding may slow P-waves traveling perpendicular to these weathered faces to cause the peak in anisotropy at six m-deep. As inherited fractures close due to vertical overburden, the effect of this weathering-induced anisotropy decreases. Calcite infilling of fractures may induce a secondary anisotropy reduction due to mineral scale structures (Koesoemadinata and McMechan, 2004). Therefore, weathering along bedding and inherited fractures likely impact the shallow Vp of Line 5 more than that of Line 4. This effect may obliterate the signal of any other chemical or mechanical weathering, which can explain the thick zone of < 1000 m/s Vp within the top 10 m of Line 5 (Figure 3.2e). Such processes highlight the importance of fractures for water storage and solute transport at this benchmark (e.g., Anderson et al., 1997; Montgomery et al., 1997) and other sites in sedimentary rock (Gu et al., 2020a; Gu et al., 2020b; Ma et al., 2021; Wang et al., 2021).

3.5.3 Comparison of Vp and weathering models

We compare only Line 4 to our CZ models because we expect a lower impact from bedding-induced weathering here than Line 5. We suggest that CZ(RD4m) best approximates the

shallow boundary delineated by the 1220 m/s Vp contour because this model has the lowest standard deviation of Vp among all the CZ(RD) models (Table B10). CZ(RD4m) also consistently traces the surface-parallel 1220 m/s Vp contour throughout the Line 4 profile (Figure 3.5c). This boundary could be explained by bedrock drainage of reactive groundwater (Rempe and Dietrich, 2014). However, it remains unclear if a downward-moving front of reactive rainwater could also produce a similar surface-parallel structure (Lebedeva and Brantley, 2013) or if this pattern simply reflects topography. Regardless, the weaker, less consolidated material in this oxidized layer is likely decoupled from the topographic stress field affecting fractured and unweathered bedrock below. Thus, we do not expect a soil or saprolite structure that undulates.

For the deeper boundary between fractured and unweathered bedrock, we suggest that elastic properties of sedimentary rock may be the source of some deviations between predicted and observed CZs. Here, CZ(stress2) and CZ(stress3) have lower standard deviations of Vp along their predicted boundaries at Line 4 than that of CZ(stress1; Figure 3.5c; Figure B11; Table B10). Regardless, we observe a 5 – 10 m mismatch between the exact shape and location of predicted undulations in CZ(stress1) and CZ(stress3) compared with observed Vp undulations in Line 4 (Figure 3.6). We find a similar mismatch along Line 3, particularly for CZ(stress1; Figure B13). Ma et al. (2021) observed that shales in their study area may experience deformation from topographic stress perturbations without much weathering, possibly because of the lower elastic moduli of sedimentary compared to crystalline rock. This difference may explain why topographic stress is more effective in explaining Vp in granites or schists (e.g., St. Clair et al., 2015) than here in sandstone. Therefore, a strong correlation between stress and Vp may not be expected at this benchmark site.

We examine the ability of modeled LCS to predict Vp. Across many profiles, LCS is a better predictor than depth for Vp based on an R^2 analysis (Figure B14). R^2 is consistently lower for Line 4 than Line 3. It is possible that Line 3, with E-W spur ridges, responds more to topographic stress than Line 4, with N-S spur ridges, because maximum horizontal compression is N-S oriented here. Topographic stress perturbation reaches a maximum when compression is oriented perpendicular to spur ridges (Moon et al., 2017) and could be one reason why R^2 of Line 3 is better than that of Line 4. We also acknowledge resolution limitations inherent to seismic refraction. Vp is collectively influenced by weathering, fractures, and pores within a radius on the scale of 10's of meters, similar to the Vp wavelength (e.g., Flinchum et al., 2022). Resulting Vp profiles likely smooth over weathering and lithologic heterogeneities at scales larger than the resolution of our topographic stress model in meters and observations in the CB1 borehole in centimeters. Regardless, we show that LCS can be a better predictor of Vp assuming a linear relation and that topographic stress and the bedrock drainage model can approximate some spatial variations of the 1220 and 2200 m/s Vp contours based on the CB1 borehole.

It is also possible that other mechanisms contribute to weathered bedrock structures at the benchmark site. First, the sandstone here may have been influenced by inherited and pre-existing fractures. For example, Anderson et al. (2002) documented three faults or large-scale fractures between 18 – 27 m-deep in the CB1 borehole. Relative to Line 4, these features are located near or within the large undulation of Vp. Such fractures may have delivered reactive water to this depth region, helping to generate and weather the undulation beneath the spur ridge at the benchmark. Thus, such inherited structures might cause natural variations of the deep CZ not captured by topographic stress. Second, it is possible that the bedrock has less-weathered corestones at depth (Brantley et al., 2011; Fletcher and Brantley, 2010; Pandey and Rajaram, 2016). Several isolated

bodies beneath the west end of Line 4 and the ridgetop of Line 5 have Vp > 2500 m/s surrounded by slower velocities that indicate preserved, less weathered bedrock (Figure 3.2d – e; Figure B1). Although we lack geochemical analysis, mapping (Baldwin and Beaulieu, 1973) and similar rebound values between exposed corestones and fractured bedrock across our study area suggest a similar lithology (Text B1; Table B11 – B12). The buried corestones could be similar to those exposed and related to spatially variable weathering, possibly constrained by fractures, that preserved these features. Third, mismatched undulations between stress model predictions and Vp may reflect influences from the previous locations of spur ridges if landscapes are dynamically changing over the timescale of weathering (~100 kyr considering ~20 m-deep undulation of fractured bedrock with an uplift rate of ~0.2 mm/yr,). Such landscape evolution can also leave behind the corestones of Lines 4 and 5, which may be the old cores of ridges before divide migration.

In a natural context, reactive transport and topographic stress likely work in tandem with inherited structural and weathering heterogeneities in bedrock to generate the deep CZ structures at the benchmark site. Weathering rinds on bedrock fractures (Montgomery et al., 1997) and old, solute-rich bedrock water (Anderson et al., 1997) suggest chemical weathering associated with reactive groundwater can shape the shallow, surface-parallel, and pervasively oxidized bedrock structures found here. Then, catchments may cycle through stages of incision and widening, related to topographic stress perturbations, to generate the deep and undulating fractured bedrock (e.g., Miller and Dunne, 1996; Molnar, 2004). Humidity in the temperate rainforests of coastal Oregon may enhance such weathering, beyond that predicted by topographic stress, by accelerating cracking rates along inherited fractures (Eppes and Keanini, 2017; Eppes et al., 2020). Although this region was not glaciated during the Quaternary (e.g., Reneau and Dietrich, 1991), seasonal

freeze-thaw cycles may also exacerbate fracturing and mechanical weathering (Anderson et al., 2013). Thus, interactions between reactive transport, topographic stress-induced fracturing, and the growth of inherited fractures all likely shaped the weathered CZ bedrock structures we observe through geophysical methods. Future work to quantify the time-integrated effects of fracturing and chemical weathering could help differentiate the relative impacts of different processes on the deep CZ observed at this benchmark site.

3.6 Conclusion

The wealth of historical and new data at our study area exemplifies how geological and geophysical information can combine to tell coherent stories about CZ processes. GPR and seismic refraction surveys reveal natural heterogeneities in soil and weathered bedrock structures normally concealed at the surface. We examine such heterogeneities and find Vp structures that show a shallow, surface-parallel layer of pervasively oxidized bedrock and a deep, undulating layer of fractured and unweathered bedrock at the CB1 benchmark site. Spatial variations of sandstone bedding, fractures, faults, and corestones may then induce complexities in CZ structures that are not fully captured by a bedrock drainage or topographic stress weathering model. Therefore, our combination of field observations and weathering models highlights how scientists can utilize weathering models and site-specific bedrock characteristics to understand deep CZ weathering.

3.7 Figures

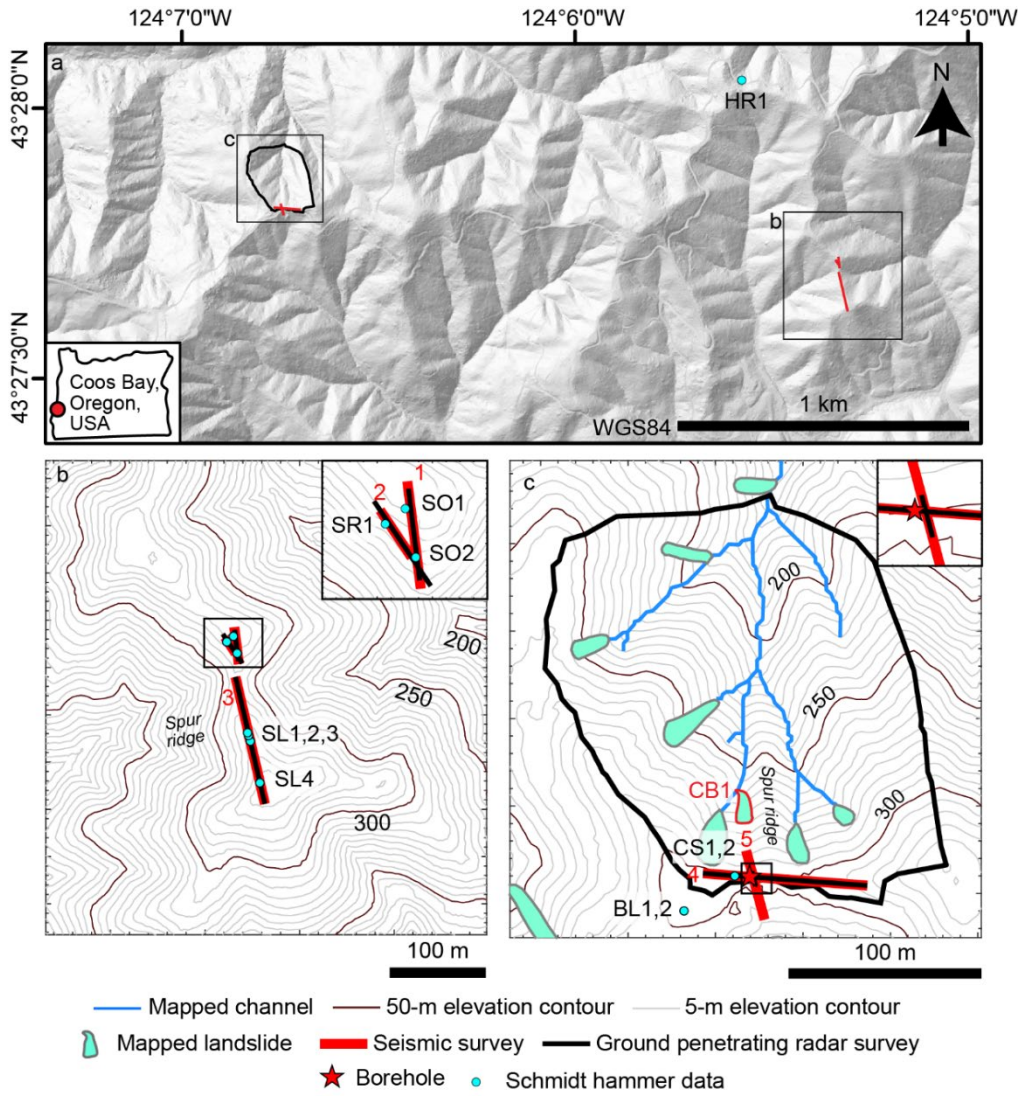

Figure 3.1. (a) Hillshade map of larger study site. (b) Contour map of eastern site showing new field data collected here. Map extent is box in (a) labeled b. Inset shows Lines 1 and 2, same extent as box in (b). (c) Contour map of benchmark site (black outline) showing mapped landslides, channels, and new field data collected here. Map extent is box in (a) labeled c. Inset shows crossing of Lines 3 and 4 to highlight short ground penetrating radar survey same extent as box in (c). Seismic and ground penetrating radars are labeled by number in red text. Schmidt hammer data are labeled by site in black text.

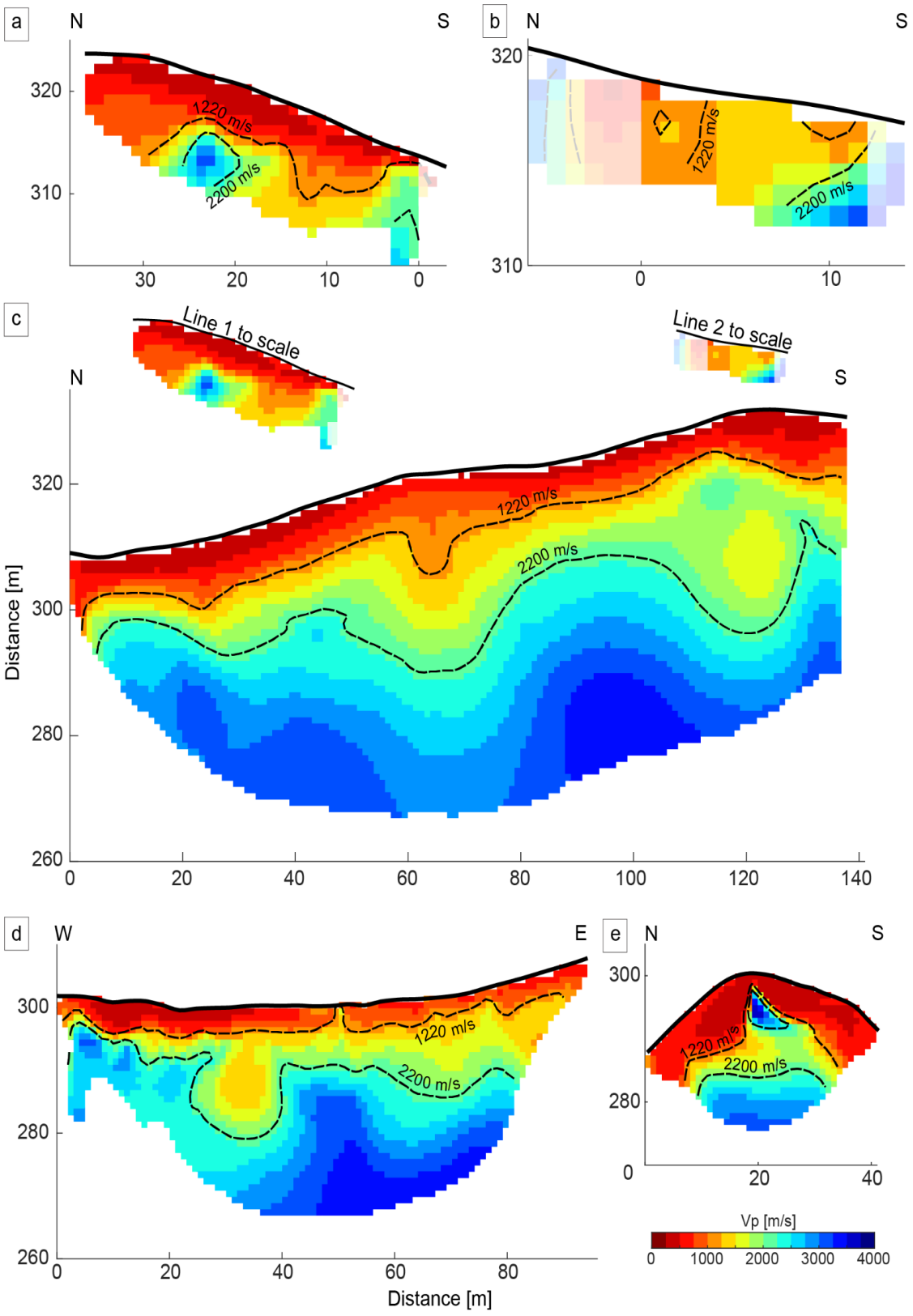
a
N
S
320
310
1220 m/s
2200 m/s
30
20
10
0
b
N
S
320
310
1220 m/s
2200 m/s
0
10
c
Line 1 to scale
Line 2 to scale
N
S
Distance [m]
320
300
280
260
1220 m/s
2200 m/s
0
20
40
60
80
100
120
140
d
W
E
300
280
260
1220 m/s
2200 m/s
0
20
40
60
80
Distance [m]
e
N
S
300
280
0
1220 m/s
2200 m/s
20
40
Vp [m/s]
0
1000
2000
3000
4000

Figure 3.2. Near-surface P-wave refraction surveys for (a) Line 1, (b) Line 2, (c) Line 3, (d) Line 4, and (e) Line 5. (c – e) are plotted to scale, with (a – b) shown to scale inset to (c). P-wave velocity (Vp) contours for 1220 and 2200 m/s, that we find corresponds to the pervasively weathered-fractured bedrock and fractured-unweathered bedrock boundary, respectively, shown as black dashed line. Inversion outside the extent of geophones is shaded out.

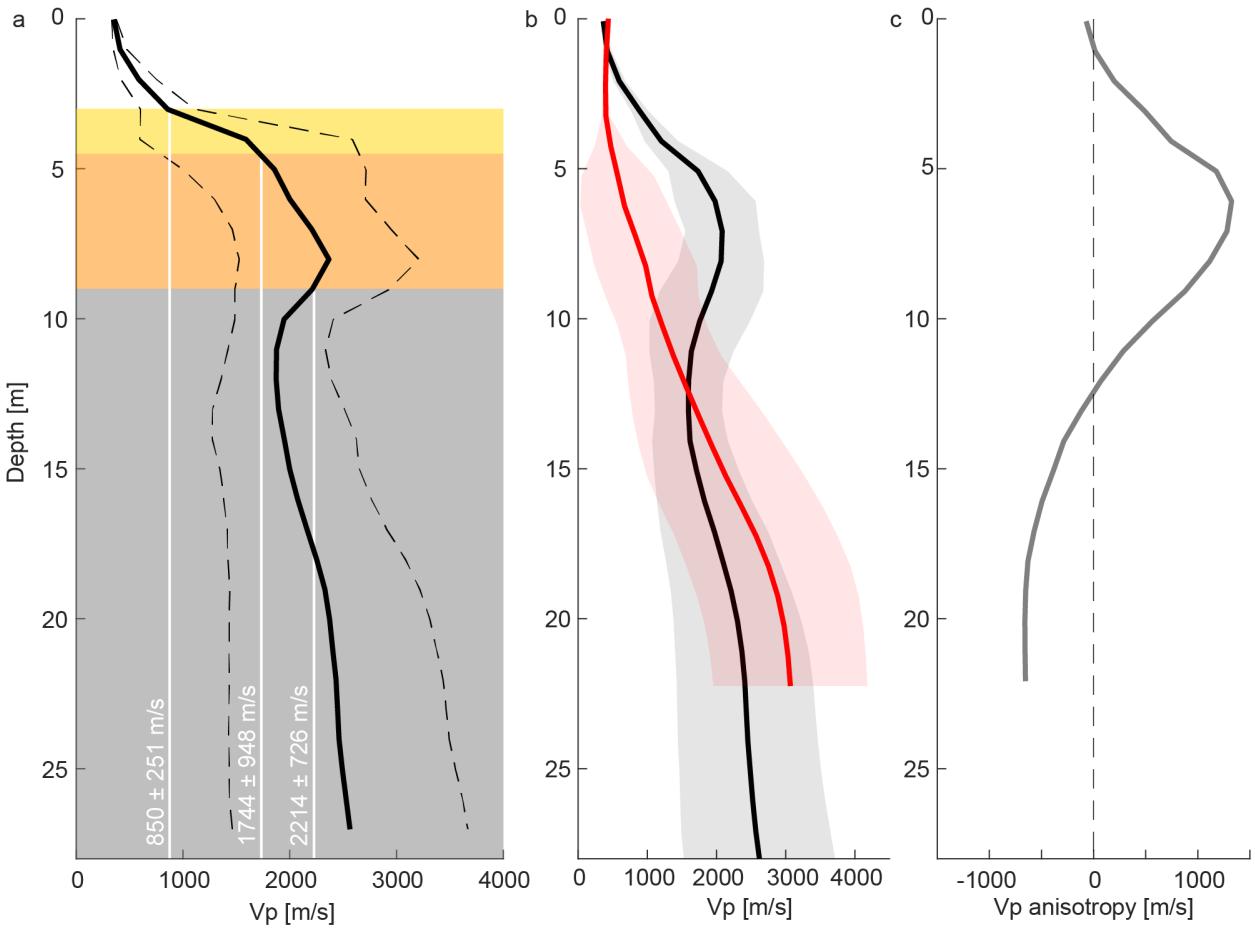

Figure 3.3. Mean P-wave velocity (Vp) profile in black from Line 4 profile at 35 m-deep CB1 borehole showing lithology from said core (white = no recovery, yellow = pervasively oxidized, orange = fractured, gray = unweathered; Anderson et al., 2002). Dashed boundaries show standard deviation from Bayesian inversion. White lines show Vp within standard deviation at weathered boundaries (b) Mean Vp profile of Line 4 (black) and Line 5 (red) where both surveys intersect, with respective shaded areas showing standard deviation from Bayesian inversion. (c) Difference between mean Vp of Line 4 and 5 at intersection, where more positive means Line 4 has higher Vp than Line 5. Dashed line means zero difference.

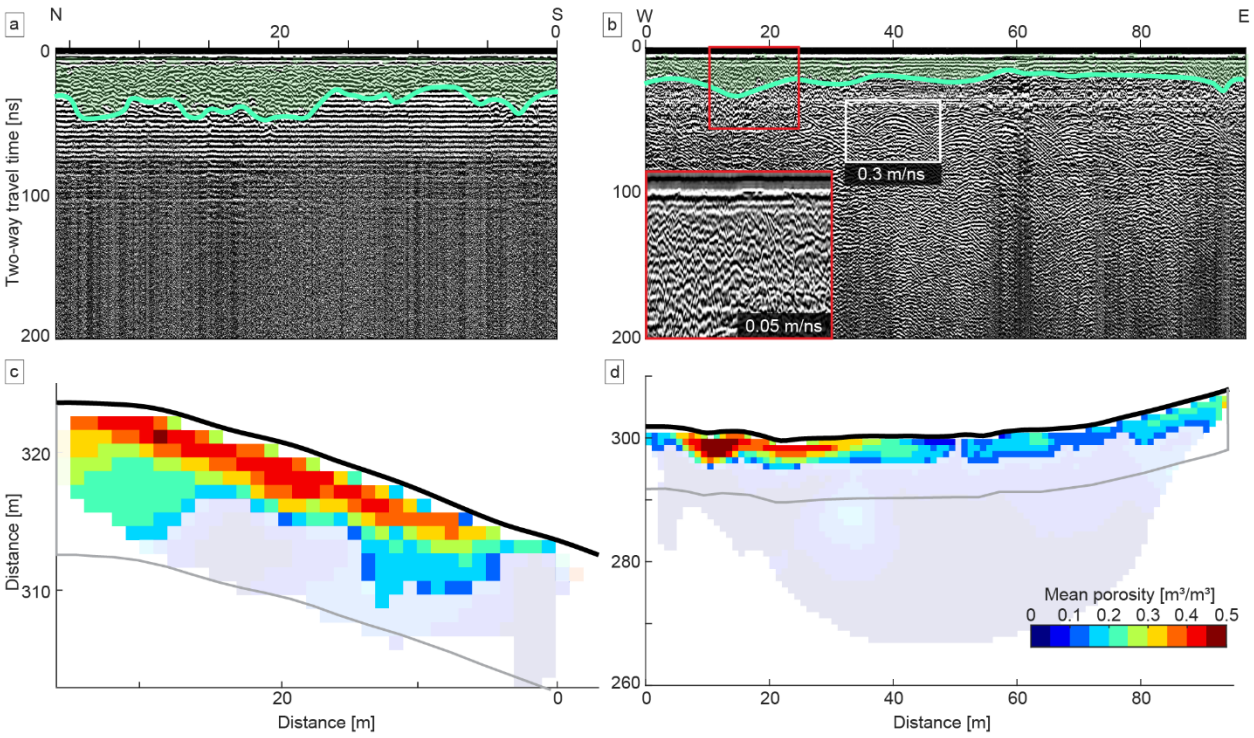

Figure 3.4. Ground penetrating radar (GPR) survey for (a) Line 1 and (b) Line 4. Teal shading and lines trace hummocky facies mapped by roughness of GPR reflectors. Inset in (b) shows close-up of red box with hyperbolas in hummocky facies indicative of 0.05 m/ns GPR velocities. Deeper hyperbolas suggest faster velocities. Results from Bayesian inversion of P-wave velocity (Vp) to porosity for (c) Line 1 and (d) Line 4. Areas shaded out have Vp > 1200 m/s characteristic of material less weathered than pervasively oxidized rock or saprolite and are excluded from the inversion. Gray line shows GPR extent assuming a GPR velocity of 0.1 m/ns. (a & c) are aligned x-scale, as is (b & d).

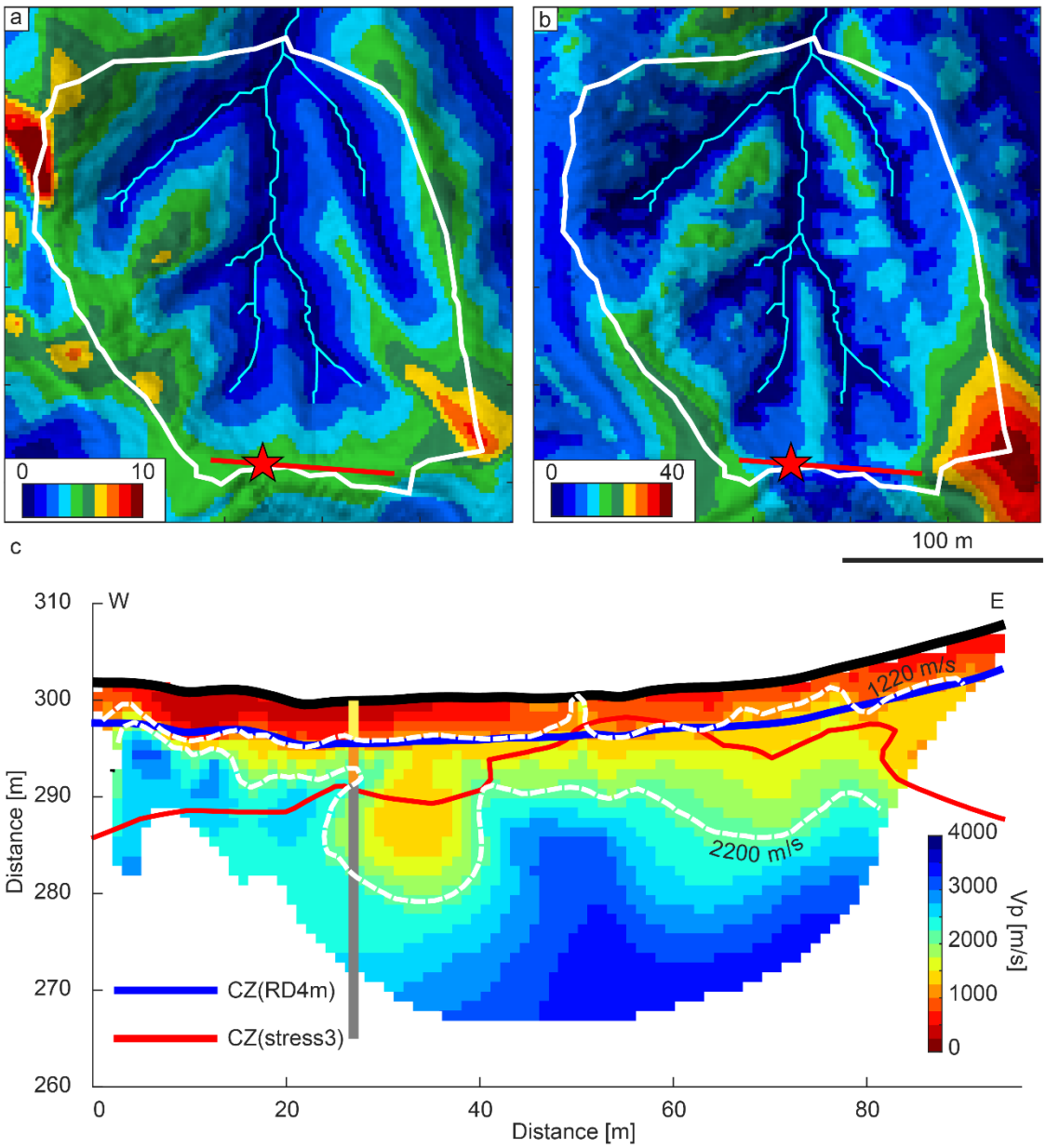
a
b
0
10
0
40
100 m
c
310
300
290
280
270
260
W
E
Distance [m]
1220 m/s
2200 m/s
CZ(RD4m)
CZ(stress3)
4000
3000
2000
1000
0
Vp [m/s]
0
20
40
60
80
Distance [m]

Figure 3.5. Modeled critical zone structures for (a) CZ(RD4m) and (c) CZ(stress3), same extent as Figure 3.1c. Color scale shows depth to unweathered bedrock in meters and is different for each panel to show variations. White outline is benchmark site, cyan lines are mapped channels, red star is location of 35 m-deep CB1 borehole, and red line is Line 4 P-wave velocity (Vp) survey. (c) Line 4 Vp profile showing predicted depth to unweathered boundary for CZ(RD4m) as blue and CZ(stress3) as red line. Dashed white lines show Vp contours of 1220 and 2200 m/s. Vertical line shows lithology from 35 m-deep CB1 borehole (yellow = pervasively oxidized, orange = fractured, gray = unweathered; Anderson et al., 2002).

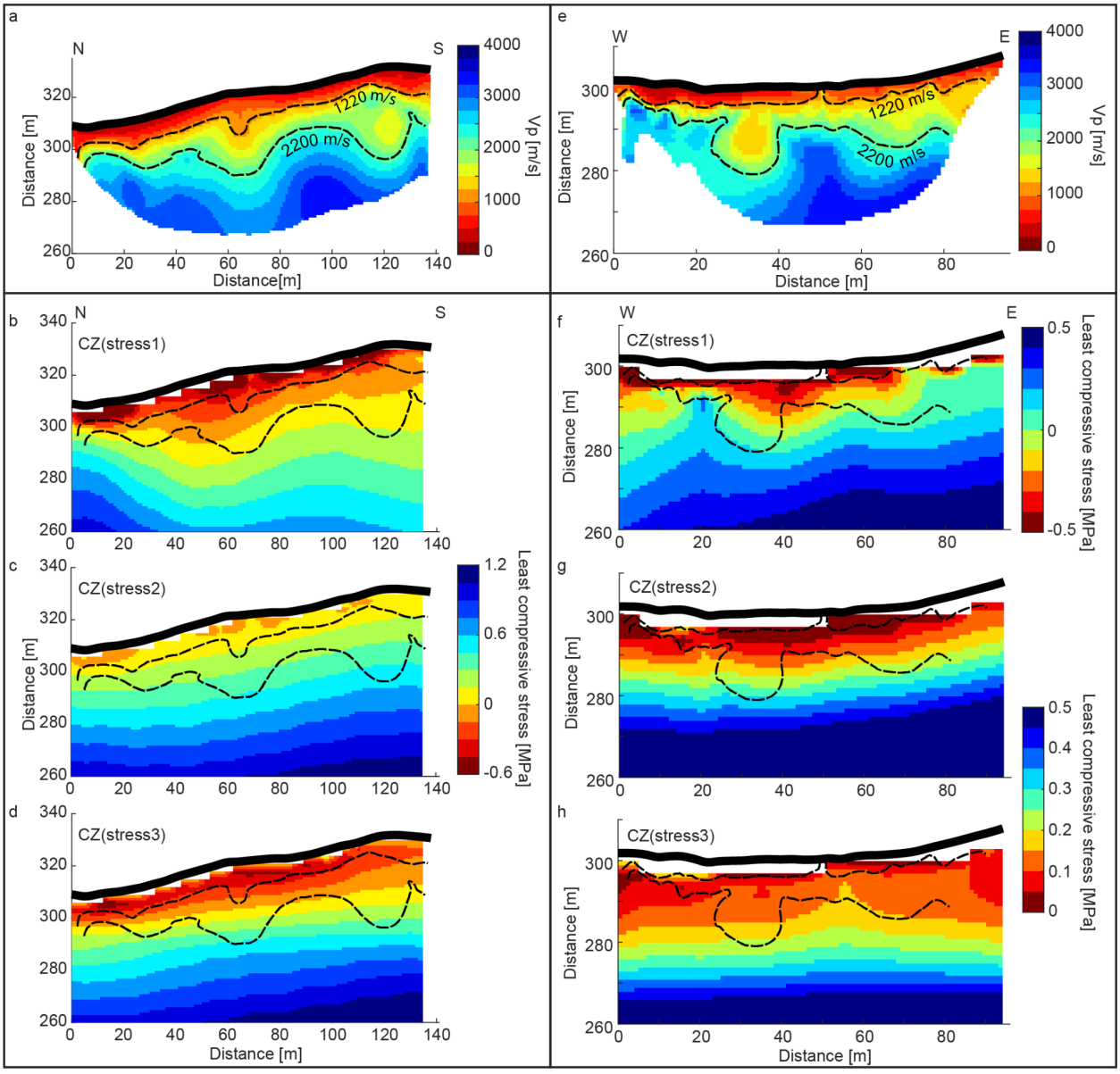

Figure 3.6. (a) P-wave refraction survey and least compressive stress profile for (b) CZ(stress1), (c) CZ(stress2), and (d) CZ(stress3) at Line 3. Black dashed lines show1220 and 2200 m/s P-wave velocity (Vp) contours. (e – h) That for Line 4. Note (f) has a different color scale than (g – h) to show variations of least compressive stress.

3.8 References

Alberti, S., Leshchinsky, B., Roering, J., Perkins, J., Olsen, M.J., 2022. Inversions of landslide strength as a proxy for subsurface weathering. Nature Communications 13, 6049. https://doi.org/10.1038/s41467-022-33798-5

Anderson, R.S., Anderson, S.P., Tucker, G.E., 2013. Rock damage and regolith transport by frost: An example of climate modulation of the geomorphology of the critical zone. Earth Surface Processes and Landforms 38, 299-316. https://doi.org/10.1002/esp.3330

Anderson, R.S., Rajaram, H., Anderson, S.P., 2019. Climate driven coevolution of weathering profiles and hillslope topography generates dramatic differences in critical zone architecture. Hydrological Processes 33, 4-19. https://doi.org/10.1002/hyp.13307

Anderson, S.P., Dietrich, W.E., Brimhall Jr, G.H., 2002. Weathering profiles, mass-balance analysis, and rates of solute loss: Linkages between weathering and erosion in a small, steep catchment. Geological Society of America Bulletin 114, 1143-1158. https://doi.org/10.1130/0016-7606(2002)114%3C1143:WPMBAA%3E2.0.CO;2

Anderson, S.P., Dietrich, W.E., Torres, R., Montgomery, D.R., Loague, K., 1997. Concentration-discharge relationships in runoff from a steep, unchanneled catchment. Water Resources Research 33, 211-225. https://doi.org/10.1029/96WR02715

Anderson, S.P., von Blanckenburg, F., White, A.F., 2007. Physical and chemical controls on the critical zone. Elements 3, 315-319. https://doi.org/10.2113/gselements.3.5.315

Baldwin, E.M., Beaulieu, J.D., 1973. Geology and mineral resources of Coos County, Oregon. Oregon Department of Geology and Mineral Industries, pp. 1 - 40.

Banwart, S., Menon, M., Bernasconi, S.M., Bloem, J., Blum, W.E., de Souza, D.M., Davidsdotir, B., Duffy, C., Lair, G.J., Kram, P., 2012. Soil processes and functions across an

international network of Critical Zone Observatories: Introduction to experimental methods and initial results. Comptes Rendus Geoscience 344, 758-772. https://doi.org/10.1016/j.crte.2012.10.007

Bear, J., 1988. Dynamics of fluids in porous media, Dover, New York.

Brantley, S.L., Buss, H., Lebedeva, M., Fletcher, R., Ma, L., 2011. Investigating the complex interface where bedrock transforms to regolith. Applied Geochemistry 26, S12-S15. https://doi.org/10.1016/j.apgeochem.2011.03.017

Brantley, S.L., Eissenstat, D.M., Marshall, J.A., Godsey, S.E., Balogh-Brunstad, Z., Karwan, D.L., Papuga, S.A., Roering, J., Dawson, T.E., Evaristo, J., 2017. Reviews and syntheses: on the roles trees play in building and plumbing the critical zone. Biogeosciences 14, 5115-5142. https://doi.org/10.5194/bg-14-5115-2017

Brantley, S.L., Goldhaber, M.B., Ragnarsdottir, K.V., 2007. Crossing disciplines and scales to understand the critical zone. Elements 3, 307-314. https://doi.org/10.2113/gselements.3.5.307

Brown, E.T., Hoek, E., 1978. Trends in relationships between measured in-situ stresses and depth, International Journal of Rock Mechanics and Mining Sciences & Geomechanics Abstracts. Pergamon, pp. 211-215.

Callahan, R.P., Riebe, C.S., Pasquet, S., Ferrier, K.L., Grana, D., Sklar, L.S., Taylor, N.J., Flinchum, B.A., Hayes, J.L., Carr, B.J., 2020. Subsurface weathering revealed in hillslope-integrated porosity distributions. Geophysical Research Letters 47, e2020GL088322. https://doi.org/10.1029/2020GL088322

Callahan, R.P., Riebe, C.S., Sklar, L.S., Pasquet, S., Ferrier, K.L., Hahm, W.J., Taylor, N.J., Grana, D., Flinchum, B.A., Hayes, J.L., 2022. Forest vulnerability to drought controlled

by bedrock composition. Nature Geoscience 15, 714-719. https://doi.org/10.1038/s41561-022-01012-2

Cronkite-Ratcliff, C., Schmidt, K.M., Wirion, C., 2022. Comparing Root Cohesion Estimates from Three Models at a Shallow Landslide in the Oregon Coast Range. GeoHazards 3, 428-451. https://doi.org/10.3390/geohazards3030022

Dietrich, W.E., Perron, J.T., 2006. The search for a topographic signature of life. Nature 439, 411-418. https://doi.org/10.1038/nature04452

Dvorkin, J., Nur, A., 2005. Critical-porosity models. Memoirs-American Association of Petroleum Geologists, 33-42.

Ebel, B.A., Loague, K., Dietrich, W.E., Montgomery, D.R., Torres, R., Anderson, S.P., Giambelluca, T.W., 2007a. Near-surface hydrologic response for a steep, unchanneled catchment near Coos Bay, Oregon: 1. Sprinkling experiments. American Journal of Science 307, 678-708. https://doi.org/10.2475/04.2007.02

Ebel, B.A., Loague, K., Vanderkwaak, J.E., Dietrich, W.E., Montgomery, D.R., Torres, R., Anderson, S.P., 2007b. Near-surface hydrologic response for a steep, unchanneled catchment near Coos Bay, Oregon: 2. Physics-based simulations. American Journal of Science 307, 709-748. https://doi.org/10.2475/04.2007.03

Eppes, M.C., Keanini, R., 2017. Mechanical weathering and rock erosion by climate-dependent subcritical cracking. Reviews of Geophysics 55, 470-508. https://doi.org/10.1002/2017RG000557

Eppes, M.C., Magi, B., Scheff, J., Warren, K., Ching, S., Feng, T., 2020. Warmer, Wetter Climates Accelerate Mechanical Weathering in Field Data, Independent of Stress-

Loading. Geophysical Research Letters 47, 2020GL089062. https://doi.org/10.1029/2020GL089062

Eppinger, B., Hayes, J.L., Carr, B., Moon, S., Cosans, C., Holbrook, W., Harman, C., Plante, Z., 2021. Quantifying depth-dependent seismic anisotropy in the critical zone enhanced by weathering of a piedmont schist. Journal of Geophysical Research: Earth Surface 126, e2021JF006289. https://doi.org/10.1029/2021JF006289

Fletcher, R., Brantley, S., 2010. Reduction of bedrock blocks as corestones in the weathering profile: Observations and model. American Journal of Science 310, 131-164. https://doi.org/10.2475/03.2010.01

Flinchum, B.A., Holbrook, W.S., Carr, B.J., 2022. What Do P-Wave Velocities Tell Us About the Critical Zone? Frontiers in Water 3, 772185. https://doi.org/10.3389/frwa.2021.772185

Flinchum, B.A., Holbrook, W.S., Rempe, D., Moon, S., Riebe, C.S., Carr, B.J., Hayes, J.L., St. Clair, J., Peters, M.P., 2018. Critical zone structure under a granite ridge inferred from drilling and three-dimensional seismic refraction data. Journal of Geophysical Research: Earth Surface 123, 1317-1343. https://doi.org/10.1029/2017JF004280

Geldart, L.P., Sheriff, R.E., 2004. Problems in exploration seismology and their solutions. Society of Exploration Geophysicists, Houston, TX.

Grana, D., 2016. Bayesian linearized rock-physics inversion. Geophysics 81, D625-D641. https://doi.org/10.1190/geo2016-0161.1

Gu, X., Heaney, P.J., Reis, F.D.A., Brantley, S.L., 2020a. Deep abiotic weathering of pyrite. Science 370, eabb8092. https://doi.org/10.1126/science.abb8092

Gu, X., Mavko, G., Ma, L., Oakley, D., Accardo, N., Carr, B.J., Nyblade, A.A., Brantley, S.L., 2020b. Seismic refraction tracks porosity generation and possible CO2 production at

depth under a headwater catchment. Proceedings of the National Academy of Sciences 117, 18991-18997. https://doi.org/10.1073/pnas.2003451117

Guo, L., Lin, H., 2016. Critical zone research and observatories: Current status and future perspectives. Vadose Zone Journal 15(9), vzj2016.06.0050. https://doi.org/10.2136/vzj2016.06.0050

Guo, L., Mount, G.J., Hudson, S., Lin, H., Levia, D., 2020. Pairing geophysical techniques improves understanding of the near-surface Critical Zone: Visualization of preferential routing of stemflow along coarse roots. Geoderma 357, 113953. https://doi.org/10.1016/j.geoderma.2019.113953

Hahm, W.J., Dralle, D.N., Sanders, M., Bryk, A.B., Fauria, K.E., Huang, M.-H., Hudson-Rasmussen, B., Nelson, M.D., Pedrazas, M.A., Schmidt, L., 2022. Bedrock vadose zone storage dynamics under extreme drought: consequences for plant water availability, recharge, and runoff. Water Resources Research 58, e2021WR031781. https://doi.org/10.1029/2021WR031781

Hayes, J.L., Riebe, C.S., Holbrook, W.S., Flinchum, B.A., Hartsough, P.C., 2019. Porosity production in weathered rock: Where volumetric strain dominates over chemical mass loss. Science Advances 5, eaao0834. https://doi.org/10.1126/sciadv.aao0834

Heidbach, O., Rajabi, M., Cui, X., Fuchs, K., Müller, B., Reinecker, J., Reiter, K., Tingay, M., Wenzel, F., Xie, F., 2018. The World Stress Map database release 2016: Crustal stress pattern across scales. Tectonophysics 744, 484-498. https://doi.org/10.1016/j.tecto.2018.07.007

Heimsath, A.M., Dietrich, W.E., Nishiizumi, K., Finkel, R.C., 2001. Stochastic processes of soil production and transport: Erosion rates, topographic variation and cosmogenic nuclides

in the Oregon Coast Range. Earth Surface Processes and Landforms: The Journal of the British Geomorphological Research Group 26, 531-552. https://doi.org/10.1002/esp.209

Higa, J.T., Formetta, G., Bellugi, D.G., Busti, R., Dietrich, W.E., Milledge D.G., Ebel, B.A., Moon, S., in prep. Deep critical zone controls on shallow landslides: insights from numerical simulations in a steep, forested landscape.

Holbrook, W.S., Riebe, C.S., Elwaseif, M., L. Hayes, J., Basler-Reeder, K., L. Harry, D., Malazian, A., Dosseto, A., C. Hartsough, P., W. Hopmans, J., 2014. Geophysical constraints on deep weathering and water storage potential in the Southern Sierra Critical Zone Observatory. Earth Surface Processes and Landforms 39, 366-380. https://doi.org/10.1002/esp.3502

Huang, M.H., Hudson-Rasmussen, B., Burdick, S., Lekic, V., Nelson, M.D., Fauria, K.E., Schmerr, N., 2021. Bayesian Seismic Refraction Inversion for Critical Zone Science and Near-Surface Applications. Geochemistry, Geophysics, Geosystems 22, e2020GC009172. https://doi.org/10.1029/2020GC009172

Iverson, R.M., Major, J.J., 1986. Groundwater seepage vectors and the potential for hillslope failure and debris flow mobilization. Water Resources Research 22, 1543-1548. https://doi.org/10.1029/WR022i011p01543

Iverson, R.M., Reid, M.E., 1992. Gravity-driven groundwater flow and slope failure potential: 1. Elastic Effective-Stress Model. Water Resources Research 28, 925-938. https://doi.org/10.1029/91WR02694

Kelsey, H.M., 1990. Late Quaternary deformation of marine terraces on the Cascadia subduction zone near Cape Blanco, Oregon. Tectonics 9, 983-1014. https://doi.org/10.1029/TC009i005p00983

Kelsey, H.M., Engebretson, D.C., Mitchell, C.E., Ticknor, R.L., 1994. Topographic form of the Coast Ranges of the Cascadia margin in relation to coastal uplift rates and plate subduction. Journal of Geophysical Research: Solid Earth 99, 12245-12255. https://doi.org/10.1029/93JB03236

Koesoemadinata, A.P., McMechan, G.A., 2004. Effects of diagenetic processes on seismic velocity anisotropy in near-surface sandstone and carbonate rocks. Journal of Applied Geophysics 56, 165-176. https://doi.org/10.1016/j.jappgeo.2004.04.003

Korup, O., Seidemann, J., Mohr, C.H., 2019. Increased landslide activity on forested hillslopes following two recent volcanic eruptions in Chile. Nature Geoscience 12, 284-289. https://doi.org/10.1038/s41561-019-0315-9

Lebedeva, M.I., Brantley, S.L., 2013. Exploring geochemical controls on weathering and erosion of convex hillslopes: beyond the empirical regolith production function. Earth Surface Processes and Landforms 38, 1793-1807. https://doi.org/10.1002/esp.3424

Lebedeva, M.I., Brantley, S.L., 2020. Exploring an ‘ideal hill': how lithology and transport mechanisms affect the possibility of a steady state during weathering and erosion. Earth Surface Processes and Landforms 45, 652-665. https://doi.org/10.1002/esp.4762

Leone, J.D., Holbrook, W.S., Riebe, C.S., Chorover, J., Ferré, T.P., Carr, B.J., Callahan, R.P., 2020. Strong slope-aspect control of regolith thickness by bedrock foliation. Earth Surface Processes and Landforms 45, 2998-3010. https://doi.org/10.1002/esp.4947

Li, G.K., Moon, S., 2021. Topographic stress control on bedrock landslide size. Nature Geoscience 14, 307-313. https://doi.org/10.1038/s41561-021-00739-8

Lindner, E.N., Halpern, J.A., 1978. In-situ stress in North America: A compilation, International Journal of Rock Mechanics and Mining Sciences & Geomechanics Abstracts. Elsevier, pp. 183-203. https://doi.org/10.1016/0148-9062(78)91225-1

Litwin, D.G., Tucker, G.E., Barnhart, K.R., Harman, C.J., 2022. Groundwater affects the geomorphic and hydrologic properties of coevolved landscapes. Journal of Geophysical Research: Earth Surface 127, e2021JF006239. https://doi.org/10.1029/2021JF006239

Ma, L., Oakley, D., Nyblade, A., Moon, S., Accardo, N., Wang, W., Gu, X., Brubaker, K., Mount, G.J., Forsythe, B., 2021. Seismic Imaging of a Shale Landscape Under Compression Shows Limited Influence of Topography-Induced Fracturing. Geophysical Research Letters 48, e2021GL093372. https://doi.org/10.1029/2021GL093372

Mavko, G., Mukerji, T., Dvorkin, J., 2009. The rock physics handbook. Cambridge University Press, Cambridge, U.K.

McGarr, A., Gay, N., 1978. State of stress in the earth's crust. Annual Review of Earth and Planetary Sciences 6, 405-436. https://doi.org/10.1146/annurev.ea.06.050178.002201

McInelly, G.W., Kelsey, H.M., 1990. Late Quaternary tectonic deformation in the Cape Arago-Bandon region of coastal Oregon as deduced from wave-cut platforms. Journal of Geophysical Research: Solid Earth 95, 6699-6713. https://doi.org/10.1029/JB095iB05p06699

McTigue, D.F., Mei, C.C., 1981. Gravity-induced stresses near topography of small slope. Journal of Geophysical Research: Solid Earth 86, 9268-9278. https://doi.org/10.1029/JB086iB10p09268

Miller, D.J., Dunne, T., 1996. Topographic perturbations of regional stresses and consequent bedrock fracturing. Journal of Geophysical Research: Solid Earth 101, 25523-25536. https://doi.org/10.1029/96JB02531

Mindlin, R.D., 1949. Compliance of elastic bodies in contact. Journal of Applied Mechanics 16(3), 259-268. https://doi.org/10.1115/1.4009973

Molnar, P., 2004. Interactions among topographically induced elastic stress, static fatigue, and valley incision. Journal of Geophysical Research: Earth Surface 109, F02010. https://doi.org/10.1029/2003JF000097

Montgomery, D.R., Dietrich, W.E., Heffner, J.T., 2002. Piezometric response in shallow bedrock at CB1: Implications for runoff generation and landsliding. Water Resources Research 38, 10-11. https://doi.org/10.1029/2002WR001429

Montgomery, D.R., Dietrich, W.E., Torres, R., Anderson, S.P., Heffner, J.T., Loague, K., 1997. Hydrologic response of a steep, unchanneled valley to natural and applied rainfall. Water Resources Research 33, 91-109. https://doi.org/10.1029/96WR02985

Montgomery, D.R., Schmidt, K.M., Dietrich, W.E., McKean, J., 2009. Instrumental record of debris flow initiation during natural rainfall: Implications for modeling slope stability. Journal of Geophysical Research: Earth Surface 114. https://doi.org/10.1029/2008JF001078

Moon, S., Perron, J., Martel, S., Holbrook, W., St. Clair, J., 2017. A model of three-dimensional topographic stresses with implications for bedrock fractures, surface processes, and landscape evolution. Journal of Geophysical Research: Earth Surface 122, 823-846. https://doi.org/10.1002/2016JF004155

Moon, S., Perron, J.T., Martel, S.J., Goodfellow, B.W., Mas Ivars, D., Hall, A., Heyman, J., Munier, R., Näslund, J.O., Simeonov, A., 2020. Present-day stress field influences bedrock fracture openness deep into the subsurface. Geophysical Research Letters 47, e2020GL090581. https://doi.org/10.1029/2020GL090581

Murphy, B.P., Johnson, J.P., Gasparini, N.M., Sklar, L.S., 2016. Chemical weathering as a mechanism for the climatic control of bedrock river incision. Nature 532, 223-227. https://doi.org/10.1038/nature17449

Murphy, W.F.I., 1982. Effects of microstructure and pore fluids on the acoustic properties of granular sedimentary materials. Stanford University.

Orlando, J., Comas, X., Hynek, S.A., Buss, H.L., Brantley, S.L., 2016. Architecture of the deep critical zone in the Río Icacos watershed (Luquillo Critical Zone Observatory, Puerto Rico) inferred from drilling and ground penetrating radar (GPR). Earth Surface Processes and Landforms 41, 1826-1840. https://doi.org/10.1002/esp.3948

Pandey, S., Rajaram, H., 2016. Modeling the influence of preferential flow on the spatial variability and time-dependence of mineral weathering rates. Water Resources Research 52, 9344-9366. https://doi.org/10.1002/2016WR019026

Pasquet, S., Marçais, J., Hayes, J.L., Sak, P.B., Ma, L., Gaillardet, J., 2022. Catchment-Scale Architecture of the Deep Critical Zone Revealed by Seismic Imaging. Geophysical Research Letters 49, e2022GL098433. https://doi.org/10.1029/2022GL098433

Plattner, A.M., 2020. GPRPy: Open-source ground-penetrating radar processing and visualization software. The Leading Edge 39, 332-337. https://doi.org/10.1190/tle39050332.1

Reid, M.E., Iverson, R.M., 1992. Gravity-driven groundwater flow and slope failure potential: 2. Effects of slope morphology, material properties, and hydraulic heterogeneity. Water Resources Research 28, 939-950. https://doi.org/10.1029/91WR02695

Rempe, D.M., Dietrich, W.E., 2014. A bottom-up control on fresh-bedrock topography under landscapes. Proceedings of the National Academy of Sciences 111, 6576-6581. https://doi.org/10.1073/pnas.1404763111

Reneau, S.L., Dietrich, W.E., 1991. Depositional history of hollows on steep hillslopes, coastal Oregon and Washington. National Geographic Research 6, 220-230.

Riebe, C.S., Hahm, W.J., Brantley, S.L., 2017. Controls on deep critical zone architecture: A historical review and four testable hypotheses. Earth Surface Processes and Landforms 42, 128-156. https://doi.org/10.1002/esp.4052

Roering, J.J., Kirchner, J.W., Dietrich, W.E., 1999. Evidence for nonlinear, diffusive sediment transport on hillslopes and implications for landscape morphology. Water Resources Research 35, 853-870. https://doi.org/10.1029/1998WR900090

Roering, J.J., Marshall, J., Booth, A.M., Mort, M., Jin, Q., 2010. Evidence for biotic controls on topography and soil production. Earth and Planetary Science Letters 298, 183-190. https://doi.org/10.1016/j.epsl.2010.07.040

Savage, W., Swolfs, H., Powers, P., 1985. Gravitational stresses in long symmetric ridges and valleys. International Journal of Rock Mechanics and Mining Sciences & Geomechanics Abstracts 22, 291-302. https://doi.org/10.1016/0148-9062(85)92061-3

Savage, W.Z., Swolfs, H.S., 1986. Tectonic and gravitational stress in long symmetric ridges and valleys. Journal of Geophysical Research: Solid Earth 91, 3677-3685. https://doi.org/10.1029/JB091iB03p03677

Schmidt, K., Roering, J., Stock, J., Dietrich, W., Montgomery, D., Schaub, T., 2001. The variability of root cohesion as an influence on shallow landslide susceptibility in the Oregon Coast Range. Canadian Geotechnical Journal 38, 995-1024. https://doi.org/10.1139/t01-031

Slim, M., Perron, J.T., Martel, S.J., Singha, K., 2015. Topographic stress and rock fracture: A two-dimensional numerical model for arbitrary topography and preliminary comparison with borehole observations. Earth Surface Processes and Landforms 40, 512-529. https://doi.org/10.1002/esp.3646

Spence, W., 1989. Stress origins and earthquake potentials in Cascadia. Journal of Geophysical Research: Solid Earth 94, 3076-3088. https://doi.org/10.1029/JB094iB03p03076

St. Clair, J., Moon, S., Holbrook, W., Perron, J., Riebe, C., Martel, S., Carr, B., Harman, C., Singha, K., Richter, D.d., 2015. Geophysical imaging reveals topographic stress control of bedrock weathering. Science 350, 534-538. https://doi.org/10.1126/science.aab2210

Takasu, T., Kubo, N., Yasuda, A., 2007. Development, evaluation and application of RTKLIB: a program library for RTK-GPS, GPS/GNSS symposium, pp. 213-218.

Thomas, A.L., 1993. POLY3D: A three-dimensional, polygonal element, displacement discontinuity boundary element computer program with applications to fractures, faults, and cavities in the earth's crust. Stanford University.

Torres, R., Dietrich, W.E., Montgomery, D.R., Anderson, S.P., Loague, K., 1998. Unsaturated zone processes and the hydrologic response of a steep, unchanneled catchment. Water Resources Research 34, 1865-1879. https://doi.org/10.1029/98WR01140

Viles, H., Goudie, A., Grab, S., Lalley, J., 2011. The use of the Schmidt Hammer and Equotip for rock hardness assessment in geomorphology and heritage science: a comparative

analysis. Earth Surface Processes and Landforms 36, 320-333. https://doi.org/10.1002/esp.2040

Von Voigtlander, J., Clark, M.K., Zekkos, D., Greenwood, W.W., Anderson, S.P., Anderson, R.S., Godt, J.W., 2018. Strong variation in weathering of layered rock maintains hillslope‐scale strength under high precipitation. Earth Surface Processes and Landforms 43, 1183-1194. https://doi.org/10.1002/esp.4290

Wang, W., Nyblade, A., Mount, G., Moon, S., Chen, P., Accardo, N., Gu, X., Forsythe, B., Brantley, S.L., 2021. 3D seismic anatomy of a watershed reveals climate-topography coupling that drives water flowpaths and bedrock weathering. Journal of Geophysical Research: Earth Surface 126, e2021JF006281. https://doi.org/10.1029/2021JF006281

White, T., Brantley, S., Banwart, S., Chorover, J., Dietrich, W., Derry, L., Lohse, K., Anderson, S., Aufdendkampe, A., Bales, R., 2015. The role of critical zone observatories in critical zone science, Developments in Earth Surface Processes. Elsevier, pp. 15-78. https://doi.org/10.1016/B978-0-444-63369-9.00002-1

Zoback, M.L., Zoback, M., 1980. State of stress in the conterminous United States. Journal of Geophysical Research: Solid Earth 85, 6113-6156. https://doi.org/10.1029/JB085iB11p06113

Chapter 4: Deep critical zone controls on shallow landslides: insights from numerical simulations in a steep, forested landscape

This chapter is modified from Higa, J.T., Formetta, G., Bellugi, D.G., Busti, R., Dietrich, W.E., Milledge D.G., Ebel, B.A., Moon, S., in prep. Deep critical zone controls on shallow landslides: insights from numerical simulations in a steep, forested landscape.

4.1 Introduction

Landslides killed over 50,000 people globally between 2004 – 2016 (Froude and Petley, 2018). In the United States alone, landslides and rockfalls kill 25 – 50 people and cause an average of $1 – $3 billion of damage every year (National Research Council, 2004). Researchers have been improving landslide modeling by reexamining parameters that control slope stability. For shallow landslides that mobilize soil, such parameters include variable soil thickness (e.g., Kim et al., 2015; Onda et al., 2004; Shoaei and Sidle, 2009; Uchida et al., 2011), lateral resistance (e.g., Milledge et al., 2014; Prancevic et al., 2018), landslide shape and size (e.g., Bellugi et al., 2015a; Bellugi et al., 2015b; Bellugi et al., 2021), root cohesion (e.g., Cronkite-Ratcliff et al., 2022; Schmidt et al., 2001), and groundwater seepage (e.g., Chu-Agor et al., 2008; Fox and Felice, 2014; Iverson and Major, 1986). Field observations and experiments then suggest that groundwater exfiltration through permeable, deep, weathered, and fractured bedrock plays important roles in saturating soil and inducing shallow landslides (e.g., Anderson et al., 1997; Montgomery et al., 2002; Torres et al., 1998). However, many landslide models assume a simplified weathered subsurface and impermeable unweathered bedrock due to a limited understanding of deep bedrock structures.

Recently, researchers have been working to observe and predict natural variations of weathered and fractured bedrock near Earth's surface. This weathered bedrock constitutes the deeper part of the critical zone (CZ), where the geo-, bio-, hydro-, and atmosphere interact (Anderson et al., 2007; Brantley et al., 2007; Riebe et al., 2017). Geophysical surveys using seismic refraction tomography (e.g., Callahan et al., 2020; Flinchum et al., 2018; Pasquet et al., 2022; St. Clair et al., 2015; Wang et al., 2021) and ground penetrating radar (Guo et al., 2020; Orlando et al., 2016) suggest that structures of weathered bedrock can be complex, with spatially variable thicknesses throughout a landscape. Then, recent process-based studies examine how pre-existing, interconnected bedrock fractures (Gu et al., 2020), frost cracking (Anderson et al., 2013), reactive transport (Lebedeva and Brantley, 2013, 2020), channel incision (Anderson et al., 2019; Rempe and Dietrich, 2014), and subsurface stresses (Moon et al., 2017; St. Clair et al., 2015) weather or help to weather bedrock and shape the deep CZ. Comparisons between geophysical observations and process-based modeling suggest that these weathering models have some success in predicting deep CZ structures (e.g., Flinchum et al., 2018; Ma et al., 2021; St. Clair et al., 2015; Wang et al., 2021).

Understanding and predicting complex variations of weathered bedrock are important for improving how we model shallow landslides. Permeable weathered bedrock is a reservoir for groundwater (e.g., Holbrook et al., 2014) that can control patterns of infiltration and exfiltration over a landscape. Previous studies have shown that groundwater seepage from weathered bedrock can have a large magnitude and reduce slope stability (e.g., Iverson and Major, 1986; Montgomery et al., 1997). Subsequent sandbox and flume analogs confirm a controlling role of exfiltration on landslides and bank collapses (Chu-Agor et al., 2008; Fox and Felice, 2014; Kim et al., 2018).

However, there are limited studies that examine the effect of a catchment-wide, three-dimensionally variable, deep CZ on groundwater seepage and shallow landslide hazards.

Here, we explore the impacts of spatially varying weathered bedrock in the deep CZ on groundwater flow paths, subsequent seepage, and the occurrences and characteristics of shallow soil landslides. We compare five theoretical structures of the deep CZ that are calibrated with field measurements from a well-studied benchmark site. Then, we simulate the hydrology of these structures during realistic rainfall, estimate spatially variable soil saturation and groundwater seepage, and predict the occurrence, size, and location of shallow landslides. Our findings show that our varying CZ structures produce substantial variations in the spatial distribution and magnitude of soil saturation by modulating groundwater infiltration and exfiltration within weathered bedrock. These effects may induce potential changes in the likelihood, size distribution, and location of shallow landslides. Our work implies that characterizing deep CZ is critical for accurately predicting the timing and assessing the magnitude of shallow landslides.

4.2 Study area

The Oregon Coast Range is a highly dissected and steep mountain range in a humid climate, prone to deep-seated and shallow soil landslides (e.g., Roering et al., 2005). Here, we examine a steep, ~0.7 km^2 catchment ~15 km NE of Coos Bay, Oregon, USA, in the Oregon Coast Range as a benchmark site for modeling shallow landslides. We choose this site because of its long history as a study area for weathering, hydrologic, and landslide investigations (Figure 4.1a – b). Slopes, on average 43° here, are underlain by graywacke sandstone of the Eocene Tyee formation, dipping roughly into the slope by 8° – 17° (Baldwin, 1966; Montgomery et al., 1997). During an extensive field campaign, Montgomery et al. (1997) reports hand-augered soil thickness measurements at a landslide named CB1 in the benchmark site. Soil is thin, < 0.5 m, on adjacent

spur ridges and thick, > 1.0 m, in the CB1 hollow. Previous studies show that stochastic (e.g., tree throw; Heimsath et al., 2001) and nonlinear (e.g., landslides; Roering et al., 1999) processes can explain the distribution of thick soils here. Further studies on root cohesion at CB1 show how interactions with vegetation can affect soil transport by increasing the cohesion of colluvium and decreasing landslide occurrences (e.g., Bellugi et al., 2021; Cronkite-Ratcliff et al., 2022; Schmidt et al., 2001). Commercial forest harvesting can have the opposite effect as roots from felled trees decay, causing root cohesion to decrease and landslide occurrence to increase (Montgomery et al., 2000). These studies provide information on soil thickness variations and root cohesion parameters that are used in models of shallow landslides at this benchmark site.

Previous studies extensively examined the occurrences of shallow landslides through fieldwork and demonstrated the involvement of groundwater in shallow landslide activity at the benchmark site (e.g., Montgomery et al., 2009). There are a total of 35 shallow landslides mapped from 1987 – 1996 surrounding our benchmark site (Figure 4.1a; Montgomery et al., 2000). On 20 February 1992, a landslide occurred in a catchment directly west of CB1, named CB2, during a storm with a peak rainfall intensity of 15.5 mm/hr where water was observed exfiltrating from bedrock fractures in the landslide scar (Figure 4.1b; Montgomery et al., 2002). Then, a record storm from 15 to 20 November 1996 induced multiple landslides in the Oregon Coast Range, including a landslide in CB1 (Figure 4.1b). The final dimensions of the CB1 landslide are 5 – 9.3 m-wide and 21 – 23 m-long with an area of 157 m^2, but researchers found the initial scar was only 58 m^2 in the upper portion of the mapped landslide (Figure 4.1b; Montgomery et al., 2009). Piezometers installed in the hollow measured pressure head in soil until this landslide destroyed most field infrastructure (Montgomery et al., 2009). These works calculate soil saturation as the ratio of the pressure head above the base of soil (h [m]) over soil depth (z[m]), hereafter, h/z. The

highest *h/z* was located around fractured bedrock later exposed by the landslide (0.4 – 0.75; Montgomery et al., 2009). The lowest *h/z* was located ~5 m away (0.1 – 0.2), where fewer bedrock fractures were documented. Such patchy saturation agrees with fracture exfiltration at CB2, artificial sprinkler experiment results (Montgomery and Dietrich, 2002; Montgomery et al., 2002; Montgomery et al., 1997; Torres et al., 1998), and hydrologic modeling of soil saturation (Ebel and Loague, 2008; Ebel et al., 2007a; Ebel et al., 2008; Ebel et al., 2007b). These findings suggest that exfiltration from deep bedrock structures is likely involved in shallow landslide occurrence.

Such detailed documentation of soil parameters, saturation, and landslide timing allows researchers to model soil stability at the benchmark site and CB1. Several studies use one-dimensional infinite-slope limit equilibrium models (Montgomery and Dietrich, 1994; Rosso et al., 2006), three-dimensionally variable saturated flow (Ebel et al., 2010), two-dimensional continuum deformation (Borja and White, 2010), and root cohesion estimates (Montgomery et al., 2000) to predict landslide occurrence. Recent work developed a three-dimensional model that uses a Mohr-Coulomb approach to balance driving and resisting forces summed from all edges of a discrete landslide, accounting for measured saturation, soil thickness, and root strength at CB1 (Bellugi et al., 2015a; Bellugi et al., 2015b; Milledge et al., 2014). This model is coupled to a spectral search algorithm as a computationally efficient method to identify mutually exclusive and overlapping clusters of unstable soil. Applications of this approach evaluated controls on landslide size and location by factors including rainfall intensity, soil thickness and properties, and root cohesion (Bellugi, 2012; Bellugi et al., 2015b; Bellugi et al., 2021). However, these slope stability models assume either soil directly over impermeable bedrock or test one configuration of weathered bedrock at depth, which may be structurally complex in reality and impact the occurrence of shallow soil landslides.

Previous studies have attempted to quantify the spatial variation of deep CZ structures at CB1 based on extensive observations of colluvium, saprolite, and weathered and fractured bedrock (e.g., Anderson et al., 2002; Montgomery et al., 1997). Hand-augered data suggest that weathered bedrock thins downslope at CB1 (Montgomery et al., 1997). One 35 m-deep borehole at the top of CB1 found that weathered bedrock transitions from pervasively oxidized to fractured and partially oxidized sandstone with depth, hereafter the CB1 borehole (Figure 4.1c; Anderson et al., 2002). The boundary between pervasively oxidized and fractured bedrock is 4.5 m-deep. Then, a boundary between fractured and unweathered bedrock was found 9 m-deep in the CB1 borehole. Porosity observations from this core and soil pits agree with other studies that suggest hydraulic conductivity increases towards the surface, although values from the same weathered layer can vary by orders of magnitude (Anderson et al., 1997; Ebel et al., 2007a; Ebel et al., 2007b; Montgomery et al., 2002; Montgomery et al., 1997). Tracer studies then highlight the contribution of groundwater from fractured bedrock into surface soils at relatively localized areas around channels (Anderson et al., 1997). Rempe and Dietrich (2014) used these measurements of weathered boundaries and hydraulic conductivities to calibrate a bedrock weathering model based on the drainage of groundwater through a hillslope and into a channel. At CB1, the model could predict a weathered bedrock layer 9 m-thick at the ridgeline that thins downslope towards the hollow, reproducing weathered bedrock that becomes thinner downslope. Together, these studies show how field observations can be used to model weathered bedrock structures in the deep CZ not easily discernable from geologic observations made at the surface.

Extensive past investigations highlight natural variations of deep weathered bedrock structures and groundwater flow through fractures that can potentially impact shallow landslides. We utilize the detailed subsurface observations, hydrologic data, and landslide mapping described

above to calibrate weathering, hydrologic, and slope stability models. We use these models to (1) construct theoretical, yet realistic weathered structures, (2) simulate groundwater seepage flow through the deep CZ, and (3) assess the impact of this flow on shallow soil landslide occurrence, size, and location.

4.3 Methods

4.3.1 Critical zone models and properties

We generate five theoretical CZ models using different assumptions of underlying bedrock properties and structures. We assume that CZ architecture consists of soil on top, optional weathered bedrock in the middle, and unweathered bedrock on the bottom. We modeled the spatial variation of soil thickness (Section 4.3.1.1), which is applied to all CZ models. Then, we predict the spatial variation of weathered bedrock thickness based on two weathering models: a bedrock drainage and a topographic stress model (Section 4.3.1.2 and 4.3.1.3). Our models are calibrated using field observations of rock properties (e.g., Rempe and Dietrich, 2014) and tectonic stress (e.g., Heidbach et al., 2018).

Due to limited field information on deep CZ structures, we do not capture the full, natural variability of weathered material here. Thus, examining the effect of bedrock heterogeneities, such as fractures, on shallow landslides is beyond the scope of this manuscript. Here, we intend to simulate theoretical, endmember processes of the deep CZ that represent plausible, three-dimensional variations of hydrology and shallow landslide occurrence at the benchmark site.

4.3.1.1 Soil

We model the spatial distribution of soil thickness following Dietrich et al.(1995) and Bellugi et al. (2015b) using a landscape evolution model that couples an exponential soil production function (Heimsath et al., 2001) and a nonlinear soil diffusion model (Roering et al.,

1999; Text C1). This coupled model simulates soil production at every cell, transports this soil based on topography, and outputs a map of predicted soil thickness. We model soil production and transport for over 6000 years at this site to match field measurements (Montgomery, 1991). We then use a post-landslide, 2 m-resolution LiDAR digital elevation model (DEM; Roering et al., 1999) of the benchmark site and parameters calibrated from measurements of local erosion rates (0.05 – 0.15 mm/yr; Heimsath et al., 2001; Reneau and Dietrich, 1990; Roering et al., 1999). We also provide the locations of channels as boundary conditions for hillslope transport. These channels are calculated from flow accumulation with a channelization threshold of 400 m^2 (Orlandini et al., 2003) and corrected based on field-mapped locations of channel heads (Montgomery et al., 2000).

4.3.1.2 Weathered bedrock model: bedrock drainage

We use a weathering model based on bedrock drainage and channel incision following Rempe and Dietrich (2014) to include weathered bedrock in our landslide modeling. This model uses a one-dimensional, steady-state form of the Boussinesq equation for groundwater flow to solve for the elevation of the groundwater table (Bear, 1988). We assume that water below this boundary is chemically equilibrated with the surrounding, saturated bedrock and thus unreactive. Therefore, the calculated groundwater table is a proxy for the weathered-unweathered bedrock boundary.

Rempe and Dietrich (2014) calibrated this weathering model based on field data at CB1, including measurements of channel incision rate, rock and soil bulk density (Anderson et al., 2002), soil diffusivity, critical slope (Roering et al., 1999), and hillslope length. From these parameters, they estimate a ratio of hydraulic conductivity to porosity, K/θ [m/s], to measure the ratio of subsurface flow capacity to storage capacity. Subsequently, they calculate fluvial relief of the

surface of unweathered bedrock, Z_b [m], and topographic fluvial relief, Z_s [m], along a two-dimensional section starting from the CB1 borehole and ending at the channel head of the CB1 hollow. The ratio of fluvial bedrock relief, Z_{b0} [m], to fluvial surface relief, Z_{s0} [m], specifically at the CB1 ridgeline was estimated to be 0.83 (Rempe and Dietrich, 2014). Here, we expand this theory to estimate three-dimensional CZ structure across the benchmark site.

We follow Rempe and Dietrich (2014) to create two CZ models based on a calibration with different weathered boundaries in the CB1 borehole. To do this, we first calculate channel networks in a LiDAR DEM (larger extent than Section 4.3.1.1 to capture surrounding streams) using a drainage area incision threshold of 1500 m^2 with the MATLAB toolbox TopoToolbox (Schwanghart and Scherler, 2014). This threshold places the head of the CB1 channel near the bottom of the mapped landslide, similar to mapped channels (Montgomery et al., 2000). Then, we calculate a map of Z_s as the topographic relief of any grid cell and the channel cell into which water from that particular cell will flow. We explore a simple case to calculate Z_b from Z_s by assuming that constant ratios of Z_{b0}/Z_{s0} at the CB1 borehole are (1) equivalent to Z_b/Z_s and (2) hold across the entire benchmark site. We assume two rounded values for Z_b/Z_s: 0.9 and 0.8. These ratios are calibrated to match the 4.5 m-deep boundary between pervasively oxidized and fractured bedrock and the 9 m-deep boundary between fractured and unweathered bedrock in the CB1 borehole (Figure 4.1c). The 9 m-deep boundary is equivalent to the depth to unweathered bedrock modeled by Rempe and Dietrich (2014). We multiply the map of Z_s by our Z_b/Z_s ratios to obtain two maps of estimated Z_b. Lastly, we subtract Z_b from Z_s to calculate the modeled thickness of weathered bedrock and smooth this map with a moving circular radius of 5 m. Thus, we output two maps of depth to unweathered bedrock for estimating deep CZ weathered structures across the benchmark.

This simplified approach to the bedrock drainage model assumes a constant Z_{b0}/Z_{s0} for every ridgeline, which is not correct when considering that Z_b/Z_s varies with hillslope length. We examine the distribution of hillslope length throughout the benchmark site and refer readers to CZ models that utilize fuller considerations of formulations in Rempe & Dietrich (2014; Higa et al., in prep; Text B3).

4.3.1.3 Weathered bedrock model: topographic stress

We model the variation of weathered bedrock thickness based on three-dimensional subsurface stress field calculations following the approach described in St. Clair et al. (2015) and Moon et al. (2017). These studies examine the topographic stress field, which is calculated as the combination of ambient tectonic compression, gravitational loading, and topographic perturbations on geologic stress fields assuming simple material properties (e.g., linear elastic and homogenous rock). Several studies have shown that topographic stress can vary depending on location and likely influences the subsurface extent of open fractures (e.g., McTigue and Mei, 1981; Miller and Dunne, 1996; Molnar, 2004; Moon et al., 2017; Moon et al., 2020; Savage et al., 1985; Savage and Swolfs, 1986; St. Clair et al., 2015). Comparisons between topographic stress predictions and near-surface seismic refraction tomography at the benchmark site show the potential for bedrock weathering to be influenced by least compressive principal stresses (LCS) in the topographic stress field (e.g., Higa et al., in prep). However, the correspondence is not as strong as in other studies (St. Clair et al., 2015). Nonetheless, we use topographic stress as a weathering mechanism to illustrate an endmember CZ model with deep and variable weathered bedrock.

We calibrate a topographic stress model for the benchmark site using stress magnitude measurements from the World Stress Map 2016 (Heidbach et al., 2018) and previous work (Brown and Hoek, 1978; Lindner and Halpern, 1978). To do this, we estimate ambient tectonic stresses

and depth gradients using in situ stress measurements from across the west coast of the United States and Canada. This compilation has 14 data points, from which we can use a linear least squares regression to determine a best-fit tectonic stress magnitude and depth gradient for maximum horizontal, minimum horizontal, and vertical stresses (Higa et al., in prep; Text B4; Table B6). These approximations provide the ambient tectonic stress field component of topographic stress.

Next, we transform the 2 m-resolution LiDAR DEM (Section 4.3.1.1) to model the topographic stress field with the ambient tectonic conditions above following Moon et al. (2017). We convert the DEM into a triangular mesh with leg lengths of ~5 m that increase to ~50 m outside the benchmark to reduce computational time. Then, we calculate topographic stresses within an observation grid encompassing the benchmark site. This grid has a horizontal resolution of 5 m x 5 m and a vertical resolution of 3 m (64 elements in the E-W direction, 64 elements N-S, and 99 elements vertically, extending ~100 m beneath the lowest point in the benchmark site).

Lastly, we simulate the topographic stress field under the benchmark site assuming linear-elastic, homogenous, and isotropic material using the boundary element model Poly3D (Thomas, 1993). We used inputs of the constrained ambient tectonic conditions, topographic mesh, and observation grids to obtain a total stress field. From these total stresses, we index the LCS magnitude 9 m-deep in the CB1 borehole and use this value as a threshold for fracture openness, assuming LCS represents bedrock fracturing across the entire site. Thus, we create an isosurface where LCS equals that threshold value as a spatially variable map of depth to unweathered bedrock. We mask this depth to unweathered bedrock within 5 m of the surface to avoid artifacts induced by the topographic mesh by setting depths < 5 m to a shallow value of 0.02 m. Then, we resample the maps of depth to unweathered bedrock from 5 m- to 2 m-resolution and smooth the maps using

a moving circular window of radius 5 m. Finally, we output a map of depth to unweathered bedrock across the benchmark based on topographic stress.

4.3.1.4 Five critical zone structures from weathering models and field data

In total, we create five main critical zone structures to constrain theoretical yet realistic hydrology and shallow landslide responses at the benchmark site (Table C1). CZ(soil, lowK) has modeled soil thickness directly above practically impermeable unweathered bedrock with low hydraulic conductivity. This assumption is similar to previous landslide models at this benchmark (e.g., Milledge et al., 2014). CZ(soil) also has modeled soil thickness above unweathered bedrock. However, unweathered bedrock is five orders of magnitude more permeable than CZ(soil, lowK), similar to that used in previous hydrologic models. CZ(RD4m) has modeled soil thickness, weathered bedrock based on Rempe and Dietrich (2014) using a constant Z_b/Z_s of 0.9, and unweathered bedrock at the bottom. CZ(RD9m) is similar to CZ(RD4m), using a constant Z_b/Z_s of 0.8. Then, CZ(stress) has modeled soil thickness, weathered bedrock based on topographic stress, and unweathered bedrock at the bottom.

In addition, we perform sensitivity tests to examine the to examine how our slope stability calculations of shallow landslides vary depending on soil thickness and root cohesion. We take CZ(RD4m) as a base model and apply a constant soil thickness of one meter across the catchment, hereafter CZ($RD4m_{soil}$; Figure C1). We also recalculate root cohesion based on two reexaminations of root strength that use more complex stress redistribution models at our site (Text C3; Figure C2; Cronkite-Ratcliff et al., 2022).

4.3.2 Hydrologic model, parameterization, rainfall conditions, and output

We use the hydrologic model GEOtop 2.0 (Endrizzi et al., 2014) to simulate variably saturated water fluxes through CZ structures. This model uses a three-dimensional finite volume

approach to predict surface and subsurface flow accounting for the lag time between overland and subsurface flow coupling (Panday and Huyakorn, 2004). GEOtop 2.0 calculates unsaturated and saturated flow by solving three-dimensional Richards equations (Richards, 1931), using the van Genuchten soil water retention curves (SWRC; Van Genuchten, 1980) and the Mualem soil water conductivity function (SWCF; Mualem, 1976). Thus, we calculate saturated and unsaturated subsurface flow through layered CZs with water content and hydraulic conductivity that varies with matric potential (Endrizzi et al., 2014). The model also calculates overland flow by extending the validity of Darcy's Law to surface flow (Gottardi and Venutelli, 1993) and by channel routing using the shallow water equation neglecting inertia (Endrizzi et al., 2014)**.** GEOtop 2.0 has been utilized to calculate soil pressure head at multiple layers, infinite-slope factor of safety, and landslide occurrences (e.g., Formetta and Capparelli, 2019; Formetta et al., 2016; Tufano et al., 2021).

To apply GEOtop 2.0, we divide the site into 9,696 CZ column types with specific soil SWRC and SWCF that describe the soil and weathered and unweathered bedrock column at every cell in the model area with a horizontal resolution of 2 m. We discretize the CZ column into cells totaling 40 m-deep, where the vertical resolution of cells increases with depth from 0.05 m to 0.5 m to decrease computational time (Table C2). Next, we allow flow out of the model domain through the CZ and impose an impermeable boundary condition below 40 m-deep. We also test a case of a permeable boundary condition from the surface to 24 m-deep. We then impose realistic hydrologic parameters for residual and saturated water content, field capacity, *a* and *n* parameters for soil water retention curves, specific storativity, and field averaged porosity and hydraulic conductivity to each geologic layer in a CZ column type (Table C3; Anderson et al., 2002; Ebel et al., 2007a; Ebel et al., 2007b; Endrizzi et al., 2014; Torres et al., 1998).

Then, we input the natural rainfall record of the CB1 storm from 00:00 1 November 1996 to 20:00 18 November 1996, recorded at ten-minute intervals using a National Oceanic and Atmospheric Administration and National Weather Service network rain gauge at the Southwest Oregon Regional Airport ~12 km from the benchmark site (Figure 4.2a). We obtain daily-averaged rainfall intensities by averaging the rainfall from 24 hours before any point in the record. We do this averaging to compare our landslide modeling results with the historically mapped landslides, which may not have occurred during the CB1 storm but have corresponding daily-averaged rainfall intensities that might correlate to antecedent conditions similar to that which we model during this specific storm. We then use a three-month warm-up period for the model following previous studies (e.g., Ebel et al., 2007b) and an integration time of five minutes to simulate the temporal evolution of hydrology at the benchmark site. We input our CZ column types, hydrologic parameters, rainfall records, integration times, and boundary conditions into GEOtop 2.0 to output maps of h/z (Section 4.2) and three-dimensional components of hydraulic gradient at specific times of interest for landslide modeling (Section 4.3.3.3) indexed from the soil-bedrock boundary (Section 4.3.1.4).

4.3.3 Slope stability model and landslide analyses

4.3.3.1 Model description

We adopt a multidimensional slope stability model coupled with a spectral search algorithm to predict shallow landslide occurrence, size, and location by testing the stability of clusters of grid cells (Bellugi et al., 2015a; Bellugi et al., 2015b; Milledge et al., 2014). This model represents the landscape as a graph with vertices corresponding to soil columns and edges to the forces that can develop between them. Using a spectral graph-theoretical approach, similar to that proposed by Shi and Malik (2000) in the context of image segmentation, the algorithm partitions

the landscape graph by minimizing an objective function, in this case the ratio of all the resistances acting on a cluster of cells and the total driving force contributed by those cells. This method produces a set of testable clusters of soil columns that may or may not fail as a shallow landslide. Predicted landslides are assumed to mobilize all soil in a cell, thus extending to the soil-bedrock boundary.

To define the forces and resistances acting on each cell and to test the stability of each cluster produced by the search algorithm, we modify a Mohr-Coulomb limit-equilibrium slope stability model that calculates the factor of safety as the ratio of driving to resisting forces on entire soil clusters (Milledge et al., 2014). This model assumes a rigid block failure on a plane parallel to the ground surface at the soil-bedrock interface. Using these assumptions, the model performs a force balance considering gravitationally induced driving forces, resistive forces resulting from friction and root cohesion, as well as active, passive, and at-rest earth pressures acting on the boundaries of a landslide. Specifically, it calculates (1) resisting lateral forces R_l, (2) resisting forces on downslope faces R_d, (3) net driving forces on upslope faces R_u, (4) basal shear resisting forces R_b, and (5) basal driving forces F_b.

Here, we modify the basal resisting and driving force calculations of Milledge et al. (2014) to include the effects of groundwater seepage between bedrock and soil, assuming these effects are negligible on the lateral, upslope, and downslope faces. We adopt the formulation of Iverson and Major (1986) and calculate the magnitude of the basal seepage vector, i_{mag} [m/m], as

$$i_{mag} = \sqrt{{i_x}^2 + {i_y}^2 + {i_z}^2}, \tag{4.1}$$

where the components of hydraulic gradient in the x, y, and z directions are i_x, i_y, and i_z [m/m], respectively, which are output from GEOtop 2.0 (Section 4.3.2).

Next, we calculate the angular orientation λ [deg.] of the seepage vector (Figure 4.2b). λ is measured in the downslope direction relative to the outward-directed ground surface-normal vector (Iverson and Major, 1986). We solve for λ using the dot product of the slope normal vector and the seepage vector. A λ value of 0° – 90° indicates exfiltrating groundwater flow and that of 90° – 180° indicates infiltrating groundwater flow, both oriented downslope.

Then, we calculate a modified form of the slope-parallel basal driving force F_b [N] that considers seepage forces as

$$F_b = LWg[sin(\theta)(\rho_s z - \rho_w h) + \rho_w i_{mag} h sin(\lambda)], \quad (4.2).$$

Where plan view cell length is L [m], plan view cell width is W [m], g is gravitational acceleration [m/s^2], topographic slope is θ [deg.], soil density is ρ_s [kg/m^3] vertical soil thickness is z [m], and water density is ρ_w [kg/m^3]. Similarly, we calculate the basal resisting force R_b [N] considering seepage forces as

$$R_b = LWg[cos(\theta)(\rho_s z - \rho_w h) - \rho_w i_{mag} h cos(\lambda)]tan(\phi) + C_b LW, \quad (4.3)$$

where ϕ [deg.] is the soil friction angle and C_b [Pa] is the basal root cohesion.

The factor of safety FoS [N/N] of an entire soil cluster is the sum of all resisting forces from all cells divided by the sum of all driving forces from all cells, defined as (Bellugi et al., 2015a; Bellugi et al., 2015b; Milledge et al., 2014)

$$FoS = \frac{\sum_{all} R_b + \sum_{lateral} R_l + \sum_{down} R_d - \sum_{up} R_u}{\sum_{all} F_b}, \quad (4.4).$$

FoS includes lateral, downslope, and upslope resisting and driving forces at the edges of a cell cluster. Refer to Milledge et al. (2014) for derivations of R_l, R_d, and R_u.

We also calculate cell-by-cell *FoS* considering basal forces of each cell assuming an infinite-slope approximation at the benchmark site (Bellugi et al., 2015a; Bellugi et al., 2015b). To examine the effect of variable groundwater seepage forces, we compare differences of *FoS* with and without the consideration of groundwater seepage forces (i.e., i_{mag} and λ; Text C2). We subtract infinite-slope *FoS* with seepage minus that without seepage to obtain a difference map, where negative and positive values indicate locations where seepage decreases and increase *FoS*, respectively.

4.3.3.2 Model parameterization and application

We apply the spectral clustering landslide model over the spatial domain of the benchmark site during specific times of interest. We consider four different times, 17 November 1996 20:00 and 18 November 1996 06:00, 18:00, and 20:00 when the daily-averaged rainfall intensities were 1.01, 2.37, 5.00, and 5.86 mm/hr, respectively (Figure 4.2a). 1.01 mm/hr represents an intensity at which we do not expect landslides to occur. 2.37 and 5.00 mm/hr represent intensities during which researchers observed landslides at the benchmark site in 1992 and 1987, respectively (Montgomery et al., 2000). 5.86 mm/hr is the daily-averaged rainfall intensity for the CB1 landslide. We output maps of *h/z*, i_{mag}, and λ from GEOtop 2.0 at these times as the hydrologic inputs of our landslide model.

We use modeled soil thickness (Section 4.3.1.1), root cohesion (Text C3), and soil properties as our geologic inputs. The LiDAR DEM of the benchmark site is then the spatial

domain of our landslide model. We set model parameters as $L = W = b = 2$ m, $\rho_s = 1400$ kg/m^3, $\rho_w = 1000$ kg/m^3, $g = 9.81$ m/s^2, $\phi = 40°$ following Bellugi et al. (2015a; 2015b), which are calibrated to the benchmark site (Heimsath et al., 2001; Montgomery et al., 2009; Roering et al., 1999). Here, we follow Milledge et al. (2014) and Bellugi et al. (2015a, 2015b) to calculate C_b using previously established root cohesion from CB1 (Schmidt et al., 2001). We also test different values of C_b on root strength based on recent studies and presented in Appendix C (Text C3; Figure C2; Cronkite-Ratcliff et al., 2022).

This landslide model then outputs maps of all overlapping soil clusters predicted to be unstable (i.e., $FoS < 1$; Figure 4.2c). Overlapping clusters are mutually exclusive in the real world and overestimate realistic numbers of discrete landslides. Thus, we interpret these maps as the density of where landslides are concentrated or landslide footprints of total unstable areas. We also record the total number of overlapping unstable cell clusters and the total area predicted as a landslide footprint at our specific times of interest to compare these outputs with a consideration of infinite-slope FoS (Text C2).

For each discrete, overlapping, and unstable cell cluster, we calculate landslide size as the area of each cell cluster and topographic position as topographic index, which is defined in Dietrich et al. (1992) as

$$Topographic\ index = log_{10}(\frac{A}{bsin(\theta)}), \quad (4.5)$$

where the upstream contributing drainage area to a cell is A [m^2] and cell size is b [m]. We present the median topographic index considering each cell in an unstable cluster. Low index values indicate landslides in steep, nonconvergent areas. High index values indicate those farther down

the valley axis where drainage area is larger and slope is gentler (Bellugi et al., 2015b). As each model may predict a large number of unstable cell clusters, we analyze the frequency distribution of landslide area and topographic index to examine how landslide size and location evolve over a rainstorm.

4.4 Results

4.4.1 Modeled critical zone structures

Modeled soil thickness varies from 0 – 3 m-deep (Figure 4.3) with a mean of ~0.6 m (Table C1). The thickest soils tend to be in topographic hollows, mainly at the heads of mapped channels, mostly around 2 m-deep. We also show some thick soils branching from mapped channels where the topography is slightly convergent (e.g., northwest Figure 4.3a). At the CB1 landslide, the modeled soil thickness is > two meters, where the corresponding scar was mapped (Figure 4.3i). Then, soil thickness decreases away from the CB1 scar upslope and downslope. All five CZ models use this spatial distribution of soil thickness. CZ(soil, lowK) and CZ(soil) are the thinnest CZ with only this soil on top of unweathered bedrock.

Modeled weathered bedrock in deep CZ structures show large spatial variations and different magnitudes of thickness depending on the model scenario (Figure 4.3; Table C1). CZ(RD4m) has a layer of weathered bedrock that increases in thickness away from channels, up to ~9 m-deep at ridges. CZ(RD9m) has a similar pattern to CZ(RD4m) because both are based on the Z_b/Z_s ratio. However, weathered bedrock in CZ(RD9m) is approximately double the thickness of CZ(RD4m), up to 18 m-deep at ridges. Using calibrated stresses and stress gradients, CZ(stress) has the thickest weathered bedrock layer, up to 40 m-deep at ridges (Figure 4.3; Text B4; Table B6). However, CZ(stress) also has the widest range of depths to unweathered bedrock, with bedrock at the surface at channels (i.e., 0 m-deep), deepening towards ridges. This model produces

spatial variations of bedrock structure associated with three-dimensional topography, such as the shallowing of unweathered bedrock around where the CB1 scar was mapped (Figure 4.3l).

4.4.2 Modeled three-dimensional transient hydrology

We present ranges of *h/z*, i_{mag}, and λ for all CZ models at the time of the CB1 landslide in Figure 4.4 and other timesteps in Figures C3 – C7 (Table C4). i_{mag}, and λ have values where $h/z > 0$. In all CZ models at all timesteps, *h/z* spans the full range of 0 – 1 (Figure 4.4a - e; Figure C4 – C7). However, the extent of soil saturation where $h/z > 0$ varies significantly depending on the CZ model at the time of the CB1 landslide when rainfall intensity is the highest. Thinner and less permeable CZ models (i.e., CZ(soil, lowK), CZ(soil), and CZ(RD4m)) tend to be more saturated than thicker CZ models with more weathered and permeable bedrock (i.e., CZ(RD9m) and CZ(stress)). At the time of the CB1 landslide, the 95% confidence interval of i_{mag} is mostly between 0.4 – 1.1 (Figure C3a – e) for all CZ models and most λ indicate downslope and exfiltrating seepage vectors, with 95% confidence interval ranges between 50° – 85° (Figure 4.4f – o; Figure C3f – j; Table C4).

4.4.3 Modeled shallow landslides

We find varying patterns of landslide occurrence, size, and location depending on CZ models due to variations in soil saturation and seepage forces. At all timesteps, we first find that when we include variable seepage forces, *FoS* based on cell-by-cell infinite-slope stability including variable seepage forces (defined in Text C2) decreases for all CZ models, particularly centered at channels (Figure 4.5a – e; Figure C4 – C7). At the time of the CB1 landslide, approximately 53% of the CZ(soil, lowK) model experiences a reduction in *FoS* after considering variable seepage, ~40 percentage points more than the CZ(stress) model with the lowest areal reduction (Table C5). Examining overlapping unstable cell clusters, we show a decrease in the

coverage of landslide footprints from thin to thick CZ models at most timesteps (Figure 4.5f – j; Figure 4.6a – b; Table C5). In addition, CZ(soil, lowK), CZ(soil), CZ(RD4m), and CZ(RD9m) have more cell clusters deemed unstable than CZ(stress) at most timesteps (Figure 4.6c – d). Exceptions to these trends occur early in the CB1 storm when CZ(RD4m) has a higher coverage than CZ(soil) and CZ(stress) has more unstable clusters than all but CZ(soil, lowK).

Second, predicted landslides in CZ(soil, lowK) and CZ(soil) have a wider range of sizes than most models with thicker weathered bedrock (Table C6). The distributions of sizes early in the CB1 storm are similar for all models (Figure 4.7a – e). However, these distributions diverge later in the storm sequence when CZ(soil, lowK) has landslides > 1500 m^2 while CZ(stress) only has landslides < 1000 m^2 at the time of the CB1 landslide. This pattern corresponds to a general decrease in the range of 95% confidence intervals of landslide size at the time of the CB1 landslide, from 4.0 – 364.0 m^2 to 12.0 – 260.0 m^2 for CZ(soil, lowK) and CZ(stress), respectively. We compare these ranges to that of the CB1 scar of ~58 m^2 (Montgomery et al., 2009).

Lastly, examining daily-averaged rainfall intensities of 2.37, 5.00, and 5.86 mm/hr, the cumulative distribution functions (CDF) of median topographic indices show measurable differences in the location of predicted landslides depending on CZ model (Figure 4.7f – j). At the time of the CB1 landslide, when the daily-averaged intensity is 5.86 mm/hr, most CDFs are to the right of that from mapped landslides. However, CZ(stress) at this time has more landslides with median topographic indices < 2 $\log_{10}$([m]), with its corresponding CDF more centered at that of mapped landslides (Figure 4.7j).

4.5 Discussion

4.5.1 Permeable bedrock in the critical zone modulates groundwater seepage and landslide occurrence, size, and location

We find that the spatial extent of saturated soil and the number of potential landslides differ depending on permeable CZ structures. It is likely that thinner CZs, with limited amounts of weathered bedrock, can produce more saturated seepage flow through the soil layer that is connected throughout the hillslope (Figure 4.4). Such increased soil saturation and pore pressure for CZ(soil, lowK) may be responsible for the highest percentage of area where seepage vectors reduce *FoS* (Figure 4.5a; Table C5). Reduction of infinite-slope *FoS* due to seepage likely highlights the role of weathered bedrock-induced exfiltration on increasing the unstable area (Figure 4.6a – b) and number of overlapping landslide occurrences (Figure 4.6c – d) for CZ(soil, lowK) out of all five CZ models (Formetta et al., in prep).

Conversely, thicker weathered bedrock in the CZ(stress) model allows groundwater to infiltrate into the deep CZ, funneling water away from soil and decreasing landslide occurrences. CZ(stress) also has a shallowing of depth to unweathered bedrock localized at channels. This configuration likely localizes exfiltrating seepage (Figure 4.4o), decreases *FoS* (Figure 4.5e), and increases landslide occurrence (Figure 4.5j) at convergent topography. Therefore, both the greater groundwater storage in hillslopes and focusing of destabilizing seepage vectors near channels may have led to landslide predictions to be concentrated at channels for CZ(stress). However, at a daily-averaged rainfall intensity of 1.01 mm/hr, CZ(stress) has more unstable cell clusters than most other models (Figure 4.6c – d). This may be due to seepage vectors that are concentrated at channels and destabilize many small landslides. Regardless, at higher rainfall intensities, the

thinner CZ models surpass CZ(stress) in number of unstable cell clusters, likely due to the greater extent of saturated soils.

Our simulations indicate that landslide size generally increases with increasing rainfall intensity. This result is consistent with previous work that showed small, highly susceptible landslides can be triggered early in storms before peak rainfall and that large landslides can only be activated when a catchment is most saturated (Bellugi et al., 2015b). Large standard deviations of mean landslide size, comparable in order of magnitude to said mean, may be attributed to heavy tails of landslide size distribution with a few exceptionally large (>1000 m^2) predicted landslides (Figure 4.7a – e; Table C6). Such large landslides likely include upper portions of the hillslope with high resisting forces (the result of thin soil and strong root cohesion) that require a high driving force only fulfilled by mobilizing a larger and heavier landslide during peak saturation. This mechanism is likely why landslide size increases with increasing rainfall intensity in the more saturated CZ(soil, lowK), CZ(soil), and CZ(RD) models (Figure 4.7a – d; Bellugi et al., 2015a; Bellugi et al., 2015b).

However, we find that the CZ(stress) model with less saturated soil does not exhibit as stark an increase in landslide size (Figure 4.7e). This is consistent with soil saturation patterns that are generally less saturated, but also localized and concentrated where the weathered bedrock shallows near channels in CZ(stress). Interestingly, the range of landslide sizes predicted from this scenario is most similar in range observed from the seven landslides mapped in the benchmark site from 1987 – 1996 (Figure 4.7e; Montgomery et al., 2000).

CDFs of median topographic indices suggest measurable differences in landslide position depending on rainfall intensity and CZ model (Figure 4.7f – j). Nonetheless, our modeled landslides at the time of the CB1 landslide have similar distributions of topographic index

compared with those mapped in the field. In particular, landslides from thicker CZs tend to have higher indices, suggesting our modeled landslides are more downstream than mapped ones. For CZ(stress), landslides shift downstream throughout the entire CB1 storm that we model (Figure 4.7j). Similarly, Bellugi et al. (2015b) found a downslope shift of landslides that was attributed to higher h/z in channels, which could mobilize thinner soils on gentler channel slopes only when rainfall intensities were relatively high. We suggest that this phenomenon is relevant for CZ(stress).

At low daily-averaged rainfall intensities, CDFs of median topographic indices are often shifted to values smaller than those mapped. This effect is potentially due to bias from the small number of landslides that we predict when the catchment is still relatively dry. Landslides at this time are likely the most susceptible cell clusters that can be unstable when saturation is low. Thus, our modeled landslides at this time may be farther uphill from channels, where slopes are steeper and driving forces are higher, compared to the location of mapped landslides. However, CZ(soil, lowK) has an order of magnitude more unstable clusters than other CZ models (Figure 4.6c – d), which is likely due to high h/z at channels early in the CB1 storm. This effect may cause the opposite trend here, with landslides of higher topographic indices than those mapped (Figure 4.7f).

4.5.2 Soil thickness and weathered bedrock may jointly control shallow landslide characteristics

Our results suggest that understanding the spatial extent and variations of deep CZ weathered structures is important for predicting the occurrence, size, and location of shallow landslides. However, our models focus on assessing the first-order impact of weathered bedrock variation on shallow landslides based on limited information and simple assumptions of soil thickness and properties (Section 4.3.1.1). First, our soil production and transport model does not include the cyclic filling and evacuation of hollows from landsliding and creep processes (Dietrich and Dunne, 1978), tree throw, or burrowing animals (Heimsath et al., 2001). Thus, these results

represent an upper bound on landslide occurrence, assuming a landscape that has no initial landslides and hollows filled with thick soil. Through this lens, we observe several landslide hotspots without corresponding mapped landslides (Figure 4.5f – j). These predicted landslides might capture those that predate historical mapping, thus occurring in areas where soils are presently thin and evacuated. Conversely, we may be predicting future landslides if the hollow has not recently failed. Together, we interpret that our landslide predictions are the likely maximum possible landslide occurrences because we consider soil thickness accumulated over 6000 years without the cyclic evacuation by landslides.

Interestingly, our sensitivity test on soil thickness with a constant thickness of one meter, CZ(RD4m$_{soil}$), shows areas of instability extending upslope on topographic noses where field observations find thin, stable soils (Figure C1; Montgomery et al., 1997). We also find that the number of unstable cell clusters and the total unstable area is higher for CZ(RD4m$_{soil}$) compared to CZ(RD4m; Figure C1e – f). Our spectral clustering algorithm may allow the overestimation of large landslides that extend up hillslopes and include soils that are thicker and more susceptible to failure than in reality. Many studies examined the effect of variable versus constant soil thickness on slope stability (e.g., Kim et al., 2015; Onda et al., 2004; Shoaei and Sidle, 2009; Uchida et al., 2011). Using an infinite-slope approach and 181 soil depth measurements, Uchida et al. (2011) concluded that a constant average soil thickness might underestimate landslides for a given rainfall intensity. Our results also agree with this previous work, suggesting that parameterization of soil thickness variation is important for accurate shallow landslide prediction.

In addition to realistic soil thickness, correct calibration of parameters like cohesion and angle of internal friction was also shown to be important for improving the accuracy of landslide prediction (Kim et al., 2015). Currently, we include a simple parameterization of root cohesion

with a constant surface value that decays exponentially with depth (e.g., Milledge et al., 2014). Other spatial variations in soil structure may affect soil stability. For example, vertical layering of different soil types and permeabilities can also affect slope stability by inducing hydrologic heterogeneities like shallow perched water tables (Shoaei and Sidle, 2009). Other properties, like the inclusion of coarse rock fragments, can also impact the spatial variation of soil saturation within the top meters of soil where shallow landslides occur (Jarecke et al., 2021). Regardless, deep CZ exfiltration can also overprint soil parameters, causing stronger soils to be more unstable than weaker soils due to spatially variable seepage from bedrock fractures (Onda et al., 2004). Altogether, future studies to examine the distribution of soil thickness, cohesion, and angle of internal friction could improve the accuracy of shallow landslide models.

4.5.3 Limitations in our modeling of bedrock weathering, subsurface hydrology, and shallow landslides

Our integrated modeling aims to simulate bulk groundwater flow and landslide predictions using theoretical CZ models without specifying fracture distributions or networks. Previous work at CB1 found that fracture flow is important for groundwater fluxes and landslide hazards (e.g., Montgomery et al., 1997). However, we currently do not have detailed information on the discrete fracture network at this site nor the modeling capability to simulate preferential flow within fractured bedrock. The three-dimensional Richards equations in GEOtop 2.0 assume unsaturated flow through porous media without discretized fractures. Instead, we simulate the spatially varying boundary of weathered and unweathered bedrock with bulk hydraulic conductivities across two to seven orders of magnitude depending on the CZ models used (Table C3). With our varying CZ scenarios, we aim to capture the bulk behavior of natural groundwater flow through fractures in

weathered bedrock that have spatial variations. Our work highlights the impact of exfiltration from weathered bedrock on overlying soil saturation and subsequent landslides.

Similarly, we do not claim that this deep weathered bedrock structure is a good approximation of the real CZ, only that its bulk behavior produces shallow landslides of similar size to those mapped (Figure 4.7e). Focusing on the CB1 landslide, other hydrologic models that simulate discharge from weirs at the bottom of the CB1 hollow reproduce measured discharge using weathered bedrock most similar to CZ(RD4m; Formetta et al., in prep; Ebel et al., 2007b). These models use DEMs and measured soil thickness at 1 m-resolution, different from the 2 m-resolution and modeled soil thickness used here. Also, our weathered bedrock layer assumes no vertical gradation of porosity or hydraulic conductivity, which is different from field observations (Anderson et al., 2002; Montgomery et al., 2002; Montgomery et al., 1997). Lastly, our comparison of mapped landslides and modeled, overlapping unstable cell clusters may examine slightly different populations, as overlapping cell clusters are possible landslide configurations, not the configuration most likely to occur. Bellugi et al. (2015a) describes workflows to prune overlapping landslides by the most unstable cell cluster or that with an *FoS* closest to but less than one. The former method highlights the most unstable cluster and the latter highlights the first cluster that becomes unstable. It is unclear which pruning method best approximates landslides that occur in nature. Thus, we present unpruned landslides representing a larger population of unstable cell clusters. Regardless, our analyses of landslides resulting from hydrology under different CZs shows the effect of spatially varying deep weathered bedrock on landslide occurrence, size, and location. We acknowledge that future work to include fracture flow based on spatial variations of

fracture networks may allow for more accurate assessments of shallow landslide occurrence, size, and location.

4.5.4 Hydrologic connectivity in the critical zone and implications for landslide timing

Our findings suggest that CZs can provide additional controls on the timing of the hydrologic response to rainfall and shallow landslide occurrences. We find that thin CZs of CZ(soil, lowK) and CZ(soil) may accelerate the hydrologic connectivity of hillslope-channel soils by limiting vertical flow and forcing water to flow slope-parallel. This process creates wet antecedent conditions relatively early in a storm and induces the lateral growth of areas with saturated and susceptible soil (Figure C4 – C7; Beiter et al., 2020; Hahm et al., 2019). However, thicker CZs with larger groundwater storage capacities may require more time to fill and saturate the surface. Studies in other locations find that thick CZs can support less drought-resistant plants due to higher groundwater storage capacities that supply consistent moisture to vegetation during dry seasons (Hahm et al., 2022; Hahm et al., 2019).

On a shorter timescale, if an individual storm remains at a high intensity for a long duration, thicker weathered bedrock may eventually fill up and saturate surface soils to the point of failure, but the timing of shallow landslides is delayed. Here, vertical groundwater flow in thick CZs may inhibit hydrologic connectivity of hillslope–channel soils until unweathered bedrock approaches the surface at channels to cause lateral flow with an upwards, exfiltrating component (Formetta et al., in prep; Onda et al., 2004). This result is similar to how researchers observed groundwater movement dominated by vertical percolation during dry periods (Detty and McGuire, 2010) and how dry antecedent conditions can delay hillslope-channel hydrologic connectivity after rainfall (Beiter et al., 2020). Therefore, efforts to image the CZ with geophysical methods may

improve the prediction of landslide timing if variable, realistic CZ structures play important roles in hydrologic connectivity, groundwater exfiltration, and landslide occurrence.

4.6 Conclusion

In this study, we test a landslide model that includes the effect of groundwater exfiltration from permeable bedrock in the CZ on slope stability in a steep, forested site. Our findings demonstrate that incorporating CZs of different shapes and depths can result in theoretical yet realistic disparities in landslide occurrence, size, and location. Shallower CZs exhibit higher predicted landslide occurrences with heavy-tailed size distributions that shift upstream, whereas deeper and variable CZs have fewer predicted landslides of smaller size distributions that converge near or downstream of mapped ones. We suggest that permeable bedrock in the CZ may modulate shallow landslide characteristics in concert with soil thickness and material properties. Groundwater seepage and exfiltration from such permeable bedrock are likely important factors for predicting the occurrence, location, size, and timing of real-world shallow landslides. Thus, our results suggest that groundwater storage capacity in weathered bedrock can control hydrologic connectivity between hillslope and channel soils that saturate and increase soil instability on steep terrain. Further investigations on deep CZ structures can enhance our prediction of landslide occurrence, size, location, and timing.

4.7 Figures

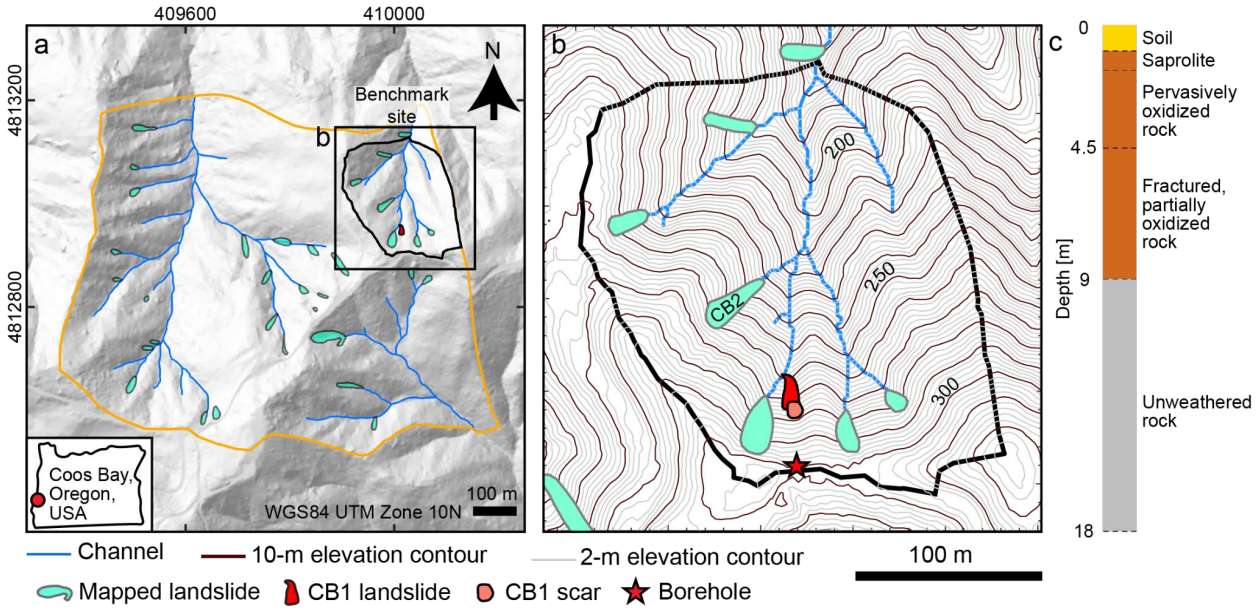

Figure 4.1. (a) Map of the benchmark (black outline) and surrounding study sites (orange outline; Bellugi et al., 2015a; Bellugi et al., 2015b) near Coos Bay, Oregon, USA. Landslides mapped between 1987 – 1996. (b) Benchmark site showing CB1 landslide and location of 35 m-deep CB1 borehole. Ten-meter contours labeled every 50 m. (c) Schematic of top 18 m from the CB1 borehole colored by three weathered layers (yellow = soil, orange = weathered bedrock, gray = unweathered bedrock) discretized in our weathering, hydrologic, and landslide models compared with weathered units from Anderson et al. (2002).

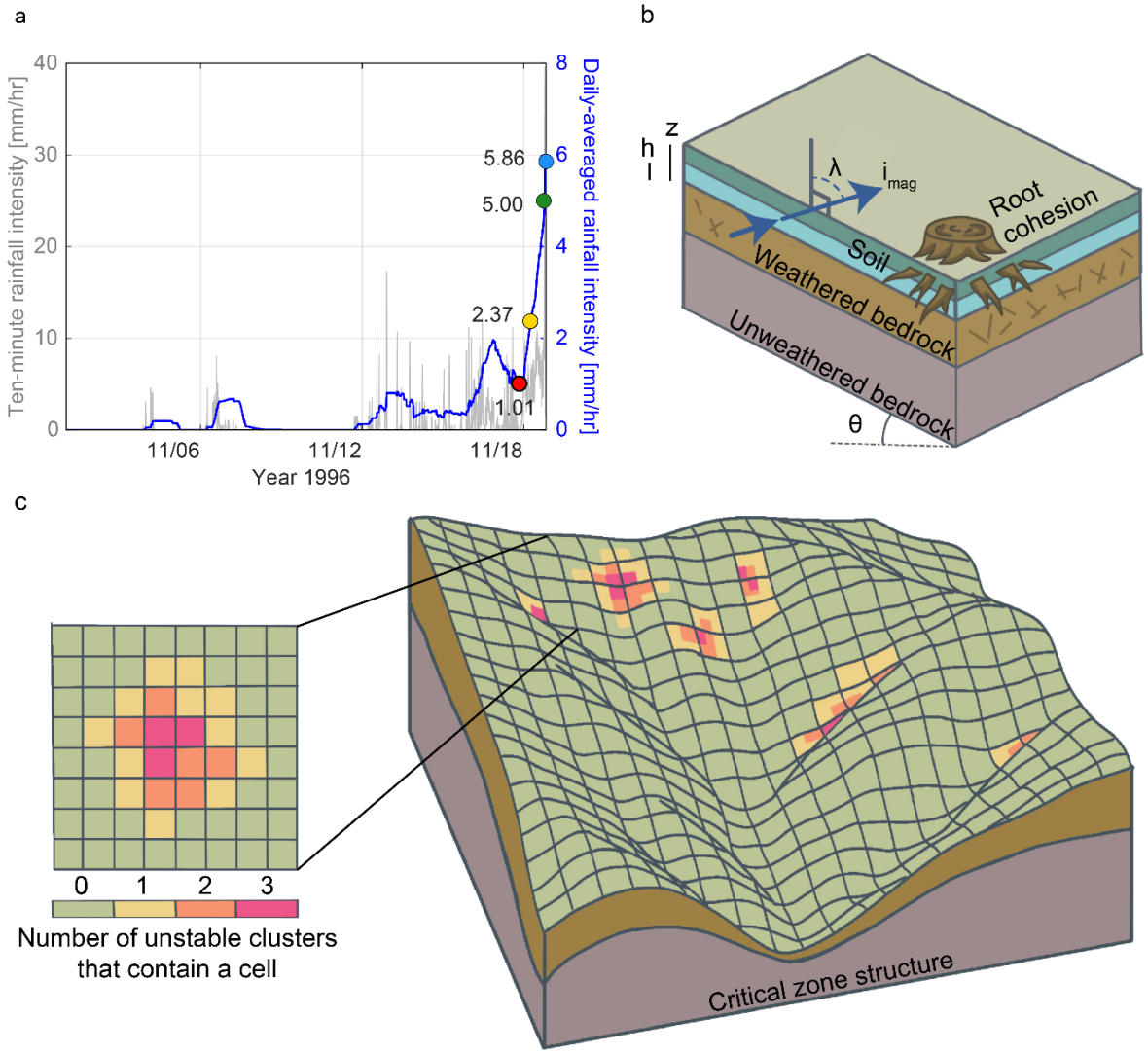

Figure 4.2. (a) Ten-minute and daily-averaged rainfall record of the CB1 storm. GEOtop output times labeled by colored point and daily-averaged rainfall intensity in mm/hr. (b) Schematic of critical zone structure and hydrologic outputs that affect slope stability in a single cell of our landslide model. h = pressure head in soil [m], z = soil thickness [m], i_{mag} = seepage magnitude [m/m], λ = seepage orientation [deg.], θ = topographic slope [deg.] (c) Schematic oblique view of benchmark site looking roughly south, discretized into cells colored by number of discrete and unstable cell clusters that include a specific cell in the landscape. Figure 4.2c modified from Bellugi et al., (2015a).

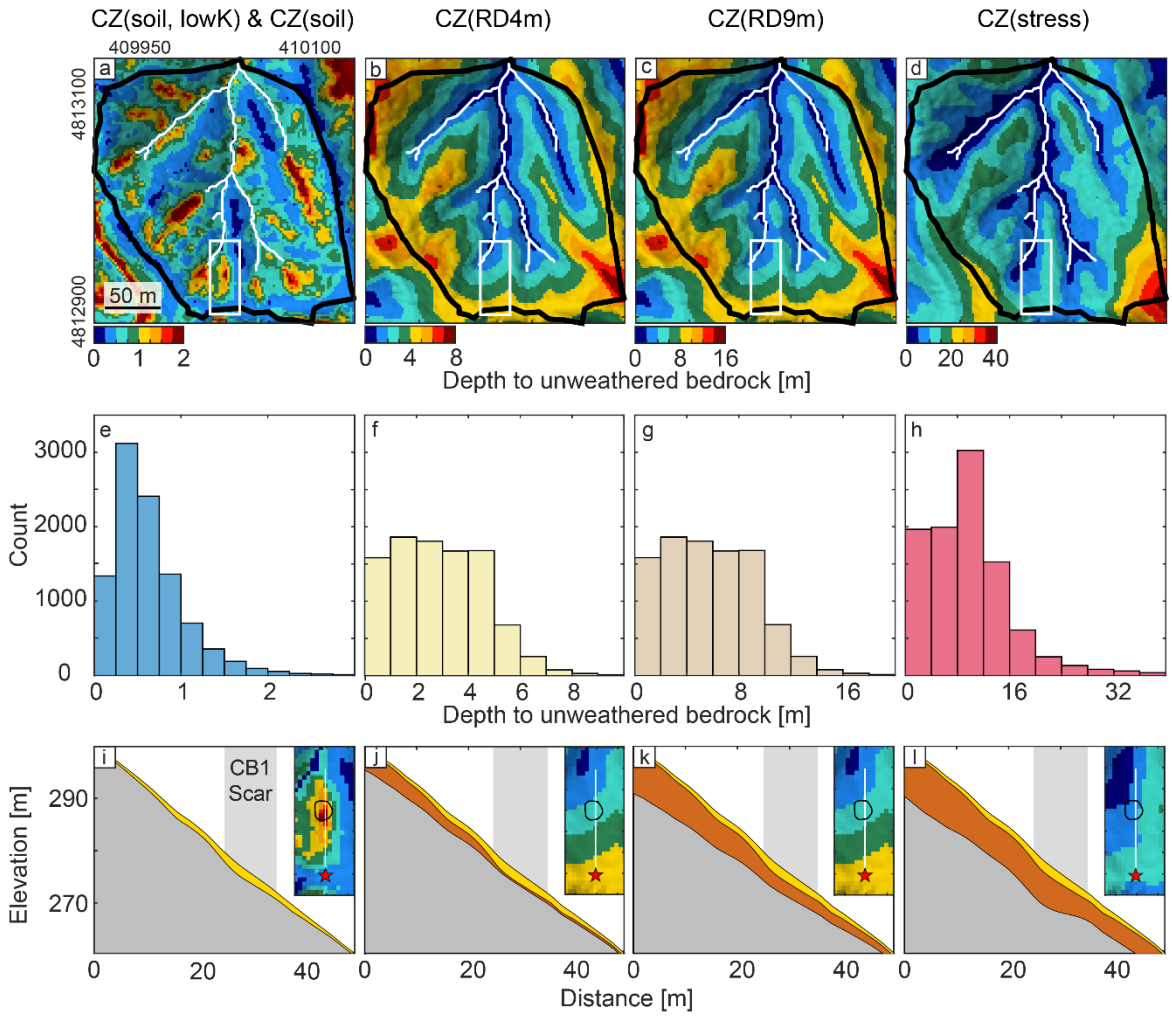

Figure 4.3. (a – d) Map of depth to unweathered bedrock for different critical zone models. White lines are channels, black polygon is benchmark site, white box is inset for (i). (e – h) Histogram of depth to unweathered bedrock by total count of cells in each depth bin. (i – l) Cross section of critical zone structure along white line in the inset, where yellow is soil, orange is weathered bedrock, and gray is unweathered bedrock. (inset) Map of depth to unweathered bedrock using the same color scale as corresponding critical zone model in (a – d). Black outline is CB1 scar, red star is 35 m-deep CB1 borehole. Projection: WGS84 UTM Zone 10N.

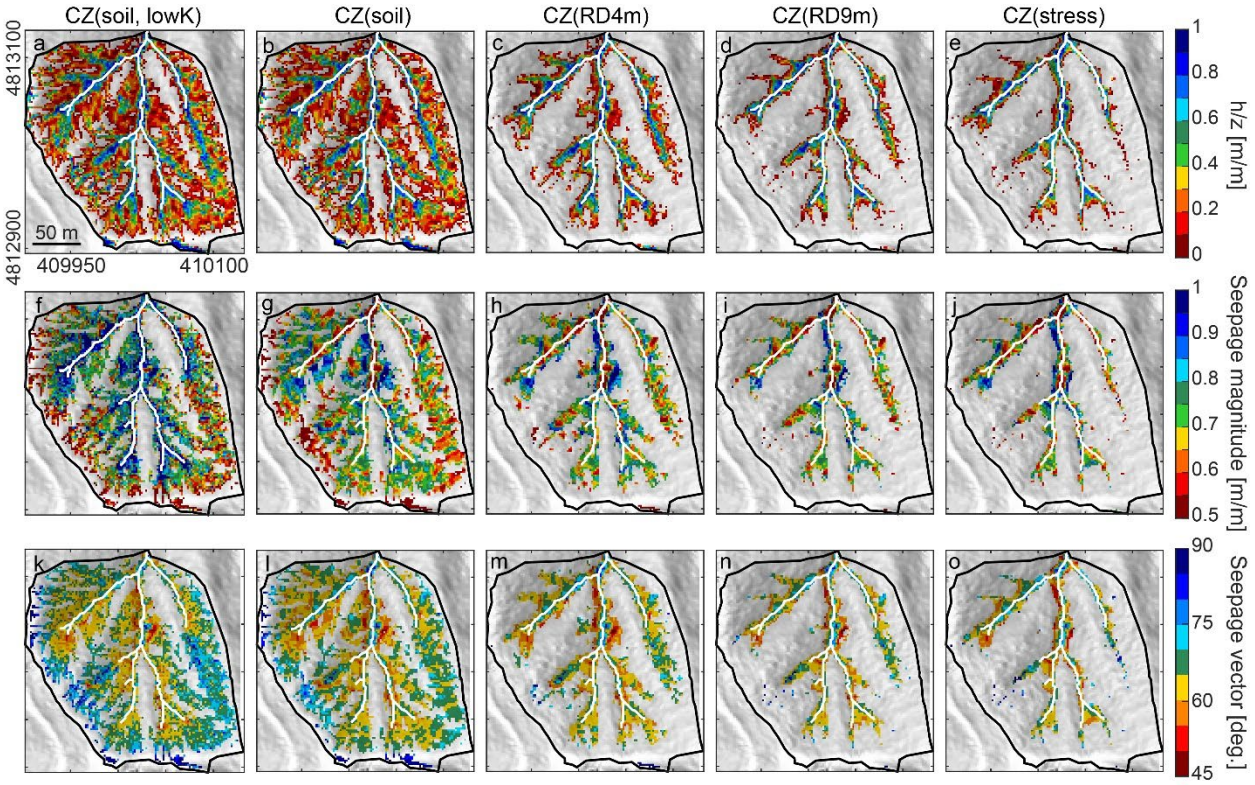

Figure 4.4. (a – e) Ratio of pressure head in soil h and soil thickness z, (f – j) seepage vector magnitude i_{mag}, and (k – o) seepage vector orientation λ for different critical zone models at the time of the CB1 landslide, 18 November 1996 20:00. Streams shown as white lines. Benchmark site outline in black. Projection: WGS84 UTM Zone 10N.

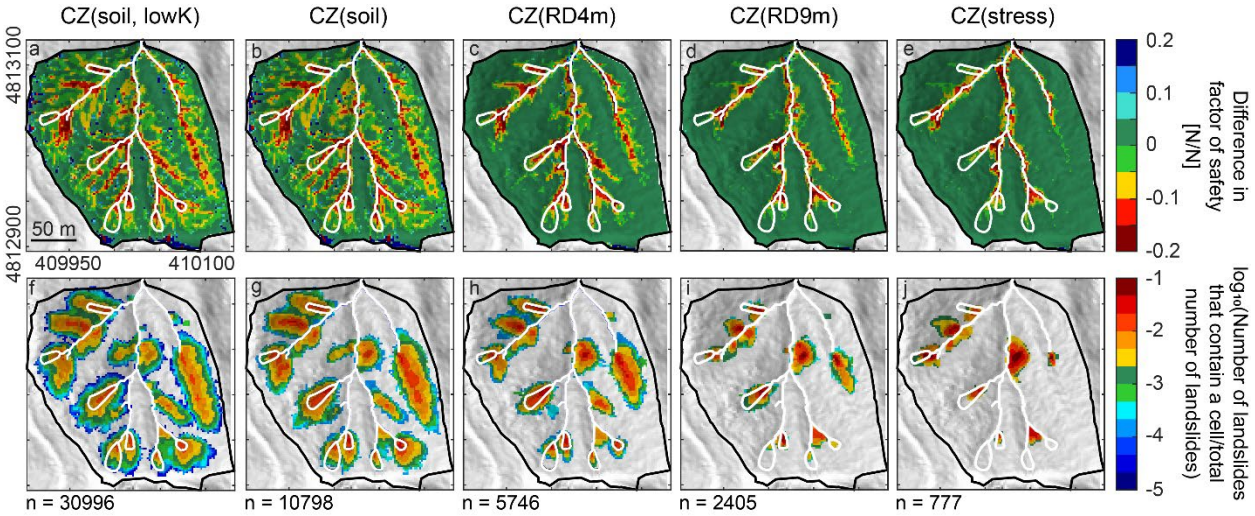

Figure 4.5. (a – e) Infinite-slope factor of safety considering variable seepage vector orientation minus that considering surface-parallel flow, and (f – j) $\log_{10}$ of the number of unstable cell clusters including a specific cell, normalized by total number of landslides *n* for different critical zone models at time of the CB1 landslide, 18 November 1996 20:00. Streams and mapped landslides shown as white lines and polygons, respectively. Benchmark site outline in black. Projection: WGS84 UTM Zone 10N.

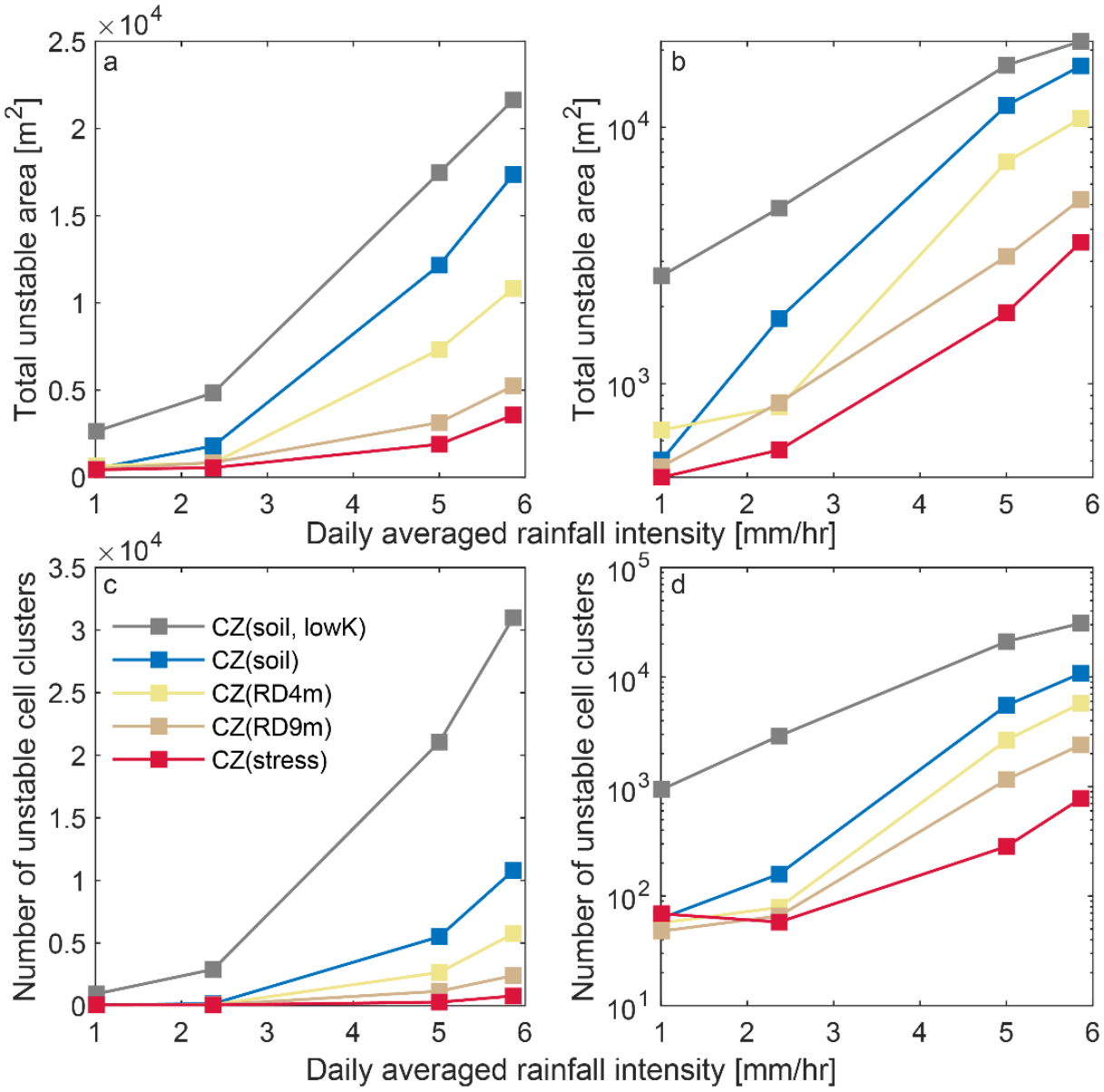

Figure 4.6. Change in the area of the benchmark site that is predicted to be unstable in at least one cell cluster versus daily-averaged rainfall intensity of the CB1 storm for different critical zone structures in (a) linear and (b) semi-log scales. Change in the total number of modeled unstable cell clusters versus daily-averaged rainfall intensity of the CB1 storm for different critical zone structures in (c) linear and (d) semi-log scales.

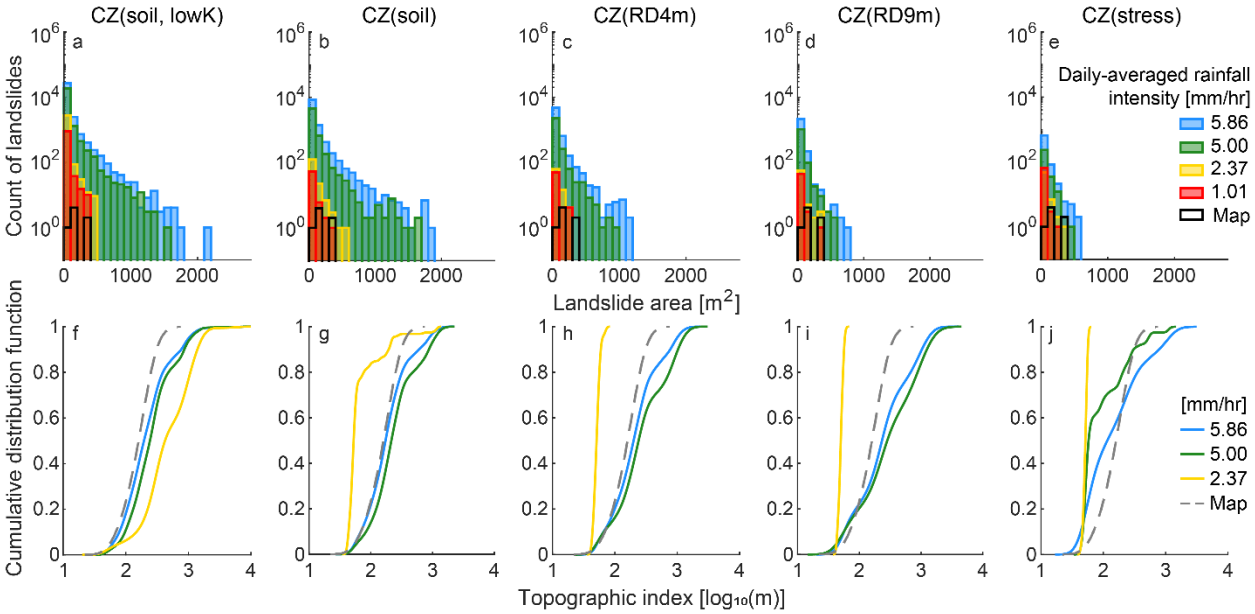

Figure 4.7. (a – e) Size distribution of unstable cell cluster by count in 100 m^2 bins at daily-averaged rainfall intensities of interest during the CB1 storm compared with distribution of mapped landslide size and (f – j) cumulative distribution functions of the median topographic index of each cell cluster through the CB1 storm for different critical zone models compared against that of mapped landslides. We do not show results for 1.01 mm/hr because the population of landslides at that time is relatively small. The CB1 landslide occurred when the daily-averaged rainfall intensity was 5.86 mm/hr.

4.8 References

Anderson, R.S., Anderson, S.P., Tucker, G.E., 2013. Rock damage and regolith transport by frost: An example of climate modulation of the geomorphology of the critical zone. Earth Surface Processes and Landforms 38, 299-316. https://doi.org/10.1002/esp.3330

Anderson, R.S., Rajaram, H., Anderson, S.P., 2019. Climate driven coevolution of weathering profiles and hillslope topography generates dramatic differences in critical zone architecture. Hydrological Processes 33, 4-19. https://doi.org/10.1002/hyp.13307

Anderson, S.P., Dietrich, W.E., Brimhall Jr, G.H., 2002. Weathering profiles, mass-balance analysis, and rates of solute loss: Linkages between weathering and erosion in a small, steep catchment. Geological Society of America Bulletin 114, 1143-1158. https://doi.org/10.1130/0016-7606(2002)114%3C1143:WPMBAA%3E2.0.CO;2

Anderson, S.P., Dietrich, W.E., Torres, R., Montgomery, D.R., Loague, K., 1997. Concentration-discharge relationships in runoff from a steep, unchanneled catchment. Water Resources Research 33, 211-225. https://doi.org/10.1029/96WR02715

Anderson, S.P., von Blanckenburg, F., White, A.F., 2007. Physical and chemical controls on the critical zone. Elements 3, 315-319. https://doi.org/10.2113/gselements.3.5.315

Baldwin, E.M., 1966. Some revisions of the geology of the Coos Bay area, Oregon. The Ore Bin 28, 189-203.

Bear, J., 1988. Dynamics of fluids in porous media, Dover, New York.

Beiter, D., Weiler, M., Blume, T., 2020. Characterising hillslope–stream connectivity with a joint event analysis of stream and groundwater levels. Hydrology and Earth System Sciences 24, 5713-5744. https://doi.org/10.5194/hess-24-5713-2020

Bellugi, D., 2012. What controls shallow landslide size across landscapes? University of California, Berkeley.

Bellugi, D., Milledge, D.G., Dietrich, W.E., McKean, J.A., Perron, J.T., Sudderth, E.B., Kazian, B., 2015a. A spectral clustering search algorithm for predicting shallow landslide size and location. Journal of Geophysical Research: Earth Surface 120, 300-324. https://doi.org/10.1002/2014JF003137

Bellugi, D., Milledge, D.G., Dietrich, W.E., Perron, J.T., McKean, J., 2015b. Predicting shallow landslide size and location across a natural landscape: Application of a spectral clustering search algorithm. Journal of Geophysical Research: Earth Surface 120, 2552-2585. https://doi.org/10.1002/2015JF003520

Bellugi, D.G., Milledge, D.G., Cuffey, K.M., Dietrich, W.E., Larsen, L.G., 2021. Controls on the size distributions of shallow landslides. Proceedings of the National Academy of Sciences 118, e2021855118. https://doi.org/10.1073/pnas.2021855118

Borja, R.I., White, J.A., 2010. Continuum deformation and stability analyses of a steep hillside slope under rainfall infiltration. Acta Geotechnica 5, 1-14. https://doi.org/10.1007/s11440-009-0108-1

Brantley, S.L., Goldhaber, M.B., Ragnarsdottir, K.V., 2007. Crossing disciplines and scales to understand the critical zone. Elements 3, 307-314. https://doi.org/10.2113/gselements.3.5.307

Brown, E.T., Hoek, E., 1978. Trends in relationships between measured in-situ stresses and depth, International Journal of Rock Mechanics and Mining Sciences & Geomechanics Abstracts. Pergamon, pp. 211-215.

Callahan, R.P., Riebe, C.S., Pasquet, S., Ferrier, K.L., Grana, D., Sklar, L.S., Taylor, N.J., Flinchum, B.A., Hayes, J.L., Carr, B.J., 2020. Subsurface weathering revealed in hillslope-integrated porosity distributions. Geophysical Research Letters 47, e2020GL088322. https://doi.org/10.1029/2020GL088322

Chu-Agor, M., Fox, G., Cancienne, R., Wilson, G., 2008. Seepage caused tension failures and erosion undercutting of hillslopes. Journal of hydrology 359, 247-259. https://doi.org/10.1016/j.jhydrol.2008.07.005

Cronkite-Ratcliff, C., Schmidt, K.M., Wirion, C., 2022. Comparing Root Cohesion Estimates from Three Models at a Shallow Landslide in the Oregon Coast Range. GeoHazards 3, 428-451. https://doi.org/10.3390/geohazards3030022

Detty, J., McGuire, K., 2010. Topographic controls on shallow groundwater dynamics: implications of hydrologic connectivity between hillslopes and riparian zones in a till mantled catchment. Hydrological Processes 24, 2222-2236. https://doi.org/10.1002/hyp.7656

Dietrich, W., Dunne, T., 1978. Sediment budget for a small catchment in a mountainous terrain. Zeitschrift für Geomorphologie Supplementband 29, 191–206.

Dietrich, W.E., Reiss, R., Hsu, M.L., Montgomery, D.R., 1995. A process-based model for colluvial soil depth and shallow landsliding using digital elevation data. Hydrological processes 9, 383-400. https://doi.org/10.1002/hyp.3360090311

Dietrich, W.E., Wilson, C.J., Montgomery, D.R., McKean, J., Bauer, R., 1992. Erosion thresholds and land surface morphology. Geology 20, 675-679. https://doi.org/10.1130/0091-7613(1992)020%3C0675:ETALSM%3E2.3.CO;2

Ebel, B.A., Loague, K., 2008. Rapid simulated hydrologic response within the variably saturated near surface. Hydrological Processes: An International Journal 22, 464-471. https://doi.org/10.1002/hyp.6926

Ebel, B.A., Loague, K., Borja, R.I., 2010. The impacts of hysteresis on variably saturated hydrologic response and slope failure. Environmental Earth Sciences 61, 1215-1225. https://doi.org/10.1007/s12665-009-0445-2

Ebel, B.A., Loague, K., Dietrich, W.E., Montgomery, D.R., Torres, R., Anderson, S.P., Giambelluca, T.W., 2007a. Near-surface hydrologic response for a steep, unchanneled catchment near Coos Bay, Oregon: 1. Sprinkling experiments. American Journal of Science 307, 678-708. https://doi.org/10.2475/04.2007.02

Ebel, B.A., Loague, K., Montgomery, D.R., Dietrich, W.E., 2008. Physics-based continuous simulation of long-term near-surface hydrologic response for the Coos Bay experimental catchment. Water Resources Research 44. https://doi.org/10.1029/2007WR006442

Ebel, B.A., Loague, K., Vanderkwaak, J.E., Dietrich, W.E., Montgomery, D.R., Torres, R., Anderson, S.P., 2007b. Near-surface hydrologic response for a steep, unchanneled catchment near Coos Bay, Oregon: 2. Physics-based simulations. American Journal of Science 307, 709-748. https://doi.org/10.2475/04.2007.03

Endrizzi, S., Gruber, S., Dall'Amico, M., Rigon, R., 2014. GEOtop 2.0: simulating the combined energy and water balance at and below the land surface accounting for soil freezing, snow cover and terrain effects. Geoscientific Model Development 7, 2831-2857. https://doi.org/10.5194/gmd-7-2831-2014

Flinchum, B.A., Steven Holbrook, W., Rempe, D., Moon, S., Riebe, C.S., Carr, B.J., Hayes, J.L., St. Clair, J., Peters, M.P., 2018. Critical zone structure under a granite ridge inferred from

drilling and three-dimensional seismic refraction data. Journal of Geophysical Research: Earth Surface 123, 1317-1343. https://doi.org/10.1029/2017JF004280

Formetta, G., Capparelli, G., 2019. Quantifying the three-dimensional effects of anisotropic soil horizons on hillslope hydrology and stability. Journal of Hydrology 570, 329-342. https://doi.org/10.1016/j.jhydrol.2018.12.064

Formetta, G., Capparelli, G., Versace, P., 2016. Evaluating performance of simplified physically based models for shallow landslide susceptibility. Hydrology and Earth System Sciences 20, 4585-4603. https://doi.org/10.5194/hess-20-4585-2016

Formetta, G., Higa, J.T., Busti, R., Bellugi, D.G., Ebel, B.A., Dietrich, W.E., Milledge, D.G., Moon, S., in prep. Unraveling subsurface hydrology in the critical zone: a combined approach of field measurements and numerical models.

Fox, G.A., Felice, R.G., 2014. Bank undercutting and tension failure by groundwater seepage: predicting failure mechanisms. Earth Surface Processes and Landforms 39, 758-765. https://doi.org/10.1002/esp.3481

Froude, M.J., Petley, D.N., 2018. Global fatal landslide occurrence from 2004 to 2016. Natural Hazards and Earth System Sciences 18, 2161-2181. https://doi.org/10.5194/nhess-18-2161-2018

Gottardi, G., Venutelli, M., 1993. A control-volume finite-element model for two-dimensional overland flow. Advances in Water Resources 16, 277-284. https://doi.org/10.1016/0309-1708(93)90019-C

Gu, X., Heaney, P.J., Reis, F.D.A., Brantley, S.L., 2020. Deep abiotic weathering of pyrite. Science 370, eabb8092. https://doi.org/10.1126/science.abb8092

Guo, L., Mount, G.J., Hudson, S., Lin, H., Levia, D., 2020. Pairing geophysical techniques improves understanding of the near-surface Critical Zone: Visualization of preferential routing of stemflow along coarse roots. Geoderma 357, 113953. https://doi.org/10.1016/j.geoderma.2019.113953

Hahm, W.J., Dralle, D.N., Sanders, M., Bryk, A.B., Fauria, K.E., Huang, M.-H., Hudson-Rasmussen, B., Nelson, M.D., Pedrazas, M.A., Schmidt, L., 2022. Bedrock vadose zone storage dynamics under extreme drought: consequences for plant water availability, recharge, and runoff. Water Resources Research 58, e2021WR031781. https://doi.org/10.1029/2021WR031781

Hahm, W.J., Rempe, D.M., Dralle, D.N., Dawson, T.E., Lovill, S.M., Bryk, A.B., Bish, D.L., Schieber, J., Dietrich, W.E., 2019. Lithologically controlled subsurface critical zone thickness and water storage capacity determine regional plant community composition. Water Resources Research 55, 3028-3055. https://doi.org/10.1029/2018WR023760

Heidbach, O., Rajabi, M., Cui, X., Fuchs, K., Müller, B., Reinecker, J., Reiter, K., Tingay, M., Wenzel, F., Xie, F., 2018. The World Stress Map database release 2016: Crustal stress pattern across scales. Tectonophysics 744, 484-498. https://doi.org/10.1016/j.tecto.2018.07.007

Heimsath, A.M., Dietrich, W.E., Nishiizumi, K., Finkel, R.C., 2001. Stochastic processes of soil production and transport: Erosion rates, topographic variation and cosmogenic nuclides in the Oregon Coast Range. Earth Surface Processes and Landforms: The Journal of the British Geomorphological Research Group 26, 531-552. https://doi.org/10.1002/esp.209

Higa, J.T., Formetta, G., Bellugi, D.G., Busti, R., Dietrich, W.E., Ebel, B.A., Milledge D.G., Moon, S., in prep. Spatially varying critical zone structures at a steep, forested site near Coos Bay, Oregon.

Holbrook, W.S., Riebe, C.S., Elwaseif, M., L. Hayes, J., Basler-Reeder, K., L. Harry, D., Malazian, A., Dosseto, A., C. Hartsough, P., W. Hopmans, J., 2014. Geophysical constraints on deep weathering and water storage potential in the Southern Sierra Critical Zone Observatory. Earth Surface Processes and Landforms 39, 366-380. https://doi.org/10.1002/esp.3502

Iverson, R.M., Major, J.J., 1986. Groundwater seepage vectors and the potential for hillslope failure and debris flow mobilization. Water Resources Research 22, 1543-1548. https://doi.org/10.1029/WR022i011p01543

Jarecke, K.M., Bladon, K.D., Wondzell, S.M., 2021. The influence of local and nonlocal factors on soil water content in a steep forested catchment. Water Resources Research 57, e2020WR028343. https://doi.org/10.1029/2020WR028343

Kim, M.S., Onda, Y., Kim, J.K., Kim, S.W., 2015. Effect of topography and soil parameterisation representing soil thicknesses on shallow landslide modelling. Quaternary International 384, 91-106. https://doi.org/10.1016/j.quaint.2015.03.057

Kim, M.S., Onda, Y., Uchida, T., Kim, J.K., Song, Y.S., 2018. Effect of seepage on shallow landslides in consideration of changes in topography: case study including an experimental sandy slope with artificial rainfall. Catena 161, 50-62. https://doi.org/10.1016/j.catena.2017.10.004

Lebedeva, M.I., Brantley, S.L., 2013. Exploring geochemical controls on weathering and erosion of convex hillslopes: beyond the empirical regolith production function. Earth Surface Processes and Landforms 38, 1793-1807. https://doi.org/10.1002/esp.3424

Lebedeva, M.I., Brantley, S.L., 2020. Exploring an 'ideal hill': how lithology and transport mechanisms affect the possibility of a steady state during weathering and erosion. Earth Surface Processes and Landforms 45, 652-665. https://doi.org/10.1002/esp.4762

Lindner, E.N., Halpern, J.A., 1978. In-situ stress in North America: A compilation, International Journal of Rock Mechanics and Mining Sciences & Geomechanics Abstracts. Elsevier, pp. 183-203. https://doi.org/10.1016/0148-9062(78)91225-1

Ma, L., Oakley, D., Nyblade, A., Moon, S., Accardo, N., Wang, W., Gu, X., Brubaker, K., Mount, G.J., Forsythe, B., 2021. Seismic Imaging of a Shale Landscape Under Compression Shows Limited Influence of Topography-Induced Fracturing. Geophysical Research Letters 48, e2021GL093372. https://doi.org/10.1029/2021GL093372

McTigue, D.F., Mei, C.C., 1981. Gravity-induced stresses near topography of small slope. Journal of Geophysical Research: Solid Earth 86, 9268-9278. https://doi.org/10.1029/JB086iB10p09268

Milledge, D.G., Bellugi, D., McKean, J.A., Densmore, A.L., Dietrich, W.E., 2014. A multidimensional stability model for predicting shallow landslide size and shape across landscapes. Journal of Geophysical Research: Earth Surface 119, 2481-2504. https://doi.org/10.1002/2014JF003135

Miller, D.J., Dunne, T., 1996. Topographic perturbations of regional stresses and consequent bedrock fracturing. Journal of Geophysical Research: Solid Earth 101, 25523-25536. https://doi.org/10.1029/96JB02531

Molnar, P., 2004. Interactions among topographically induced elastic stress, static fatigue, and valley incision. Journal of Geophysical Research: Earth Surface 109, F02010. https://doi.org/10.1029/2003JF000097

Montgomery, D.R., 1991. Channel initiation and landscape evolution. University of California, Berkeley.

Montgomery, D.R., Dietrich, W.E., 1994. A physically based model for the topographic control on shallow landsliding. Water resources research 30, 1153-1171. https://doi.org/10.1029/93WR02979

Montgomery, D.R., Dietrich, W.E., 2002. Runoff generation in a steep, soil-mantled landscape. Water Resources Research 38, 7-1-7-8. https://doi.org/10.1029/2001WR000822

Montgomery, D.R., Dietrich, W.E., Heffner, J.T., 2002. Piezometric response in shallow bedrock at CB1: Implications for runoff generation and landsliding. Water Resources Research 38, 10-11. https://doi.org/10.1029/2002WR001429

Montgomery, D.R., Dietrich, W.E., Torres, R., Anderson, S.P., Heffner, J.T., Loague, K., 1997. Hydrologic response of a steep, unchanneled valley to natural and applied rainfall. Water Resources Research 33, 91-109. https://doi.org/10.1029/96WR02985

Montgomery, D.R., Schmidt, K.M., Dietrich, W.E., McKean, J., 2009. Instrumental record of debris flow initiation during natural rainfall: Implications for modeling slope stability. Journal of Geophysical Research: Earth Surface 114. https://doi.org/10.1029/2008JF001078

Montgomery, D.R., Schmidt, K.M., Greenberg, H.M., Dietrich, W.E., 2000. Forest clearing and regional landsliding. Geology 28, 311-314. https://doi.org/10.1130/0091-7613(2000)28%3C311:FCARL%3E2.0.CO;2

Moon, S., Perron, J., Martel, S., Holbrook, W., St. Clair, J., 2017. A model of three-dimensional topographic stresses with implications for bedrock fractures, surface processes, and landscape evolution. Journal of Geophysical Research: Earth Surface 122, 823-846. https://doi.org/10.1002/2016JF004155

Moon, S., Perron, J.T., Martel, S.J., Goodfellow, B.W., Mas Ivars, D., Hall, A., Heyman, J., Munier, R., Näslund, J.O., Simeonov, A., 2020. Present-day stress field influences bedrock fracture openness deep into the subsurface. Geophysical Research Letters 47, e2020GL090581. https://doi.org/10.1029/2020GL090581

Mualem, Y., 1976. A new model for predicting the hydraulic conductivity of unsaturated porous media. Water Resources Research 12, 513-522. https://doi.org/10.1029/WR012i003p00513

National Research Council, 2004. Partnerships for reducing landslide risk: assessment of the national landslide hazards mitigation strategy. National Academies Press, Washington.

Onda, Y., Tsujimura, M., Tabuchi, H., 2004. The role of subsurface water flow paths on hillslope hydrological processes, landslides and landform development in steep mountains of Japan. Hydrological Processes 18, 637-650. https://doi.org/10.1002/hyp.1362

Orlandini, S., Moretti, G., Franchini, M., Aldighieri, B., Testa, B., 2003. Path-based methods for the determination of nondispersive drainage directions in grid-based digital elevation models. Water Resources Research 39. https://doi.org/10.1029/2002WR001639

Orlando, J., Comas, X., Hynek, S.A., Buss, H.L., Brantley, S.L., 2016. Architecture of the deep critical zone in the Río Icacos watershed (Luquillo Critical Zone Observatory, Puerto Rico) inferred from drilling and ground penetrating radar (GPR). Earth Surface Processes and Landforms 41, 1826-1840. https://doi.org/10.1002/esp.3948

Panday, S., Huyakorn, P.S., 2004. A fully coupled physically-based spatially-distributed model for evaluating surface/subsurface flow. Advances in Water Resources 27, 361-382. https://doi.org/10.1016/j.advwatres.2004.02.016

Pasquet, S., Marçais, J., Hayes, J.L., Sak, P.B., Ma, L., Gaillardet, J., 2022. Catchment-Scale Architecture of the Deep Critical Zone Revealed by Seismic Imaging. Geophysical Research Letters 49, e2022GL098433. https://doi.org/10.1029/2022GL098433

Prancevic, J.P., Lamb, M.P., Palucis, M.C., Venditti, J.G., 2018. The role of three-dimensional boundary stresses in limiting the occurrence and size of experimental landslides. Journal of Geophysical Research: Earth Surface 123, 46-65. https://doi.org/10.1002/2017JF004410

Rempe, D.M., Dietrich, W.E., 2014. A bottom-up control on fresh-bedrock topography under landscapes. Proceedings of the National Academy of Sciences 111, 6576-6581. https://doi.org/10.1073/pnas.1404763111

Reneau, S.L., Dietrich, W.E., 1990. Depositional history of hollows on steep hillslopes, coastal Oregon and Washington. National Geographic Research 6, 220-230.

Richards, L.A., 1931. Capillary conduction of liquids through porous mediums. Physics 1, 318-333. https://doi.org/10.1063/1.1745010

Riebe, C.S., Hahm, W.J., Brantley, S.L., 2017. Controls on deep critical zone architecture: A historical review and four testable hypotheses. Earth Surface Processes and Landforms 42, 128-156. https://doi.org/10.1002/esp.4052

Roering, J.J., Kirchner, J.W., Dietrich, W.E., 1999. Evidence for nonlinear, diffusive sediment transport on hillslopes and implications for landscape morphology. Water Resources Research 35, 853-870. https://doi.org/10.1029/1998WR900090

Roering, J.J., Kirchner, J.W., Dietrich, W.E., 2005. Characterizing structural and lithologic controls on deep-seated landsliding: Implications for topographic relief and landscape evolution in the Oregon Coast Range, USA. Geological Society of America Bulletin 117, 654-668. https://doi.org/10.1130/B25567.1

Rosso, R., Rulli, M.C., Vannucchi, G., 2006. A physically based model for the hydrologic control on shallow landsliding. Water Resources Research 42. https://doi.org/10.1029/2005WR004369

Savage, W., Swolfs, H., Powers, P., 1985. Gravitational stresses in long symmetric ridges and valleys. International Journal of Rock Mechanics and Mining Sciences & Geomechanics Abstracts 22, 291-302. https://doi.org/10.1016/0148-9062(85)92061-3

Savage, W.Z., Swolfs, H.S., 1986. Tectonic and gravitational stress in long symmetric ridges and valleys. Journal of Geophysical Research: Solid Earth 91, 3677-3685. https://doi.org/10.1029/JB091iB03p03677

Schmidt, K., Roering, J., Stock, J., Dietrich, W., Montgomery, D., Schaub, T., 2001. The variability of root cohesion as an influence on shallow landslide susceptibility in the Oregon Coast Range. Canadian Geotechnical Journal 38, 995-1024. https://doi.org/10.1139/t01-031

Schwanghart, W., Scherler, D., 2014. TopoToolbox 2–MATLAB-based software for topographic analysis and modeling in Earth surface sciences. Earth Surface Dynamics 2, 1-7. https://doi.org/10.5194/esurf-2-1-2014

Shi, J., Malik, J., 2000. Normalized cuts and image segmentation. IEEE Transactions on pattern analysis and machine intelligence 22, 888-905. https://doi.org/10.1109/34.868688

Shoaei, G., Sidle, R.C., 2009. Variation in soil characteristics and hydrologic properties associated with historic land use near a recent landslide, Nagano Prefecture, Japan. Geoderma 153, 37-51. https://doi.org/10.1016/j.geoderma.2009.07.012

St. Clair, J., Moon, S., Holbrook, W., Perron, J., Riebe, C., Martel, S., Carr, B., Harman, C., Singha, K., Richter, D.d., 2015. Geophysical imaging reveals topographic stress control of bedrock weathering. Science 350, 534-538. https://doi.org/10.1126/science.aab2210

Thomas, A.L., 1993. POLY3D: A three-dimensional, polygonal element, displacement discontinuity boundary element computer program with applications to fractures, faults, and cavities in the earth's crust. Stanford University.

Torres, R., Dietrich, W.E., Montgomery, D.R., Anderson, S.P., Loague, K., 1998. Unsaturated zone processes and the hydrologic response of a steep, unchanneled catchment. Water Resources Research 34, 1865-1879. https://doi.org/10.1029/98WR01140

Tufano, R., Formetta, G., Calcaterra, D., De Vita, P., 2021. Hydrological control of soil thickness spatial variability on the initiation of rainfall-induced shallow landslides using a three-dimensional model. Landslides 18, 3367-3380. https://doi.org/10.1007/s10346-021-01681-x

Uchida, T., Tamur, K., Akiyama, K., 2011. The role of grid cell size, flow routing algorithm and spatial variability of soil depth on shallow landslide prediction, 5th International Conference on Debris-Flow Hazards Mitigation: Mechanics, Prediction and Assessment. Casa Editrice Università La Sapienza Rome, Italy, pp. 149-157. https://doi.org/10.4408/IJEGE.2011-03.B-018

Van Genuchten, M.T., 1980. A closed-form equation for predicting the hydraulic conductivity of unsaturated soils. Soil Science Society of America Journal 44, 892-898. https://doi.org/10.2136/sssaj1980.03615995004400050002x

Wang, W., Nyblade, A., Mount, G., Moon, S., Chen, P., Accardo, N., Gu, X., Forsythe, B., Brantley, S.L., 2021. 3D seismic anatomy of a watershed reveals climate-topography coupling that drives water flowpaths and bedrock weathering. Journal of Geophysical Research: Earth Surface 126, e2021JF006281. https://doi.org/10.1029/2021JF006281

Conclusion

This dissertation summarizes the impact of fractures on surface and near-surface processes over a wide range of spatial and temporal scales. Using diverse methods, including field mapping, remote sensing, geochronology, geophysical surveying, and numerical and process-based modeling, I document the present configuration of fractures, faults, and weathering, then relate these features to their geological past. Such observations may allow geologists and stakeholders to understand better the processes that control landscape evolution and natural hazards in the context of Earth's history. I reiterate below the key points from Chapters 2 to 4, implications for understanding geologic processes, and possible future directions.

Chapter 2 and Higa et al. (2022) summarize the first constraints on the activity of a mostly normal fault system on the Isla Ángel de la Guarda (IAG) microcontinent. This chapter shows that the Almeja fault zone is in strike with the offshore and active North Salsipuedes Basin and is likely to have been active since the late Quaternary. Because this fault system is east of the nearby Pacific-North America plate boundary, these results suggest that continental rifting of the microcontinent is ongoing and represents a larger plate boundary-scale reorganization in the Gulf of California. A follow-up study may reveal more topographic signatures of continental rifting on IAG. For example, examining hillslope and stream channel topography may be able to differentiate between areas of relatively low and high tectonic activity (Clubb et al., 2020; Wobus et al., 2006). Signals of high tectonic activity near the active Almeja fault zone in the southern mountain range of IAG could support kinematic linkage between onshore and offshore normal faults. Such an improved understanding could help geologists understand the present evolution of this dynamic plate boundary.

Chapter 3 describes geophysical and modeling efforts to observe and explain critical zone (CZ) weathering at the well-studied benchmark site near Coos Bay. These results show two main weathered boundaries at the CB1 catchment: one shallow, surface-parallel layer of pervasively weathered rock and one deep, undulating layer of fractured and unweathered bedrock. Comparisons with process-based weathering models suggest that site-specific weathering along fractures and bedding or divide migration can also affect the CZ profile. Future work to include the effect of such weathering or inelastic accumulation of rock fractures (e.g., Baden et al., 2022; Slim et al., 2015) or airborne geophysical surveys to observe fracturing could improve the mismatch between modeled and observed CZ profiles. These efforts can lead to better predictions of bedrock fractures and groundwater storage at outcrop- to landscape-scales, which recent studies suggest control plant responses to droughts (e.g., Callahan et al., 2022) that may become more frequent because of anthropogenic climate change. Thus, more studies utilizing the Coos Bay benchmark site can improve society's response to a rapidly changing world.

Chapter 4 uses CZ weathering models from Chapter 3 to include weathered zone hydrology in shallow soil landslide modeling. CZ structure may impact soil stability in a natural landscape by inducing non-surface-parallel seepage at the boundary between soil and weathered bedrock below. More permeable, weathered bedrock in the CZ causes downward seepage that keeps the soil overlying thick CZs dry and stable. Then, upward-oriented seepage can focus where weathered bedrock thickness thins, increasing landslide occurrence. Differences in soil saturation caused by variable CZ structures also control shallow landslide size, location, and timing during a rainstorm. Some next steps include improving model abilities, such as the ability to model fracture flow, which observations (e.g., Montgomery et al., 1997) and flume experiments (e.g., Kim et al., 2018) suggest are important for shallow landslides. The Mohr-Coulomb modeling approach here

could also be modified to produce distributions of normal and shear stresses at the base of shallow landslides, important for comparing the stress magnitudes of unstable soil masses with CZ-influenced pore pressures. Future studies at a location where fracture patterns are well documented or improvements in how geologists estimate fractures concealed by soil would be beneficial for enhancing our ability to predict landslides. If the occurrence of such geomorphic natural disasters continues to increase in modern times (Cendrero et al., 2020), a better understanding of landslides can advance how we prepare for natural disasters worldwide.

These chapters address some scientific and societal benefits of studying fractures. Implications range from predicting plate boundary instabilities to understanding processes that affect small but destructive shallow landslides. Subsequent studies to improve the modeling of these surface and near-surface processes can further our knowledge of how fractures affect small- and large-scale geology. Addressing these gaps is a timely problem considering issues regarding land use, water resources, and natural disasters facing people today. Ultimately, studying fractures is one part of improving how human society handles Earth's finite resources and dangerous hazards.

5.1 References

Baden, C.W., Shuster, D.L., Aron, F., Fosdick, J.C., Bürgmann, R., Hilley, G.E., 2022. Bridging earthquakes and mountain building in the Santa Cruz Mountains, CA. Science Advances 8, eabi6031. https://doi.org/10.1126/sciadv.abi6031

Callahan, R.P., Riebe, C.S., Sklar, L.S., Pasquet, S., Ferrier, K.L., Hahm, W.J., Taylor, N.J., Grana, D., Flinchum, B.A., Hayes, J.L., 2022. Forest vulnerability to drought controlled by bedrock composition. Nature Geoscience 15, 714-719. https://doi.org/10.1038/s41561-022-01012-2

Cendrero, A., Forte, L.M., Remondo, J., Cuesta‐Albertos, J.A., 2020. Anthropocene geomorphic change. Climate or human activities? Earth's Future 8, e2019EF001305. https://doi.org/10.1029/2019EF001305

Clubb, F.J., Mudd, S.M., Hurst, M.D., Grieve, S.W., 2020. Differences in channel and hillslope geometry record a migrating uplift wave at the Mendocino triple junction, California, USA. Geology 48, 184-188. https://doi.org/10.1130/G46939.1

Higa, J.T., Brown, N.D., Moon, S., Stock, J.M., Sabbeth, L., Bennett, S.E., Martín-Barajas, A., Argueta, M.O., 2022. Microcontinent Breakup and Links to Possible Plate Boundary Reorganization in the Northern Gulf of California, México. Tectonics 41, e2021TC006933. https://doi.org/10.1029/2021TC006933

Kim, M.S., Onda, Y., Uchida, T., Kim, J.K., Song, Y.S., 2018. Effect of seepage on shallow landslides in consideration of changes in topography: case study including an experimental sandy slope with artificial rainfall. Catena 161, 50-62. https://doi.org/10.1016/j.catena.2017.10.004

Montgomery, D.R., Dietrich, W.E., Torres, R., Anderson, S.P., Heffner, J.T., Loague, K., 1997. Hydrologic response of a steep, unchanneled valley to natural and applied rainfall. Water Resources Research 33, 91-109. https://doi.org/10.1029/96WR02985

Slim, M., Perron, J.T., Martel, S.J., Singha, K., 2015. Topographic stress and rock fracture: A two‐dimensional numerical model for arbitrary topography and preliminary comparison with borehole observations. Earth Surface Processes and Landforms 40, 512-529. https://doi.org/10.1002/esp.3646

Wobus, C., Whipple, K.X., Kirby, E., Snyder, N., Johnson, J., Spyropolou, K., Crosby, B., Sheehan, D., Willett, S., 2006. Tectonics from topography: Procedures, promise, and pitfalls. Special papers-Geological Society of America 398, 55. https://doi.org/10.1130/2006.2398(04)

Appendix A for Chapter 2: Microcontinent Breakup and Links to Possible Plate Boundary Reorganization in the Northern Gulf of California, México

Text A1. Terrace mapping and Holocene slip rate in terraces

Terrace generations at our sample sites were established based on local terrace tread elevation and characteristics following two regional-scale geologic maps from Sabbeth (2020), which include Quaternary terraces across different drainages. The maps from Sabbeth (2020) included our 'southern terraces' site but did not include our 'flight of terraces' and 'incised terrace' sites. We also used elevation from our 3-m resolution digital elevation model (DEM) derived from Pleiades satellite images and made finer adjustments based on our high-resolution DEMs derived from drone images (Figure 2.4; Figure A2). Here, we present subdivided terrace levels for our sites based on Sabbeth (2020), height above the active channel and local terrace generations from DEMs, and local luminescence ages. T1 is the highest terrace above the active channel at 30 – 40 m high, is one of the least vegetated terraces, and is characterized by smooth terrace treads (Sabbeth, 2020). T2 is 10 – 30 m high and is also sparsely vegetated with smooth, distinct treads (Sabbeth, 2020). T3 is 5 – 10 m high and is the most vegetated generation. Drone-derived orthophotos reveal coarse deposits on T3 that likely represent young, preserved meanders in previous ephemeral channels (Figure 2.7b). It is noted that height above the active channel is not constant for the entire extent of each terrace level. Block tilting and/or sedimentation may cause some terrace heights to decrease towards the interior of Isla Ángel de la Guarda. We also note some terraces have slightly steeper gradients than the active channel and decrease in height above the active channel towards the coast. Therefore, we default to the maximum height above the active channel if such terrace mapping is unclear to determine terrace generations at each site within ~3 km of the coast. As we only have terrace surface ages in the 'flight of terraces', we cannot confirm with ages that terrace

surfaces across the entire study site correlate with each other. Nonetheless, previous mapping and distinct surface characteristics suggest that correlative Quaternary terraces are expected here (Sabbeth, 2020). At our sample sites, we focus on providing local constraints on the correlation of terrace generations that are used to determine the timing of fault offsets.

Holocene slip rate of fault X in the 'flight of terraces' site was calculated as the difference in dip-slip displacements divided by the difference in terrace surface age. We first create a normal distribution of 300,000 depositional ages from luminescence ages and its corresponding standard deviation (Table A2). Next, we create a distribution of 300,000 dip-slip displacements, generated by a Monte Carlo simulation for fault displacement, on each faulted terrace (Duckworth et al., 2020; Thompson et al., 2002). Then, the slopes of the lines connecting points of simulated age and dip-slip displacement from two terraces were calculated using a method similar to Gold & Cowgill (2011). Ages outside one standard deviation and displacements outside the 95% confidence interval are eliminated to construct distance-time envelopes. The use of a stricter threshold for age uncertainties is to limit the number of inverted ages that must be removed in later steps. Ages and displacements from each envelope are randomly selected and combined to make up one of 300,000 possible slip histories of variable slip rates. Because terrace T3 has a ~87% probability of being younger than terrace T2 from overlapping age distributions, which was also confirmed by field observations, all simulations assuming inverse ages are eliminated, ensuring only positive slip rates. Slip rate outliers, caused by depositional ages that are very similar, are eliminated by removing rates greater than three scaled median absolute deviations. These two filters eliminate ~ 12% of simulations comparing terraces T2 and T3. 100,000 slip rate calculations are randomly chosen after this filtering to calculate the 95% confidence interval and median slip rate of fault X between the deposition of terraces T2 and T3. Figure A12 shows the full probability density and

cumulative distribution functions of surface displacement differences, surface age differences, and slip rates from this analysis between terraces T2 and T3.

Text A2. Description of semi-automatic scarp mapping

From our high-resolution digital elevation models (DEM), we performed semi-automatic scarp mapping using a publicly available template matching algorithm called Scarplet (Hilley et al., 2010; Sare et al., 2019). Scarplet assumes that step-like topographic scarps produced by slip on faults degrade through linear slope diffusion processes, such as soil creep, which are expected to dominate on moderately sloping scarps (Hanks, 2000; Hilley et al., 2010). Linear slope diffusion is used to model the evolution of an across-scarp profile according to

$$z(X,t) = a\,\mathrm{erf}\left(\frac{X}{2\sqrt{\kappa t}}\right) + bX, \tag{A1}$$

where z [m] is elevation, X [m] is across-scarp distance, t [ka] is time since scarp formation, a [m] is half of the scarp height, κ [m^2/ka] is the downhill sediment diffusivity constant, and b [m/m] is the regional slope (Hanks, 2000; Hilley et al., 2010). It follows that morphologic age (also known as the degradation coefficient; κt [m^2]), depends on the κ and t of a given scarp, where a high κt can result from either very diffusive soil material or a very old scarp age. The second derivative of Equation A1 yields the synthetic curvature template

$$\left[\frac{\partial^2 z}{\partial X^2}\right]_{template} = \frac{-aX}{2\kappa t\sqrt{\pi\kappa t}}\exp\left(\frac{-X^2}{4\kappa t}\right). \tag{A2}$$

This template can be used as the search template for scarp-like topography in the curvature domain of real topography because the curvature of scarp-like topography decays to zero at both ends of the across-scarp profile. Therefore, the signal for scarp curvature is ubiquitous for all scarp-like

topography and can be searched for in a digital topographic dataset. This template is propagated out of the X-Y plane to a manually specified template scarp length. The algorithm will then search for scarp-like landforms with the template length using a variable orientation of θ to model different scarp orientations.

To find scarp amplitude and signal-to-noise ratio (*SNR*) for every DEM pixel, Scarplet first calculates the curvature of the DEM. Then, the template is normalized by

$$W(X,Y) = \frac{\left[\frac{\partial^2 z}{\partial X^2}\right]_{template}}{\int_{-\infty}^{\infty}\int_{-\infty}^{\infty}\left[\frac{\partial^2 z}{\partial X^2}\right]_{template} dXdY}, \quad \text{(A3)}$$

where X and Y are the in-plane and out-of-plane directions of the curvature, respectively. Amplitude A [m] is obtained by convolving DEM curvature with the normalized template W by

$$A = \left[\frac{\partial^2 z}{\partial X^2}\right]_{surface,\theta} * W, \quad \text{(A4)}$$

where W is the normalized template and * is the convolution operator defined as

$$Q * P = \int_{-\infty}^{\infty}\int_{-\infty}^{\infty}[Q(x - x_o, y - y_0) \times P(x,y)]dxdy, \quad \text{(A5)}$$

which is equivalent to the Fast Fourier Transform, where Q and P are arbitrary functions of x_o and y_o.

Signal-to-noise ratio *SNR* is defined as

$$SNR = \frac{A^2}{E^2}, \tag{A6}$$

where E is the misfit between the template and DEM curvature defined as

$$E^2 \times n = A^2 \int_{-\infty}^{\infty} \int_{-\infty}^{\infty} \left[\frac{\partial^2 z}{\partial X^2}\right]^2_{template} dx_1 dy_1 - 2A \left(\left[\frac{\partial^2 z}{\partial X^2}\right]_{surface,\theta} * \left[\frac{\partial^2 z}{\partial X^2}\right]_{template} \right) +$$

$$\left(\left[\frac{\partial^2 z}{\partial X^2}\right]_{surface,\theta} * M \right)^2, \tag{A7}$$

where M is a masking function that equals one when W is not equal to zero and zero when W is equal to zero, and n is the number of ones in M. The highest *SNR* is used to identify the best-fit κt and A for every pixel by varying θ. A value of *SNR* can be used as a threshold to predict tectonic (fault scarp) and non-tectonic (non-fault scarp) pixels. For an in-depth explanation of the Scarplet algorithm, refer to Hilley et al. (2010) and Sare et al., (2019).

Text A3. Evaluating and defining binary classifiers for scarp-like landforms

We evaluated the performance of semi-automatic template matching results by comparing scarps identified by template matching with those from our remote- and field-mapping. To do this, we created receiver operating characteristic curves that compare the true positive rate (*TPR*) and false positive rate (*FPR*) from template matching using a binary classifier (Figure A3a). A variable threshold value of signal-to-noise ratio (*SNR*) can act as such a binary classifier, where pixels with a $\log_{10}(SNR)$ above the threshold are classified as scarps (the positive condition) and those below as non-scarps (the negative condition).

Before comparing results from template matching and remote- and field-mapping to calculate *TPR* and *FPR* at different thresholds, we must address that template matching identifies fault scarp surfaces and not the fault trace where the remote- and field-mapping is centered. We use 10 m and 30 m buffers around our remote- and field-mapped faults for the Central Terraces and South Volcanic Hills, respectively, to evaluate the overlap between both methods (e.g., Figure A11). These buffers comprise the master map we will compare with our template matching results. A wider buffer was used for the South Volcanic Hills because of wider scarps in the more coherent volcanic lithology. Areas identified as a scarp from our template matching analysis that fall within this buffer are classified as true tectonic faults and those outside as non-tectonic, following Sare et al., (2019). Here, values for the true positive rate *TPR* introduced above are calculated by

$$TPR = \frac{TP}{P} \tag{A8}$$

where *TP* is the total number of true fault scarp pixels correctly identified by the $\log_{10}(SNR)$ threshold as truly positive and *P* is the total number of positive, fault scarp pixels inside the buffers from the master map. Values for false positive rate *FPR* are calculated by

$$FPR = \frac{FP}{N} \tag{A9}$$

where *FP* is the total number of non-fault scarp pixels identified by the $\log_{10}(SNR)$ threshold as falsely positive (non-fault scarp pixels inside the 10 and 30 m buffer) and *N* is the total number of negative, non-fault scarp pixels outside the buffers from the master map. By incrementally increasing the threshold $\log_{10}(SNR)$, we can obtain a series of true and false positive rates to construct receiver operating characteristic curves (Figure A3a). The area under the receiver operating characteristic curve (AUROC) provides a metric for evaluating the diagnostic ability of such a binary classifier when compared to our remote- and field-mapped fault scarps, where an AUROC closer to 1 indicates a perfect binary classifier and closer to 0.5 indicates a random classifier.

In addition to *TPR* and *FPR*, we calculate the true negative rate *TNR* as $1 - FPR$ and the false negative rate *FNR* as $1 - TPR$ for a given threshold. Precision is calculated as

$$\text{Precision} = \frac{TP}{TP+FP} \tag{A10}$$

and accuracy is calculated as

$$\text{Accuracy} = \frac{TP+TN}{P+N} \quad \text{(A11)}$$

where *TN* is the number of non-fault scarp pixels correctly identified by the variable $\log_{10}(SNR)$ threshold as truly negative. Refer to Sare et al. (2019) for further explanation of classifier metrics, applications, and errors for template matching scarp identification.

The first post-processing step in producing our final template matching maps is to filter our raw maps with an *SNR* threshold, similar to the process described above. We determine such a threshold value by considering the median *SNR* for entire regions, median *SNR* within buffers of the master map, and *SNR* from a best classifier analysis. Generally, the threshold value with the shortest "distance to a perfect classifier" (i.e., the point (0,1) on Figure A3a) is considered the best classifier. However, our analysis shows that a range of $\log_{10}(SNR)$ produces similar distances and performance levels (Figure A3b). Sare et al., (2019) used the median *SNR* from their entire mapped region as a binary classifier for fault scarps. However, our mapped regions contain many likely non-fault scarps (Text A5 for post-processing), which may influence the distribution of *SNR*. Thus, we examine the median *SNR* from fault scarp pixels within buffers around our remote- and field-mapped faults for terrace and volcanic lithologies as our threshold (Figure A3).

For the Central Terraces, the median *SNR* of pixels within the 10 m fault buffer is 247. As the area under the receiver operating curve was calculated using $\log_{10}(SNR$; Figure A3a), we show that $\log_{10}(247)$ and $\log_{10}(250)$ have indistinguishable distances to (0,1; Figure A3b). Thus, we use 250 as our threshold value for the binary classifier for scarp-like landforms in the Central Terraces (Figure A3b). Our chosen *SNR* value of 250 is the ~60^{th} percentile of *SNR* for the entire Central Terraces region (Figure A3c).

For the south volcanic hills, the median *SNR* for pixels within the 30 m buffer is 399, which corresponds to ~57th percentile of *SNR* from entire the South Volcanic Hills. Unfortunately, the North Volcanic Hills region has only one overlapping remote- and field-mapped fault, which makes it difficult to obtain representative *SNR* distributions within a buffer. To ensure our threshold works for both volcanic regions, we assume that the 57th percentile of *SNR* in this lithology is approximately equivalent to the median *SNR* within fault buffers. The 57th percentile of *SNR* for the entire North Volcanic Hills is ~491 (Figure A3c). We chose a threshold of 500 for both the North and South Volcanic Hills. This threshold is noticeably stricter than the median *SNR* threshold in the south, where faults are documented in more detail. Nonetheless, we note that the use of an *SNR* threshold higher than the median *SNR* within buffers in the South Volcanic Hills does not eliminate fault scarps when compared to the results for the median *SNR*. However, scarp width is reduced between 3 – 30 m. As described in Text A5, we linearize these scarps into lines before analyzing orientation. Therefore, reduced scarp width minimally affects our main scarp orientation results presented in Figure 2.3.

Text A4. Post-processing of semi-automatic template matching

Some tectonic faults may be missed by our template matching, likely due to the parameter values that we used in template matching and filtering. For example, most manually mapped scarps not identified by template matching are shorter than the template length of 200 m, interact with removed terrace risers or ridgelines, and/or have low scarp heights (< ~3 m) that cause low *SNR*. Conversely, scarps identified with high SNR may also have non-tectonic origins, such as large hillslopes in resistant volcanic rock or large terrace risers corresponding to the highest and oldest terraces. Therefore, in addition to the *SNR* threshold filters described above, we perform further,

lithology-specific, post-processing to remove these non-tectonic scarps from our final fault scarp maps.

To identify and remove larger scarp-like ridgelines from our analysis in volcanic rock, we used TopoToolbox DIVIDEobj functions (Scherler and Schwanghart, 2020; Schwanghart and Scherler, 2020) after filtering by *SNR*. We first calculated stream networks with minimum upstream drainage areas of 250 m^2 from our 3 m DEM and used this network to calculate the locations of basin divides. We then created a 5 m buffer only around lines identified as basin divides with a Strahler divide order ≥ 2 (Scherler and Schwanghart, 2020). Next, we manually drew lines corresponding to the center of scarps identified by template matching after the *SNR* filter and created a 25 m buffer around these lines. Because there are offsets between ridgelines, which are the locations of basin divides, and ridge flanks, which are the scarp-like features identified by template matching, we adjusted the location of the basin divide buffer for each region ~30 m west. This procedure allowed us to identify places where both buffers overlap and likely correspond with non-tectonic scarp-like features. We then calculated the percent areal overlap of the 5 m basin divide buffer on the 25 m template matching buffer and rejected scarps with > 13% overlap for the North Volcanic Hills and > 15% overlap for the South Volcanic Hills. Both percentages were chosen because they represent the highest percent of areal overlap for template matching buffers that correspond to actual faults confirmed in the field for each area. This process removes scarps from our template matching analysis that are likely topographic ridges unrelated to faults. We produced our final template matching products by applying an area threshold, only keeping scarps with areas > 1000 m^2 (Figure 2.3). Filtering by area is necessary to remove small patches of undesired fault scarps that remained after the removal of ridgelines.

In the Central Terraces region (Figure 2.3), we avoided the identification of non-tectonic scarp-like features, such as terrace risers, by filtering our template matching analysis to include only terrace tread surfaces after filtering by *SNR*. Risers and other steep erosional features were identified as having a tangential slope of greater than 0.08 in the 3-m resolution DEM and excluded from the results. We then manually clipped and joined areas across non-fluvial scarps to produce our final analysis area. Then, scarps with an area < 1000 m^2 were filtered out to produce our final template matching products in the Central Terraces (Figure 2.3). In some cases, our template matching analyses identified cross-cutting scarps with high *SNR* in all three regions. If a scarp was rejected based on its areal overlap, an unwanted gap was created in the remaining cross-cutting scarp. These gaps were filled by additional template matching runs using orientation constraints from the remaining scarps, which are oriented differently than the rejected scarps.

Text A5. Comparison between fault orientations

We compared the orientation of faults derived from our remote- and field-mapping and template matching analysis using statistical tests. We simplified the high-aspect-ratio areas of fault scarps from template matching by manually drawing lines along the length of the areas with ArcGIS. We then divided these lines into 3 m-long segments (similar to the resolution of the 3-m resolution DEM) and obtained the orientation of each segment using the ArcGIS Linear Directional Mean tool. Next, we divided the segmented template matching inventory into regions that correspond to the North Volcanic Hills, Central Terraces, and South Volcanic Hills and plotted their segment orientations in rose diagrams (Figure 2.3a – c). Similarly, we divided fault lines from our remote- and field-mapping into 3 m-long segments (Figure 2.3d – f) approximately based on the same three regions as our template matching analysis (Figure A4). Then, we compared the orientations across regions and methods using two-sample Kolmogorov-Smirnov and Wilcoxon rank sum tests at the 5% significance level to compare continuous distributions and the median of fault orientations, respectively.

Text A6. Luminescence sampling and laboratory procedures

We collected sediment samples from outcrops of faulted sedimentary material exposed in cut banks of incised arroyos (terrace fill material) or from pits hand-dug into the treads of terraces (terrace surface material) and depressions (depression surface material), targeting soft, sandy lenses (Table A2). These sediments derive from the intermediate to mafic volcanic bedrock that comprises the main mountain range of Isla Ángel de la Guarda or reworked marine sedimentary sequences. In the UCLA luminescence laboratory, we separated K-feldspar sand grains for single-grain luminescence dating. Under dim amber lighting conditions, the collected samples were wet-sieved to isolate the 175 – 200 micron fraction. With lithium metatungstate heavy liquid, we separated the most potassic fraction with a density < 2.565 g/cm^3.

To calculate the geologic dose rate for luminescence dating, cosmic ray contributions were estimated according to the geomagnetic latitude, elevation, and overburden depth of samples (Prescott and Hutton, 1994). Inductively-coupled plasma mass spectrometry (ICP-MS) was used to measure the concentration of U and Th within the sediment matrix and ICP optical emission spectrometry (ICP-OES) to measure the K concentration. These values were combined with the in-situ measurements of gamma dose rate made with a calibrated EG&G ORTEC MicroNomad portable NaI scintillation counter gamma spectrometer to estimate the external geologic dose rate for each sample, assuming standard attenuation factors (Brennan et al., 1991; Guérin et al., 2012; Liritzis et al., 2013) and using the water content calculated by drying subsamples. An internal K content of 12.5 ± 0.5 wt. % was assumed (Huntley and Baril, 1997) for internal dose rate determination. Dose rate calculations and error propagation were performed using DRAC v1.2 (Durcan et al., 2015).

Luminescence measurements for calculating equivalent dose were made on a TL-DA-20 Risø automated luminescence reader, equipped with a single-grain infrared laser assembly and a ^{90}Sr beta source which delivers a dose rate of ~0.1 Gy/s at the sample location (Bøtter-Jensen et al., 2003). During each measurement cycle, samples were preheated to 250 °C for 10 s. Grains were stimulated with the infrared laser for 3 s at 50 °C and then 3 s at 225 °C to measure the IRSL and p-IR IRSL signals, respectively. An example growth curve is shown in Figure A5. A small test dose was used to normalize sensitivity changes during the measurement sequence and a 'hot bleach' with infrared diodes for 40 s at 290 °C was used to remove any remaining charge at the end of a cycle.

Appendix A Figures

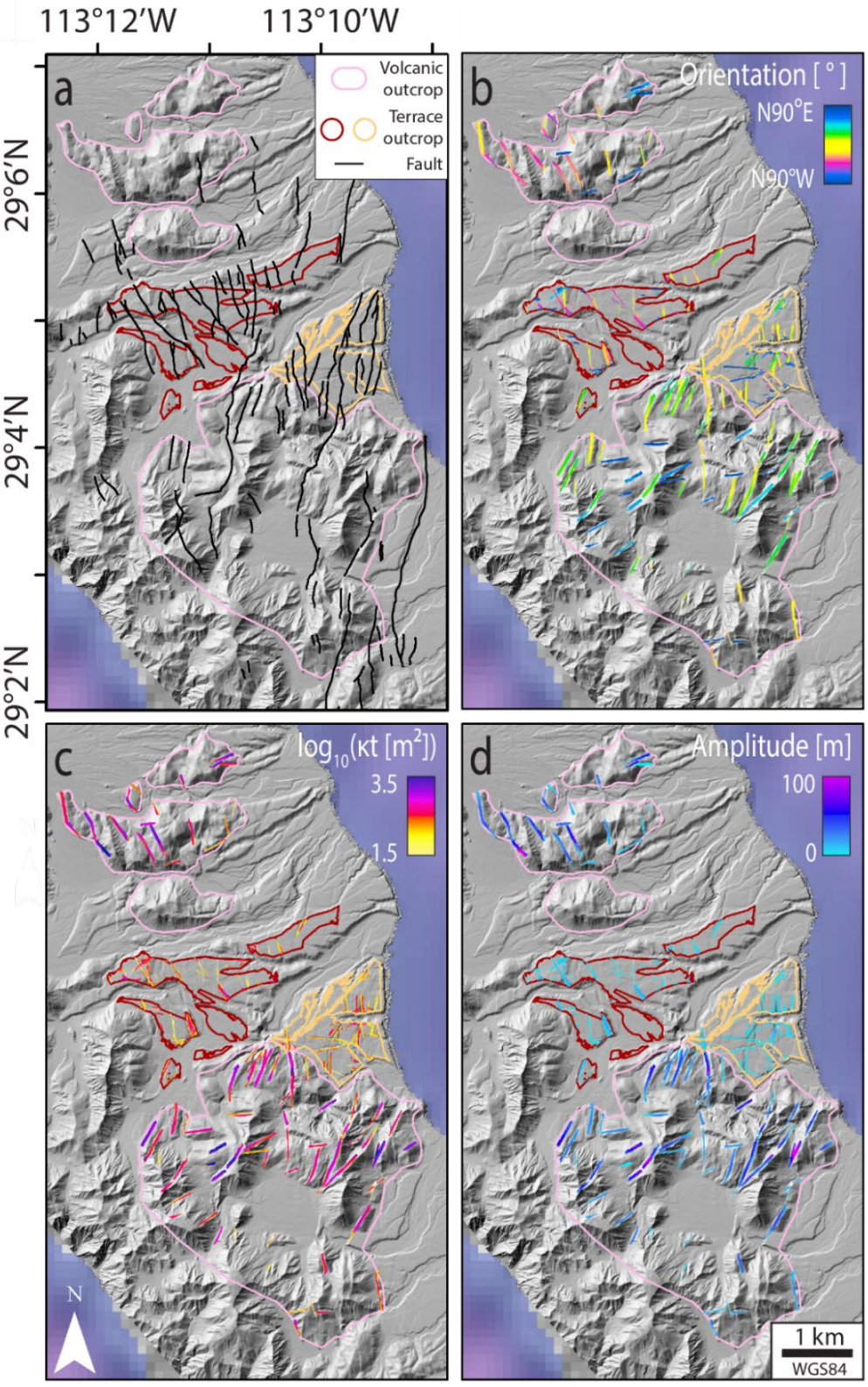

Figure A1. (a) Inventory of faults from our remote- and field-mapping (Sabbeth, 2020). Areas examined with Scarplet are outlined with pink (volcanic lithologies) and tan or maroon (non-marine terraces, east and west, respectively) polygons. Scarplet-produced maps of (b) scarp orientation, (c) scarp morphologic age κt, and (d) scarp amplitude for all regions. All results shown here have been filtered for signal-to-noise ratio, terrace risers, basin divides, and an area threshold. Basemap is 3-m resolution shaded relief extracted from 0.5-m Pleiades images and GeoMapApp (Ryan et al., 2009).

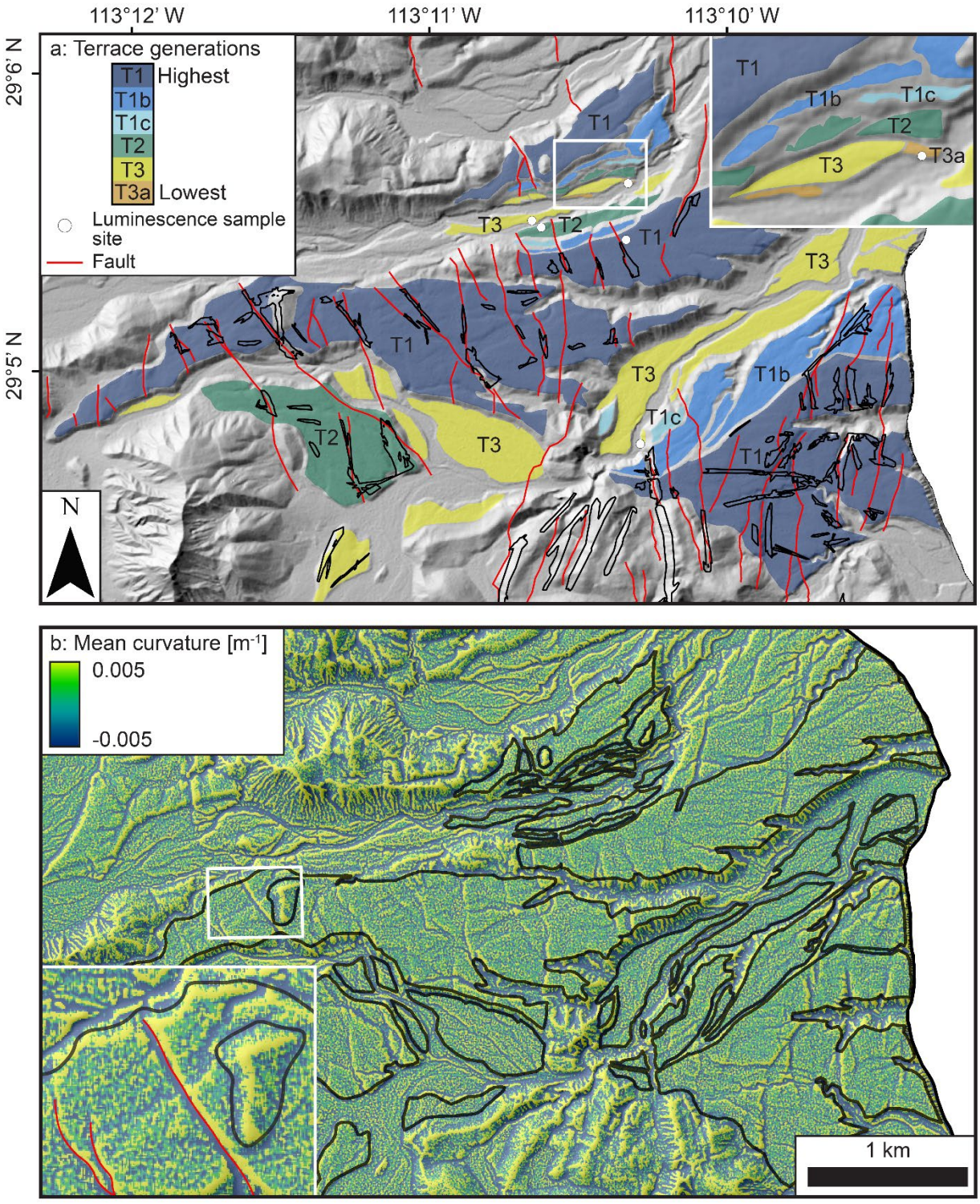
113°12' W
113°11' W
113°10' W
29°6' N
29°5' N
a: Terrace generations
T1 Highest
T1b
T1c
T2
T3
T3a Lowest
Luminescence sample site
Fault
N
b: Mean curvature [m-1]
0.005
-0.005
1 km

Figure A2. (a) Map of terraces, remote- and field-mapped faults, and luminescence sample locations in and around the Central Terraces region. Terrace nomenclature (T1, T2, T3) are based on stratigraphic framework by Sabbeth (2020), height above the active channel, local terrace generations, and local luminescence ages. The extent of these terraces is not the same as the extent analyzed with template matching, which has regions manually excluded (Figure 2.3). Thin black outlines show extent of fault scarps found from template matching. Inset shows detailed map of smaller terraces. (b) Map view of mean curvature in and around the Central Terraces. Thick black outlines are the same terraces as (a). Inset shows detailed map of area in white box. Negative and positive mean curvature on either side of faults (red lines) is indicative of concave up and concave down portions of fault scarps detected by template matching, respectively. Similar linear patterns exist at terrace risers and contacts between terraces and volcanic rock, indicated by the black outlines.

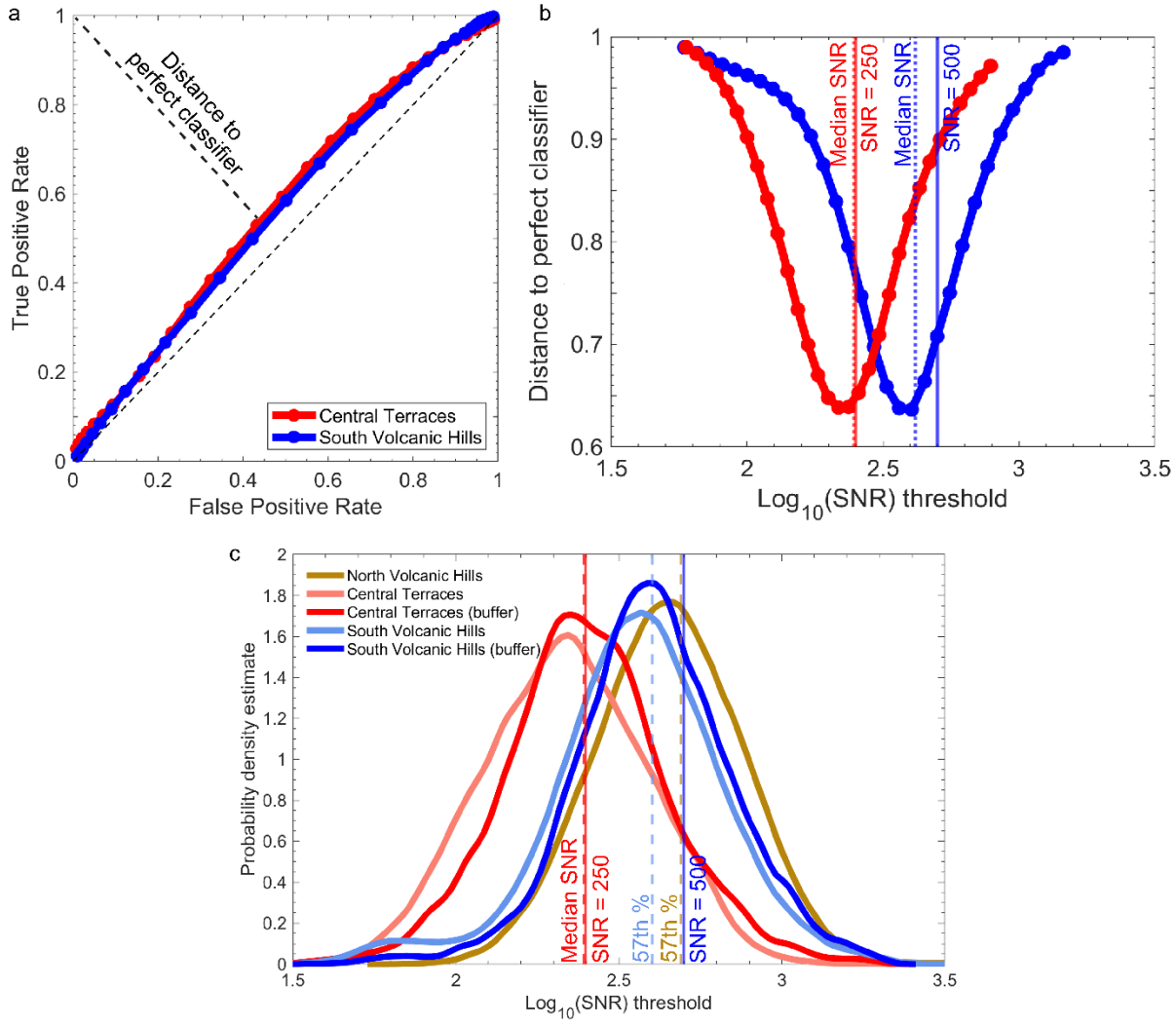

Figure A3. (a) Receiver operating characteristic (ROC) curves for signal-to-noise ratio (SNR) derived from Scarplet template matching at the Central Terraces and South Volcanic Hills using a 10 and 30 m buffer around faults from remote- and field-mapping, respectively. Dashed 1-to-1 line represents a completely random classifier with an area under the ROC (AUROC) curve of 0.5. ROC curves above the 1-to-1 line, with AUROC > 0.5, represent a better-than-random classifier. (b) $\log_{10}$ of SNR threshold against its diagnostic ability based on the distance to a perfect classifier located at (0,1) in Figure A3a and various SNR thresholds shown as vertical lines (dashed for median, solid for our chosen threshold). (c) Probability density functions for the $\log_{10}$ of SNR for

the South and North Volcanic Hills. The chosen SNR threshold of 500 (solid blue line) is close to the 57th percentile of SNR for the entire North Volcanic Hills and above that of the South Volcanic Hills (dashed gold and light blue lines, respectively). That for the Central Terraces is also shown against its median SNR (dashed red line) and our chosen SNR = 250 (solid red line).

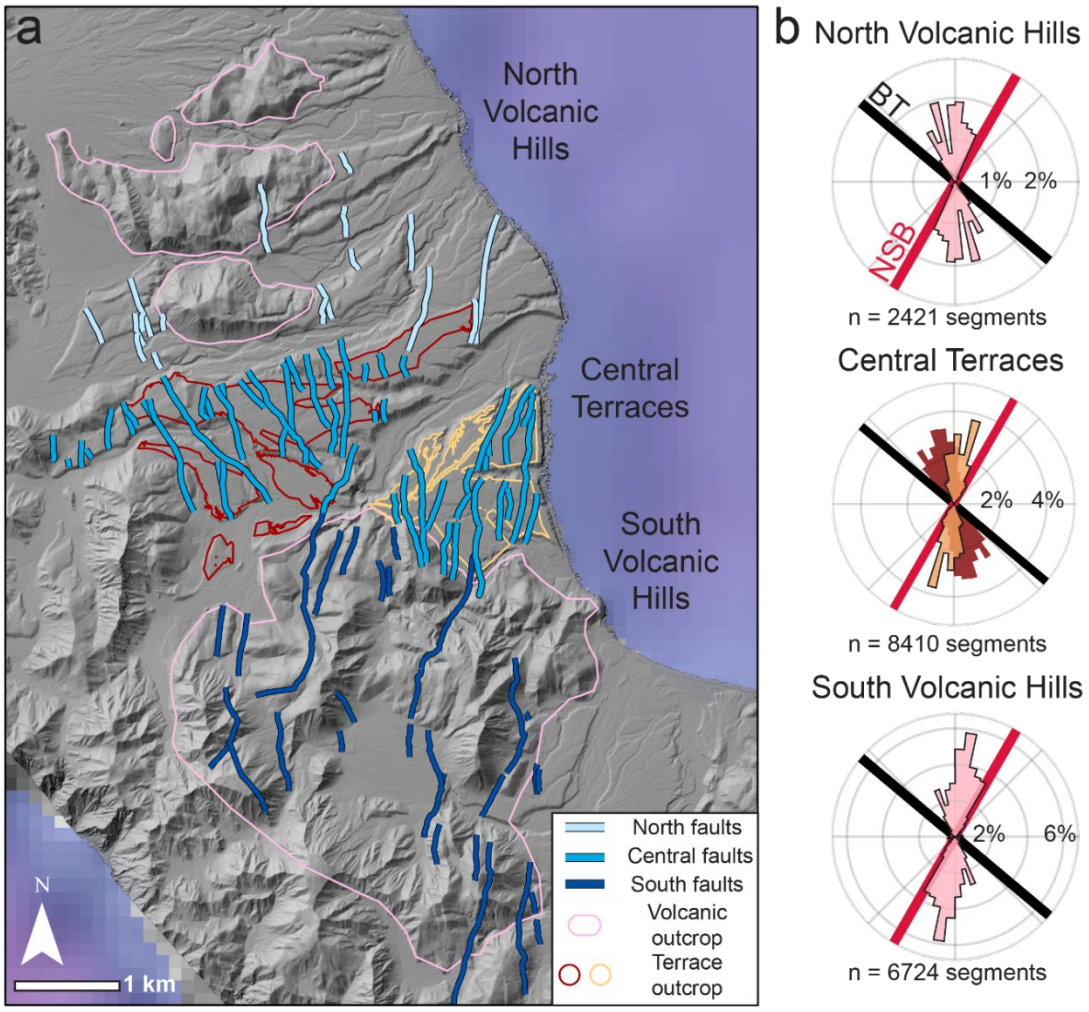

Figure A4. Remote- and field-mapping (Sabbeth, 2020) in relation to the three Scarplet search regions of Figure 2.3. Faults are colored by the region they were assigned. Extent is that shown in Figure 2.2b for Figure 2.3. (b) Rose diagrams of fault orientations obtained by analyzing our scarp inventory divided into 3-m segments. Radial unit is calculated as percent of scarps in an orientation bin, identified as 3-m segments, relative to the total number of 3-m segments from all three regions. Each rose petal is an orientation bin of 6°. Average orientation of the Ballenas transform fault (BT) and North Salsipuedes basin (NSB) near Isla Ángel de la Guarda are the thick black and red bars in each rose diagram, respectively. Basemap is 3-m resolution shaded relief extracted from 0.5-m Pleiades images and GeoMapApp (Ryan et al., 2009).

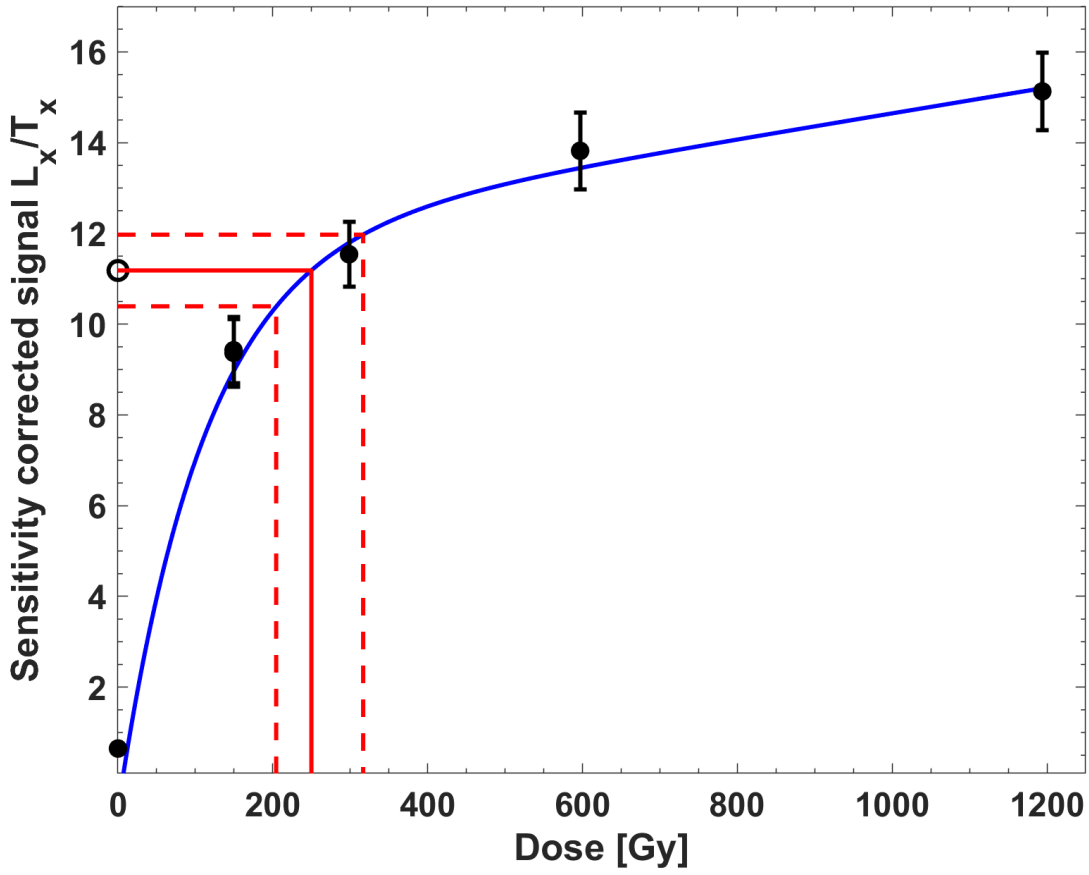

Figure A5. Example growth curve of a K-feldspar grain from sample J1321 in the 'southern terraces' site showing dose response data and errors as black circles and error bars and the natural burial luminescence signal as an open circle. Dose curve is shown in blue (exponential + linear curve fitting) and equivalent dose interpolated from the curve and errors are shown in red.

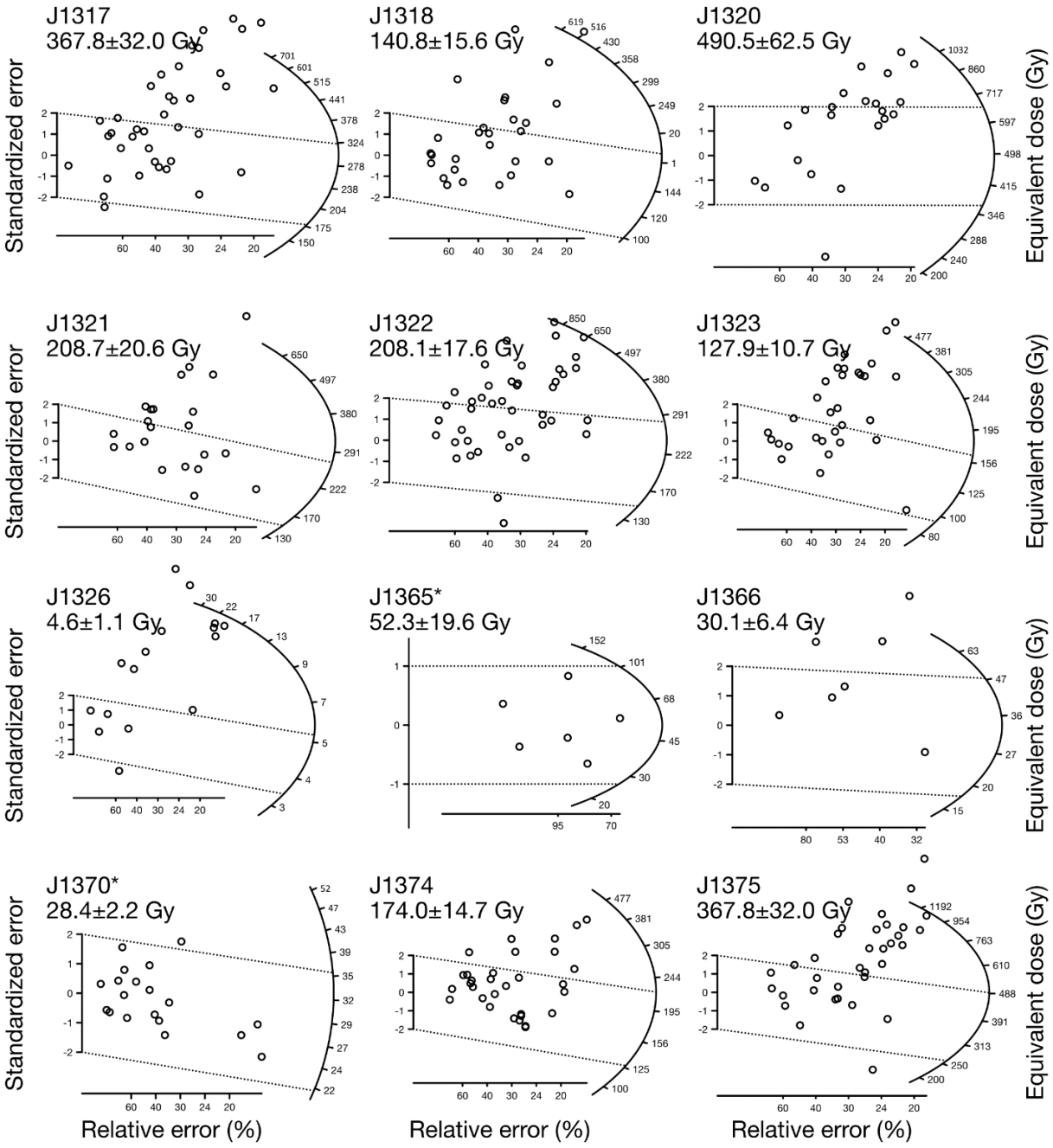

Figure A6. Radial plots of single grain equivalent dose values for all samples. Samples with asterisks were modeled using the Central Age Model (Galbraith et al., 1999). All other samples modeled with the Minimum Age Model (3 variables, overdispersion of 15%; Galbraith et al., 1999).

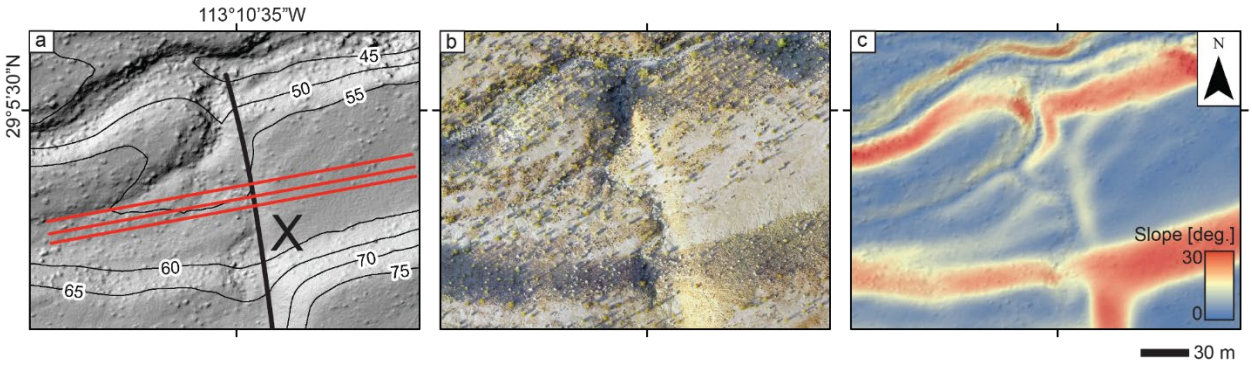

Figure A7. (a) 0.1-m resolution drone-derived shaded relief with 5 m elevation contours from 3-m resolution digital elevation extracted from 0.5-m Pleiades images, fault X, and scarp transects (red lines) at the 'flight of terraces' site. (b) Stitched orthomosaic of drone images showing surface characteristics. (c) Slope map that differentiates terrace surfaces and treads from terrace risers and fault scarps on terrace T2. Note the fluvial incision, particularly along strike of fault X.

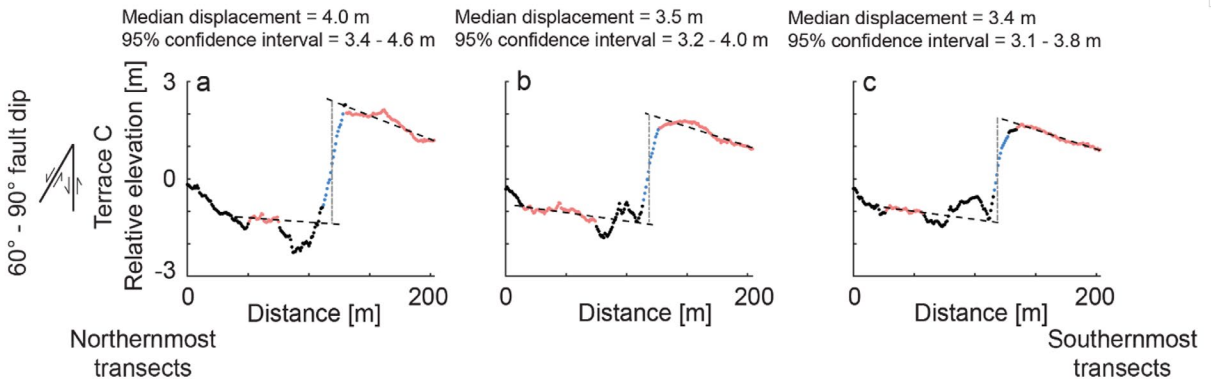

Figure A8. (a – c) Individual scarp-perpendicular topographic profiles across fault X on terrace T2. Black dashed line is the linear best-fit to points along the transect identified as the offset terrace surface shown as pink dots. Sections of the transect not included in the linear fit, interpreted as channel incision or slope wash, are shown as black dots. Points along the fault scarp are shown as blue dots. Vertical dashed gray line is vertical fault separation. Reported fault displacement is the median and 95% confidence interval from 100,000 Monte Carlo simulations that allow fault dip to vary between 60° – 90° (Duckworth et al., 2020; Thompson et al., 2002). Transects are northernmost on the left and southernmost on the right. Distance on x-axis increases towards the east. Locations of transects are shown in Figure A7.

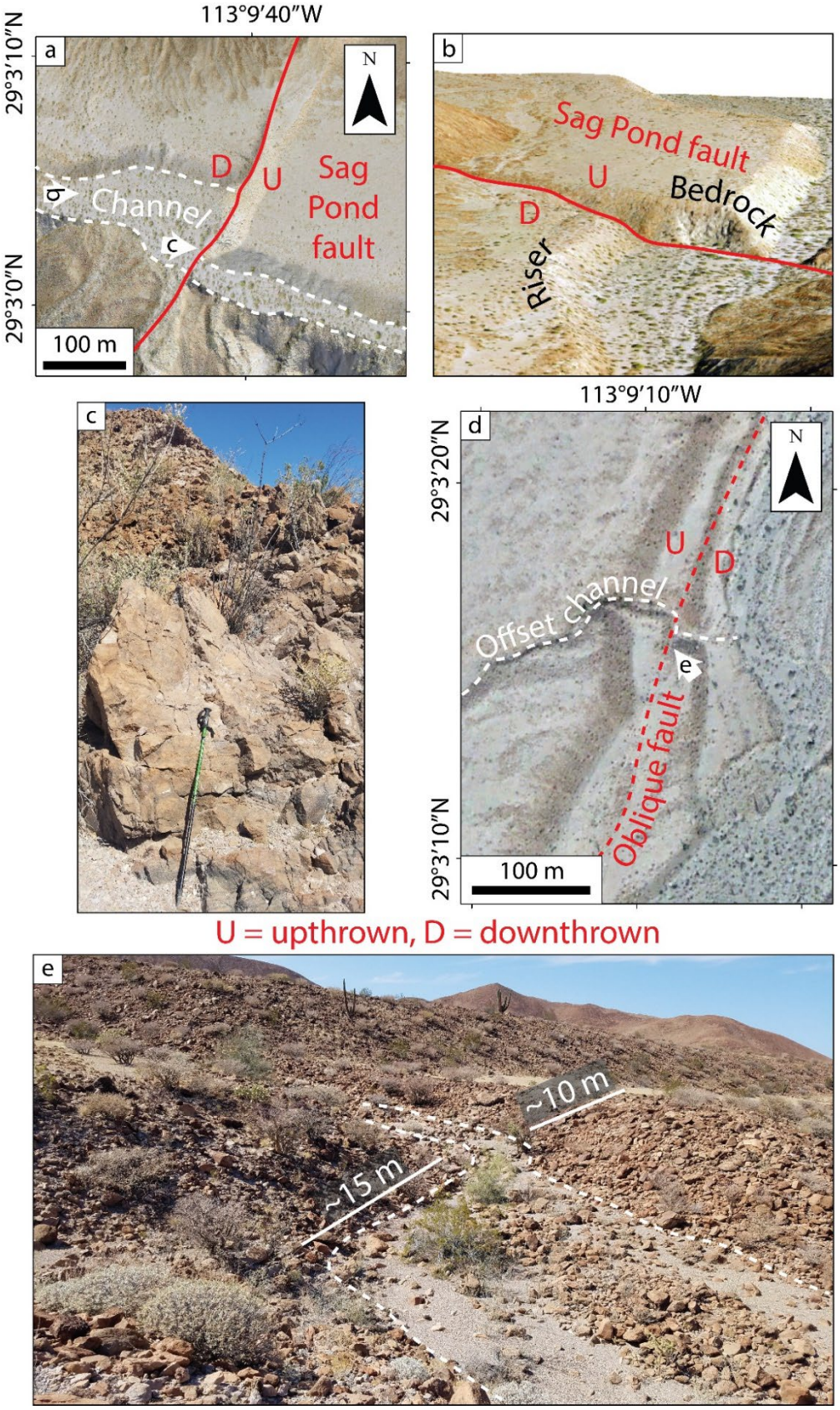
113°9′40″W
29°3′10″N
29°3′0″N
a
N
D
U
Sag
Pond
fault
q
Channel
c
100 m
b
Sag Pond fault
U
Bedrock
D
Riser
c
113°9′10″W
29°3′20″N
29°3′10″N
d
N
U
D
Offset channel
e
Oblique fault
100 m
U = upthrown, D = downthrown
e
~10 m
~15 m

Figure A9. (a) Stitched orthomosaic from drone images of apparent dextral offset on the Sag Pond fault. We conclude that this apparent offset is not tectonic and is instead due to complex erosion across this uphill-facing fault scarp. See main text for more details. Arrows show location and direction of Figures A9b and A9c. (b) Perspective view of terrace risers separated by the Sag Pond fault from drone image orthomosaics. Upthrown block exposes outcrops of volcanic bedrock. (c) Volcanic bedrock exposed below the basal strath of Quaternary terrace deposits located on the east (upthrown) side of the Sag Pond fault. (d) Satellite image from Google Earth of an apparent dextral offset of a small channel on a NNE-striking east-side-down fault (Sabbeth, 2020). This fault shows evidence for a component of dextral offset at two additional locations along strike to the south (Sabbeth, 2020). See main text for details. Arrow shows location and direction of Figure A9e. (e) Channel in a terrace dextrally offset by ~10 – 15 m (base of offset terrace risers traced by white dashed lines).

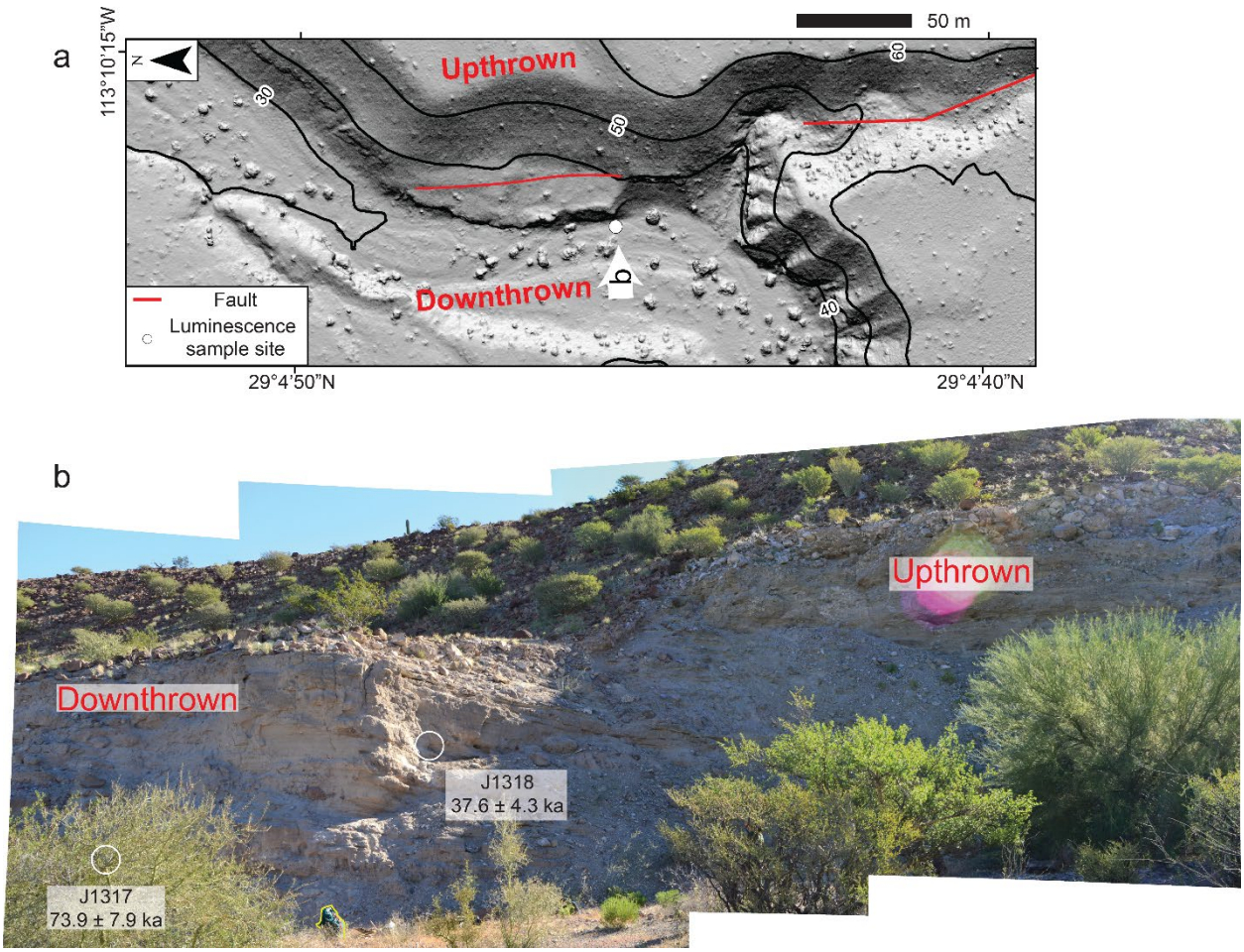

Figure A10. (a) Lower inset terrace from which luminescence samples were collected at the 'incised terrace' site. Basemap is shaded relief from ~0.1-m resolution drone digital elevation, with 10 m elevation contours from 3-m resolution digital elevation extracted from 0.5-m Pleiades images. Arrow shows location and direction of photo shown in (b). (b) Sampled cutbank on the inset terrace. The locations and ages of samples are shown in Figure 2.4b.

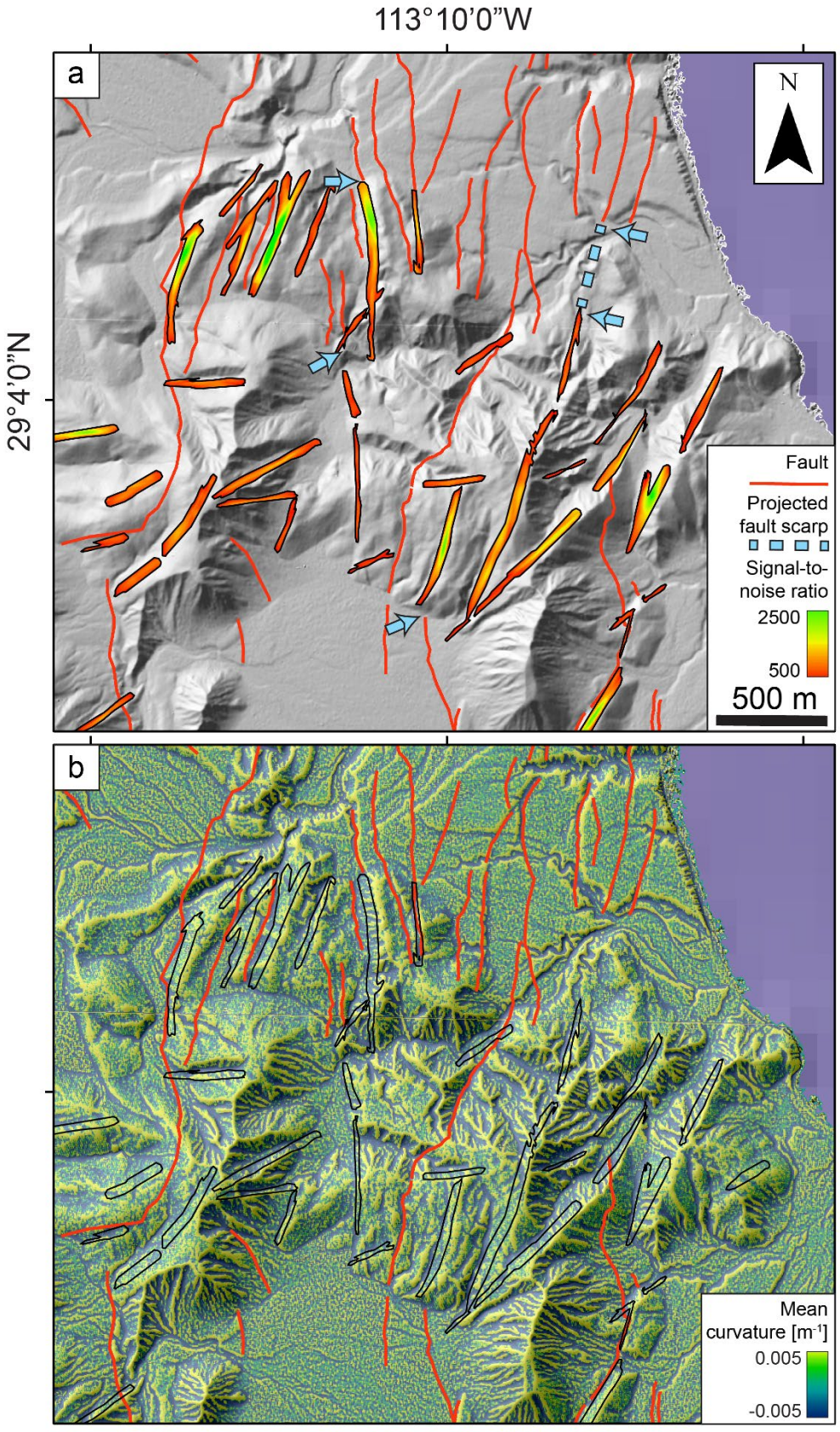
113°10'0"W
29°4'0"N
a
N
Fault
Projected fault scarp
Signal-to-noise ratio
2500
500
500 m
b
Mean curvature [m-1]
0.005
-0.005

Figure A11. (a) Faults mapped from template matching (signal-to-noise ratio shown with colors) and remote- and field-based techniques (solid red lines; Sabbeth, 2020) in the northeast quadrant of the South Volcanic Hills. Blue arrows are locations where template matched faults are relatively continuous with remote- and field-mapped faults. Dashed blue line in the upper right corner is where template matched faults project farther north along-strike with remote- and field-mapped faults in the Central Terraces. (b) Map of mean curvature. Thin black lines are the outline of faults from template matching. Basemap is 3-m resolution shaded relief extracted from 0.5-m Pleiades images.

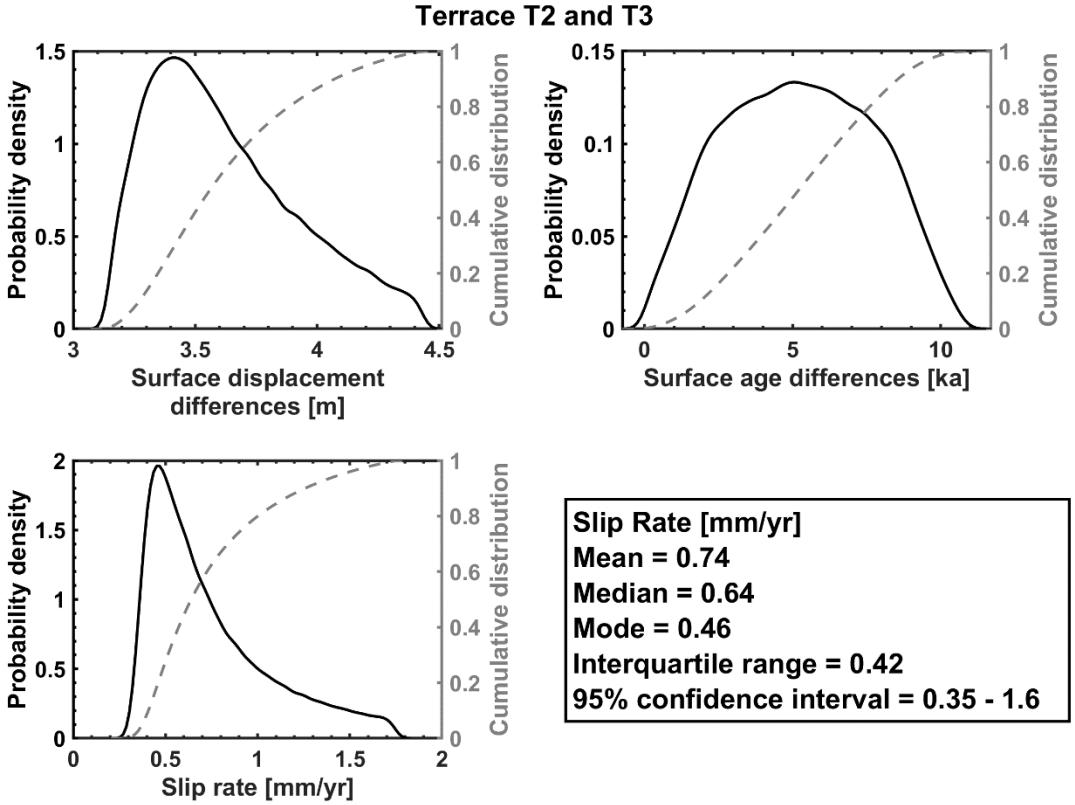

Figure A12. Probability density and cumulative distribution functions of (a) differences in surface displacement, (b) differences in terrace surface age, and (c) slip rate from 100,000 Monte Carlo simulations for the period between the deposition of terraces T2 and T3. Surface displacements are calculated following the methods described in Duckworth et al. (2020) and Thompson et al. (2002). Slip rates are calculated following methods described in Gold & Cowgill (2011). Details of methods are explained in Text A1.

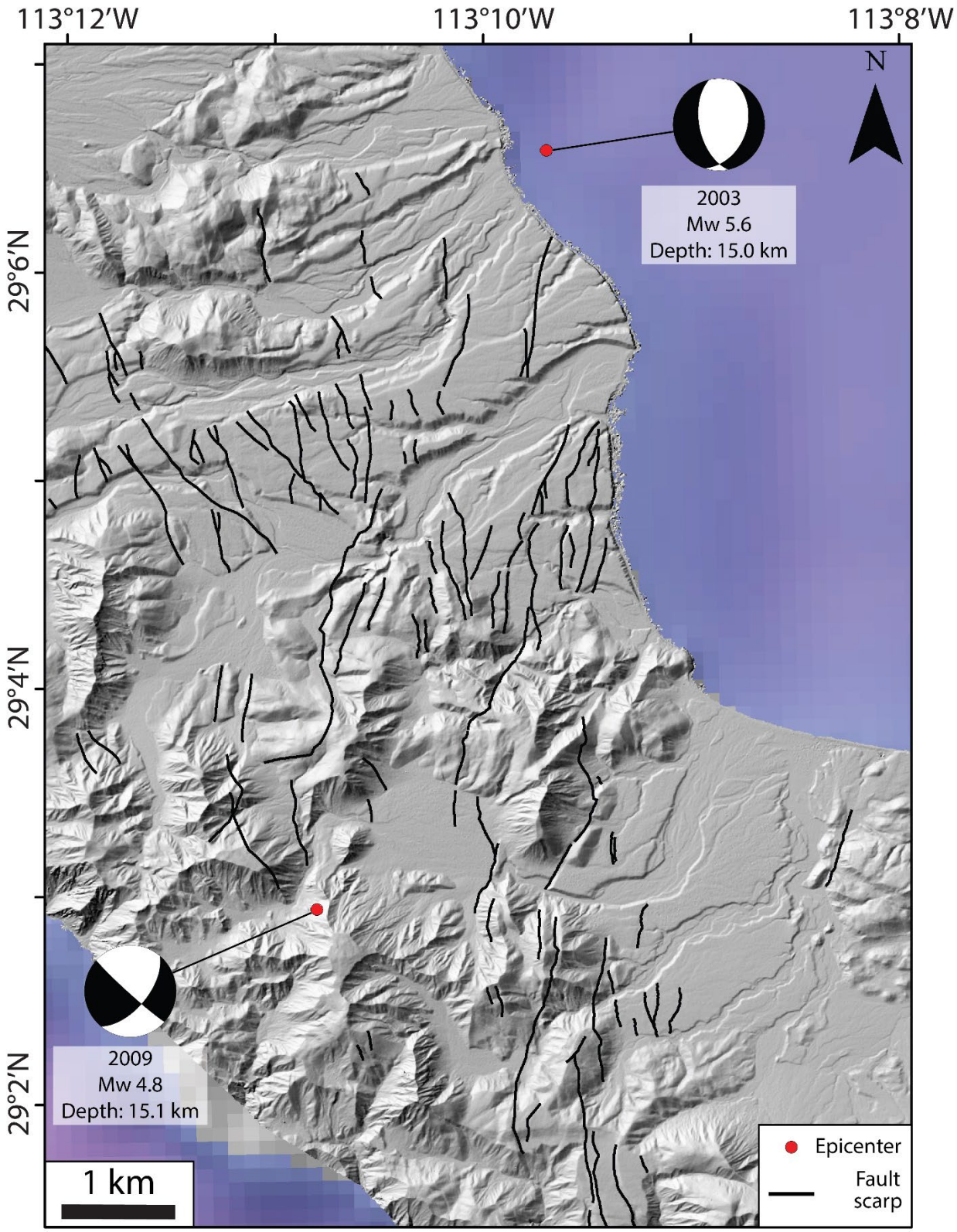
113°12′W
113°10′W
113°8′W
29°6′N
29°4′N
29°2′N
N
2003
Mw 5.6
Depth: 15.0 km
2009
Mw 4.8
Depth: 15.1 km
1 km
Epicenter
Fault scarp

Figure A13. Maps showing historic earthquakes near or on Isla Ángel de la Guarda (Castro et al., 2021; Castro et al., 2017), their focal mechanisms (Dziewonski et al., 1981; Ekström et al., 2010), and the onshore fault system mapped in this study (black lines; Sabbeth, 2020). Basemaps of topography and bathymetry are 3-m resolution shaded relief extracted from 0.5-m Pleiades images and GeoMapApp (Ryan et al., 2009), respectively.

Appendix A Tables

Table A1. Classification metrics for binary fault classifiers on Isla Ángel de la Guarda.

Location	SNR	$\log_{10}$ (SNR)	TPR	FPR	TNR	FNR	Precision	Accuracy	AUROC	Total Pixels
Central Terraces	250	2.40	0.47	0.38	0.62	0.53	0.11	0.61	0.57	303583
Central Terraces (post-processed)	250	2.40	0.33	0.12	0.88	0.67	0.22	0.83	N/A	303583
South Volcanic Hills	500	2.70	0.33	0.28	0.72	0.67	0.12	0.68	0.56	1149983
South Volcanic Hills (post-processed)	500	2.70	0.08	0.06	0.94	0.92	0.12	0.85	N/A	1149983

SNR = signal-to-noise ratio, TPR = true positive rate, FPR = false positive rate, TNR = true negative rate, FNR = false negative rate, AUROC = area under the receiver operating characteristic curve. Total Pixels based on 3-m resolution digital elevation extracted from 0.5-m Pleiades images. AUROC is N/A for post-processed results because it represents a single point on a receiver operating characteristic curve.

Table A2. Dosimetry data, equivalent doses, and single grain post-infrared infrared stimulated luminescence (p-IR IRSL) ages.

Figure	Lab code	Sample type	Latitude [°N] *	Longitude [°W] *	Elevation [m a.s.l.]	Depth [m]	K [%]	Th [ppm]	U [ppm]	Measured gamma dose-rate [Gy/ka]	Geologic dose-rate [Gy/ka]	Equivalent dose [Gy]	p-IR IRSL age [ka]
Fig. 2.5b	J1324	Terrace surface	29.0907	113.1723	87	0.38	2.1	5.9	1.92	0.8711 ± 0.0034	3.64 ± 0.11	in saturation	in saturation
	J1326	Terrace surface	29.0939	113.1716	68	0.38	3.3	8.5	2.32	0.9845 ± 0.0037	4.78 ± 0.16	4.6 ± 1.1	1 ± 0.2
Fig. 2.5b	J1365	Terrace surface	29.0914	113.1771	67	0.38	2.4	7.4	2.09	1.2943 ± 0.0041	4.47 ± 0.13	52.3 ± 19.6	11.7 ± 4.4
	J1366	Terrace surface	29.0918	113.1776	57	0.32	2.4	8.7	1.98	1.4059 ± 0.0038	4.65 ± 0.13	30.1 ± 6.4	6.5 ± 1.4
Fig. 2.6a	J1317	Terrace fill	29.0790	113.1710	41	7	1.9	4.6	1.84	0.8193 ± 0.0029	3.29 ± 0.1	243.5 ± 24.8	73.9 ± 7.9
	J1318	Terrace fill	29.0790	113.1710	41	3	2.2	4.8	1.51	0.9738 ± 0.0036	3.74 ± 0.12	140.8 ± 15.6	37.6 ± 4.3
Fig. 2.6b	J1370	Depression surface	29.0546	113.1589	102	0.47	1.3	5.9	1.55	0.7867 ± 0.0031	3.04 ± 0.09	28.4 ± 2.2	9.4 ± 0.8
Fig. 2.6c	J1320	Terrace fill	29.0518	113.1415	14	7	2.1	5.4	1.64	1.0739 ± 0.0038	3.78 ± 0.11	490.5 ± 62.5	129.7 ± 17
	J1321	Terrace fill	29.0518	113.1415	14	6.6	2.2	6.9	1.77	1.0604 ± 0.0038	3.93 ± 0.12	208.7 ± 20.6	53.1 ± 5.5
	J1322	Terrace fill	29.0518	113.1415	14	6	2.2	7.3	2.09	1.0482 ± 0.0037	4 ± 0.12	208.1 ± 17.6	52 ± 4.7
	J1375	Terrace fill	29.0518	113.1415	14	4	1.9	6.4	1.53	1.0427 ± 0.0037	3.67 ± 0.11	367.8 ± 32	100.2 ± 9.2
Fig. 2.6d	J1323	Terrace fill	29.0494	113.1411	21	1.5	2.1	5.9	2.04	0.9908 ± 0.0033	3.78 ± 0.11	127.9 ± 10.7	33.9 ± 3
	J1374	Terrace fill	29.0494	113.1411	21	0.4	1.8	4.3	1.37	N/A ± N/A	3.42 ± 0.08	174 ± 14.7	51 ± 4.5

*Sample locations provided use the WGS84 projection.

Appendix A References

Brennan, B., Lyons, R., & Phillips, S. (1991). Attenuation of alpha particle track dose for spherical grains. *International Journal of Radiation Applications and Instrumentation. Part D. Nuclear Tracks and Radiation Measurements, 18*(1-2), 249-253. https://doi.org/10.1016/1359-0189(91)90119-3

Bøtter-Jensen, L., Andersen, C., Duller, G. A., & Murray, A. S. (2003). Developments in radiation, stimulation and observation facilities in luminescence measurements. *Radiation Measurements, 37*(4-5), 535-541. https://doi.org/10.1016/S1350-4487(03)00020-9

Castro, R., Carciumaru, D., Collin, M., Vetel, W., Gonzalez-Huizar, H., Mendoza, A., & Pérez-Vertti, A. (2021). Seismicity in the Gulf of California, Mexico, in the period 1901–2018. *Journal of South American Earth Sciences, 106*, 103087. https://doi.org/10.1016/j.jsames.2020.103087

Castro, R., Stock, J., Hauksson, E., & Clayton, R. (2017). Active tectonics in the Gulf of California and seismicity (M> 3.0) for the period 2002–2014. *Tectonophysics, 719*, 4-16. https://doi.org/10.1016/j.tecto.2017.02.015

Duckworth, W. C., Amos, C. B., Schermer, E. R., Loveless, J. P., & Rittenour, T. M. (2020). Slip and strain accumulation along the Sadie Creek fault, Olympic Peninsula, Washington. *Journal of Geophysical Research: Solid Earth*, 2020JB020276. https://doi.org/10.1029/2020JB020276

Durcan, J. A., King, G. E., & Duller, G. A. (2015). DRAC: Dose Rate and Age Calculator for trapped charge dating. *Quaternary Geochronology, 28*, 54-61. https://doi.org/10.1016/j.quageo.2015.03.012

Dziewonski, A., Chou, T. A., & Woodhouse, J. (1981). Determination of earthquake source parameters from waveform data for studies of global and regional seismicity. *Journal of Geophysical Research: Solid Earth, 86*(B4), 2825-2852. https://doi.org/10.1029/JB086iB04p02825

Ekström, G., Nettles, M., & Dziewoński, A. (2012). The global CMT project 2004–2010: Centroid-moment tensors for 13,017 earthquakes. *Physics of the Earth and Planetary Interiors, 200–201*, 1–9. https://doi.org/10.1016/j.pepi.2012.04.002

Galbraith, R. F., Roberts, R. G., Laslett, G. M., Yoshida, H., & Olley, J. M. (1999). Optical dating of single and multiple grains of quartz from Jinmium rock shelter, northern Australia: Part I, experimental design and statistical models. *Archaeometry, 41*(2), 339-364. https://doi.org/10.1111/j.1475-4754.1999.tb00987.x

Guérin, G., Discamps, E., Lahaye, C., Mercier, N., Guibert, P., Turq, A., et al. (2012). Multi-method (TL and OSL), multi-material (quartz and flint) dating of the Mousterian site of Roc de Marsal (Dordogne, France): correlating Neanderthal occupations with the climatic variability of MIS 5–3. *Journal of Archaeological Science, 39*(10), 3071-3084. https://doi.org/10.1016/j.jas.2012.04.047

Hanks, T. C. (2000). The age of scarplike landforms from diffusion-equation analysis. *Quaternary Geochronology: Methods and Applications, 4*, 313-338. https://doi.org/10.1029/RF004p0313

Hilley, G., DeLong, S., Prentice, C., Blisniuk, K., & Arrowsmith, J. (2010). Morphologic dating of fault scarps using airborne laser swath mapping (ALSM) data. *Geophysical Research Letters, 37*(4). https://doi.org/10.1029/2009GL042044

Huntley, D. J., & Baril, M. (1997). The K content of the K-feldspars being measured in optical dating or in thermoluminescence dating. *Ancient TL, 15*(1), 11-13.

Liritzis, I., Stamoulis, K., Papachristodoulou, C., & Ioannides, K. (2013). A re-evaluation of radiation dose-rate conversion factors. *Mediterranean Archaeology and Archaeometry, 13*(3), 1-15.

Prescott, J. R., & Hutton, J. T. (1994). Cosmic ray contributions to dose rates for luminescence and ESR dating: large depths and long-term time variations. *Radiation measurements, 23(2-3)*, 497-500. https://doi.org/10.1016/1350-4487(94)90086-8

Ryan, W., Carbotte, S., Coplan, J., O'Hara, S., Melkonian, A., Arko, R., & Bonczkowski, J. (2009). Global multi-resolution topography synthesis. *Geochemistry, Geophysics, Geosystems, 10*(3), Q03014. https://doi.org/10.1029/2008GC002332

Sabbeth, L. (2020). *Provenance, structural geology, and sedimentation of the Miocene and Pliocene Californias,* (Doctoral dissertation). Retrieved from CaltechTHESIS. (https://resolver.caltech.edu/CaltechTHESIS:09212020-084147468). California Institute of Technology.

Sare, R., Hilley, G. E., & DeLong, S. B. (2019). Regional-Scale Detection of Fault Scarps and Other Tectonic Landforms: Examples From Northern California. *Journal of Geophysical Research: Solid Earth, 124*(1), 1016-1035. https://doi.org/10.1029/2018JB016886

Scherler, D., & Schwanghart, W. (2020). Drainage divide networks–Part 1: Identification and ordering in digital elevation models. *Earth Surface Dynamics, 8*, 245-259. https://doi.org/10.5194/esurf-8-245-2020

Schwanghart, W., & Scherler, D. (2020). Divide mobility controls knickpoint migration on the Roan Plateau (Colorado, USA). *Geology, 48 (7):* 698–702. https://doi.org/10.1130/G47054.1

Thompson, S. C., Weldon, R. J., Rubin, C. M., Abdrakhmatov, K., Molnar, P., & Berger, G. W. (2002). Late Quaternary slip rates across the central Tien Shan, Kyrgyzstan, central Asia. *Journal of Geophysical Research: Solid Earth, 107*(B9), ETG 7-1-ETG 7-32. https://doi.org/10.1029/2001JB000596

Appendix B for Chapter 3: Spatially varying critical zone structures at a steep, forested site near Coos Bay, Oregon

Text B1. Schmidt hammer rock hardness measurements

We use an Original Schmidt Concrete Test Hammer, Type N, to measure rock hardness based on a dimensionless rebound value (RV), where a higher RV indicates stronger material. Recent studies use Schmidt hammers to infer weathering extent in constant lithologies (e.g., Goudie, 2006; Murphy et al., 2016). Here, we take at least eight measurements at a site or averaged across an outcrop to determine a characteristic, mean RV. Measurements are spaced at least two cm-apart. Some individual measurements record an RV of 10, which is the lowest sensitivity of our Schmidt hammer. Thus, when values of 10 are included in the mean RV of a site, this average represents a maximum RV. We also separate measurements made horizontally on vertical faces or vertically on horizontal faces.

We calculate 14 mean horizontal RV sites within our study area on Tyee Sandstone (Figure B2; Table B11). The mean RV on saprolite and pervasively weathered sandstone is 13.8 ± 2.5 from locales across the study area. There is a roughly nine-point jump between the RV of the strongest pervasively oxidized rock and the weakest fractured bedrock. The mean RV on fractured bedrock is 31.2 ± 3.0. This material includes two gray corestones found at the benchmark site, ~17 m along Line 4 embedded within the roots of a Douglas fir. We only collected five RV measurements on one corestones but report this value because of its similarity with the second corestone and measurements on an exposed outcrop of gray sandstone (HR1-1; Figure B2f). We report one RV on a sandstone nodule in the outcrop beneath Line 1 with a mean of 50.4 ± 2.6. This value is ~17 points stronger than the strongest fractured rock sample. Together, more weathered material is consistently weaker than less weathered rock.

We also collect five vertical RV for sites labeled SR (along Line 2) and SL (along Line 3), measuring the strength of road material (Figure B3; Table B12). RV from SR, measured on competent but fractured sandstone, is consistently higher than that of SL that was observed to be pervasively oxidized and weathered in the field.

Text B2. Ground penetrating radar facies mapping

We map ground penetrating radar (GPR) facies based on the relative roughness of GPR reflectors. First, we reprocess our GPR surveys with GPRPy using no automatic gain control and setting contrast to 500. This process highlights shallow, discontinuous reflectors while muting deeper ones. We export this GPR profile as a TIFF file of digital number (DN) values, where 0 is the lightest and 255 is the darkest signal. For all surveys we classify by roughness, we clip the x length of the survey to 96 m-long and y length to 200 ns so that arbitrary cell dimensions are constant. Ninety-six meters represents the maximum length of a GPR survey we will perform this mapping. If a line is shorter than 96 m, we include the white space, which we clip out in post. Then, we import the TIFF file of the GPR profile into the MATLAB toolbox TopoToolbox 2 (Schwanghart and Scherler, 2014). Next, we use the function called "roughness" using the function option 'roughness' on the DN values to find the largest value difference between a cell and its surrounding cells. We then smooth this map with a moving radius five times the arbitrary cell size of the TIFF file. We use a DN difference of 80 as our threshold, where all those above this value we consider a rough GPR signal assumed to be shallow regolith disturbed by biotic or abiotic weathering processes. We apply this threshold to all GPR surveys but acknowledge that there are site-specific variations not captured automatically.

Text B3. Bedrock drainage weathering model

Rempe and Dietrich (2014) describes a bedrock weathering mechanism based on the drainage of reactive water and elevation of a steady state groundwater table. We use formulations therein to create three, three-dimensional critical zone models based on the ratio of bedrock fluvial relief Z_{b0} [m] to topographic fluvial relief Z_{s0} [m] measured at the Anderson et al. (2002) borehole and different considerations for sitewide bedrock (Z_b [m]) and topographic (Z_s [m]) fluvial relief. We explore three considerations below.

For the constant model that produces CZ(RD4m), we use the MATLAB toolbox TopoToolbox 2 (Schwanghart and Scherler, 2014) to calculate the location of channels using a drainage area of 1500 m^2 as a threshold for channelization that creates streams most similar to those historically mapped. Then, we use these channels and the function "vertdistance2stream" to calculate Z_s. We multiply this Z_s map by a constant value for Z_b/Z_s (0.9 in this case, see Main Text Section 3.4.5.1) to calculate a map of Z_b. Finally, we subtract Z_b from Z_s to calculate the predicted depth to unweathered bedrock and smooth this depth map with a moving circular radius of 5 m. This model assumes a constant hillslope length across the entire benchmark site of 76 m (Rempe and Dietrich, 2014). To test that this value is representative of the whole catchment, we plot the distribution of hillslope length measured at ridgelines and find that said distribution is relatively centered at 76 m (Figure B12).

For more complex models, we follow formulations for Z_b and Z_s in Rempe and Dietrich (2014). Assuming topography resultant of nonlinear soil transport (Roering et al., 1999), we calculate a map of Z_s using site-specific parameters (Table B5)

$$Z_s(x) = \frac{-{S_c}^2}{2\beta}\left[\sqrt{\kappa^2 + (2\beta x/S_c)^2} - \kappa ln\left(\frac{\sqrt{\kappa^2+(2\beta x/S_c)^2}+\kappa}{2\beta/S_c}\right)\right] + \frac{{S_c}^2}{2\beta}\left[\sqrt{\kappa^2 + (2\beta L/S_c)^2} - \kappa ln\left(\frac{\sqrt{\kappa^2+(2\beta L/S_c)^2}+\kappa}{2\beta/S_c}\right)\right], \quad \text{(B1)}$$

where x is distance from ridgetop [m], S_c is critical slope [m/m], κ is soil diffusivity [m^2/yr], and L is hillslope length. Then, β is $(\rho_r/\rho_s)C_0$ where ρ_r is bulk rock density [g/cm^3], ρ_s is bulk soil density [g/cm^3], and C_0 is channel incision rate [mm/yr]. Z_b depends on the steady state elevation of the groundwater table (Bear, 1988). Thus, we calculate Z_b by (Rempe and Dietrich, 2014)

$$Z_b(x) = \frac{\theta C_0}{K}(L^2 - x^2), \quad \text{(B2)}$$

where θ [m^3/m^3] is bedrock porosity and K [m/s] is bedrock hydraulic conductivity. These parameters are expressed as the ratio K/θ [m/s] and assumed to be 10^{-11} m/s at CB1 (Rempe and Dietrich, 2014). However, measured values of both θ and K vary by orders of magnitude and are difficult to estimate over the spatial scale of the study site. See Rempe and Dietrich (2014) for more details on this method.

For the variable model, we hold all previously established variables constant (Table B5) except (1) hillslope length L and (2) the ratio of K/θ. First, L is measured as the horizontal distance between a cell in a landscape and the channel into which it drains using the TopoToolbox "flowdistance" function and our Lidar DEM. We apply Equations B1 and B2 using this map of spatially variable L to calculate Z_b and Z_s. We can then obtain depth to the weathered-unweathered bedrock by subtracting Z_b from Z_s, hereafter CZ(RDvar). Second, as K varies by orders of magnitude at this benchmark site (e.g., Montgomery et al., 2002), we perform a sensitivity test on K/θ to reproduce a depth to unweathered bedrock of 4.5 m at the location of the 35 m-deep CB1

borehole by iterating the exponent of K/θ from -10.95 to -11.2 by 0.025 increments, which is centered around that estimated of 10^{-11} m/s. We find this K/θ to be $10^{-11.025}$ m/s for CZ(RDvar).

For the topography model, we substitute natural topographic variations into Z_s. We first calculate every surface water accumulation path in the elevation of the study site. Then, we subtract the elevation of the entire path by that at its bottommost end, so all cells in stream channels have an adjusted elevation of 0 m. This modified topographic surface is now analogous to Z_s using real topographic variation instead of theoretical. We subtract the Z_b calculated by Equation B2 from this new Z_s to obtain a map of depth to the weathered-unweathered bedrock interface from natural topography, hereafter CZ(RDtopo). We use the same sensitivity test as CZ(RDvar) to find the best-fit K/θ. We find this K/θ to be $10^{-11.125}$ m/s for CZ(RDtopo).

Text B4. Topographic stress model and ambient tectonic stress compilation

Following Moon et al. (2017), we prepare a 2 m-resolution LiDAR DEM for topographic stress modeling. First, we clip a subset of the DEM and use the MATLAB function tukeywin to taper edge elevation of the DEM to mean elevation using a length ratio of the taper window of 0.2. Then, we subtract that mean elevation from the DEM so the taper is to a relative elevation of 0 m to maintain horizontal stress equilibrium. We place the edges of the DEM manually along similar elevations near the mean and at least one hillslope length away from the area of interest to reduce edge effects. We use MOVE software to transform this DEM into a triangular mesh with leg lengths ~5 m-long within the area of interest, up to 50 m-long at the DEM edges to reduce computational time. Then, we create a three-dimensional grid within which we calculate stresses. Although the dimensions of this grid differs for different areas of interest, we use a constant plan view resolution of 5 m and vertical resolution of 3 m at all sites. We extend the lower boundary of this grid at least 60 m below the lowest point in the area of interest and only consider stresses calculated within this grid that are below the topographic surface. Lastly, we apply the Poly3D model (Thomas, 1993) assuming a linear elastic and homogenous material and parameters defined in Table B7.

We also produce a compilation of 14 data points to estimate ambient tectonic compression at the benchmark site for our CZ(stress3) model (Table B6; Brown and Hoek, 1978; Heidbach et al., 2018; Lindner and Halpern, 1978). We compile data from across the west coast of North America because stress measurements near southwestern Oregon are sparse. In many cases, sources provide the maximum and minimum horizontal stresses ($\sigma^a H$ and $\sigma^a h$, respectively) and the vertical stress ($\sigma^a V$) from ambient tectonics (compression positive) for our tectonic stress compilation. When these values are not provided but principal stress values are, vertical stress is

estimated as vertical overburden from the measurement depth of available principal stresses using an average rock density of 2650 kg/m3 by $\sigma^a V = \rho g h$, where ρ is rock density, g is gravitational acceleration, and h is measurement depth. If a principal stress is within 3 MPa of this estimation, that component is designated as $\sigma^a V$ and the higher and lower remaining principal stresses are designated as $\sigma^a H$ and $\sigma^a h$, respectively. If not, we discard that data point. For data from the World Stress Map 2016 (Heidbach et al., 2018), we consider only locations assigned a quality assessment of E or higher on a scale from A (highest) to F (lowest). Then, for sites with more than one entry, we weight magnitudes of $\sigma^a H$, $\sigma^a h$, and $\sigma^a V$ by the inverse of the total number of entries. Finally, we calculate weighted linear regressions of $\sigma^a H$, $\sigma^a h$, and $\sigma^a V$ against measurement depth to extrapolate stress magnitudes at the surface and estimate stress magnitude gradient with depth (Figure B4). We orient $\sigma^a H$ N-S based on geologic evidence near the benchmark site (Section 3.2).

Text B5. Site description of geophysical surveys

At the time of the survey, Line 1, located ~ 2 km east of CB1 (Figure 3.1b), was clear-cut with little vegetation > 1 m-tall. Here, the underlying sandstone strikes roughly parallel to the survey (Baldwin and Beaulieu, 1973). Line 1 begins in the south from an unpaved road and climbs a 2 – 3 m-high rise from 0 -15 m. Atop the rise from 15 – 36 m, we find cut stumps, low vegetation, and thick grasses. An exposure directly to the west of Line 1 shows friable, weathered, bedded, light tan sandstone or saprolitic sandstone. The surface of this layer is bioturbated by large tree roots (Figure B5a – d). This bedded sandstone is underlain by more massive, weathered sandstone.

Line 2 runs north to south for 12 m on competent, weathered and fractured, yellow to gray sandstone that forms the surface of an unpaved road directly beneath Line 1 (Figure 3.1b; Figure B5e – h). This road outcrop becomes obscured by vegetation and soil past the end of the survey.

We performed Line 3 directly south of Lines 1 and 2, surveyed from north to south going up a ridge to a cleared landing site that is likely flattened at the top by construction work (Figure 3.1b; Figure B6). Similar to Lines 1 and 2, bedding strikes roughly parallel to the survey orientation. The first 50 m from north to south is covered by a layer of dark gravel, possibly construction fill. Moving south up a ~20 m-high hill, we find pervasively oxidized sandstone exposed in the road. Line 3 has a total relief of 23.5 m with adjacent, E-W oriented spur ridges and zero-order channels on either side of the line (Figure B6a – b).

We performed Line 4 at the ridgeline of the benchmark site above CB1, surveyed from west to east along the ridgeline road (Figure 3.1c; Figure B7). Here, the underlying sandstone strikes roughly parallel to the survey, dipping into the E-W oriented ridge (Montgomery et al., 1997). The west end begins on a forested rise, from 0 – 25 m along Line 4, which was once a landing site; the topmost layer here was presumably removed by road construction. Topography

steepens directly to the north of the line into the benchmark site's hollows, including CB1. We install geophones on the rise in soft soil and pervasively weathered material. We find some < 10 cm exposures of weathered, orange to yellow sandstone on the rise. Line 4 flattens along a roadbed from 25 – 70 m along the survey. The CB1 borehole and crossing with Line 5 are located at 27 m and 29 m, respectively. The effect of road metal becomes apparent at 35 – 50 m as we took extra effort to install geophones into the harder material. Here, the line is approximately 1 – 5 m away from the northern slope into the benchmark site's hollows. A N-S oriented spur ridge east of CB1 and a hollow to the east of this ridge is located at roughly 35 – 55 m and 55 – 65 m, respectively. Line 4 begins to climb a forested ridge with no evidence of construction at ~ 70 m. At an outcrop directly south of this ridge, we find mostly fractured but unoxidized, gray sandstone. Here, we find no weathered bedrock exposed at the surface despite the competent sandstone in this outcrop.

We also performed Line 5 at the benchmark site, surveyed from the north end approximately 20 m downslope into the CB1 hollow towards the south (Figure 3.1c; Figure B8). Here, the underlying sandstone strikes roughly perpendicular to the survey (Montgomery et al., 1997). Slopes are steep, ~40°, and covered by dense undergrowth and a dark brown soil mantle with evidence of burrowing. The line reaches the ridgeline road at 20 – 25 m and crosses Line 4 at 19 m. The CB1 borehole is ~2 m west of this crossing. Line 5 then descends into another forested slope towards the south. Similar to the north slope, we find a soft, dark brown soil mantle with few exposures of weathered bedrock.

Appendix B Figures

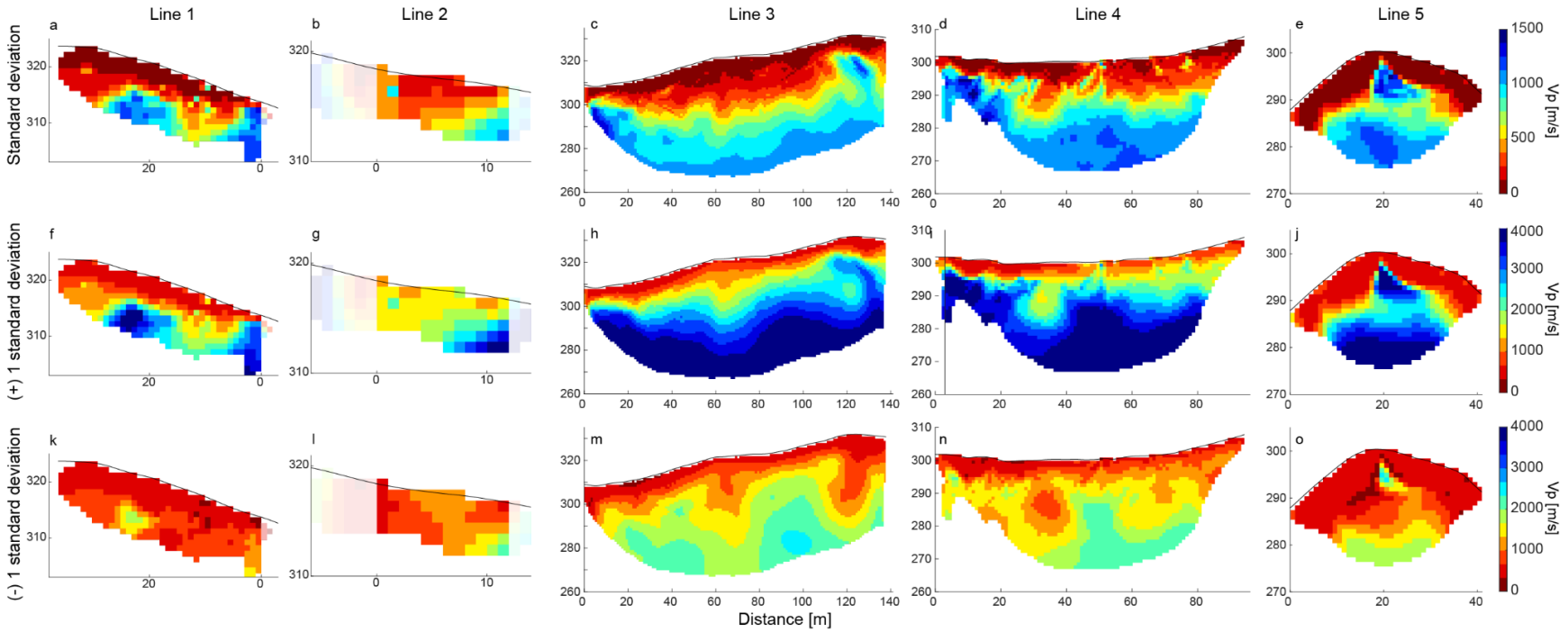

Figure B1. (a – e) Standard deviation of P-wave velocity (Vp), (f – j) average Vp plus one standard deviation, and (k – o) minus one standard deviation for Lines 1 – 5 (Huang et al., 2021). Inversion outside the extent of geophones is shaded out.

Figure B2. Horizontal Schmidt hammer measurement sites for (a) SO1, (b) SO2 with (inset) SO2-2, ~1 m to the left of the figure, (c) HR1-1 with (inset) close-up of site, (d) B1-1 outcrop, (e) B2-1 outcrop, and (f) CS1 and CS2. Squares indicate Schmidt hammer measurements for that specific location, circles indicate Schmidt hammer measurements averaged for an entire exposure.

Figure B3. Vertical Schmidt hammer measurement sites for (a) SR1-1, (b) SL1-1, (c) SL2-1, (d) SL3-1, and (e) SL4-1. Squares indicate Schmidt hammer measurements for that specific location, circles indicate Schmidt hammer measurements averaged for an entire exposure.

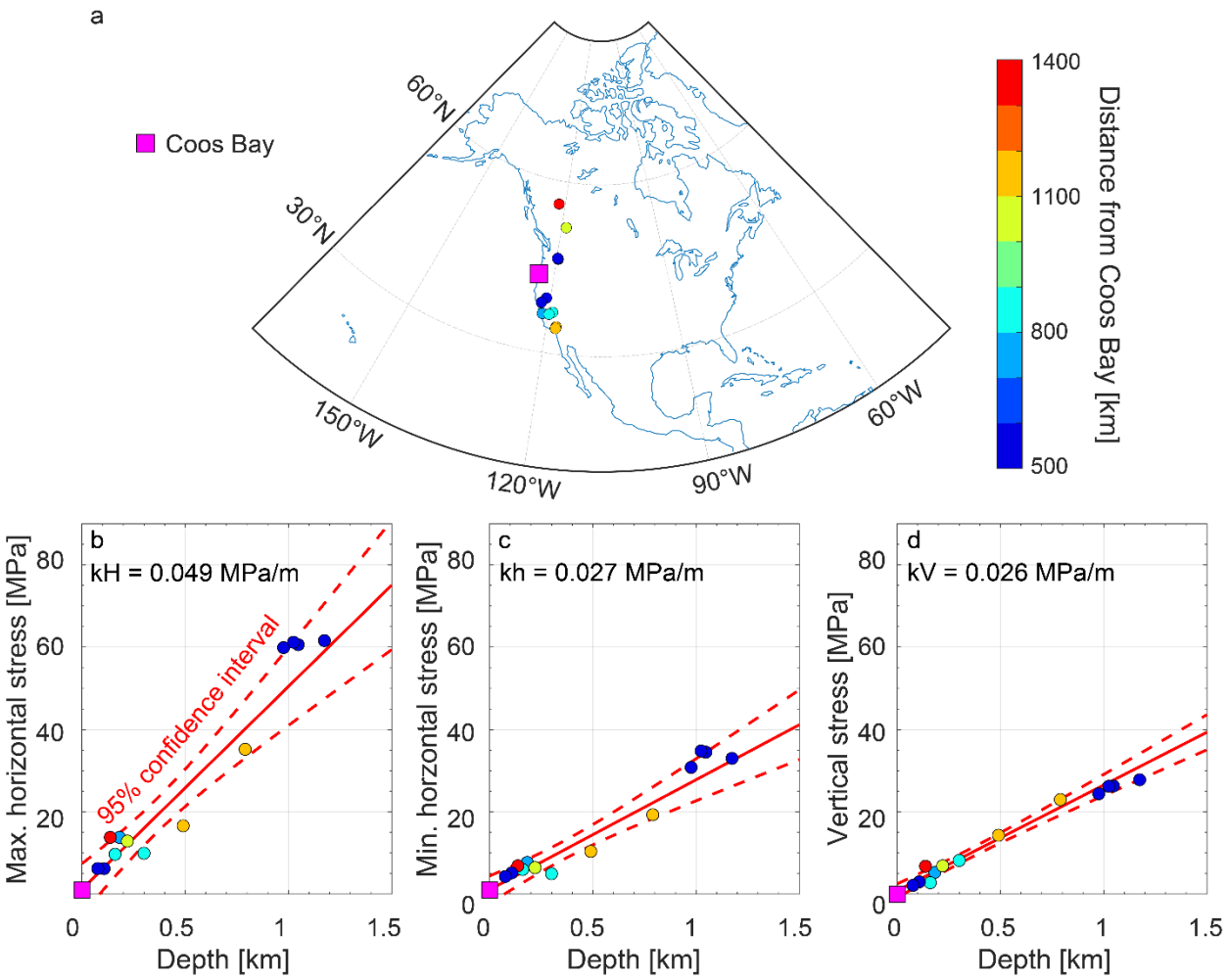

Figure B4. (a) Location of in-situ stress magnitude and orientation from the World Stress Map 2016 (Heidbach et al., 2018) and other sources (Brown and Hoek, 1978; Lindner and Halpern, 1978) for our stress compilation. (b) Depth versus maximum horizontal, (c) minimum horizontal, and (d) vertical stress magnitude [MPa], where kH, kh, and kV are the best-fit slope of the linear regression line in red that represents the stress magnitude gradient with depth. All circular points are colored by distance from Coos Bay, Oregon, USA [km]. Pink square represents (a) location of Coos Bay or (b – d) stress magnitude at the surface (y-intercept) of the benchmark site estimated from the regression of 1 MPa, 1 MPa, and 0 MPa for maximum horizontal, minimum horizontal, and vertical stress, respectively.

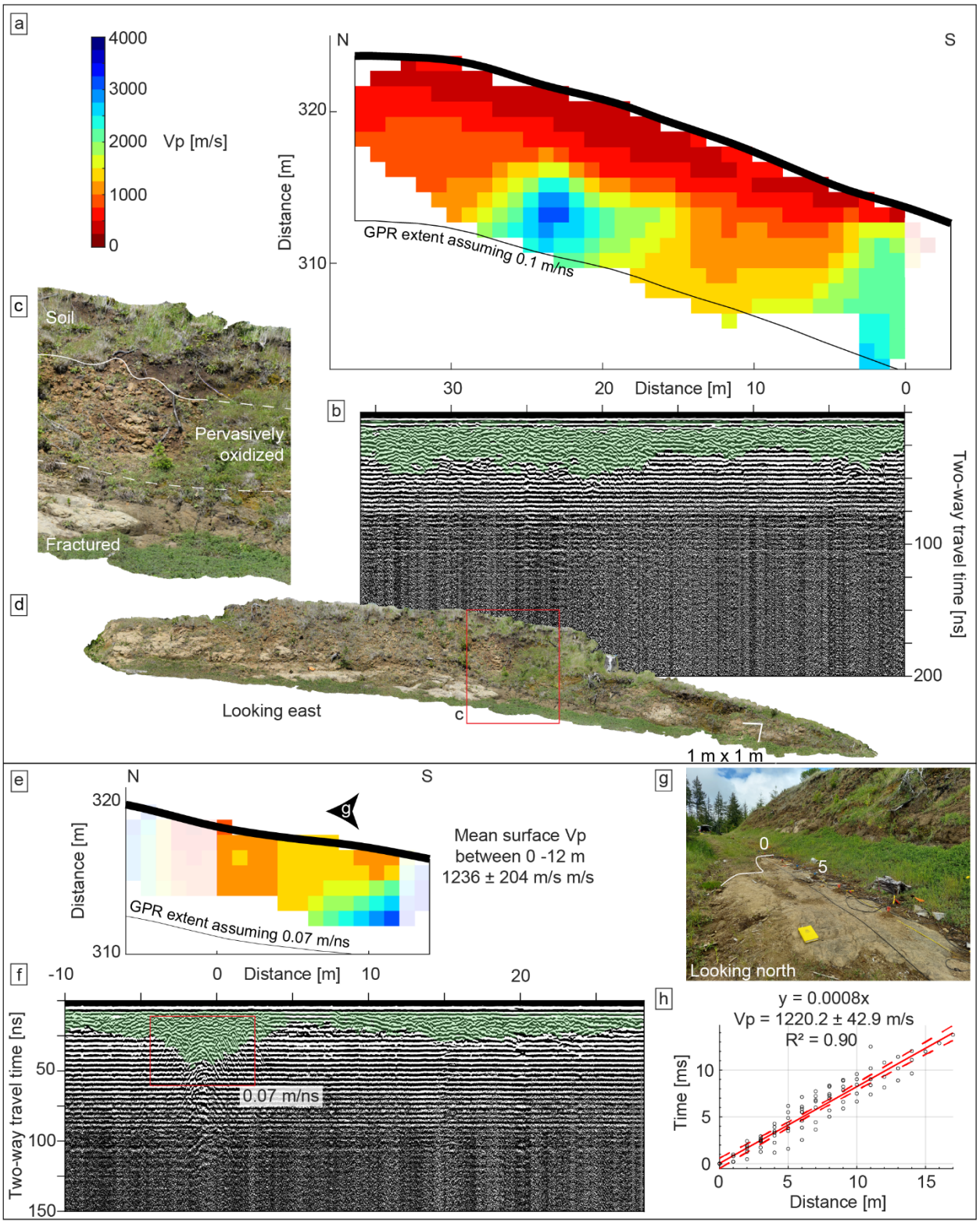

Figure B5. (a) P-wave velocity (Vp) tomogram results of Line 1. North end on left, south end on right. Black outline indicates extent of Line 1 ground penetrating radar (GPR) survey assuming a

radar velocity of regolith of 0.1 m/ns. Inversion outside the extent of geophones is shaded out. (b) GPR results with distance on x axis same as (a) and two-way travel time [ns] on y axis. Green area delineates a heterogenous GPR facies with relatively rough reflectors. (c) Annotated weathered profile of outcrop over which we performed Line 1; extent is red box in (d) of full outcrop model. (a), (b), and (d) have the same x scale, (a) and (d) also have the same y scale. (e) Vp tomogram results of Line 2, same as (a), including color scale. (f) GPR results, same as (b) for Line 2. Red box shows hyperbola used to estimate GPR velocities. (e) and (f) have the same x scale. (g) First seven meters of Line 2 over competent bedrock with geophones 0 and 5 annotated taken at location annotated in (e). (h) Distance from sledgehammer shot versus first-arrival traveltime fit to a linear least squares best fit line (solid red), with 95% confidence interval (dashed red). Equation of best fit shown, where x is distance [m], y is time [s], and slope is 0.0008 s/m.

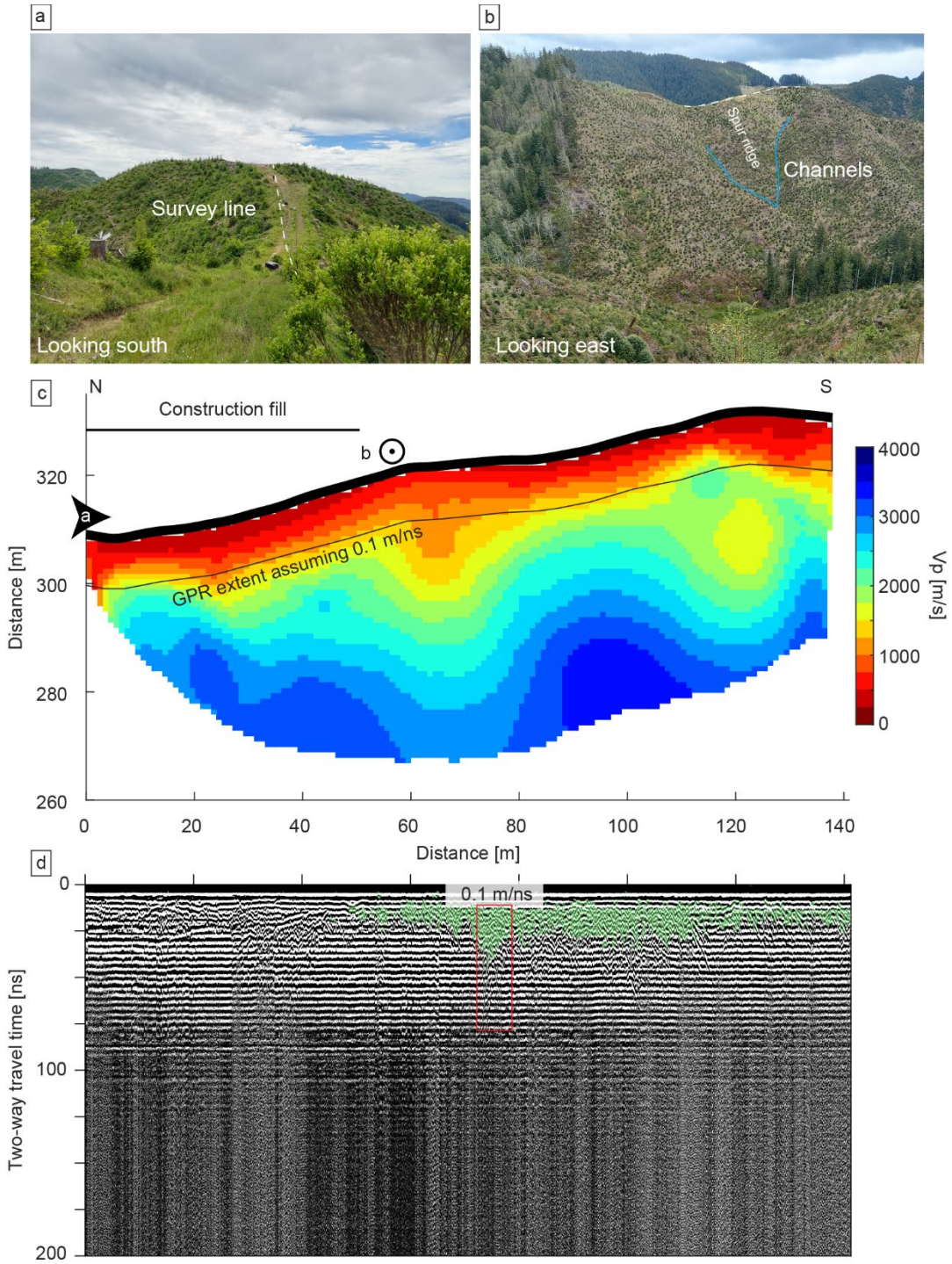

Figure B6. (a) View of Line 3 looking south towards a landing top. (b) View of Line 3 looking east, showing two zero-order channels with a ridge in between them that flank the survey. Location and vantage of (a) and (b) shown in (c). (c) P-wave velocity (Vp) tomogram results of Line 3. North

end on left, south end on right. Black outline indicates extent of Line 3 ground penetrating radar (GPR) survey assuming a radar velocity of regolith of 0.1 m/ns. (d) GPR results with distance on x axis same as (c) and two-way travel time [ns] on y axis. Red box shows hyperbola used to estimate GPR velocities. Green area delineates a heterogenous GPR facies with relatively rough reflectors. Facies mapping not performed from 0 – 45 m due to possible road fill in that section observed in the field.

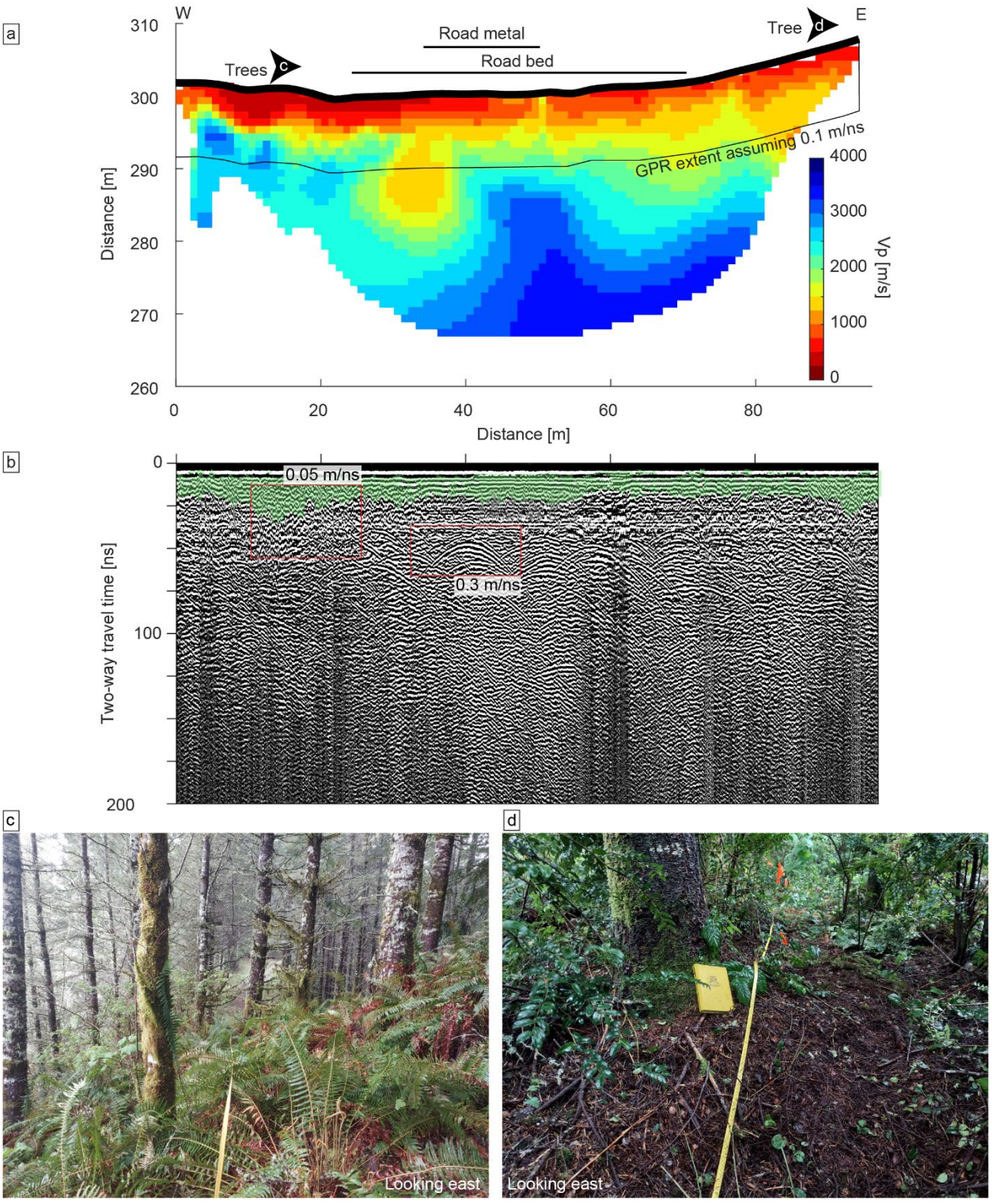

Figure B7. (a) P-wave velocity (Vp) tomogram results of Line 4. West end on left, east end on right. Black outline indicates extent of Line 4 ground penetrating radar (GPR) survey assuming a

radar velocity of regolith of 0.1 m/ns. (b) GPR results with distance on x axis same as (a) and two-way travel time [ns] on y axis. Red box shows hyperbola used to estimate GPR velocities. Green area delineates a heterogenous GPR facies with relatively rough reflectors. Facies mapping performed where we observed the road bed to highlight differences between natural and human-influenced reflectors. (c) View of Line 4 looking east through a forested section of the line. (d) View of Line 4 looking east at ~90 m showing where the surveys approach a tree. Location and vantage of (c) and (d) shown in (a).

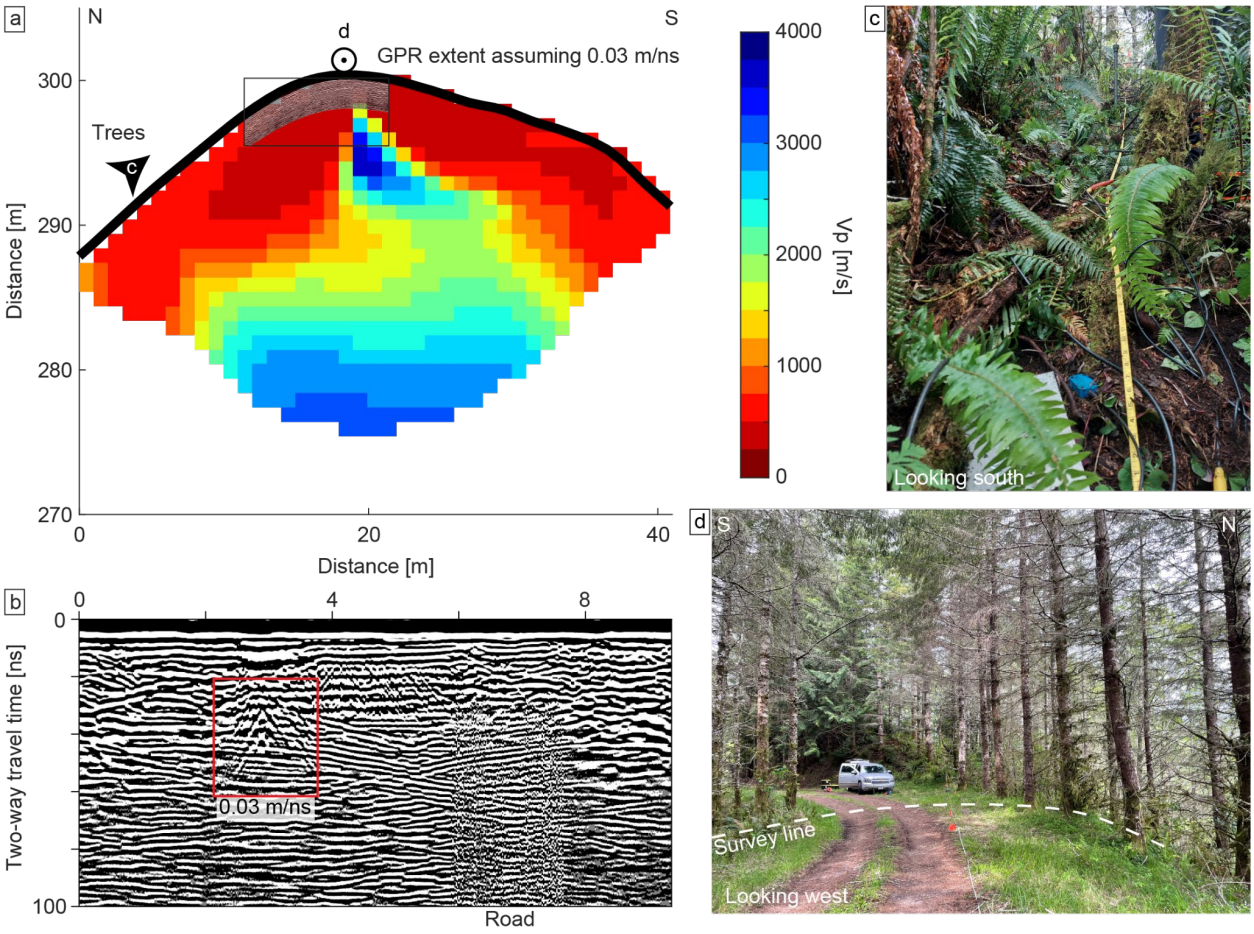

Figure B8. (a) P-wave velocity (Vp) tomogram results of Line 5. North end on left, south end on right. Black box shows extent of Line 5 ground penetrating radar (GPR) survey assuming a radar velocity of regolith of 0.03 m/ns. (b) GPR results with distance [m] on x axis and two-way travel time [ns] on y axis. Red box shows hyperbola used to estimate GPR velocities. (c) View of Line 5 looking south and upslope showing vegetation debris and soil. (d) View of Line 5 looking west at where the Vp and GPR surveys cross a road. Location and vantage of (c) and (d) shown in (a).

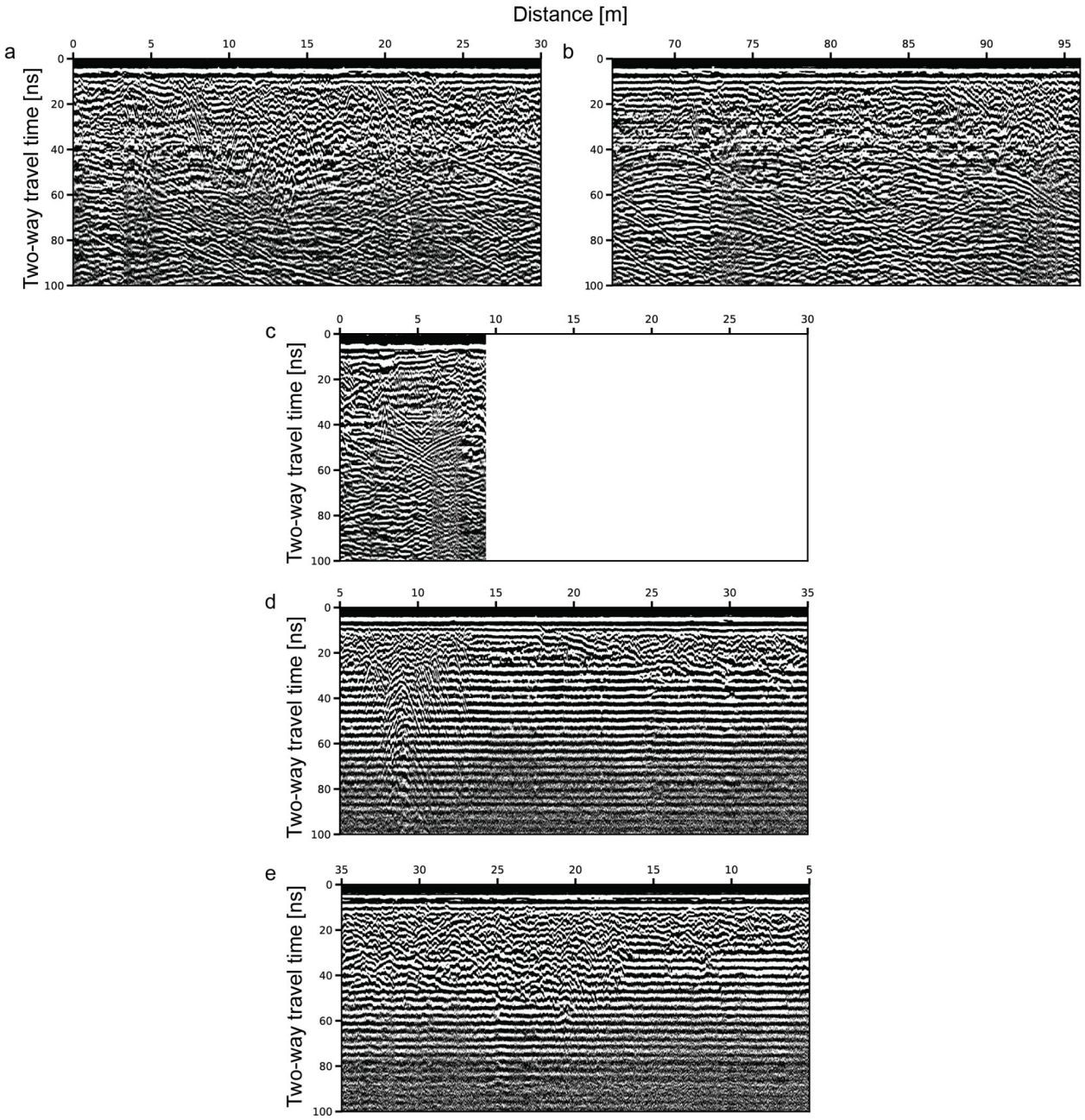

Figure B9. Ground penetrating radar profiles at (a) 0 – 30 m along Line 4, (b) 66 – 96 m along Line 4, (c) 0 – 30 m along Line 5, (d) 5 – 35 m along Line 2, and (e) 5 – 35 m along Line 1, all at the same x and y resolutions.

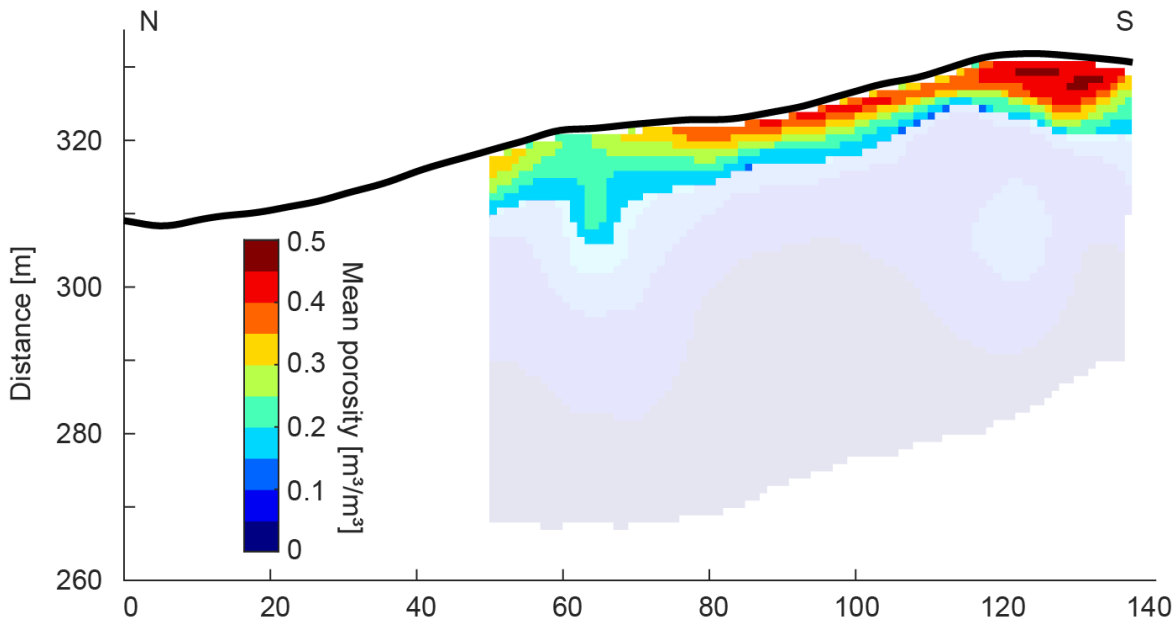

Figure B10. Results from Bayesian inversion of P-wave velocity (Vp) to porosity for Line 3. Areas shaded out have Vp > 1200 m/s characteristic of material less weathered than pervasively oxidized rock or saprolite and are excluded from the inversion. We also exclude the first 50 m of Line 3 due to observed shallow construction fill in that section.

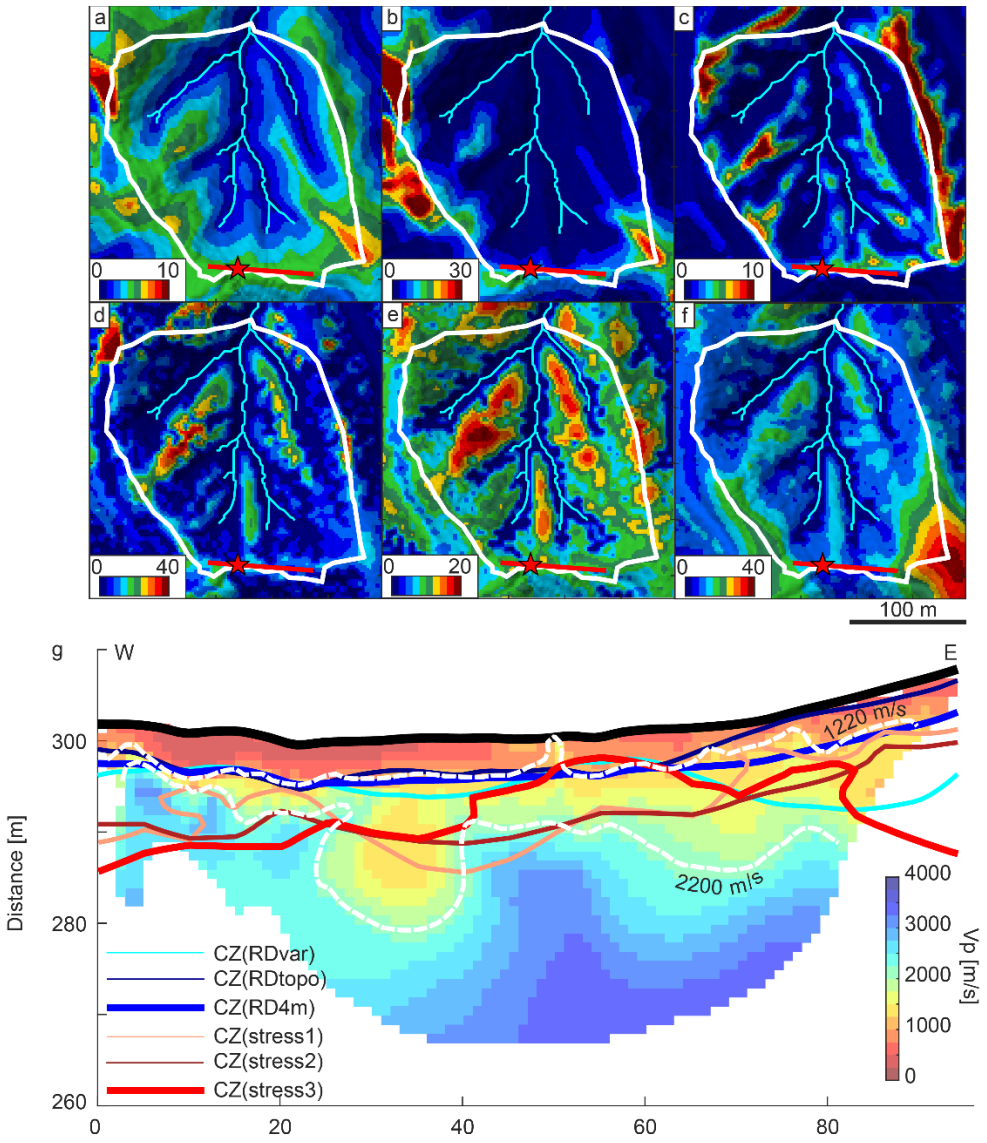

Figure B11. Modeled critical zone structures for (a) CZ(RD4m), (b) CZ(RDvar), and (c) CZ(RDtopo), (d) CZ(stress1), (e) CZ(stress2), and (f) CZ(stress3), same extent as Figure 1c. Color scale shows depth to unweathered bedrock in meters and is different for some structures to show variations. White outline is benchmark site, cyan lines are mapped channels, red star is location of 35 m-deep CB1 borehole, and red line is Line 4 P-wave velocity (Vp) survey. (g) Line 4 Vp profile showing predicted depth to unweathered boundary for critical zone models. Dashed white lines show Vp contours of 1220 and 2200 m/s.

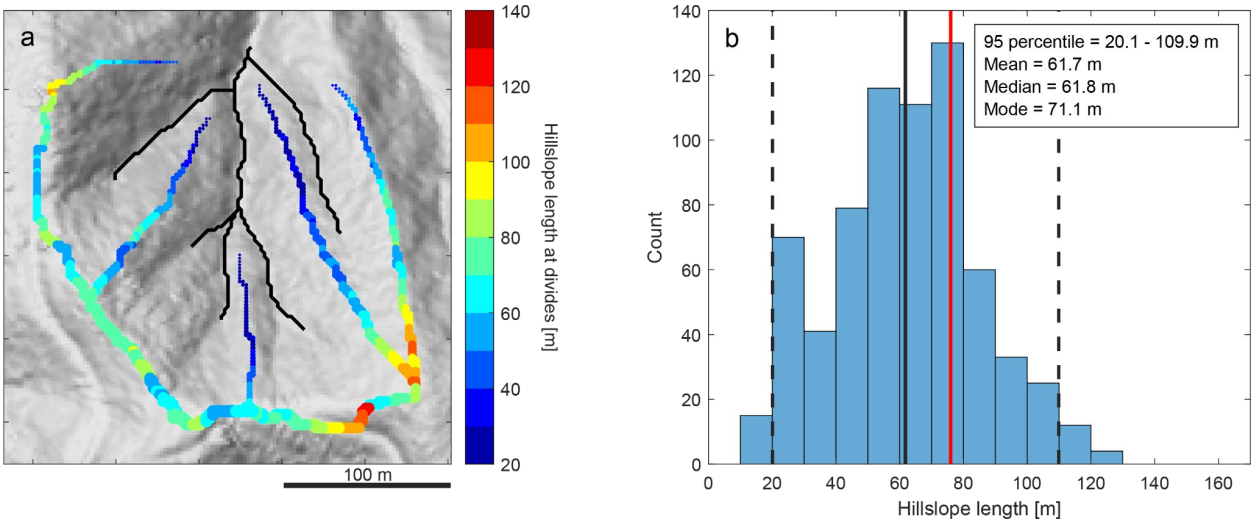

Figure B12. (a) Hillslope lengths of the benchmark site measured at drainage divides of Straher order one (Scherler and Schwanghart, 2020). Black lines are channels of a 1500 m^2 drainage area incision threshold used to calculate drainage divide locations. Same extent as Figure 3.1c. (b) Histogram of hillslope length at drainage divides. Y-axis is the count of 2 m-resolution cells in a map of hillslope length that coincides with a divide segment within each 10 m-wide bin. Dashed line is 95% confidence interval, black line is mean hillslope length, red line is a hillslope length of 76 m (Rempe and Dietrich, 2014).

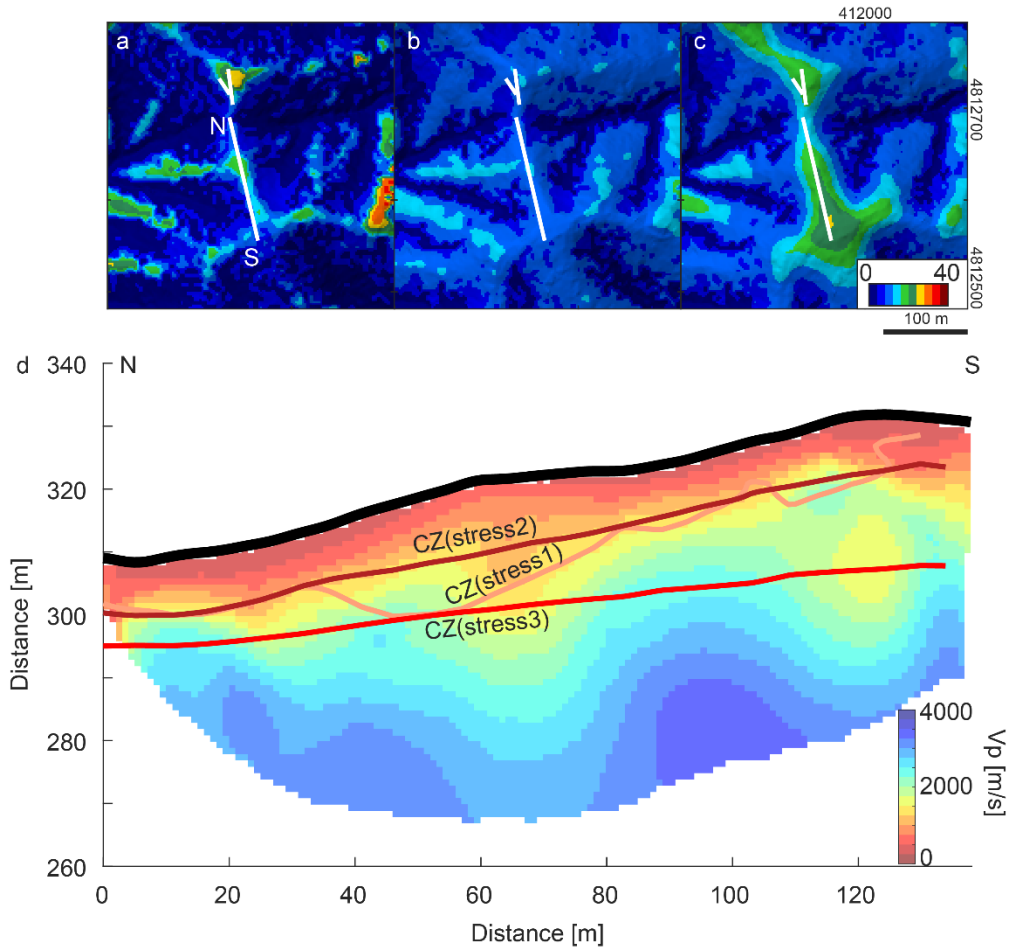

Figure B13. (a) CZ(stress1), (b) CZ(stress2), and (c) CZ(stress3) depth to unweathered bedrock maps in meters, with Lines 1, 2, and 3 shown as white lines. WGS84 UTM zone 10N. (d) Line 3 P-wave velocity (Vp) profile with lines indicating the top of unweathered bedrock for those three topographic stress weathering models.

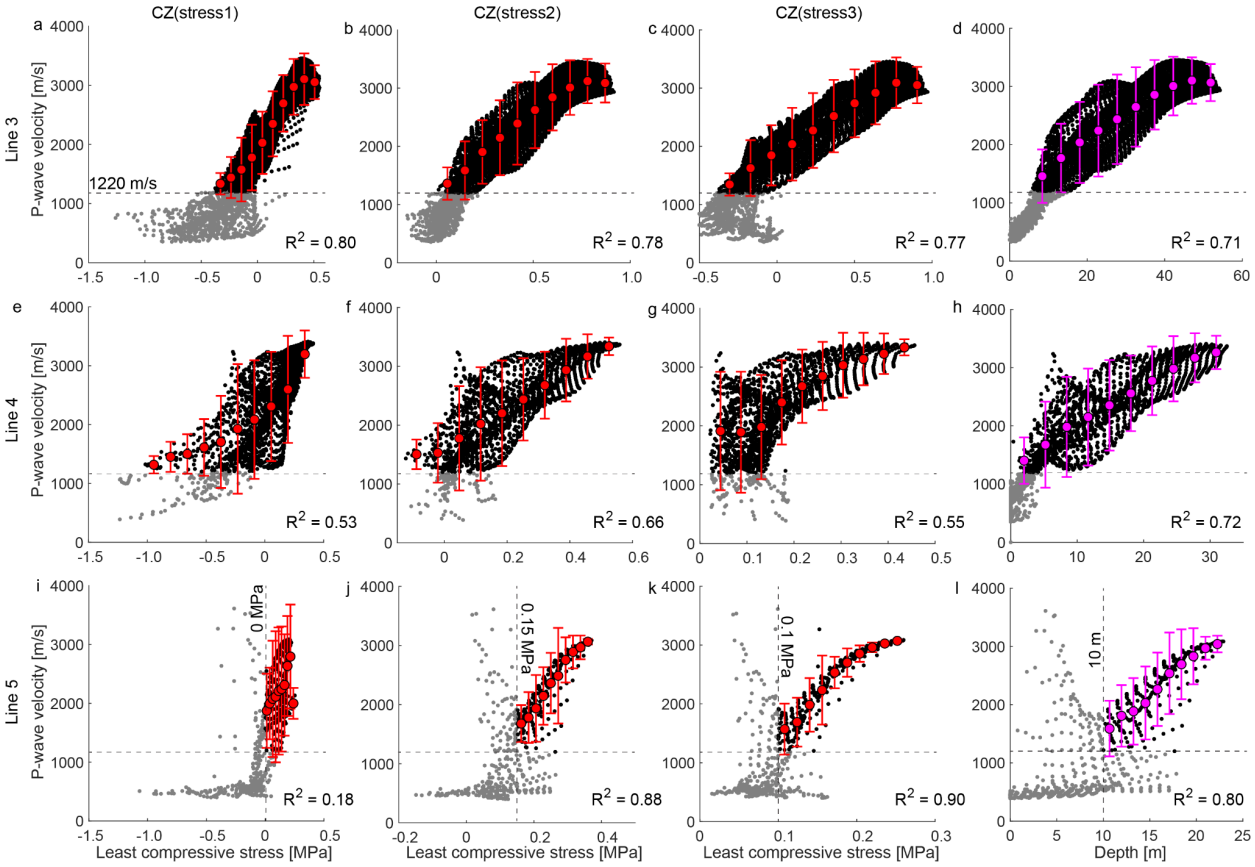

Figure B14. (a) Least compressive stress from CZ(stress1), (b) CZ(stress2), (c) CZ(stress3), and (d) depth against P-wave velocity along Line 3. Black points used in linear regression for binning in 10 equally spaced bins of widths depending on data range, two sigma error bars, and R^2 statistics. Gray points below a P-wave velocity of 1200 m/s are not used in regression due to association with saprolite and pervasively oxidized bedrock that may not be affected by topographic stress. (e – h) That for Line 4. (i – l) That for Line 5. (i), (j), (k), and (l) does not regress least compressive stresses less than 0 MPa, 1.5 MPa, and 1 MPa and depths less than 10 m, respectively, to not include large corestone in the regression. Note x-axis scales may be different to show trends.

Appendix B Tables

Table B1. Seismic refraction survey parameters.

Name	Date	Length [m]	# of geophones	Geophone spacing [m]	Shot spacing [m]	# start off-end shots	# end off-end shots
Line 1	31/05/2022	36	36	1	3	1	1
Line 2	31/05/2022	12	12	1	3	2	1
Line 3	01/06/2022	144	48	3	9	None	None
Line 4	27/05/2022	96	96	1	3	None	None
Line 5	28/05/2022	48	48	1	3	None	None

Table B2. Bayesian inversion parameters for seismic refraction surveys.

Name	Resolution [m]	Iterations	Mean misfit [ms]
Line 1	1	1 x 10^5	1.90
Line 2	1	1 x 10^5	0.97
Line 3	1	1 x 10^6	1.76
Line 4	1	1 x 10^6	1.26
Line 5	1	1 x 10^6	2.08

Table B3. Mineralogy and elastic properties for porosity inversion (Anderson et al., 2002; Mavko et al., 2009).

Mineralogy	Percentage*	Bulk modulus** [GPa]	Shear modulus** [GPa]	Density* [kg/m^3]
Quartz	50	37.0	44.0	2650
Feldspar	10	37.5	15.0	2620
Clay	40	25.0	9.0	2550

* Estimated from average of pervasively oxidized CB43, CB35, and CB33 (Anderson et al., 2002)

** From Mavko et al. (2009)

Table B4. Variation of mean porosity for sensitivity tests, testing all combinations of critical porosity (0.36 – 0.40 m^3/m^3, 0.01 m^3/m^3-increments; Dvorkin and Nur, 2005) and contact number (4 – 14 grains, 1-grain increments; Mavko et al., 2009; Murphy, 1982).

Name	95% confidence interval of mean porosity in sensitivity test [m3/m3]
Line 1	0.19 – 0.35
Line 3	0.19 – 0.35
Line 4	0.15 – 0.28

Table B5. Previously established parameters for the bedrock drainage model (Rempe and Dietrich, 2014).

Channel incision rate	0.1 mm/yr
Rock bulk density	2.65 g/cm^3
Soil bulk density	1.35 g/cm^3
Characteristic hillslope length	76 m
Soil diffusivity	0.005 m^2/yr
Critical slope	1.2 m/m
Hydraulic conductivity to porosity ratio	10^{-11} m/s

Table B6. Fourteen ambient tectonic stress measurements from the North American west coast for topographic stress modeling. All IDs with prefix wsm are from the 2016 World Stress Map (Heidbach et al., 2018), BH are from British Columbia (Brown and Hoek, 1978), and LH are from Central California (Lindner and Halpern, 1978). Minimum horizontal stresses = $\sigma^a h$, maximum horizontal stress = $\sigma^a H$, vertical stress = $\sigma^a V$. Compression positive. Capitalized reference abbreviations are defined by Heidbach et al. (2018).

ID	Latitude	Longitude	Depth	Minimum horizontal stress [MPa]	Maximum horizontal stress [MPa]	Vertical stress [MPa]	Regression weight	Reference 1	Reference 2
wsm00959	34.730	-117.780	0.49	10.4	16.6	14.3	1	HICKZO1988	
wsm01136	34.450	-117.870	0.79	19.3	35.2	23	1	ZOBATS1980B	
wsm04086	36.690	-121.350	0.182	7.7	13.8	5.3	1	ZOBATS1980B	
wsm04093	37.150	-119.000	0.16	6	9.7	2.8	1	HAIMXX1979	
wsm04036	46.438	-119.574	1.024	34.8	61.2	26.2	0.2	PAILKI1987	
wsm20464	46.580	-119.750	1.047	34.5	60.6	26.3	0.2	ADAMXX1987	PAILKI1987
wsm20465	46.607	-119.753	0.976	30.8	59.9	24.4	0.2	ADAMXX1987	PAILKI1987
wsm20466	46.492	-119.583	1.024	34.8	61.2	26.2	0.2	ADAMXX1987	PAILKI1987
wsm20467	46.567	-119.780	1.174	33	61.6	27.8	0.2	ADAMXX1987	PAILKI1987
BH61	55.984	-122.143	0.137	6.9	13.8	6.8	1	Brown and Hoek 1978	Imrie and Jory 1968
BH62	52.077	-118.565	0.22	6.44	12.88	6.9	1	Brown and Hoek 1978	Imrie and Campbell 1976
BH65	36.735	-119.788	0.3	4.9733	9.95	8.2	1	Brown and Hoek 1978	Haimson 1978
LH52	39.466	-121.000	0.1067	5.17	6.21	3.0093	1	Lindner and Halpern 1978	Merrill, Williamson, Rapehan, & Kruse 1964
LH69	38.567	-122.033	0.0762	4.31	6.22	2.1491	1	Lindner and Halpern 1978	Bureau of Reclamation (personal comm.)

Table B7. Rock elastic properties (Moon et al., 2017) and grid resolutions for Poly3D modeling.

Poisson's ratio	0.25
Young's modulus	$5x10^{10}$ Pa
Rock density	2650 kg/m^3
Cohesion	$3x10^5$ Pa
Unconfined compressive strength	$3x10^6$ Pa
Friction angle	20°
Eastern site grid dimensions (X x Y x Z)	67 x 67 x 70 cells 335 x 335 x 210 m
CB1 site grid dimensions (X x Y x Z)	64 x 64 x 99 cells 320 m x 320 m x 297 m

Table B8. Range of inverted P-wave velocities (Vp) and porosities for geophysical survey locations.

Name	95% confidence interval of Vp [m/s]	Mean inverted porosity [m3/m3]			95% confidence interval of porosity [m3/m3]
Line 1	415 – 2720	0.28	±	0.09	0.14 – 0.44
Line 2	1009 – 2766	N/A			N/A
Line 3	442 – 3351	0.28	±	0.09	0.16 – 0.45
Line 4	461 – 3355	0.22	±	0.10	0.10 – 0.48
Line 5	408 – 3040	N/A			N/A

Table B9. Statistics of depth to predicted weathered boundary in all variations of critical zone models.

Name	Mean depth [m]	95% confidence interval [m]	Depth at CB1 borehole [m]	Percent landscape < 0.5 m-deep [%]
CZ(RD4m)	2.9 ± 1.7	0.4 – 6.4	4.5	5.8
CZ(RDvar)	2.6 ± 5.9	0.0 – 15.1	4.9	58.9
CZ(RDtopo)	1.7 ± 2.2	0.0 – 7.6	4.2	43.6
CZ(stress1)	6.7 ± 7.6	0.0 – 26.9	8.5	27.8
CZ(stress2)	8.0 ± 4.9	0.0 – 17.2	9.5	12.9
CZ(stress3)	9.5 ± 6.7	0.0 – 25.9	9.1	11.5

Table B10. Mean and median P-wave velocity (Vp) along the boundary predicted by a critical zone model interpolated from the Line 4 Vp profile.

Model	Mean Vp [m/s]			Median Vp [m/s]
CZ(RD4m)	1327.7	±	123.1	1313.9
CZ(RDvar)	1462.9	±	273.0	1478.4
CZ(RDtopo)	1086.3	±	236.5	1127.9
CZ(stress1)	1958.7	±	516.3	1887.6
CZ(stress2)	1977.8	±	420.8	1952.3
CZ(stress3)	1695.4	±	482.0	1563.0

Table B11. Schmidt hammer rebound values taken horizontally, ordered by mean rebound value. Colors in lithology column delineate jumps in mean rebound value > 5. Gray cells in measured rebound values are measurements below instrument sensitivity. Red cells in measured rebound values highlight sites with < 8 measurements. n is number of measured rebound values.

Code	Easting	Northing	Lithology	Measured rebound values												n	Mean	Standard deviation	Coefficient of variation
BL1-1	409982	4812890	Sandstone saprolite	12	11	11	11	11	12	11	12	12	11	12		19**	10.8	0.8	0.07
SO2-1	411934	4812715	Sandstone weathered	12	12	12	18	12	12	10	10					8*	12.3	2.5	0.20
SO1-1	411930	4812733	Sandstone weathered	15	14	16	14	11	10	10	10					8*	12.5	2.5	0.20
SO2-4	411934	4812715	Sandstone weathered	16	16	16	12	10	10	10	10					8*	12.5	3.0	0.24
BL2-1	409982	4812890	Sandstone saprolite	13	13	14	12	16	12	15	13	13	16	14	14	12	13.8	1.4	0.10
SO1-2	411930	4812733	Sandstone weathered	15	16	12	14	14	14	15	14					8	14.3	1.2	0.08
SO2-2	411934	4812715	Sandstone weathered	16	16	18	15	18	16	14	10					8*	15.4	2.6	0.17
SO2-3	411934	4812715	Sandstone weathered	13	20	20	16	18	22	22	21					8	19.0	3.2	0.17
SO1-4	411930	4812733	Sandstone weathered	30	30	28	26	26	25	29	28					8	27.8	1.9	0.07
SO1-3	411930	4812733	Sandstone weathered	29	30	30	30	20	30	28	27					8	28.0	3.4	0.12
CS1-1	410011	4812910	Sandstone corestone	34	28	26	35	42								5†	33.0	6.3	0.19
HR1-1	411598	4813341	Sandstone fractured	27	37	30	33	35	32	30	34	40	38			10	33.6	4.0	0.12
CS2-1	410011	4812910	Sandstone corestone	27	30	33	27	37	38	42	35					8	33.6	5.4	0.16
SO1-5	411930	4812733	Sandstone nodule	52	50	52	45	48	52	52	52					8	50.4	2.6	0.05

* Includes measurements below instrument sensitivity (= 10)

** Includes eight measured rebound values of 10

† Only has five measurements (refer to Appendix B, Text B1)

Table B12. Schmidt hammer rebound values taken vertically, ordered by mean rebound value. Colors in lithology column delineate jumps in mean rebound value > 5. Gray cells in measured rebound values are measurements below instrument sensitivity. n is number of measured rebound values.

Code	Easting	Northing	Lithology	Measured rebound values												n	Mean	Standard deviation	Coefficient of variation
SL1-1	411945	4812631	Sandstone weathered	11	12	12	11	12	12	12	13	10	10			10*	11.5	1.0	0.08
SL2-1	411946	4812628	Sandstone weathered	13	14	16	14	14	13	12	16	15	15			10	14.2	1.3	0.09
SL4-1	411958	4812578	Sandstone weathered	14	13	17	16	15	15	14	13	14	14			10	14.5	1.3	0.09
SL3-1	411948	4812622	Sandstone weathered	16	16	15	16	15	14	16	15	16	15			10	15.4	0.7	0.05
SR1-1	411923	4812727	Sandstone weathered	28	28	25	28	32	25	30	31	18	24	25	23	12	26.4	3.9	0.15

* Includes measurements below instrument sensitivity (= 10)

Appendix B References

Anderson, S.P., Dietrich, W.E., Brimhall Jr, G.H., 2002. Weathering profiles, mass-balance analysis, and rates of solute loss: Linkages between weathering and erosion in a small, steep catchment. Geological Society of America Bulletin 114, 1143-1158. https://doi.org/10.1130/0016-7606(2002)114%3C1143:WPMBAA%3E2.0.CO;2

Bear, J., 1988. Dynamics of fluids in porous media, Dover, New York.

Brown, E.T., Hoek, E., 1978. Trends in relationships between measured in-situ stresses and depth, International Journal of Rock Mechanics and Mining Sciences & Geomechanics Abstracts. Pergamon, pp. 211-215.

Dvorkin, J., Nur, A., 2005. Critical-porosity models. Memoirs-American Association of Petroleum Geologists, 33-42.

Heidbach, O., Rajabi, M., Cui, X., Fuchs, K., Müller, B., Reinecker, J., Reiter, K., Tingay, M., Wenzel, F., Xie, F., 2018. The World Stress Map database release 2016: Crustal stress pattern across scales. Tectonophysics 744, 484-498. https://doi.org/10.1016/j.tecto.2018.07.007

Huang, M.H., Hudson‐Rasmussen, B., Burdick, S., Lekic, V., Nelson, M.D., Fauria, K.E., Schmerr, N., 2021. Bayesian Seismic Refraction Inversion for Critical Zone Science and Near‐Surface Applications. Geochemistry, Geophysics, Geosystems 22, e2020GC009172. https://doi.org/10.1029/2020GC009172

Lindner, E.N., Halpern, J.A., 1978. In-situ stress in North America: A compilation, International Journal of Rock Mechanics and Mining Sciences & Geomechanics Abstracts. Elsevier, pp. 183-203. https://doi.org/10.1016/0148-9062(78)91225-1

Mavko, G., Mukerji, T., Dvorkin, J., 2009. The rock physics handbook. Cambridge University Press, Cambridge, U.K.

Montgomery, D.R., Dietrich, W.E., Heffner, J.T., 2002. Piezometric response in shallow bedrock at CB1: Implications for runoff generation and landsliding. Water Resources Research 38, 10-11. https://doi.org/10.1029/2002WR001429

Moon, S., Perron, J., Martel, S., Holbrook, W., St. Clair, J., 2017. A model of three‐dimensional topographic stresses with implications for bedrock fractures, surface processes, and landscape evolution. Journal of Geophysical Research: Earth Surface 122, 823-846. https://doi.org/10.1002/2016JF004155

Murphy, W.F.I., 1982. Effects of microstructure and pore fluids on the acoustic properties of granular sedimentary materials. Stanford University.

Rempe, D.M., Dietrich, W.E., 2014. A bottom-up control on fresh-bedrock topography under landscapes. Proceedings of the National Academy of Sciences 111, 6576-6581. https://doi.org/10.1073/pnas.1404763111

Roering, J.J., Kirchner, J.W., Dietrich, W.E., 1999. Evidence for nonlinear, diffusive sediment transport on hillslopes and implications for landscape morphology. Water Resources Research 35, 853-870. https://doi.org/10.1029/1998WR900090

Scherler, D., Schwanghart, W., 2020. Drainage divide networks–Part 1: Identification and ordering in digital elevation models. Earth Surface Dynamics 8, 245-259. https://doi.org/10.5194/esurf-8-245-2020

Schwanghart, W., Scherler, D., 2014. TopoToolbox 2–MATLAB-based software for topographic analysis and modeling in Earth surface sciences. Earth Surface Dynamics 2, 1-7. https://doi.org/10.5194/esurf-2-1-2014

Thomas, A.L., 1993. POLY3D: A three-dimensional, polygonal element, displacement discontinuity boundary element computer program with applications to fractures, faults, and cavities in the earth's crust. Stanford University.

Appendix C for Chapter 4: Deep critical zone controls on shallow landslides: insights from numerical simulations in a steep, forested landscape

Text C1. Soil production

Following Bellugi et al. (2015a, 2015b) and citations therein, the rate of soil production that decays exponentially with depth is calculated as (Heimsath et al., 2001)

$$-\frac{\partial z_b}{t} = \varepsilon e^{-\alpha z cos(\theta)}, \quad \text{(C1)}$$

where the height of the soil-bedrock boundary above a datum is z_b [m], time is t [yr], vertical soil thickness is z [m], soil production rate at 0 m soil thickness is ε [m/yr] (0.000268 m/yr), the soil production rate constant is α [1/m] (0.0003 1/m; Heimsath et al., 2001), and topographic slope is θ [deg.]. Annual nonlinear soil flux per unit contour width q [m^2/yr] is calculated as (Roering et al., 1999)

$$q = \frac{D\nabla z_t}{1-(|\nabla z_t|/S_c)^2}, \quad \text{(C2)}$$

where the diffusion coefficient is D [m^2/yr] (0.0032 m^2/yr), topographic elevation above a datum is z_t [m], and critical slope is S_c [m/m] (1.25 m/m; Roering et al., 1999). The soil thickness of channels is set to a thin value of 0.02 m, assuming streams will remove all soil transported into them.

Text C2. Infinite-slope stability with and without groundwater seepage

We use outputs from GEOtop 2.0, soil thickness, and root strength to calculate a simple consideration of infinite-slope stability at the benchmark site without and with the effect of variable groundwater seepage (Iverson and Major, 1986). We calculate slope-parallel seepage infinite-slope factor of safety $FoS_{\infty sp}$ as

$$FoS_{\infty sp} = \frac{b^2 g[cos(\theta)(\rho_s z - \rho_w h)]tan(\phi) + b^2 C_b sec(\theta)}{b^2 g sin(\theta)\rho_s z}, \quad \text{(C3)}$$

and variable seepage infinite-slope factor of safety FoS_{∞} as

$$FoS_{\infty} = \frac{b^2 g[cos(\theta)(\rho_s z - \rho_w h) - \rho_w i_{mag} h cos(\lambda)]tan(\phi) + b^2 C_b sec(\theta)}{b^2 g[sin(\theta)(\rho_s z - \rho_w h) + \rho_w i_{mag} h sin(\lambda)]}, \quad \text{(C4)}$$

where cell size is b [m], gravitational acceleration is g [m/s^2], topographic slope is θ [deg.], soil density is ρ_s [kg/m^3] vertical soil thickness is z [m], water density is ρ_w [kg/m^3], pressure head above the base of soil is h [m], basal seepage vector magnitude is i_{mag} [m/m], the orientation of i_{mag} relative to slope is λ [deg.], soil friction angle is ϕ [deg.], and basal root cohesion is C_b [Pa]. We then subtract $FoS_{\infty} - FoS_{\infty sp}$ to determine the difference in factor of safety between both methods, where a negative value indicates variable seepage reduces factor of safety compared with slope-parallel seepage.

Text C3. Root cohesion

Local and global compilations show that root density and root cohesion in soils decrease with depth (e.g., Roering, 2008). Schmidt et al. (2001) examined the effect of roots on soil cohesion and landslides at CB1. The forest here was logged and replanted with Douglas fir in 1987 and 1988, respectively (Montgomery et al., 2000, 2009). Other plants include blue elderberry, thimbleberry, foxglove, and Himalayan blackberry (Schmidt et al., 2001). Within the CB1 landslide scarp, average root cohesion was estimated to be 4600 Pa (Schmidt et al., 2001). This cohesion is calculated using the Wu and Waldron model (WWM) assuming simultaneous root failure (Wu, 1976; Waldron, 1977; Wu et al., 1979).

Recent work improved modeling of root cohesion by considering the progressive breakage of root fiber bundles and redistribution of loads (hereafter the fiber bundle model [FBM]; Pollen and Simon, 2005) and the elasticity of root bundles (hereafter the root bundle model-Weibull [RBMw]; Schwarz et al., 2013). Updated values of average root cohesion at CB1 using the FBM and RBMw are 1200 Pa and 800 Pa, respectively (Cronkite-Ratcliff et al., 2022). Cronkite-Ratcliff et al (2022) suggests these lower average cohesion values result from removing the assumption in the WWM that all roots fail at once due to the summed cohesion of an entire root bundle. Previous studies suggest that lower root cohesions in landslide models would cause landslide number to increase, size to decrease, and location to shift upslope (Bellugi, 2012; Bellugi et al., 2015b).

Applying these two models using field data, we use an integral method to solve for parameters for the average basal C_{rb} [Pa] and lateral C_{rl} [Pa] root cohesion, calculated as (Milledge et al., 2014)

$$C_{rb} = C_{r0}e^{-zj}, \quad \text{(C5)}$$

$$C_{rb} = \frac{C_{r0}}{jz}(1 - e^{-zj}), \quad \text{(C6)}$$

where C_{r0} [Pa] is the maximum root cohesion at the surface, z [m] is failure plane depth (equivalent to soil depth at each cell), and j [m^{-1}] is an e-folding length scale. C_{r0} and j are obtained by fitting an exponential function to observations of root cohesion with depth reported by Montgomery et al. (2009) for the CB1 scar, such that the average root cohesion of the function approaches that reported in Cronkite-Ratcliff et al. (2022) for the FMB and RBMw. We integrate to a depth of 0.94 m following Milledge et al. (2014).

C_{r0} and j used in Bellugi et al. (2015a; 2015b), on which we base our landslide model, are 21,666 Pa and 4.96 m^{-1}, respectively. These values were obtained by the same exponential function integration described above, with the constraint that the average lateral root cohesion matches the value reported by Schmidt et al. (2001). Here, we find that best-fit C_{r0} and j for the FBM are 1647 Pa and 0.71 m^{-1}, respectively. Those for the RBMw are 1625 Pa and 1.74 m^{-1}, respectively. Applying the FBM and RBMw C_{r0} and j parameters in CZ(RD4m) as CZ(RD4m$_{FBM}$) and CZ(RD4m$_{RBMw}$), respectively, we find that landslide occurrence increases, size distributions gain heavier tails toward large landslides, and location shifts downslope, somewhat different from previous predictions that have smaller landslides that shift upslope (Figure C2; Bellugi, 2012). These applications overpredict landslide occurrence by the number and footprint of overlapping landslides compared to results from the WWM. Thus, we report WWM results in the Main Text. Although studies suggest the FBM and RBMw models more accurately represent root failure (Cronkite-Ratcliff et al., 2022), the stronger root strength from the WWM may capture bulk properties of soil cohesion. Several studies suggest interactions between root systems of different

trees and tree spacing may increase root cohesion, which we may capture with the WWM (e.g., Sakals and Sidle, 2004; Schwarz et al., 2010). See Milledge et al. (2014) for more details on the integral method.

Appendix C Figures

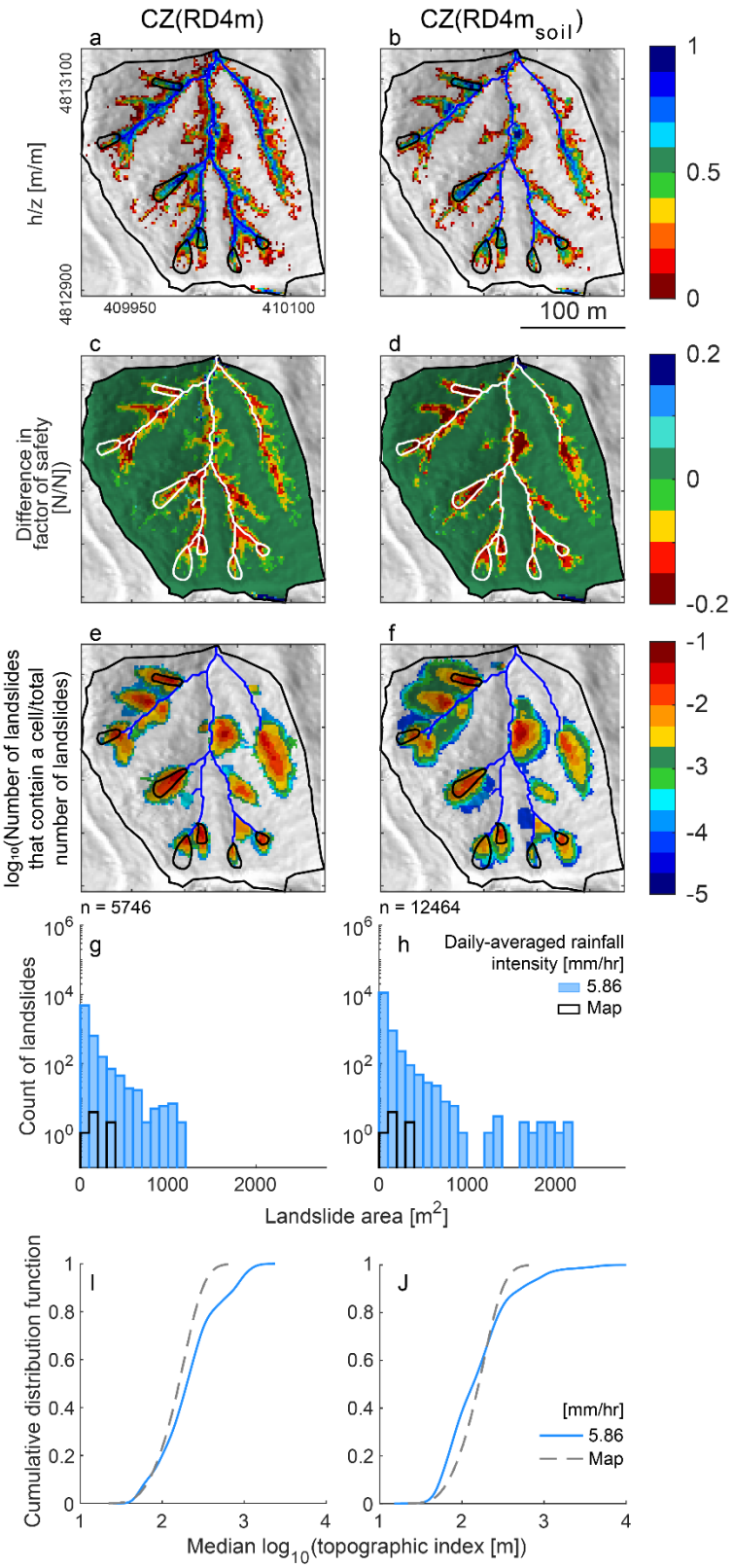

Figure C1. (a – b) Ratio of pressure head in soil h and soil thickness z, (c – d) infinite-slope factor of safety considering variable seepage vector orientation minus that considering surface-parallel flow, and (e – f) $\log_{10}$ of the number of unstable cell clusters including a specific cell, normalized by total number of landslides n for CZ(RD4m) and CZ($RD4m_{soil}$) at 18 November 1996 20:00. Blue lines = streams, black outlines = mapped landslides, large black outline = benchmark site. Streams and mapped landslides shown as white in (c – d). WGS84 UTM Zone 10N. (g – h) Histograms of modeled (blue) and mapped (black) landslide size and (i – j) cumulative distribution function of topographic index for all overlapping, unstable cell clusters at that time.

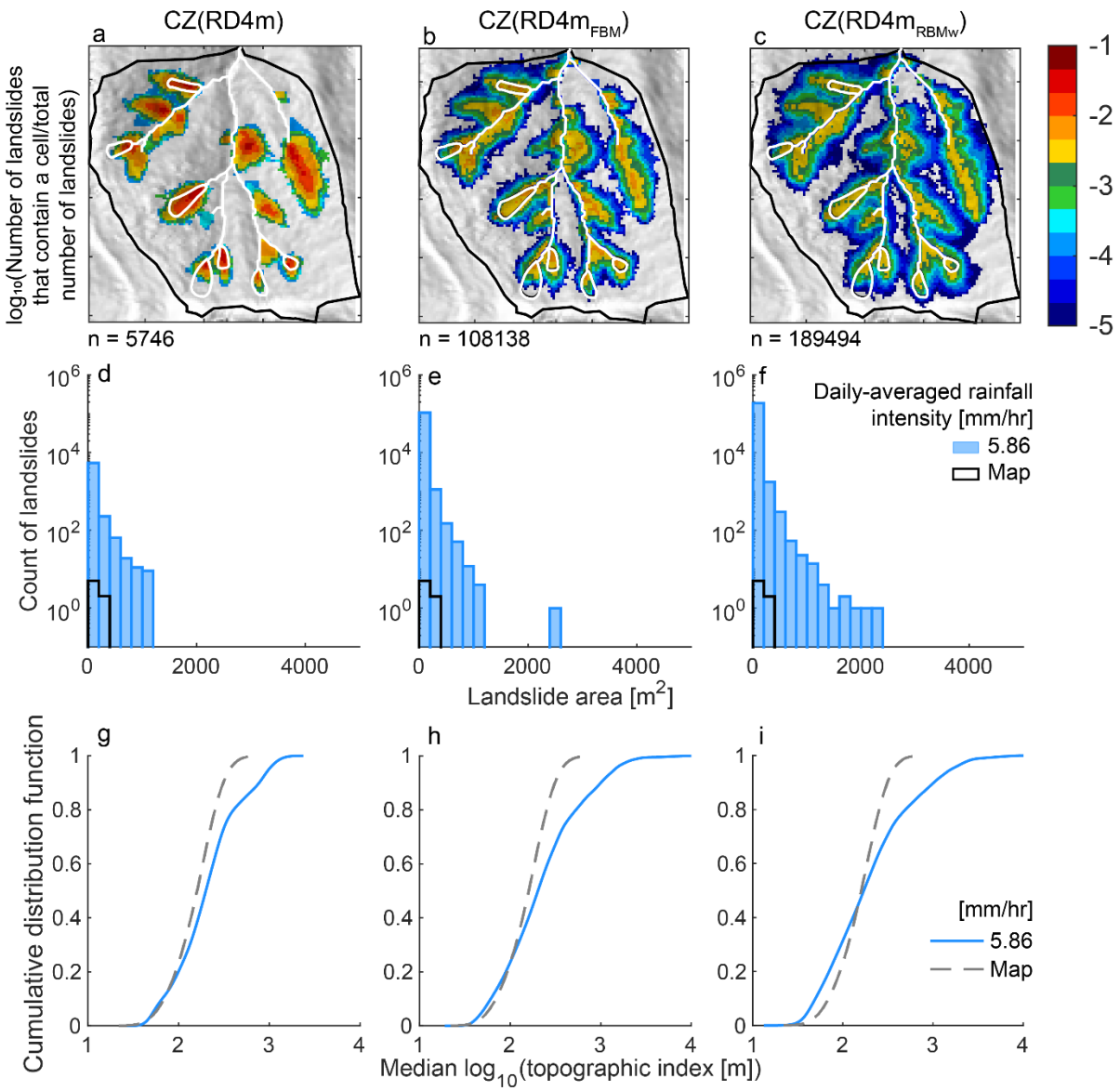

Figure C2. (a – c) $\log_{10}$ of the number of unstable cell clusters including a specific cell, normalized by total number of landslides n for CZ(RD4m), CZ(RD4m$_{FBM}$) using the fiber bundle model (FBM), and CZ(RD4m$_{RBMw}$) using the root bundle model-Weibull (RBMw) at 18 November 1996 20:00. Streams and mapped landslides shown as white lines. WGS84 UTM Zone 10N. (d – f) Histograms of modeled (blue) and mapped (black) landslide size and (g – i) cumulative distribution function of topographic index for all overlapping, unstable cell clusters at that time.

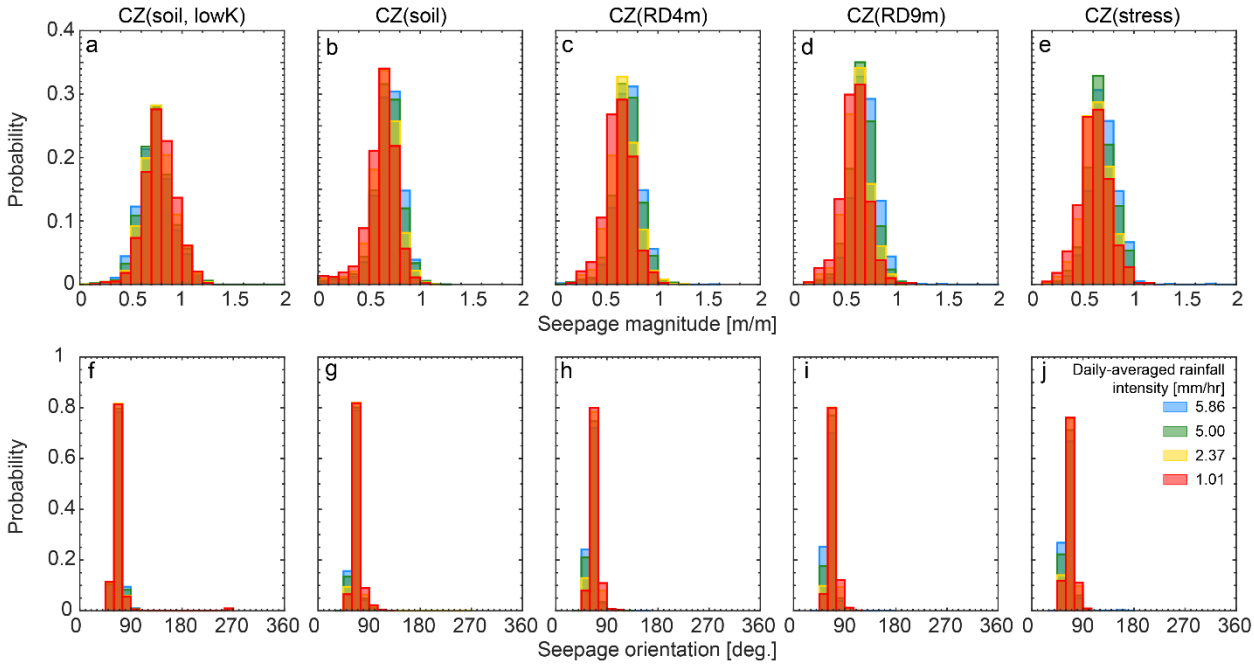

Figure C3. Histograms of (a – e) seepage magnitude i_{mag} in 0.1 m/m bins and (f – j) seepage vector orientation λ in 15° bins at daily-averaged rainfall intensities during the CB1 storm for different critical zone models.

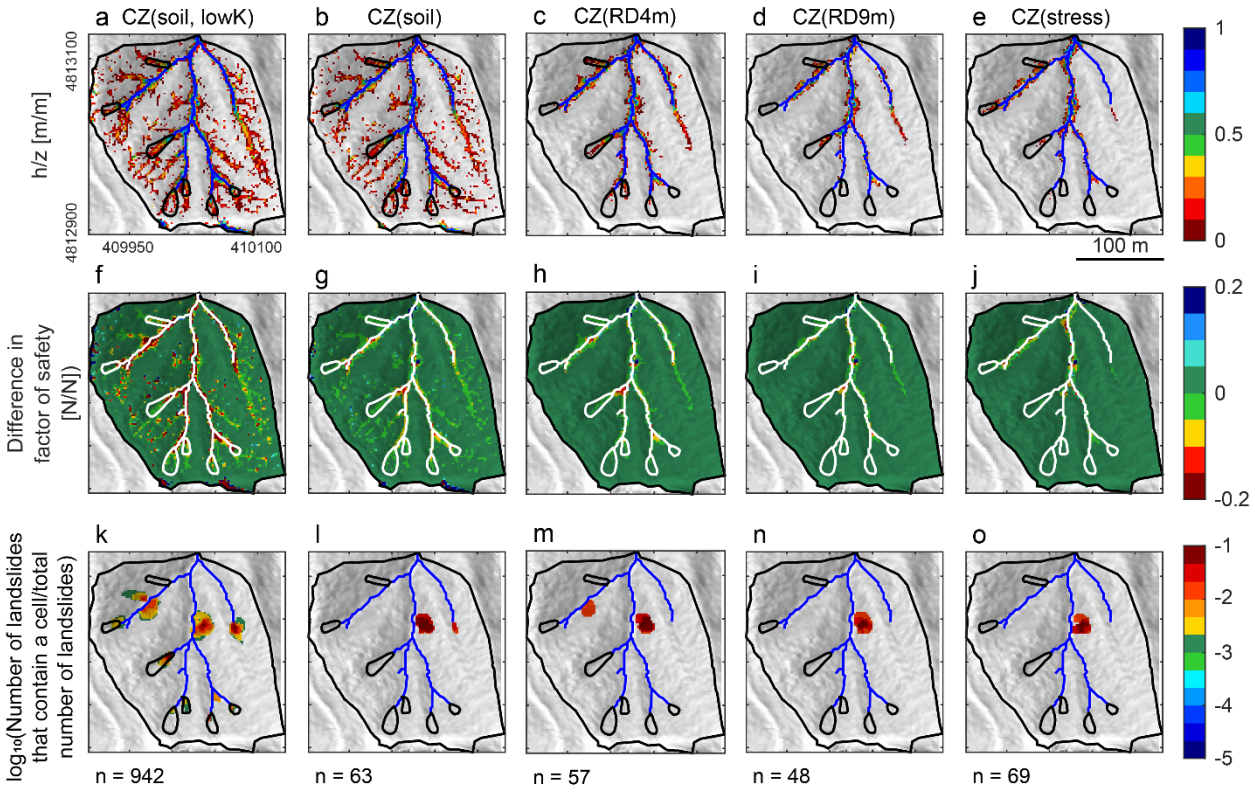

Figure C4. (a – e) Ratio of pressure head in soil *h* and soil thickness *z*, (f – j) infinite-slope factor of safety considering variable seepage vector orientation minus that considering surface-parallel flow, and (k – o) $\log_{10}$ of the number of unstable cell clusters including a specific cell, normalized by total number of landslides *n* for different critical zone models at 17 November 1996 20:00. This time corresponds to a daily-averaged rainfall of 1.01 mm/hr. Blue lines = streams, black outlines = mapped landslides, large black outline = benchmark site. Streams and mapped landslides shown as white in (f – j). WGS84 UTM Zone 10N.

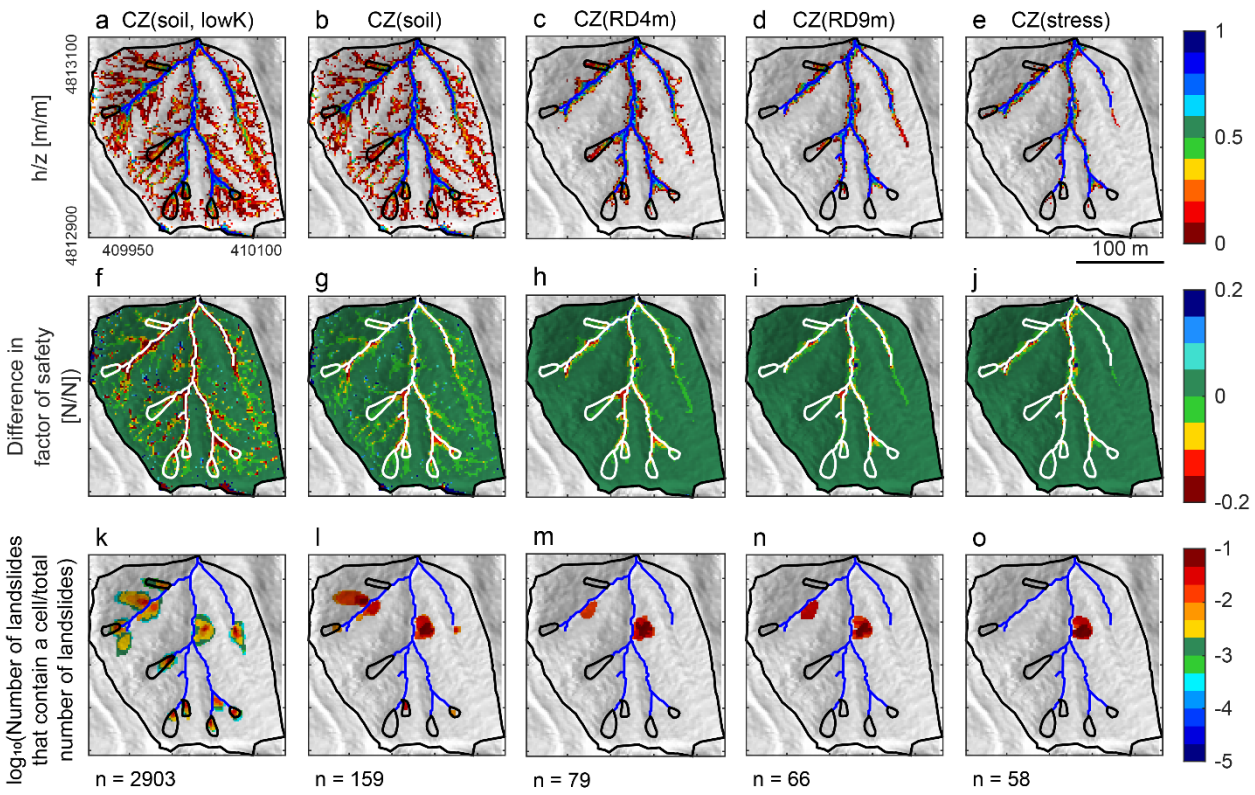

Figure C5. (a – e) Ratio of pressure head in soil *h* and soil thickness *z*, (f – j) infinite-slope factor of safety considering variable seepage vector orientation minus that considering surface-parallel flow, and (k – o) $\log_{10}$ of the number of unstable cell clusters including a specific cell, normalized by total number of landslides *n* for different critical zone models at 18 November 1996 06:00. This time corresponds to a daily-averaged rainfall of 2.37 mm/hr. Blue lines = streams, black outlines = mapped landslides, large black outline = benchmark site. Streams and mapped landslides shown as white in (f – j). WGS84 UTM Zone 10N.

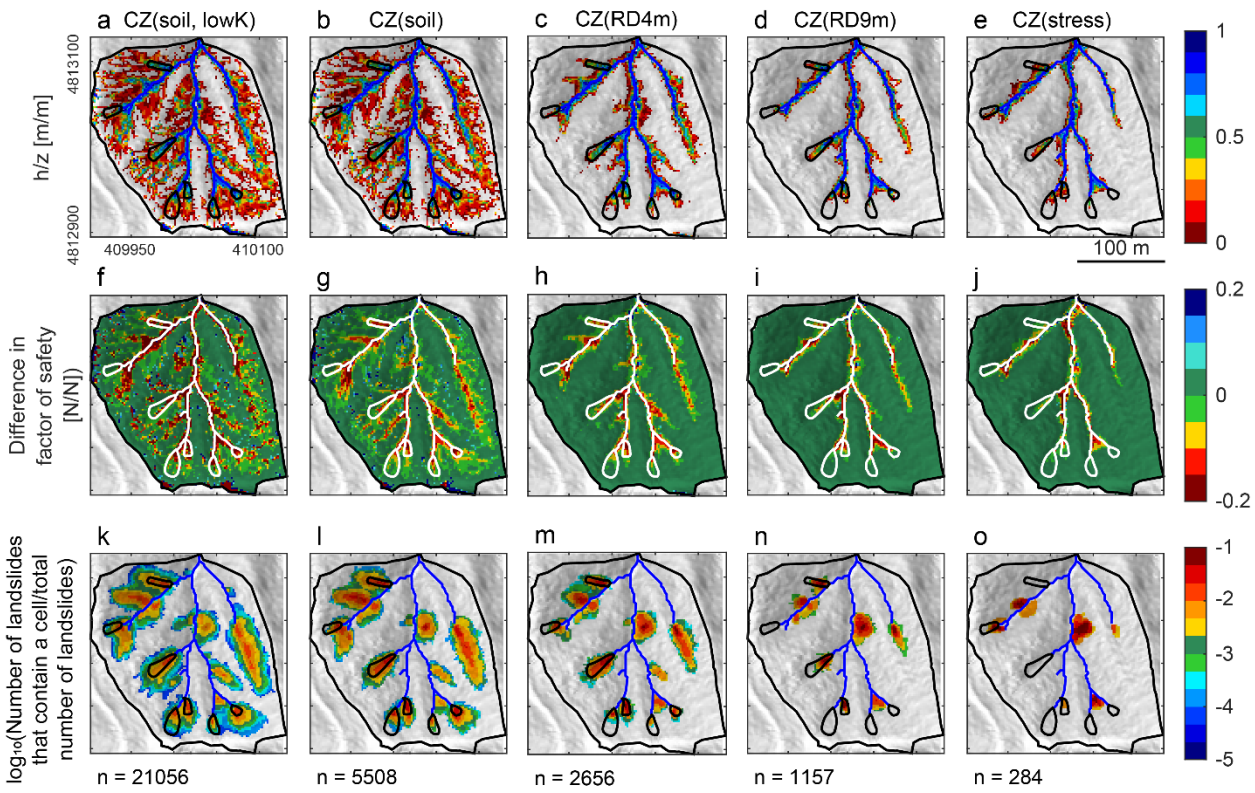

Figure C6. (a – e) Ratio of pressure head in soil h and soil thickness z, (f – j) infinite-slope factor of safety considering variable seepage vector orientation minus that considering surface-parallel flow, and (k – o) $\log_{10}$ of the number of unstable cell clusters including a specific cell, normalized by total number of landslides n for different critical zone models at 18 November 1996 18:00. This time corresponds to a daily-averaged rainfall of 5.00 mm/hr. Blue lines = streams, black outlines = mapped landslides, large black outline = benchmark site. Streams and mapped landslides shown as white in (f – j). WGS84 UTM Zone 10N.

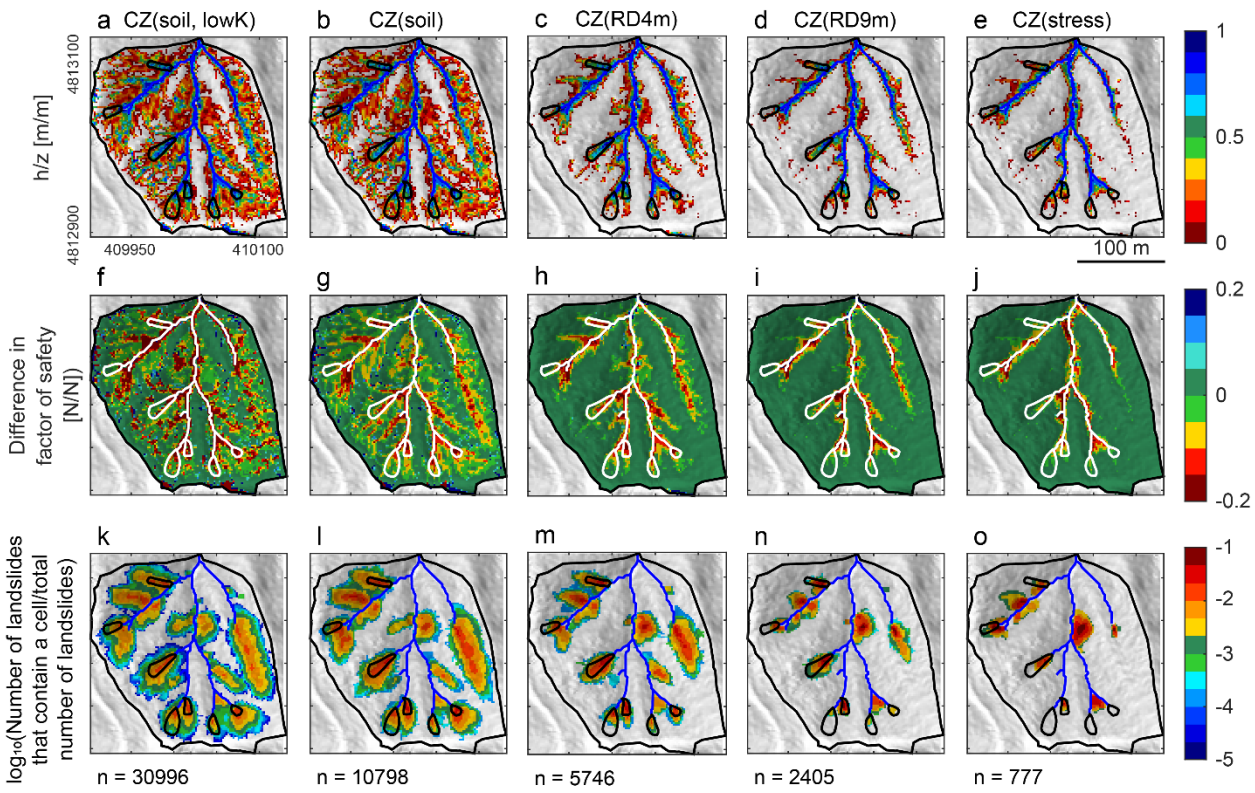

Figure C7. (a – e) Ratio of pressure head in soil h and soil thickness z, (f – j) infinite-slope factor of safety considering variable seepage vector orientation minus that considering surface-parallel flow, and (k – o) $\log_{10}$ of the number of unstable cell clusters including a specific cell, normalized by total number of landslides n for different critical zone models at 18 November 1996 20:00. This time corresponds to a daily-averaged rainfall of 5.86 mm/hr. Blue lines = streams, black outlines = mapped landslides, large black outline = benchmark site. Streams and mapped landslides shown as white in (f – j). WGS84 UTM Zone 10N.

Appendix C Tables

Table C1. Statistics for depth to unweathered bedrock at different critical zone models.

Name	Mean depth [m]			95% confidence interval [m]	Depth at CB1 borehole [m]	Percent landscape < 0.5 m-deep [%]
CZ(soil, lowK) & CZ(soil)	0.6	±	0.4	0.0 – 1.7	0.2	46.1
CZ(RD4m)	2.9	±	1.7	0.4 – 6.4	4.5	5.8
CZ(RD9m)	5.8	±	3.5	0.7 – 12.8	9	0.6
CZ(stress)	9.5	±	6.3	0.4 – 25.9	9.6	3.1

Table C2. Soil column discretization for GEOtop 2.0.

Depth interval [m]	Vertical cell resolution [m]	Number of cells
0 – 2.5	0.05	50
2.5 – 3.5	0.1	10
3.5 – 5.5	0.2	10
5.5 – 23.5	0.3	60
23.5 – 40	0.5	33

Table C3. Hydrologic properties of critical zone used for GEOtop 2.0 (Anderson et al., 2002; Ebel et al., 2007a; Ebel et al., 2007b; Endrizzi et al., 2014; Torres et al., 1998)

Layer	Residual water content [m^3/m^3]	Saturated water content [m^3/m^3]	Field capacity [m^3/m^3]	a [1/m]	N [-]	Specific storativity [1/m]	Porosity [m^3/m^3]	Saturated hydraulic conductivity [m/s]
Soil	0.25	0.45	0.3	0.018	2.8	$1x10^{-7}$	0.5	$3x10^{-4}$
Weathered bedrock	0.08	0.15	0.1	0.004	1.25	$1x10^{-7}$	0.15	$7x10^{-5}$
Unweathered bedrock	0.08	0.15	0.1	0.004	1.25	$1x10^{-7}$	0.12	CZ(soil, lowK) $5x10^{-12}$ or all else $5x10^{-7}$

Table C4. Soil seepage magnitude and orientation for different critical zone models at the time of the CB1 landslide at the soil-weathered bedrock boundary.

Model	Percent benchmark saturated [%]	Mean seepage magnitude [m/m]	Seepage magnitude 95% confidence interval [m/m]	Mean seepage orientation [deg.]	Seepage orientation 95% confidence interval [deg.]
CZ(soil, lowK)	68.4	0.7 ± 0.3	0.4 - 1.1	68.1 ± 15.0	56.2 – 85.7
CZ(soil)	65.6	0.7 ± 0.1	0.4 – 0.9	65.5 ± 7.9	55.0 – 82.8
CZ(RD4m)	31.7	0.7 ± 0.1	0.4 - 1.0	64.0 ± 7.0	53.4 – 78.3
CZ(RD9m)	21.4	0.7 ± 0.1	0.4 – 0.9	64.0 ± 7.2	53.0 – 78.8
CZ(stress)	17.5	0.7 ± 0.2	0.4 - 1.0	64.5 ± 9.9	51.7 – 81.6

Table C5. Landslide number and area from spectral search algorithm coupled with a slope stability model for different critical zone models at the time of the CB1 landslide.

Model	Number of unstable cell clusters	Area of benchmark unstable [sq. m]	Percent benchmark predicted unstable [%]	Percent benchmark with factor of safety reduction [%]
CZ(soil, lowK)	30996	21640	55.9	52.7
CZ(soil)	10798	17356	44.8	52.3
CZ(RD4m)	5746	10828	28.0	28.1
CZ(RD9m)	2405	5240	13.5	18.8
CZ(stress)	777	3564	9.2	15.2

Table C6. Landslide size and topographic indices from spectral search algorithm coupled with a slope stability model for different critical zone models at the time of the CB1 landslide.

Model	Mean landslide size [sq. m]	95% confidence interval of landslide size [sq. m]	Mean topographic index $\log_{10}$([m])	95% confidence interval of topographic index $\log_{10}$([m])
CZ(soil, lowK)	59.1 ± 110.2	4.0 - 364.0	2.33 ± 0.36	1.72 - 3.08
CZ(soil)	84.4 ± 135.3	12.0 - 450.2	2.27 ± 0.33	1.70 - 3.01
CZ(RD4m)	67.6 ± 96.5	12.0 - 339.4	2.32 ± 0.36	1.70 - 3.06
CZ(RD9m)	48.0 ± 56.6	12.0 - 184.0	2.38 ± 0.43	1.70 - 3.16
CZ(stress)	58.6 ± 67.3	12.0 - 260.0	2.15 ± 0.44	1.67 - 3.07

Appendix C References

Bellugi, D., 2012. What controls shallow landslide size across landscapes? University of California, Berkeley.

Bellugi, D., Milledge, D.G., Dietrich, W.E., Perron, J.T., McKean, J., 2015. Predicting shallow landslide size and location across a natural landscape: Application of a spectral clustering search algorithm. Journal of Geophysical Research: Earth Surface 120, 2552-2585. https://doi.org/10.1002/2015JF003520

Cronkite-Ratcliff, C., Schmidt, K.M., Wirion, C., 2022. Comparing Root Cohesion Estimates from Three Models at a Shallow Landslide in the Oregon Coast Range. GeoHazards 3, 428-451. https://doi.org/10.3390/geohazards3030022

Milledge, D.G., Bellugi, D., McKean, J.A., Densmore, A.L., Dietrich, W.E., 2014. A multidimensional stability model for predicting shallow landslide size and shape across landscapes. Journal of Geophysical Research: Earth Surface 119, 2481-2504. https://doi.org/10.1002/2014JF003135

Montgomery, D.R., Schmidt, K.M., Dietrich, W.E., McKean, J., 2009. Instrumental record of debris flow initiation during natural rainfall: Implications for modeling slope stability. Journal of Geophysical Research: Earth Surface 114. https://doi.org/10.1029/2008JF001078

Montgomery, D.R., Schmidt, K.M., Greenberg, H.M., Dietrich, W.E., 2000. Forest clearing and regional landsliding. Geology 28, 311-314. https://doi.org/10.1130/0091-7613(2000)28%3C311:FCARL%3E2.0.CO;2

Pollen, N., Simon, A., 2005. Estimating the mechanical effects of riparian vegetation on stream bank stability using a fiber bundle model. Water Resources Research 41. https://doi.org/10.1029/2004WR003801

Rempe, D.M., Dietrich, W.E., 2014. A bottom-up control on fresh-bedrock topography under landscapes. Proceedings of the National Academy of Sciences 111, 6576-6581. https://doi.org/10.1073/pnas.1404763111

Sakals, M., Sidle, R.C., 2004. A spatial and temporal model of root cohesion in forest soils. Canadian Journal of Forest Research 34, 950-958. https://doi.org/10.1139/x03-268

Schmidt, K., Roering, J., Stock, J., Dietrich, W., Montgomery, D., Schaub, T., 2001. The variability of root cohesion as an influence on shallow landslide susceptibility in the Oregon Coast Range. Canadian Geotechnical Journal 38, 995-1024. https://doi.org/10.1139/t01-031

Schwarz, M., Giadrossich, F., Cohen, D., 2013. Modeling root reinforcement using a root-failure Weibull survival function. Hydrology and Earth System Sciences 17, 4367-4377. https://doi.org/10.5194/hess-17-4367-2013

Schwarz, M., Lehmann, P., Or, D., 2010. Quantifying lateral root reinforcement in steep slopes–from a bundle of roots to tree stands. Earth Surface Processes and Landforms: The Journal of the British Geomorphological Research Group 35, 354-367. https://doi.org/10.1002/esp.1927

Waldron, L., 1977. The shear resistance of root-permeated homogeneous and stratified soil. Soil Science Society of America Journal 41, 843-849. https://doi.org/10.2136/sssaj1977.03615995004100050005x

Wu, T.H., 1976. Investigation of landslides on Prince of Wales Island, Alaska, Alaska Geotechnical Report. Report, Department of Civil Engineering, Ohio State University.

Wu, T.H., McKinnell III, W.P., Swanston, D.N., 1979. Strength of tree roots and landslides on Prince of Wales Island, Alaska. Canadian Geotechnical Journal 16, 19-33. https://doi.org/10.1139/t79-003